University of Cyprus

Department of Mechanical and Manufacturing Engineering

Fabrication, Characterization and Applications of Electrospun Polymer-based Nanocomposite Membranes

Ph.D. Thesis

Ioanna Savva

2014

University of Cyprus

Department of Mechanical and Manufacturing Engineering

Fabrication, Characterization and Applications of Electrospun Polymer-based Nanocomposite Membranes

Ioanna Savva

A dissertation submitted in partial fulfillment of the requirements for the degree of Doctor of Philosophy at the University of Cyprus

September 2014

University of Cyprus

Department of Mechanical and Manufacturing Engineering

Fabrication, Characterization and Applications of Electrospun Polymer-based Nanocomposite Membranes

by

Ioanna Savva

A dissertation submitted in partial fulfillment of the requirements for the degree of Doctor of Philosophy in Mechanical and Manufacturing Engineering

Doctoral Committee

Constantinos Tsitsilianis

Maria Vamvakaki

Ioannis Giapintzakis

Theodora Kyratsi

Theodora Krasia-Christoforou

September 2014

Ioanna Savva

Fabrication, Characterization and Applications of Electrospun Polymer-based Nanocomposite Membranes

This Ph.D Thesis has been carried out in partial fulfillment of the requirements for the degree of Doctor of Philosophy at the Department of Mechanical and Manufacturing Engineering and approved on the 30th September, 2014 by the Doctoral Committee

Doctoral Committee

Research advisor: Theodora Krasia-Christoforou, Assistant Professor

Other members:

Constantinos Tsitsilianis, Professor, Department of Chemical Engineering, University of Patras, Greece

Maria Vamvakaki, Associate Professor, Department of Materials Science and Technology, University of Cretes, Crete, Greece

Ioannis Giapintzakis, Professor, Department of Mechanical and Manufacturing Engineering, University of Cyprus, Cyprus

Theodora Kyratsi, Associate Professor, Department of Mechanical and Manufacturing Engineering, University of Cyprus, Cyprus

Approval of Doctoral Committee

Constantinos Tsitsilianis: .....

Maria Vamvakaki: .....

Ioannis Giapintzakis: .....

Theodora Kyratsi: .....

Theodora Krasia-Christoforou: .....

This dissertation is dedicated to all the people I love and appreciate…

Acknowledgments

Reaching the end of my Ph.D, I would like to express my gratitude to everyone who helped me, each one in their own way, to achieve this goal. First and foremost, I would like to show my deepest gratitude and appreciation to my supervisor, Dr. Theodora Krasia-Christoforou for her support professional and moral, as well as her endless interest and guidance throughout the years we have worked together. She has supported me in a number of ways during the experimental work and the hard writing-up period. I have learned a lot of things from her and her enthusiasm, that was highly motivational, prompted me to try harder for the best even during tough periods.

Furthermore I would like to thank my co-workers in the Polymers laboratory of the Mechanical and Manufacturing Engineering department and especially Dr. Petri Papaphilippou, Dr. Maria Demetriou and Dr. Mariliz Achilleos, for their cooperation and friendship. They have been always very helpful and good advisors in many situations. Besides the perfect collaboration and understanding between us, a nice friendship was also developed and I really hope that this friendship will last for many years.

I would also like to thank all the people whose contribution in this work was valuable:

Prof. Ladislau Vekas (University Politechnica Timisoara, Romania), Ms. Oana Marinica (Research Center for Engineering of Systems with Complex Fluids, University ‘‘Politehnica’’ Timisoara, Timisoara, Romania) and Ms. Alina Taculescu (Center for Fundamental and Advanced Technical Research from Timisoara of the Romanian Academy), for the magnetic characterization experiments and for kindly providing us the OA.Fe_3O_4 NPs.

Prof. Panayiotis Koutentis (Department of Chemistry, University of Cyprus) and Dr. Andreas Kalogirou for performing the catalytic experiments in selected organic reactions employing our materials as heterogeneous catalytic supports. We also thank this group for

providing access to the TGA and DSC apparatus and especially Ms. Styliana Mirallai for her assistance.

Regarding the TGA measurements we are also grateful to Prof. Konstantinos Chrissafis (Department of Physics, Aristotle University of Thessaloniki, Greece) for performing the TGA analysis in some of the MMA-*co*-AEMA systems.

Prof. Ioannis Paschalidis (Department of Chemistry, University of Cyprus) and especially the Ph.D candidate Maria Efstathiou for their collaboration in the evaluation of the prepared membranes as adsorbents for heavy metal ions.

Dr. Andreani Odysseos from the Biomedical Tissue Engineering/Nanobiotechnology Lab, EPOS-Iasis R&D, for her valuable help with the preparation of the biological media used in the drug delivery experiments.

Prof. Costas Patrickios and his research group (Department of Chemistry, University of Cyprus), for providing access to the DSC apparatus.

Dr. Theodora Kyratsi and her group (Department of Mechanical and Manufacturing Engineering, University of Cyprus), for their assistance with the XRD measurements.

Prof. Ioannis Giapintzakis and especially the Ph.D candidate Charis Orfanidou (Department of Mechanical and Manufacturing Engineering, University of Cyprus) for providing access to the sputtering unit and for their assistance.

Dr. Eugeniu Vasile (University Politehnica of Bucharest, Faculty of Applied Chemistry and Material Science, Department of Oxide Materials and Nanomaterials, Bucharest, Romania) and Ms. Eugenia Vasile (University Politehnica of Bucharest, Faculty of Medical Engineering, Department of Bioengineering and Biotechnology) for carrying out the TEM measurements.

Dr. Yiannis Sarigiannis (Department of Materials Science, University of Patras) for performing the magnetic hyperthermia experiments and Dr. Aristides Bakandritsos (Department of Materials Science, University of Patras) for useful discussions.

We also thank the University of Cyprus and the Cyprus Research Promotion Foundation and the programs NEAYPODOMH/NEKYP/0308/02, KOINA/MNT-ERA.NET/0311/01 and KY-POY/0609/01 for financial support.

Finally, I would like to thank my partner Melios Price for his tireless patience throughout these years, his moral support and his understanding in times when the mind wandered to the laboratory and research. Lastly I would like to show my gratitude to my family, Savvas, Andri, Nikoletta, Spyros, and Savvia for their understanding, patience, and support moral and financial. I am grateful for their irreplaceable contribution, support and help...

Περίληψη

Η παρούσα διδακτορική διατριβή επικεντρώνεται στην παρασκευή (με τη μέθοδο της ηλεκτρόκλωσης), το χαρακτηρισμό και τις εφαρμογές καινοτόμων πολυμερικών ινωδών μεμβρανών. Συγκεκριμένα παρασκευάστηκαν διαφορετικά είδη πολυμερικών μεμβρανών νανοσύνθετων και μη, όπου το κάθε σύστημα στόχευε και σε συγκεκριμένη εφαρμογή, βάσει των ξεχωριστών ιδιοτήτων του. Η πρώτη ομάδα πολυμερικών μεμβρανών ήταν βασισμένη στο υδρόφιλο και βιοσυμβατό ομοπολυμερές πολυαιθυλενοξείδιο, και στο υδρόφοβο και βιοαποικοδομήσιμο πολυλακτικό οξύ καθώς επίσης και σε προπαρασκευασμένα νανοσωματίδια μαγνητίτη επικαλυμμένα με ολεϊκό οξύ. Οι μεμβράνες αυτές μελετήθηκαν τόσο σε βιοϊατρικές όσο και σε περιβαλλοντικές εφαρμογές. Συγκεκριμένα, μελετήθηκε η ικανότητα χρησιμοποίησής τους σαν συστήματα ελεγχόμενης απελευθέρωσης της φαρμακευτικής ουσίας παρακεταμόλης σε υδατικά διαλύματα, τόσο στην παρουσία όσο και στην απουσία μαγνητικών νανοσωματιδιων. Επιπλέον η ύπαρξη μαγνητικών νανοσωματιδίων σε αυτές τις μεμβράνες επέτρεψε τη μελέτη τους σε διεργασίες μαγνητικής υπερθερμίας υπό την επίδραση εναλλασσόμενου μαγνητικού πεδίου. Όσο αφορά τις περιβαλλοντικές εφαρμογές οι προαναφερθέντες μεμβράνες μελετήθηκαν ως υποστρώματα για τη δέσμευση επιβλαβών μεταλλοϊόντων (θορίου, ουρανίου, ευρωπίου) και του οργανικού ρύπου πράσινου του μαλαχίτη από υδατικά διαλύματα. Η δεύτερη ομάδα πολυμερικών μεμβρανών ήταν βασισμένη σε λειτουργικά μεθακρυλικά συμπολυμερή που περιείχαν ομάδες β-κετοεστέρα και αρωματικούς δακτυλίους στις δομές τους τα οποία συντέθηκαν με χρήση του πολυμερισμού ελευθέρων ριζών. Λειτουργικές μεμβράνες αυτού του τύπου παρασκευάστηκαν τόσο στην απουσία όσο και στην παρουσία μαγνητικών νανοσωματιδίων με την τεχνική της ηλεκτρόκλωσης στοχεύοντας στη δέσμευση επιβλαβών μεταλλοϊόντων καθώς επίσης και στη δέσμευση των οργανικών ρύπων μετρονιδαζόλης και 1,2 διχλωροβενζόλιου από υδατικά διαλύματα. Τέλος παρασκευάστηκαν πολυμερικές ινώδεις μεμβράνες βασισμένες στο υδατοδιαλυτό ομοπολυμερές πολυβινυλοπυρρολιδόνη. Ανάμεσα σε άλλα η πολυβινυλοπυρρολιδόνη συνδυάστηκε με μεταλλικά νανοσωματίδια παλλαδίου και οξειδίου του χαλκού (Ι) οδηγώντας σε καινοτόμες μεμβράνες με ικανότητα χρήσης ως ετερογενή καταλυτικά υποστρώματα σε επιλεγμένες οργανικές αντιδράσεις. Για την εξεύρεση των βέλτιστων συνθηκών και την επιτυχή παρασκευή όλων των μεμβρανών διεξήχθηκε συστηματική μελέτη και μεταβολή διαφόρων πειραματικών παραμέτρων που αφορούσαν τη διαδικασία της ηλεκτρόκλωσης. Οι παραγόμενες μεμβράνες χαρακτηρίστηκαν ως προς τη σύσταση τους, τα μορφολογικά και θερμικά τους χαρακτηριστικά καθώς και ως προς τις μαγνητικές τους ιδιότητες στην περίπτωση των νανοσύνθετων μεμβρανών που περιείχαν μαγνητικά νανοσωματίδια.

Abstract

The present Ph.D. thesis focuses on the fabrication (by means of the electrospinning technique), characterization and applications of novel polymer fibrous membranes. More precisely, different types of pristine polymer and polymer-based organic-inorganic nanocomposite membranes were prepared, aiming toward their evaluation in different applications depending on their properties. The first type of polymer membranes was based on the hydrophilic and biocompatible polyethylene oxide (PEO) and the hydrophobic and biodegradable poly(L-lactic acid) ((PLLA) combined with pre-formed oleic acid-coated magnetite nanoparticles ($OA.Fe_3O_4$). These membranes - containing or not $OA.Fe_3O_4$ - were evaluated in biomedical and environmental applications. More precisely, their applicability in controlled drug delivery was investigated by employing paracetamol as a proof-of-concept pharmaceutical. In the case of the magnetite-containing membranes, the presence of the $OA.Fe_3O_4$ allowed for their investigation in magnetic hyperthermia processes when placed under an alternating magnetic field. As far as environmental applications is concerned, the aforementioned membranes were evaluated as adsorbents for harmful metal ions (thorium, uranium, europium) and for the organic dye malachite green (MG) from aqueous media. The second membrane type was based on functional methacrylic copolymers possessing β-ketoester and aromatic side-chain moieties, prepared by free radical polymerization. Functional electrospun membranes were fabricated in the absence and presence of $OA.Fe_3O_4$, aiming toward their evaluation as adsorbents for the removal of harmful metal ions and organic pollutants namely metronidazole and 1,2-dichlorobenzene from aqueous media. The third type of electrospun fibrous polymer membranes was based on the hydrophilic homopolymer polyvinyl pyrrolidone (PVP). Among others, PVP was combined with metal (Pd) and metal oxide (Cu_2O) nanoparticles resulting to the generation of polymer-based nanocomposite electrospun membranes that were further evaluated as heterogeneous catalytic substrates in selective organic reactions. The successful generation of fibrous membranes required the determination of the optimal experimental parameters involved in the electrospinning process. The obtained membranes were characterized in regards to their composition, morphology, thermal and magnetic properties (where applicable).

Contents

Preface

This Ph.D. Thesis entitled **"Fabrication, Characterization and Applications of Electrospun Polymer-based Nanocomposite Membranes"** has been carried out in partial fulfillment of the requirements for the degree of Doctor of Philosophy at the Department of Mechanical and Manufacturing Engineering, University of Cyprus. The Thesis is divided in 7 chapters.

The **1st Chapter "Introduction to Polymers"** provides a brief introduction to polymers and to the polymerization method used in this study. The **2nd Chapter "Electrospinning"** describes the process which was used for the fiber generation, namely electrospinning and the influencing process and solution parameters. In the **3rd Chapter "Polymer-based Nanocomposite Electrospun Membranes"** a literature review on the fabrication and applicability of electrospun nanocomposite membranes in the biomedical, environmental and catalysis fields is carried out. In the **4th Chapter**, an outline of the "**Characterization Methods"** used in the present study is provided. The **5th Chapter "Experimental Section"** describes the experiments and methods employed for the fabrication and characterization of three different families of electrospun (nanocomposite) fibrous membranes as well as the experimental protocols followed for their evaluation in the aforementioned (biomedical, environmental and catalysis) fields. The **6th Chapter "Results and Discussion"** presents and analyses the obtained results related to (i) polymer synthesis and molecular characterization, (ii) membrane fabrication and characterization in regards to their morphology, thermal, compositional and magnetic (where applicable) properties and (iii) their evaluation in biomedical (drug delivery, hyperthermia), environmental (water remediation processes for the removal of metal ions and organic pollutants including aromatic hydrocarbons, antibiotics and organic dyes) and in catalysis (as heterogeneous catalytic supports employed in organic synthesis) applications. Finally, the **7th Chapter "Conclusions"** provides some concluding remarks.

List of Publications

1. Savva I., Krasia-Christoforou T., *"Evaluation of electrospun polymer-Fe_3O_4 nanocomposite mats in malachite green adsorption",* RSC Advances (submitted) **2014**.

2. Savva I., Kalogirou A. S., Chatzinicolaou A., Papaphilippou P., Pantelidou A., Vasile E. Vasile E., Koutentis P. A., Krasia-Christoforou T., *"PVP-crosslinked electrospun membranes with embedded Pd and Cu_2O nanoparticles as effective heterogeneous catalytic supports"* RSC Advances, 4, **2014**, 44911-44921.

3. Savva I., Krasia-Christoforou T., *"Electrospun magnetoactive fibrous nanocomposites: fabrication and applications in biomedicine"*, Book chapter in: Magnetic Nanoparticles: Synthesis, Physicochemical Properties and Role in Biomedicine, Ed. N.P. Sabbas, Nova Science Publishers Inc., New York, **2014**, 163-199.

4. Savva I., Constantinou D., Marinica O., Vasile E., Vekas L., Krasia-Christoforou T. *"Fabrication and characterization of superparamagnetic poly(vinyl pyrrolidone)/poly(L-lactide)/Fe_3O_4 electrospun membranes"*, Journal of Magnetism and Magnetic Materials 352, **2014**, 30-35.

5. Savva I., Efstathiou M., Krasia-Christoforou T., Pashalidis I. *"Adsorptive removal of U(VI) and Th(IV) from aqueous solutions using polymer based electrospun PEO/PLLA fibrous membranes",* Journal of Radioanalytical & Nuclear Chemistry, 298, **2013**, 1991-1997.

6. Savva I., Odysseos A., Evaggelou L., Taculescu A., Marinica O., Vekas L., Vasile E., Krasia-Christoforou T., "*Fabrication, characterization, and evaluation in drug release properties of magnetoactive poly(ethylene oxide)−poly(L-lactide)",* Biomacromolecules, 14, **2013**, 4436-4446.

7. Savva I., Krekos G., Taculescu A., Marinica O., Vekas L., Krasia-Christoforou T., *"Fabrication and Characterization of Magneto-responsive Electrospun Nanocomposite Membranes Based on Methacrylic Random Copolymers and Magnetite Nanoparticles"*, Journal of Nanomaterials, 2012, **2012**, Article ID 578026, 9 pages.

List of Figures

List of Tables

Abbreviations

^{1}H NMR	Proton nuclear magnetic resonance
AEMA	2-(acetoacetoxy) ethyl methacrylate
AIBN	2,2'-azobis(isobutyronitrile)
Arz(III)	Arsenazo
BzMA	Benzyl methacrylate
$CHCl_3$	Chloroform
DCB	1,2 dichlorobenzene
DMEM	Dulbecco's modified eagles medium buffered saline
DPBS	Dulbecco's phosphate buffered saline
DSC	Differential scanning calorimetry
ECM	Extracellular matrix
EDX	X-ray spectrometer
EtOAc (EA)	Ethyl acetate
EtOH	Ethanol
EtOH	Ethanol
Eu(III)	Trivalent europium
FCS	Fetal calf serum
H_c	Coercive field
HRTEM	High resolution transmission electron microscopy
MeOH	Methanol
MET	Metronidazole
MG	Malachite green
MMA	Methyl methacrylate
M_R	Remnant magnetization
M_s	Saturation Magnetization
M_w	Molecular weight
MWD	Molecular weight distribution
NPs	Nanoparticles
$OA.Fe_3O_4$	Oleic acid-coated iron oxide nanoparticles
PE	polyethylene

PEO	Poly(ethylene oxide)
PLLA	Poly(L-lactide)
PSA	Penicillin/Streptomycin/Amphotericin
PSA	Polystyrene
PVP	Poly(vinyl pyrrolidone)
SEC	Size exclusion chromatography
SEM	Scanning electron microscopy
SPIONS	Superparamagnetic nanoparticles
T_c	Curie temperature
TEM	Transmission electron microscopy
T_g	Glass transition temperature
TGA	Thermal gravimetric analysis
Th(IV)	Tetravalent thorium
THF	Tetrahydrofuran
T_N	Neel temperature
U(VI)	Hexavalent uranium
UV-vis	Ultraviolet-visible spectrometer
VSM	Vibrating sample magnetometer
XRD	X-ray powder diffraction

1

Introduction to Polymers

1.1. Definition of Polymers

Polymers or macromolecules are materials which we meet daily in our life, in the form of plastics, fibers, rubbers and so on. The definition of "polymers" or "macromolecules" refers to high-molecular weight substances, the structure of which depends on the repeating monomer units. A monomer is a small molecule, with low molecular weight, compared to a polymer, which is joined together to form a long polymer chain. For example ethylene is a monomer that can be polymerized to polyethylene or polythene, one of the simplest polymers in regards to chemical structure **(scheme 1.1)**. In this polymer, the repeating units are $-CH_2-$ groups (one carbon atom with two attached hydrogen atoms), and all carbons are connected by single covalent bonds (1).

$$CH_2=CH_2 \longrightarrow \quad ---CH_2-CH_2--- \longrightarrow$$

$$-CH_2-CH_2-CH_2-CH_2-.....-CH_2-CH_2-CH_2-CH_2-$$

Scheme 1.1: *Polyethylene obtained via polymerization of ethylene.*

Polymers that contain only a single type of repeating unit are known as homopolymers; they can be provided in different shapes as linear, branched, crosslinked/network and star polymers depending on the way the monomer units are connected to each other as a consequence of the synthetic methodology followed, as illustrated in **figure 1.1**. A **linear polymer** consists of a long chain of skeletal atoms which are attached to the substituent groups. A **branched polymer** can be visualized as a linear polymer with branches of the same basic structure as the main chain. In **crosslinked polymers** chemical bonds exist between the chains, and **star polymers** have arms radiating from a common core.

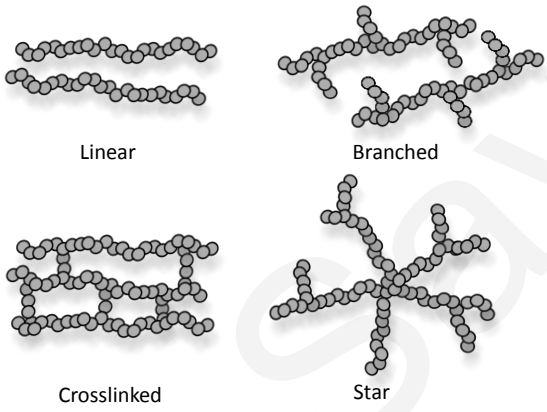

Figure 1.1: *Structures which are generated in homopolymers (consisting of a single type of monomer) from the different placement of monomer units along the chain.*

Polymers containing two or more different monomeric units, are known as copolymers. The different copolymer structures are generated from the way of placement of the repeating units along the chain. Those are classified to random, alternating, block copolymers, and graft copolymers.

Random copolymers consist of different monomer units which have no definite order or arrangement along the chain. **Alternating copolymers,** as the name implies, contain a regular alternating sequence of two or more monomer units. **Block copolymers** have a long segment or block of one monomer followed by a block of a second monomer joined together covalently in a head-to-tail configuration, in a linear arrangement. Finally, **graft copolymers** are a type of copolymers in which the chains of one monomer is grafted onto the main chain of the other monomer. All of the above-mentioned structures are illustrated in **figure 1.2** (2).

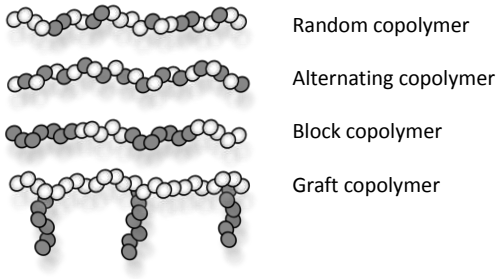

Figure 1.2: *Structures which are generated in copolymers (consisting of two different monomers) from the different placement of monomer units along the chain.*

Polymers might be categorized in physical (natural) for example natural rubber, starch and cellulose, biopolymers for example DNA and proteins and synthetic for example plastics. It is also worth mentioning that polymers provide many benefits such as light weight, low cost, and easy industrial production. However, polymers are usually hardly biodegradable resulting to environmental pollution.

Many properties of polymers depend on the microscopic arrangement of the polymeric chains and on the temperature. Polymers may be found in the amorphous or in a semicrystalline (partially crystalline) state. The terms amorphous designate a lack of order and chains are arranged in a random manner, while in semicrystalline morphology there are domains in which the polymer chains are packed in an order array. These "crystalline" domains are embedded in an amorphous polymer matrix. Generally the presence of crystallinity within a polymer alters its properties including thermal, mechanical, optical etc. compared to the pure amorphous analogue. Regarding the mechanical properties, at low temperatures amorphous polymers deform elastically, like glass, at small elongation. At high temperatures the behavior is viscous, like liquids. At intermediate temperatures they behave like a rubbery solid, which is termed as viscoelastic (3).

Figure 1.3 shows the phase transitions of amorphous and semicrystalline polymers occurring upon temperature increase. While both amorphous and semicrystalline thermoplastics, are hard, rigid solids and behave like glass at low temperature, by increasing the temperature the polymers lose their glasslike properties, and change into a rubbery elastomeric or a flexible plastic morphology. This transition point is known as the glass transition temperature, T_g, and for many polymers it is the most important feature.

The chemical composition of the polymer chains, the molecular weight, the degree of crystallinity, and the presence of additive (e.g. plastisizers) affect T_g. The viscoelastic properties of the polymers are eventually lost as the temperature continues to increase above the T_g, since the thermal energy provided enables the chains to move. When finally the chains are capable of moving freely, the polymer behaves like a viscous liquid. Those phenomena apply in both amorphous and semicrystalline polymers, nevertheless, above T_g, amorphous polymers behave in a different manner to semicrystalline (4; 2). As the temperature increases in an amorphous polymer, the hard rubbery phase gradually moves to a soft state, extensible elastomeric phase, then to a gum, and finally to a liquid, and only a gradual change in properties is perceptible. Crystalline polymers, on the other hand, retain their rubbery elastomeric or flexible properties above the T_g, until the temperature reaches the melting point, T_m. This point is the highest temperature at which polymer crystallites can exist, and above this point, the material may be liquid, viscoelastic or rubber depending on its molar mass.

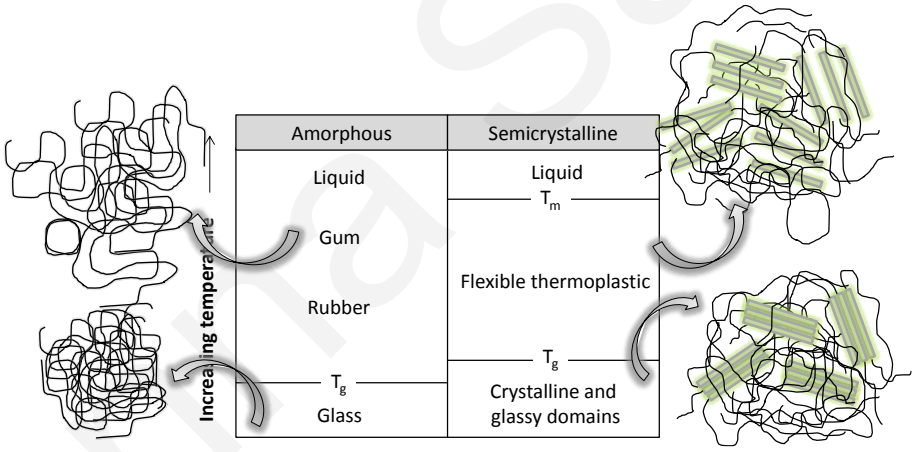

Figure 1.3: *Phase transitions occurring in amorphous and semicrystalline polymers upon temperature increase.*

1.2. Polymerization Methods

Radical polymerization is one of the most widely used processes for the commercial production of high molecular weight polymers and generally, for the preparation of a large number of polymeric materials. A wide range of monomers can be polymerized by free radical polymerization under less demanding reaction conditions compared to other polymerization methods such as ionic polymerizations.

Free radical polymerization is of high importance in technology, since it is simple to implement and inexpensive in relation to competitive technologies, polymers are produced in large quantities and the process is less sensitive to impurities and atmospheric conditions. Moreover, it may occur in the bulk liquid phase (absence of solvent), or in solution (presence of solvent), and it is also tolerant to protic and aqueous solvent media and to certain reactive functional groups, for example OH, NR_2, COOH, $CONR_2$. Moreover, it can be used with a large variety of monomers including meth(acrylates), styrene, (meth)acrylamides, butadiene, and vinyl acetate. However, the major drawbacks of conventional radical polymerizations are related to the lack of control over the polymer structure. Polymers with high molecular weights and high polydispersities are generally produced, due to the slow initiation, fast propagation and subsequent transfer or termination processes (5).

Polymerizations by a free-radical mechanism, include three steps: The initiation step, at which the radicals are formed, the propagation step (chain propagation/transfer), at which the addition of monomer molecules to the active chain end takes place, accompanied by the regeneration of the terminal active site and the transfer of the active site to another molecule resulting to the polymer growth, and finally the termination, where radical termination reactions occur, and the active chain centers are destroyed. The molecule that has lost the active site is known as "dead" and cannot be further used in chain propagation. The molecule that has accepted the active site may initiate the formation of a new chain. These three steps are presented in **figure 1.4** (6; 7; 2; 5).

Initiation process takes place in two steps. At first, decomposition of the initiator yields initiator radicals R^*. This is followed by the addition of R^* to monomer M, to give a new radical M_1^* (rate constants k_d and k_i). In the initial propagation step (rate constant k_p), M_1^* adds to another monomer molecule to form a new radical, M_2^*, which, in turn adds to M to form M_3^*, and so on. Finally, termination occurs principally by radical coupling or disproportionation (rate constants k_{tc} and k_{td}). Organic peroxides or hydroperoxides (e.g. benzoyl peroxide), azo comounds (e.g. azobisisobutylnitrile (AIBN) or organometallic reagents (e.g. silver alkyls) are some types of reagents acting as free radical polymerization initiators.

Recent advances in free radical polymerization have let to the development of synthetic methods that enable the preparation of well-defined polymers. These methods are the controlled radical polymerization (CRP) techniques which have been extensively

investigated, due to their high versatility and potential commercial applications. Atom transfer radical polymerization (ATRP), nitroxide-mediated polymerization (NMP), and reversible addition-fragmentation chain transfer (RAFT) polymerization, are the three major controlled radical polymerization techniques (8; 9).

1. Initiation

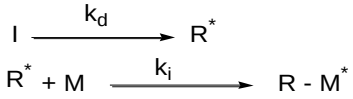

2. Propagation

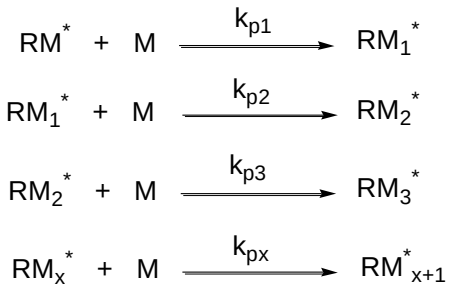

3. Termination

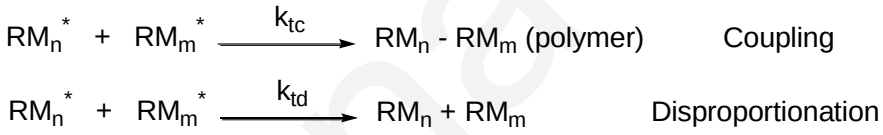

Where, **I** = Initiator, **R** = Initiator Radical, **M** = Monomer

Figure 1.4: *Reaction mechanism of free radical polymerization.*

The control character in radical polymerizations is based on two requirements. Firstly, initiation should be fast, providing a constant concentration of growing polymers chains. Secondly, because of the persistent radical effect, the majority of these growing polymer chains are dormant species. However, these dormant species have the ability to grow because of the establishment of a dynamic equilibrium between dormant species and growing radicals. By keeping the concentration of active species or propagating radicals sufficiently low during the polymerization, termination is prevented (10; 8).

2

Electrospinning

Electrospinning, also known as electrostatic spinning technique, was first observed by L. Rayleigh in 1897 and was first patented in the United States in 1902, by J. F. Cooley and W. J. Morton who were the first who patented devices to spray liquids through the application of an electrical charge. In 1914 J. Neleny reported that a liquid jet could be emitted from a charged liquid droplet in the presence of an electrical field (11). In 1934, electrospinning became a valid technique to produce small-sized fibers, when A. Formhals patented a process and apparatus to spin synthetic fibers using electric charges and designed a movable device that allowed the fiber collection in a stretched state (12; 13). In 1939 an improved process was developed in order to overcome the problem of incomplete solvent evaporation, associated with his earlier apparatus (14). Researchers after A. Formhals focused on better understanding of the electrospinning process. In 1969, D. G. Taylor published on the jet formation process in which the droplet behavior of the polymer solution at the edge of a capillary under an electric field was examined. Significantly, he obtained the characteristic value of the cone referred as the “Taylor Cone” (15). Since the early 1990s, D. H. Reneker and co-workers employed the electrospinning process for the generation of one-dimensional (1D) polymer nanostructures provoking the attention of many researchers (16; 17; 18).

Although currently there are several methods that can be used to prepare one dimensional (1D) nanomaterials namely drawing (19), self-assembly (20; 21), melt-blow (22), phase-separation (21) and template synthesis (23), the most popular and versatile fiber fabrication method used for the production of synthetically or naturally-derived fibrous materials is electrospinning (24). Electrospinning can be used to produce continuous polymer (nano)fibers (25; 26; 17) with diameters ranging from micrometers (10-100 μm) down to a few nanometers (10-100 nm) (25) and lengths up to meters (26). Its simplicity, cost-effectiveness and applicability not only to pristine synthetic and natural polymers (27; 25) but also to composites, enables the development of polymer-based fibrous nanocomposites *via* the combination of polymers with inorganic nanofillers (28).

Despite the simplicity of the elctrospinning set-up, the electrospinning mechanisms are rather complicated including the Taylor Cone theory (29), the Bending Instability theory (30), the Electrically Forced Jet-Stability theory (31), and so on.

2.1. Overview of the electrospinning process

A simple electrospinning set-up consists of four major components: A high-voltage power supply, a syringe with a metallic needle, known as spinneret (containing the polymer solution or melt), a syringe pump used for delivering the solution through the spinneret at a constant and controllable rate and a grounded conductive collector, on which the produced fibers are collected **(figure 2.1)**.

Direct current (DC) power supplies are usually used for electrospinning, although the use of alternating current (AC) potential is also feasible (32). A high-voltage power supply is connected with both the needle and the collector. The positive electrode (anode) of the power supply is connected to the needle and the negative (cathode) is grounded to the collector (33). In a typical fiber-generating process, a syringe is filled with a polymer solution and a high voltage (up to 30 kV) (34; 32) is applied between the syringe nozzle and the collector. The syringe may be placed perpendicularly, letting the polymer fluid drop with the help of gravity, or horizontally in respect to the grounded collector (35; 19; 24).

By applying the high voltage, the pendent drop of the polymer solution at the needle tip of the spinneret is highly electrified and the induced charges are evenly distributed over the

droplet surface. The electrostatic repulsion forces developed between the surface charges and the columbic force (electrostatic force) exerted by the external electric field are the major electrostatic forces on the droplet. Under these electrostatic interactions the hemispherical surface of the fluid at the tip of the needle's syringe elongates forming a conical fluid structure, called the Taylor cone (25). The charged droplet is subjected to the electrostatic forces obtaining a conical shape, where under a critical voltage value a thin polymer jet is ejected from the tip of the Taylor cone. Specifically, at a critical voltage (e.g. once the strength of the electric field has surpassed a threshold value) the electrostatic repulsive forces overcome the surface tension of the solution and force a jet to erupt from the tip of the Taylor cone. The jet follows a direct path towards the grounded collector for a very short distance from its origin and reaches a bending instability point. After this point the jet begins to whip as illustrated in **figure 2.1** (36).

If the voltage is sufficiently high, a stable jet will form near the tip of the Taylor cone. The electrified jet is only stable near the tip of the spinneret, after which the unstable state of the jet is observed in the space between the capillary tip and the collector, during which the jet undergoes a stretching and a rapid whipping process (37). In solution electrospinning, as the charged jet accelerates toward lower-potential regions, the solvent evaporates whereas the resulting increase in the electrostatic repulsion of the charged polymer causes the fibers to elongate and reduce their diameters. With the combination of jet-bending instability and solvent evaporation, the jet eventually becomes solidified on the collector in the form of randomly oriented (nano)fibers (38; 39; 40; 41; 27).

2.2. Influencing parameters

In general, the process parameters affect fiber sizes and morphologies but the exact relationship is unique to each polymer-solvent system. However, after vital research on the basics of the electrospinning process, researchers investigated the relationship between processing and solution parameters and the obtained structural fiber morphology. The major challenge of the electrospinning process lies in the optimization of all the above-mentioned parameters, to achieve desirable nanofibers' morphology and properties (13).

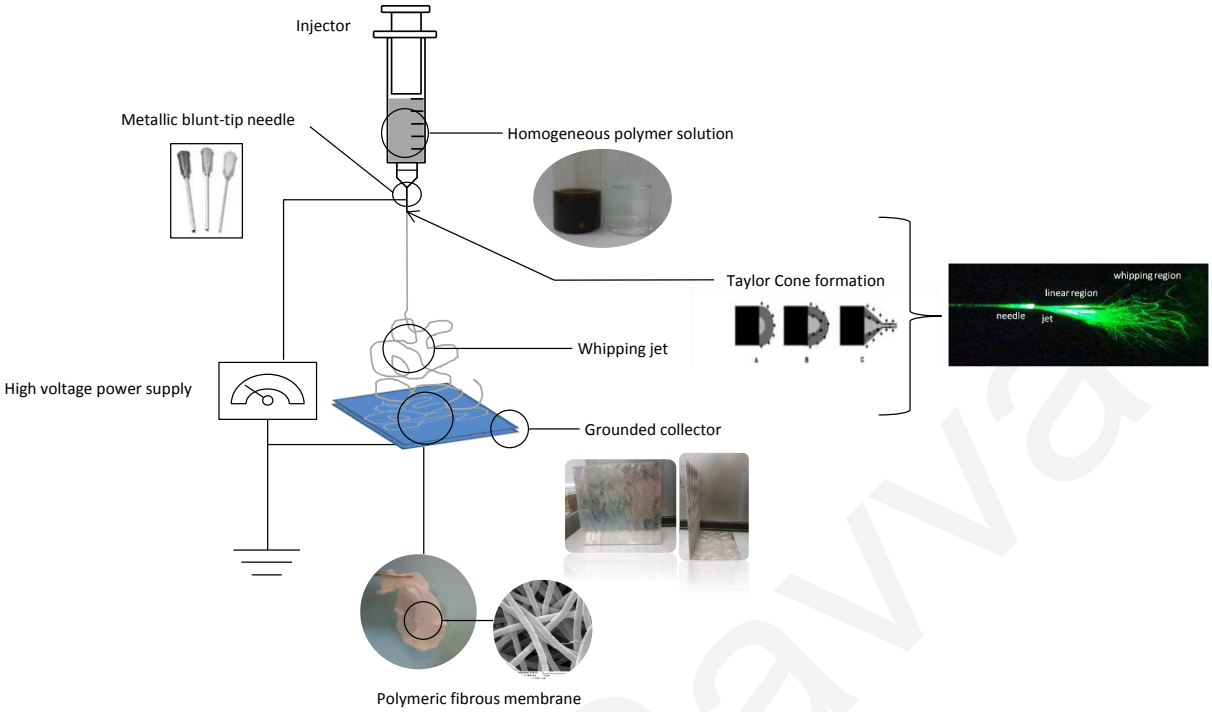

Figure 2.1: *Schematic presentation of a basic electrospinning set-up.*

In polymer nanofibers derived from electrospinning, it is desirable that the fiber diameters are consistent and controllable, the fiber surface is defect-free, and continuous single nanofibers are collectable. However, research carried out throughout the years has shown that the above-mentioned targets are by no means easily achievable (42; 25), and the success of the whole process is governed by different parameters which are classified in terms of the solution properties (43; 44; 45; 42), process parameters (26; 42), and ambient parameters (26; 27; 43; 45).

Based on those parameters, dissimilar results may be obtained using the same polymer and electrospinning set-up. Thus, it is difficult to give quantitative relationships that can be applied across a broad range of polymer/solvent systems. However, there are general trends which are useful when determining the optimum conditions for a certain system.

2.2.1. Solution parameters

Viscosity/Concentration/Molecular weight: Solution viscosity which is governed by the polymer solution concentration, and polymer molecular weight, strongly influences the dimensions and morphologies of electrospun polymeric fibers (46). The solution concentration must be high enough for allowing chain entanglement effects to take place. If the solution is too dilute then the formation of polymer droplets instead of fibers before reaching the collector will occur, due to surface tension effects (47). Consequently, at low polymer concentrations, the generation of beads and droplets has been observed. On the other hand, in too concentrated solutions, of high viscosity, the solution flow rate through the capillary is hindered. The jet will be less likely to break up into droplets because the high viscoelastic forces would dampen the Rayleigh breaking mechanism based on the fact that the viscoelastic forces never act against the surface tension (39; 25).

Some researchers support that the fiber diameter is not related to the polymer solution concentration/viscosity, whereas others indicate that concentration has a major influence on the fiber diameter (48; 49; 50; 51). H. L. Simons showed that the fibers derived from low viscosity solutions tend to be shorter and finer, compared to the fibers obtained from more viscous solutions which appear to be relatively continuous and thicker (52; 45; 53).

The polymer molecular weight (MW) influences considerably the rheological and electrical properties of a solution such as viscosity, surface tension, conductivity and dielectric strength (54). Researchers have been examining the relationship between MW and the morphological and dimensional characteristics of electrospun fibers (55). From such studies it has been concluded that an increase in MW leads to the reduction in the number of beads and droplets generated during electrospinning. Additionally, polymers characterized by a narrow molecular weight distribution (MWD) led to the formation of uniform fibers at a lower concentration compared to solutions prepared using a broad MWD polymer of the same chemical composition. Moreover, it was found that the diameters of the electrospun fibers depended strongly on the MW of the polymer (43; 54), i.e. when using a low MW polymer, there is a tendency toward the formation of beaded structures, whereas upon increasing the MW continuous fibers are generated. In the latter case, the fiber diameter increases upon increasing the polymer MW (37; 54). Finally, polymers of extra high molecular weight are generally more difficult to spin. This may be attributed to the rapid rise in viscosity when the solvent evaporates off during the spinning operation (52).

Conductivity/Solution charge density: Solution conductivity also influences the morphology and diameters of the resulting fibers (56). An increased conductivity enhances the charge density at the surface of the solution jet, resulting in more electric charges in the jet. As the charges carried by the jet increase, higher elongation forces are imposed to the jet under the electrical field, resulting in thinner fiber diameters as well as reduced tendency of droplet formation during the process (57; 58; 59). The increase of the net charge density could be realized by adding salts (27; 35; 50). However, the increase of charge density is not in line with the applied electrical field, since higher electrical field does not result in fewer beads and smoother fibers (25; 45). Furthermore, it has been shown that the radius of the electrospun nanofiber jet is inversely related to the cube root of the electrical conductivity of the solution (57; 39).

Surface tension: The impact of surface tension on the morphology and dimensions of electrospun fibers has also been investigated (43). Surface tension plays a critical role in the electrospinning process since –based on different studies– it has been demonstrated that solutions with lower surface tension lead to the effective elimination of beads and the generation of fibers with larger diameters (27). Researchers pointed that by reducing the surface tension of a polymer solution, which seems more likely to be a function of solvent composition, and negligibly dependent on the polymer concentration, fibers could be obtained without beads (16; 25; 47; 60). Different solvents may lead to different values of surface tension (25; 45). Generally, solutions characterized by a high surface tension lead to the generation of sprayed droplets owing to jet instability (31). However, the use of a low surface tension solvent does not always lead to beaded-free electrospun fibers. Basically, surface tension determines the upper and lower boundaries of the electrospinning window if all other variables are held constant (37).

Dipole moment/Dielectric constant: Very few studies so far have carried out an in-depth investigation of the effect of the dipole moment and the dielectric constant on the morphology of the fibers derived from electrospinning. In one example, polystyrene (PS) was electrospun into fibers starting from polymer solutions in eighteen different solvents (61). The solvents with high dipole moment values were those resulting to the successful fabrication of PS electrospun fibers. Moreover, the number of PS fibers produced per unit time was found to correlate to the dipole moment and the dielectric constant (37; 38; 22).

2.2.2. Processing parameters

Applied voltage: The strength of the applied electric field considerably influences the electrospinning process. J. M. Deitzel *et al.* (2001) have reported that the change in the spinning current is related to the change in the instability mode. Specifically, they showed that an increase in applied field causes a change in the shape of the jet initiating point, and hence the structure and morphology of the fibers (18; 45). P. K. Baumgarten *et al.* (1971) showed that by increasing the applied voltage an increase on fiber length with small changes in fibers' diameter were obtained (58), while S. Megelksi *et al.* (2002) reported on the decreasing of fiber diameters with voltage increase (62). In contract with S. Megelksi, M. M. Demir *et al.* (2002), K. Garg *et al.* (2011) etc. reported that the jet diameters seem to increase with increasing voltage due to the ejection of more fluid in a jet (51; 34). Many studies show that by increasing the electric field strength the bead density is decreased (27), while a further increase leads to the decrease in the stability of the initiating jet resulting to the formation of more bead defects along the electrospun fibers (63; 45). Moreover, under high voltage the jet velocity increases and the solution is removed from the tip more quickly. The Taylor cone shape oscillates and becomes asymmetrical, when the volume of the droplet on the tip becomes smaller (34). Concluding, researchers evident that there is an optimal electric field strength range for a certain polymer/solvent system, as either too weak or too strong fields will lead to the formation of beaded fibers (45; 63)

Polymer flow rate: The polymer flow rate has also an impact on the dimension and geometry of the produced electrospun fibers as well as on the porosity of the fibrous material. Both, the fiber diameter and the pore size increase with increasing flow rate. Additionally, at high flow rates a significant amount of beaded defects can be observed, due to the incapacity of fibers to dry completely "in flight" before reaching the collector. Incomplete fiber drying also leads to the formation of ribbon-like fibers as compared to fibers with a circular cross section (64). In general, it was found that lower flow rates yield continuous fibers with smaller diameters (43), while an increase in fiber and pore diameters is observed with an increase in the polymer flow rate (18; 62).

Needle tip-to-collector distance: Although the distance between the needle-tip and the collector is not a parameter that is influencing primarily the electrospinning process, it can still influence the fiber morphology and size, because of their dependence on the deposition time, evaporation rate, and whipping or instability interval (18). By increasing the distance from the Taylor cone, the fiber diameter decreases, whereas the formation of

wet fibers and beaded structures is usually obtained by shortening the distance between the needle-tip and the collector. The latter may be attributed to inadequate drying of the polymer fiber prior to reaching the collector; consequently, a minimum distance is required to allow the fibers sufficient time to dry before reaching the collector (65; 26; 62; 64). Finally, a decrease in the needle-to-collector distance may result to the formation of shorter fibers (66).

Collector composition/Geometry: The modification of collectors for fiber direction control has been widely investigated. Different geometries of the conductive collectors have been successfully developed including a cylindrical collector with high rotating speed, a cylindrical collector based on a pair of a split electrodes, a thin wheel collector with sharp edge, and a frame collector (38; 42; 27; 24). It is noteworthy to mention that the more conductive collectors dissipated the charge of the fibers, whereas when this charge was not dissipated (i.e. in the cases where non-conductive collectors are used), the fibers repelled one another, resulting to the generation of a more porous structure (60; 43). Furthermore, porous collectors, such as paper and copper mesh, led to the production of less-packed structures compared to fibers collected on aluminum foil (43).

2.2.3. Ambient parameters

Temperature: To date, a limited number of studies examining the effects of ambient parameters around the spinneret, like the surrounding air, humidity, vacuum conditions, surrounding gas, etc. exist (58; 18). As far as the temperature effect is concerned, it has been demonstrated that by increasing the temperature, fibers with smaller diameters are obtained due to the decrease of the polymer solution viscosity (43).

Humidity: An increase in the humidity level results to the appearance of small circular pores on the surface of the fibers while a further increase leads to pore coalescing, and the drying of the fibers is prevented (18; 43; 58). All the above-mentioned electrospinning parameters and their effect on the fiber morphology are summarized in **table 2.1**.

Table 2.1: *Effects of the electrospinning parameters on fiber morphology.*

Influencing parameter	Effect on fiber morphology	References
Solution properties		
Concentration/Polymer molecular weight/Viscosity	Low concentration/viscosity results to beaded fibers and droplets, while by increasing the concentration/viscosity fewer beads and droplet-free fibers are obtained.	(25; 39; 46; 47)
	Low polymer molecular weight/viscosity (regardless of concentration) also generates beaded fibers, whereas polymers of extra high molecular weight are more difficult to spin.	(37; 43; 52; 54; 55)
	Fibers obtained from low viscosity solution tend to be shorter and finer, compared to the fibers generated from more viscous solutions which appear to be relatively continuous and thicker.	(45; 52; 53)
Conductivity/Solution charge density	An increased conductivity results in fewer beads and thinner fiber diameters as well as reduces the tendency of droplet formation during the process.	(57; 58; 59)
	The increase of the net charge density could be realized *via* the addition of salts in the polymer solution.	(27; 35; 50)
Surface tension	By reducing the surface tension of the polymer solution, fibers can be obtained without beads.	(16; 25; 47; 60)
	Solutions with lower surface tension lead to the effective elimination of beads and the generation of fibers with larger diameters.	(27)
	Different solvents may contribute differently on the surface tension.	(25; 45)
Dipole moment and dielectric constant	Solvents with high dipole moment values result to the successful fabrication of electrospun fibers.	(61)
Process parameters		
Applied voltage	The increase of the spinning current (related to the change in the instability mode) causes an increase on fiber length.	(18; 45; 58)
	The increase of the voltage leads to the decrease of the beads, while further increase results to the formation of beaded fibers due to the decrease in the stability of the initiating jet.	(45; 63)
	The jet diameters, initially, seem to decrease with increasing voltage whereas further increase results to thicker diameters, due to a higher mass flow from the needle tip.	(18; 34; 51; 64)
Polymer flow rate	At too high flow rates beaded defects can be observed.	(18; 43; 62).

	Upon increasing the flow rates both diameters and pore size increase.	
Needle tip-to-collector distance	By increasing the distance, the fiber diameter decreases, whereas the formation of wet fibers and beaded structures is usually obtained by shortening the distance between the needle-tip and the collector.	(26; 62; 64; 65)
Collector composition and geometry	The more conductive collectors dissipate the charge of the fibers, whereas when this charge is not dissipated the fibers repel one another, resulting to the generation of a more porous structure.	(43; 60)
Ambient parameters		
Temperature	By increasing the temperature, fibers with smaller diameters are obtained due to the decrease of the polymer solution viscosity.	(18; 43; 58)
Humidity	An increase in the humidity level results to the appearance of small circular pores on the surface of the fibers while a further increase leads to pore coalescing, and the dry of the fibers is prevented.	(18; 43; 58)

3

Polymer-based Nanocomposite Electrospun Membranes

Fibrous polymeric materials have received considerable attention exhibiting highly promising applications since they have significant advantages in comparison to other conventional polymer forms including films (39; 27) and gels (67). Various polymers have been successfully electrospun into ultrafine fibers in recent years (27; 25). This process exhibits promising results in diverse fields producing nonwoven mats which have been investigated for their use as materials in lithium ion batteries, in electronic micro- and nanodevices, as catalytic substrates, and as air filtration membranes. Moreover, electrospun mats have been also investigated for their superior adsorption potential of pollutants, as gas sensors, and drug carriers (57).

In addition of being a simple processing technique for fabricating (nano)fibers, electrospinning allows the co-processing of polymer mixtures as well as chemical cross-linking to take place, providing a variety of pathways for manipulating the chemical composition of the fibers. The above-mentioned processes provide useful properties to the

resulting fibrous materials including mechanical strength, elasticity, porosity and charged surface areas (68).

3.1. Polymer-based electrospun fibrous membranes

As previously noted, electrospinning is one of the most popular and versatile fiber fabrication techniques used for the production of synthetically or naturally-derived fibrous materials, enabling the expansion of their properties through blending and surface functionalization (63). Fibers exhibit a range of unique features and properties such as extremely long length, much thinner diameter resulting in high surface-to-volume ratio, a high density of pores as a result of the entanglement of nanofibers, good mechanical properties especially in the case of fibrous nanocomposites, high flexibility, light weight properties, and low cost (27; 68).

These outstanding properties render electrospun polymeric fibrous materials good candidates for many application including biomedical (tissue engineering, drug delivery) (68), environmental (filtration, water remediation) (69), and catalytic applications (70).

3.1.1. Electrospun polymer-based membranes for biomedical applications

The electrospinning technology has been widely used in the biomedical field. Many researchers have utilized the recent advances of this technology for producing a wide range of materials in the form of fibers, that have been used as scallfolds in tissue engineering and drug delivery systems (33).

In particular researchers have been mostly focusing on the use of polymers for the fabrication of nanofibrous tissue-engineering scaffolds (26; 71; 33), and drug-delivery vehicles (72; 73; 33), employing either biopolymers such as collagen (74; 75), alginate (76; 77), hyaluronic acid (78), chitosan (79) and starch (80) or synthetic polymers such as polyurethanes, polymethacrylates, aliphatic polyesters (poly(lactic acid) (PLLA) (81; 82), polycaprolactone (PCL) (83; 64) poly(glycolic-acid) (PGA) (84)) polyvinypyrrolidone (PVP) polyacrylonitrile (PAN), polyvinyl alcohol (PVA), polyethylene oxide (PEO) (72), and poly(ethylene terephthalate) (PET) (85).

Tissue engineering: Tissue engineering or regenerative medicine is the application of therapeutic products that utilize the combination of matrix scaffolds from natural or synthetic polymers. These sources need to be viable to human cell systems for the repair, restoration, or regeneration of damaged or failed cells or tissues provoked by injury, diseases, or congenital defects (86). Significant considerations include the nanoscale dimensions and the three dimensional (3D) structure of these scaffolds, since many biologically functional molecules, extracellular matrix (ECM) components, and cells interact in the same size range operating in 3 dimensions (42; 43).

Due to the controllable porosity and permeability of the electrospun membranes which are thought to be able to enhance cell adhesion, migration, proliferation and differentiated function, as well as their good mechanical properties (87; 18) they are suitable for replacing/mimicking the structures of natural tissues. Moreover, polymeric fibers characterized by biocompatibility, biodegrability, and high drug loading capability, can be easily fabricated by electrospinning in the required architecture/form (88; 89).

Basic requirements for an effective polymer nanofibrous scaffold in the regeneration of a tissue include a 3D structure of high surface area, high porosity and proper pore size. Additionally, the biodegradability profile is an essential parameter in materials destined for use in tissue engineering applications. The material should not evoke a sustained inflammatory or toxic response upon implantation in the body, and should have an acceptable shelf life. The degradation time of the material should match the time required for the healing or regeneration process and the degradation products should be non-toxic, and able to get metabolized and cleared from the body. Moreover, the material should have appropriate permeability and mechanical properties for the indicated application (90; 91; 84; 43; 25).

X. Zong *et al.* (2005) fabricated poly(glycolide)-based (PLGA) electrospun nanofibers, with different composition. The synthesized scaffolds were further examined with regard to their chemical compositions, degradation rate and surface properties for the attachment and growth of cardiac moycytes (CMs) to form a well-connected tissue (92). Additionally, N. Bhattarai *et al.* (2005) reported potential materials for bone tissue engineering, based on chitosan-containing nanofibers that promoted the adhesion of chondrocyte (HTB-94) and osteoblast (MG-63) cells (93).

Membranes are generally prepared using flat collecting plates resulting in a randomly oriented fibrous structure. However, native ECMs in different tissues or organs have specifically defined architectures which play an important role in determining tissue functions. Therefore, considerable attention has been given on the development of aligned-oriented nanofibers with specific topological architectures favoring specific biological responses.

C. Y. Xu *et al.* (2004) suggested that a polymer scaffold composed of aligned nanofibers of synthetic polymers poly(L-lactide-*co*-ε-caprolactone) (P(LLA-CL)) mimics the native extracellular matrix and demonstrated an improved favorable interaction of the smooth muscle cells (SMCs) and the endothelial cells (EC) with the scaffold, compared to the corresponding solvent cast polymer film (83; 64). Z. X. *et al.* (2010) successfully produced electrospun randomly-oriented and aligned poly(lactic-*co*-glycolic acid) (PLGA) nanofibers for bone tissue engineering application. Aligned nanofibers exhibited higher adhesion and proliferation of the cell, as well as guided cells growth along the longitudinal axis of generation (94).

Drug delivery: Polymer-based materials including macromolecular aggregates such as micelles (95; 96; 97), vesicles (98; 99; 100), capsules (101; 102; 103), networks (104; 105; 106) and fibrous membranes (107; 108) combined with pharmaceutical compounds have been extensively investigated in the biomedical area as drug delivery systems. The ability of such materials to act as controlled drug carriers with optimal pharmacokinetic properties is a key requirement in order to avoid the so call “burst release” (109), as well as the generation of undesirable side-effects, due to the uncontrolled drug release process.

In order to design a proper drug delivery release system, loading of the drug into electrospun nanofibrous matrices could be achieved using different methods. In the case where the drug and the polymer are soluble in the same solvent or solvent mixture and the homogeneous solution is electrospun the drug is embedded in the fabricated nanofiber scaffold. In another approach, the drug and the polymer are dissolved in a different solvent and the two solutions are loaded in separate capillaries in order to be electrospun coaxially, resulting in core-shell fibers where the drug is encapsulated selectively in the inner (core) or outer (shell) of the fiber. Another technique for drug loading is *via* adsorption of the drug onto the pre-generated electrospun nanofibrous mats upon immersing the nanofiber in a drug solution (110; 111; 112; 113; 87; 39).

Electrospun fiber mats composed of either poly(lactic acid) (PLA), poly(ethylene-*co*-vinyl acetate) (PEVA), or from a 50:50 blend of the two, have been evaluated as drug delivery vehicles for tetracycline hydrochloride (TH) as showed by Kenawy and co-workers (2002). TH release profiles from the electrospun mats were compared to the release of a commercially available drug delivery system, Actisite (Alza Corporation, Palo Alto, CA), as well as the drug release from corresponding cast films (114). Z. M. Huang and co-workers used co-axial electrospinning nanofibers, for controlled release of multi drugs, where the shell consisted of polycaprolactone (PCL) and the core consisted of two drugs, namely Resveratrol and Gentamycin Sulfate. The drugs were released in a controlled way without any initial burst release (110; 68).

The popularity of polymeric nanofibers in the biomedical field is demonstrated by the number of existing reviews focusing on the unique properties and applications of these materials in the biomedical area (71; 115; 116).

3.1.2. Electrospun polymer-based membranes for environmental applications

Protecting the water means protecting the planet means protecting the mankind. Unfortunately, the rapid development of the industrial activities leads to environmental pollution as a consequence of the industrialization process (117; 118). Heavy metal ions, aromatic compounds (including phenolic derivatives, and polycyclic aromatic compounds) pharmaceutics and dyes are often found in the environment as a result of their wide industrial uses. They are common contaminants in wastewater and many of them are known to be toxic or carcinogenic (119). This is one of the major problems that has to be solved or at least minimized.

Several methods are utilized to remove contaminants from aqueous environments, such as advanced oxidation (120), photocatalysis (121; 122), adsorption (123) precipitation (124), coagulation (125), chemical and electrochemical methodologies (126). However, most of these technologies are both costly and ineffective, particularly when the concentration of waste is very low. The adsorption technique is especially attractive because of its high efficiency, environmental friendliness, simplicity of design, and ease of operation. Activated carbon (127; 128), polymers in the form of hydrogels (123), fibers (129), and films (130), or naturally occurring materials such as sawdust, silica, peel, hen feathers etc.

(131; 132; 133) have been evaluated as adsorbents for the removal of different pollutants found at very low concentrations in aqueous solutions (134).

The term adsorption refers to a process that involves the transfer of solutes from the liquid phase to the surface of a solid matrix. More precisely, adsorption occurs whenever a solid surface is exposed to liquid or gaseous surroundings wherein the material is concentrated at the solid surface. Usually, the attraction between the solid surface and the adsorbed molecules is physical in nature; hence the adsorption is referred to as physical adsorption. In this case the attractive forces might be Van der Waals, electrostatic or hydrophobic interactions, or hydrogen bonding. The adsorption process based on physical interactions can be reversible due to the presence of weak attractive forces that can be destructed under certain conditions (126).

A promising adsorbent should generally possess a porous structure, resulting to a high surface area, which is directly correlated to the adsorbents efficiency. Among others, fibrous materials with diameters in the micro- and nanometer range have attracted considerable attention as potential adsorbents for harmful substances from aqueous media due to their high surface area and the ease of regeneration and recycling. In filtration applications the sizes of the channels and pores of the membranes can be adjusted to the sizes of the particles to be filtered/adsorbed thus obtaining high efficiency (42).

Organic pollutants include pesticides, fertilizers, phenols, plasticizers, oils, pharmaceuticals and other (135). One of the important classes of the pollutants is dye molecules, such as malachite green, acid blue, reactive yellow etc. (126; 135). Due to their complex molecular structure, synthetic organic dyes are chemically stable hence they are not easily subjected to biodegadation, they exhibit high resistance to light, temperature and oxidizers (118; 126).

X. Zhu *et al.* (2010) showed the effectiveness of polyvinyl chloride (PVC) ultrafine fibrous membranes, prepared by electrospinning, to adsorb a cationic dye from aqueous media with sorption capacity reaching up to 29.86 $mg \cdot g^{-1}$ (136). X. Fang *et al.* (2010) have reported on the fabrication of crosslinked water-stable electrospun polyethyleneimine/polyvinyl alcohol (PEI/PVA) nanofibers with an excellent dye sorption capability. Those membranes were immersed in a methyl blue (MB) solution and the adsorption kinetic profile was monitored using UV-vis spectrometry as seen in **figure 3.1**.

The adsorbed amount of MB onto the nanofibrous mats was calculated to be 209.63 mg·g^{-1} (137).

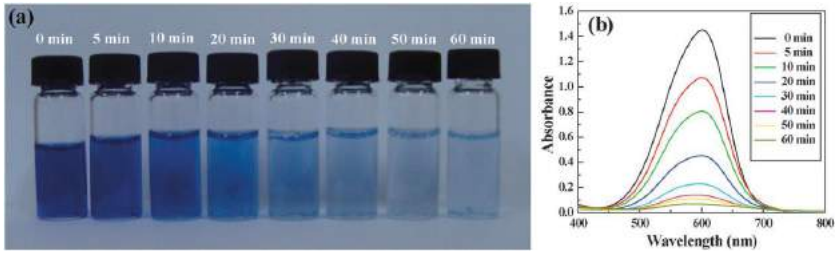

Figure 3.1: (a) *Photographs and* ***(b)*** *UV-vis spectra of methyl blue solution treated with the crosslinked PEI/PVA nanofibrous mats at different time intervals* **(137)**.

As previously mentioned polycyclic aromatic hydrocarbons (PAHs) are toxic and stable pollutants which can be widely distributed in aquatic ecosystems and transported over long distances in water. Y. Dai *et al.* (2011) employed different electrospun non-woven fibrous membranes based on poly(ε-caprolactone) (PCL), poly(D,L-lactide) (PDLLA), poly(lactide-*co*-caprolactone) (P(LA/CL)), poly(D,L-lactide-*co*-glycolide) (PDLGA) and methoxy polyethylene glycol-poly(lactide-*co*-glycolide) (MPEG-PLGA) in order to obtain their sorption ability. Through their study, they showed that electrospun fibers exhibited high sorption effectiveness for PAHs with the highest sorption capacity 4112 μg·g^{-1} being observed in the case of the PCL membranes (138).

Furthermore, with the rapid development of the industrial sector, heavy metal ions are directly or indirectly discharged into the environment increasingly, especially in developing countries (139). Heavy metal ion pollution also constitutes a serious environmental and human problem due to their harmful effects, including toxicity or carcinogenicity, nonbiodegrability, and accumulation in living organisms (140; 141).

The adsorbability of chitosan electrospun nanofibrous mats (diameter 235 nm) for copper (Cu(II)) and lead (Pb(II)) metal ions was examined in aqueous solutions by S. Haider and co-workers (2009). The neutralized chitosan nanofibrous matrices were found to be very effective in metal ion removal with adsorption capacity reaching 485.44 mg·g^{-1} and 263.15 mg·g^{-1} for Cu(II) and lead Pb(II) respectively (142).

Y. Tian *et al.* (2011) reported on the fabrication of polymethyl methacrylate (PMMA)-graft-modified cellulose acetate (CA) nonwoven electrospun membranes and evaluated

their ability to act as adsorbents for copper (Cu(II)), mercury (Hg(II)), and cadmium (Cd(II)) heavy metal ions. Through their experimental results the authors demonstrated that the membranes have high adsorption selectivity for Hg(II) (69).

In conclusion, the superior properties characterizing electrospun nano- and micro- fibrous membranes including among others structural flexibility, high surface area and porosity, resulting to a high adsorption capacity, eco-friendliness, and recycling make them excellent candidates for environmental applications especially in water remediation processes (143).

3.2. Polymer-based magnetoactive electrospun fibrous membranes

Nanocomposite materials belong to one of the most exciting and emerging classes of advanced materials receiving considerable interest due to their potential applications in many scientific and technological fields (144). These materials compris two or more phases of different chemical constituents or structures, with at least one of the phases having nanometric dimensions (145). A combination of functional inorganic/organic fillers at the nanometer scale with polymer-based fibers accomplished by electrospinning leads to novel and highly attractive nanocomposite systems exhibiting exceptional features for many applications in the biomedical field (146; 33; 147), in catalysis (148), environmental (149), and in energy-related applications (57; 145). This improved performance compared to the pristine polymer fibers arises from the combination of the properties of the individual organic and inorganic components, as well as the generation of new properties and consequently enhanced materials' performance *via* the development of organic-inorganic interfacial interaction phenomena (35; 145; 39; 150).

To date numerous examples appear in the literature dealing with the fabrication of electrospun magnetoactive polymer-based fibrous nanocomposites that mainly focus on the synthetic and characterization aspects. In such materials different types of polymers including natural polymers, biopolymers and synthetic polymers, have been combined with magnetic nanoparticles (NPs) including iron oxide (magnetite) (Fe_3O_4) (151; 152; 153; 154), maghemite (γ-Fe_2O_3) (155; 156; 157), cobalt (Co) (158), nickel (Ni) (159), iron-platinum (FePt) (160; 161) NPs etc. Iron oxide magnetic NPs are superior to other metal oxide NPs due to their biocompatibility, non-toxicity, and stability and are, by far, the most commonly employed magnetic NPs for biomedical applications (162).

3.2.1. Synthesis and surface modification of magnetic nanoparticles

Magnetic NPs offer attractive possibilities in biomedicine due to their controllable size ranging from a few nanometers up to tens of nanometers, and dimensions smaller than or comparable to those of cells (10-100 μm), viruses (20-450 nm), proteins (5-50 nm) or genes (2 nm wide and 10-100 nm long) (163). Moreover, modification of their surfaces provide them with additional functions and render them ideal candidates as contrast agents in magnetic resonance imaging (MRI), in biomolecular detection, cell tracking, and for targeted drug delivery in tumour therapy (164; 165).

Magnetic NPs of different compositions and phases have been synthesized, including iron oxides, such as Fe_3O_4 and γ-Fe_2O_3, pure metals such as Fe and Co, as well as spinel-type ferromagnets, such as $MgFe_2O_3$ and $CoFe_2O_4$ (166; 167; 168). Several procedures have been developed for the preparation of magnetic NPs, including chemical co-precipitation, thermal decomposition in organic media, and microemulsion processes (168). Co-precipitation is a facile and convenient way to synthesize iron oxides (either Fe_3O_4 or γ-Fe_2O_3) from aqueous solutions containing Fe^{2+}/Fe^{3+} salt mixtures in the presence of a base (typically NaOH or NH_4OH) under inert atmosphere at room or at elevated temperatures. The type of the salts used (e.g. chlorides, sulfates, nitrates), the Fe^{2+}/Fe^{3+} molar ratio, the reaction temperature, the pH value and ionic strength of the media influence strongly the size, shape, and composition of magnetic NPs (169; 168).

In thermal decomposition process the decomposition of iron organic precursors (e.g. carboxylates) takes place at high temperatures, after their injection to a hot solution of organic solvents (e.g. phenyl ether) in the presence of surfactants (e.g. oleic acid). During this process, parameters such as temperature, solvents, and reaction time normally play a key role in the formation of the final products. For example when the water content in the reaction set-up is increased, larger Fe_3O_4-particles are produced. The microemulsion method is composed of three phases: oil, water and surfactant, where dispersion of two immiscible liquids, such as oil and water, in the presence of surfactant occurs. The surfactant provides confinement effects that limit the particle nucleation, growth and agglomeration (170; 169).

Nevertheless, in the absence of any surface coating, magnetic iron oxide NPs have hydrophobic surfaces with a large surface-to-volume ratio. In order to reduce their large surface area, and due to the development of strong magnetic interactions, the magnetic NPs

exhibit a high tendency for agglomeration, and form large clusters, resulting in increased particle size **(figure 3.2 (a))**. These clusters show ferromagnetic or ferrimagnetic behavior due to the exhibition of strong magnetic dipole-dipole attractions between them. Moreover, the uncoated iron oxide magnetic NPs have high chemical activity, and are easily oxidized in air (especially magnetite) which results in decreasing magnetism and dispersibility (171).

When the size of the NPs is below a critical value, which depends on the material, but is typically around 10-20 nm, the particles exhibits unique magnetic properties (168). In order to obtain such small magnetic NPs, stabilizers are usually added at the time of preparation to prevent NPs aggregation **(figure 3.2 (b))** (172). More precisely, this agglomeration might be avoided if the surface of the MNPs is modified or coated with appropriate stabilizing agents such as organic surfactants (electrostatic repulsion) (e.g. sodium oleate, dodecylamine) or organic polymers (steric repulsion) (e.g. chitosan, polyethylene glycol, polyaniline), as well as bioactive molecules and structures (e.g. liposomes, peptides). Practically, in many cases the protecting shells could also be used not only for the stabilization of the iron oxide magnetic NPs, but also for further functionalization (173; 174; 175; 176; 151; 177; 162; 178).

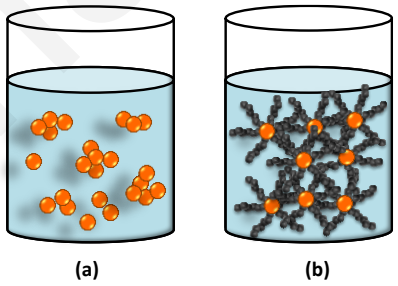

Figure 3.2: (a) *Agglomerated magnetic NPs.* ***(b)*** *Coated magnetic NPs stabilized in aqueous solution.*

Electrostatic interactions are important in the stabilization of many colloidal systems including clays and sols. Stabilization is based on the development of repulsion forces on the surface of the colloidal particles, in order to overcome the attraction forces **(figure 3.3)**. In liquid dispersion media, ionic groups can adsorb onto the surface of the colloidal particle resulting in the generation of an electrical double layer. To maintain electroneutrality, an equal number of counterions with the opposite charge will surround

the colloidal particles and give rise to overall charge-neutral double layers. In electrostatic stabilization, it is the mutual repulsion of these double layers surrounding the particles that provides stability.

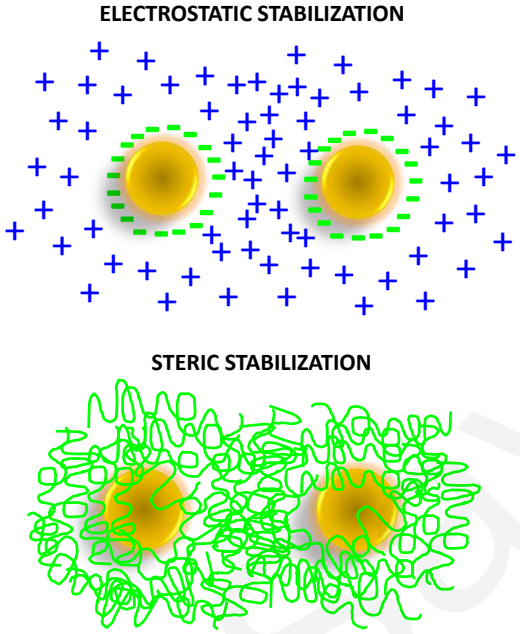

Figure 3.3: *Schematic illustration of the two basic stabilization mechanisms to stabiliz the NPs: Electrostatic and steric stabilization.*

Steric stabilization occurs when long-chain molecules cover the particle surface **(figure 3.3)**. When the colloidal particles approach one other, an effective repulsion occurs due to the limited interpenetration of the polymer chains, leading to the stabilization of the dispersion against flocculation (179). In the case of sterically stabilized NPs in various carrier liquids, the particle surface covering efficiency and consequently the balance between attractive and repulsive interactions between particles are closely related to the type and quality of the stabilizing agents used, as well as the temperature of the medium (180). Electrosteric stabilization is referred as a combination of the two above-mentioned mechanisms and can be also employed for minimizing particle aggregation based on the enhancement of the repulsive interaction forces.

Steric stabilization is advantageous compared to electrostatic stabilization. Firstly, steric stabilization is effective in both non-aqueous and aqueous media, whereas electrostatic stabilization commonly takes place in aqueous solutions. Additionally, in steric stabilization electrolyte concentration does not influence the interparticle repulsion, in

contrast to charge-stabilized colloids where the electric double-layer thickness is very sensitive to ionic strength. Finally, electrostatic stabilization is mostly effective at low colloidal concentrations, whereas steric stabilization may operate in a broader concentration range (179).

When the magnetic NPs are stabilized entirely by electrostatic repulsion mechanisms in the presence of surfactant bilayers their stability is strongly affected by external conditions such as pH and ionic strength, offering little flexibility for altering the surface properties of the particles. This is especially important especially when such colloidal systems are destined for use in biomedical applications because they are administered in a human body, and hence they have to be highly stable at both neutral pH and high ionic strength. By coating the particle surface with organic polymeric materials/surfactants that provide steric repulsion between the particles, the stabilization of magnetic NPs under such biological conditions can be significantly improved (181).

Surface modification of superparamagnetic iron oxide magnetic nanoparticles (SPIONs) can be carried out either during their synthesis or in a post-synthesis process. The ideal molecules for the stabilization of SPIONs should be biocompatible and biodegradable. One of the most widely used categories of stabilizers for SPIONs, are surfactants such as oleic acid, lauric acid, alkane sulphonic acids, and alkene phosphonic acids. These molecules consist of a hydrophobic tail and a hydrophilic head and are amphiphilic in nature. Surfactants can bind effectively onto the SPIONs surfaces and stabilize them in organic solvents. However, SPIONs in organic suspensions cannot be used for biological purposes (182; 164). This hydrophobic surface could be inverted to a hydrophilic surface, by using an amphiphilic polymeric shell, or upon introducing a surfactant bilayer.

Oleic acid (OA) is a surfactant that has been extensively used to stabilize the magnetic NPs synthesized by the traditional co-precipitation method (183; 184). J. N. K. Shimoiizaka *et al.* (1980) were the first to introduce OA as stabilizer for magnetic NPs. They employed a bilayer stabilization process by first precipitating oleic-acid-coated particles and then redispersing them in aqueous solutions of sodium dodecylbenzene sulfonate, poly(oxyethylene) nonylphenyl ethers, and di(2-ethylhexyl)-adipate, which adsorb as a second layer on top of the oleic acid (185; 186; 181). Additionally, in order to transform the SPIONs dispersion from organic to aqueous solution Y. Wang *et al.* (2003) used alpha-cyclodextrin as a host molecule, capable of forming an inclusion complex with the hydrophobic OA-coated SPIONs (187).

One of the most common ways to stabilize magnetic NP, providing colloidal stability in water through steric stabilization is the use of polymer stabilizers. In this case the repulsive forces are reinforced in order to balance the magnetic and Van der Waals attractive forces acting on the NPs (171). Additionally, the use of a polymer surface coating may provide further functions and exclusive physical and chemical characteristics thus allowing the use of MNP in various fields. However, a main drawback accompanying the anchoring of a non-magnetic polymer coating onto the MNP surface is the reduction in the saturation magnetization (M_s) (170). The polymer is bonded onto the surface of the dispersed NPs *via* adsorption or by grafting (188). Regarding the latter, polymer anchoring can be achieved *via* two alternative approaches. In the first way an initiator is immobilized onto the iron oxide magnetic NPs surface followed by polymerization. In the second way, the grafting of the polymer chain can be performed by the *in-situ* grafting of functional, pre-formed polymer chains on the NP surfaces (189).

Various polymers either synthetic or natural were successfully used as coating materials for MNP. Poly (ethylene-*co*-vinyl acetate), polyvinylpyrrolidone (PVP), polylactic-*co*-glycolic acid (PLGA), polyethylene glycol (PEG) or polyvinyl alcohol (PVA) gelatin, dextran, polylactic acids, starch, albumin, liposomes, chitosan, ethyl cellulose etc. have been used for the dispersion of SPIONs in aqueous media for the purpose of drug delivery (172). Biological molecules such as proteins, polypeptides, antibodies etc., may also bind to the surface of iron oxide magnetic NPs by chemical coupling using appropriate end-group functionalities, so as to make the NPs both stable and target specific (171; 190).

N. Jain *et al.* (2009) synthesized stable, water-based γ-Fe_2O_3 ferrofluids *via* co-precipitation followed by stabilization using a short chain, water-soluble diblock copolymer of acrylic acid and acrylamide prepared by reversible addition-fragmentation chain transfer (RAFT) controlled radical polymerization. This polymeric steric stabilizing layer remained strongly attached to the NPs surface even under extreme solution conditions (181).

L. L. Zhou *et al.* (2009) prepared polymer-coated magnetic NPs using poly((2-dimethylamino) ethyl methacrylate) (PDMAEMA), in order to develop novel potential carriers for targeted drug delivery and controllable release. The core/shell Fe_3O_4/PDMAEMA hybrid NPs were loaded with a drug and the drug release was effectively controlled by alternating the pH-value (191). The same research group reported also on the synthesis of magnetic NPs using poly(ε-caprolactone)-carbazole as a stabilizing

agent. The resulting core/shell structure was evaluated in targeted drug delivery under an externally applied magnetic field (192).

Finally, metallic NPs could be combined with magnetic NPs leading to new applications in biomedicine. Metallic core-shell types of iron oxide magnetic NPs have been extensively investigated, having an inner iron oxide core and an outer inorganic metallic shell (172). One of the simplest and efficient methods to prepare such core-shell nanostructures is the sequential growth of metallic components onto a "colloidosome" of magnetic NPs, where the metallic compounds is attached on the exposed surface of the magnetic NPs **(figure 3.4)** (193). These coatings provide NPs stability, and assist the binding of various biological ligands on the NP surfaces (172).

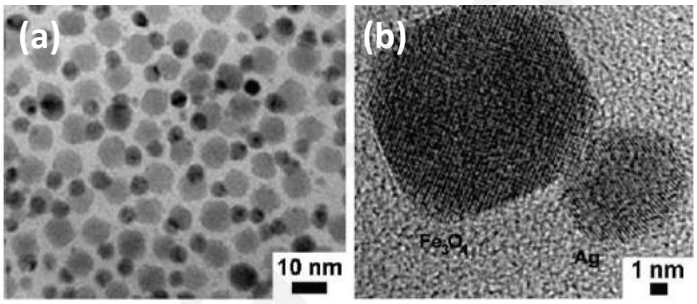

Figure 3.4: (a) *TEM and* ***(b)*** *HRTEM images of Fe_3O_4-Ag heterodimers generated at a liquid-liquid interface* **(193)**.

3.2.2. Magnetic properties of magnetic- and iron oxide-based nanoparticles

Iron oxide based crystalline structures have the general formula $Fe^{3+}O_3M^{2+}O$, where M^{2+} is a divalent metal ion such as iron (Fe), manganese (Mn), nickel (Ni), cobalt (Co), or magnesium (Mg). In magnetite the M^{2+} is the ferrous iron Fe^{2+}. Magnetite, Fe_3O_4 ($Fe^{3+}O_3Fe^{2+}O$), has a cubic inverse spinel structure with oxygen forming face cubic center (FCC) **(figure 3.5 (a))**, with lattice parameters at 8.396 Å, closed packing and Fe cations occupying interstitial tetrahedral sites and octahedral sites **(figure 3.5 (b))**. Due to electron hopping occurring between Fe^{2+} and Fe^{3+} ions in the octahedral sites at room temperature, magnetite behaves like a half-metallic material. With proper surface coating, these magnetic NPs can be dispersed into suitable solvents, forming homogeneous suspensions,

called ferrofluids that retain their solution stability and homogeneity even in the most intense magnetic fields (172; 165).

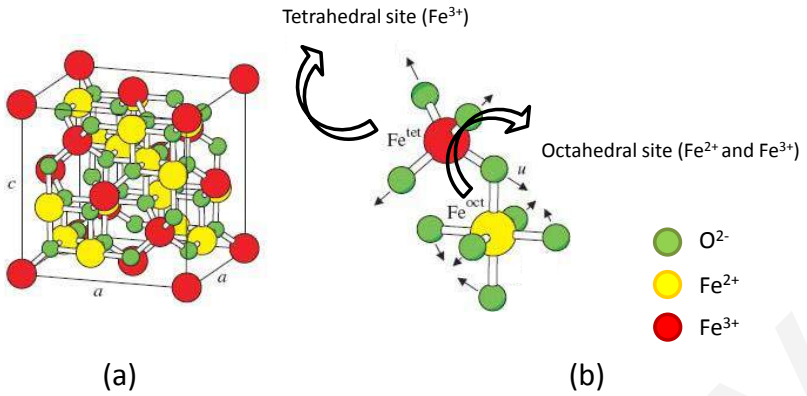

Figure 3.5: (a) *Face-centred cubic spinel structure of magnetite and* ***(b)*** *magnification of one tetrahedron and one adjacent octahedron sharing an oxygen atom* **(194)**.

Iron is a versatile element forming several phases with different oxidation states and structures, such as magnetite (Fe_3O_4–$Fe^{2+}Fe^{3+}{}_2O_4$) exhibiting ferrimagnetic, or superparamagnetic behavior when the particle diameter size is less than 15 nm, hematite (α-Fe_2O_3) that demonstrates weakly ferromagnetic or antiferromagnetic behavior, maghemite (γ-Fe_2O_3) which exhibits ferrimagnetic behavior and wüstite (FeO) that is characterized by an antiferromagnetic behavior. All these iron oxide phases have unique physicochemical properties which can be used for different applications (195; 171). For all the above-mentioned iron oxides magnetite and maghemite are the most promising and popular candidates especially for applications in the biomedical field.

When a magnetic material is placed in a magnetic field, the individual atomic moments in the material contribute to its overall response.

The magnetic field strength H, the induction magnetic field B, and the magnetization M are related according to the **equation 3.1**:

$$B = \mu_0 \cdot (H + M) \qquad \textbf{Equation 3.1}$$

where, μ_0 is the permeability *in vacuo* ($1.257 \cdot 10^6$ $H \cdot m^{-1}$), and $M = m / V$ is the magnetic moment per unit volume, where m is the magnetic moment in a volume V of the material. All materials are magnetic to some extent, with their response depending on their atomic

structure and temperature. They may be conveniently classified in terms of their volumetric magnetic susceptibility, χ **(equation 3.2)**:

$$M = \chi \cdot H \qquad \textbf{Equation 3.2}$$

where, M describes the magnetization induced in a material by H.

While the size, shape, variations occurring for example *via* doping, and shell-core design can tune the magnetic properties of the magnetic NPs based on the response of the intrinsic MNP magnetic dipole and the net magnetization in the presence and absence of an applied magnetic field, magnetic NPs are typically classified as being either diamagnetic, paramagnetic, ferromagnetic, ferrimagnetic, and antiferromagnetic. **Figure 3.6** shows the net magnetic dipole arrangement for each of these types of magnetic materials (196).

Diamagnetic materials are those which are magnetic only under an applied magnetic field. Diamagnetism which is a weak form of magnetism, occurs only in the presence of a magnetic field where magnetic moments are temporarily aligned opposite to the applied field whereas, after the external field is removed this alignment is not retained. This phenomenon is caused only by the orbital motion of the electrons under the influence of an applied field, therefore the magnetic permeability and the magnetic susceptibility are negative (-10^{-6} to -10^{-3}). Although, diamagnetism is found in all materials it can only be observed in materials that do not exhibit any other forms of magnetism (170).

Paramagnetic materials also show weak magnetization having small magnetic permeability (μ) and magnetic susceptibility (χ) in the order of 10^{-6} to 10^{-1}. In paramagnetic materials, the existing magnetic dipoles are partially oriented to the field only upon applying of an external magnetic field. These materials have unpaired electrons that in the absence of the magnetic field are randomly oriented. These electrons in the presence of an external field are aligned parallel to the applied magnetic field. This type of materials have neither coercivity nor remanence indicating that after the external field is removed the internal magnetic dipoles randomize again and no extra energy is required to demagnetize the material. Hence the material does not remain magnetized. Examples of paramagnetic materials include magnesium, molybdenum, lithium and tantalum (197; 170; 196).

Ferri- and **ferromagnetic** materials are those that are able to maintain their magnetic properties even after the magnetic field is removed exhibiting strong magnetization, only

below their corresponding Curie temperature (T_C). T_C is the temperature at which the elementary magnetic moments are randomized and the material is demagnetized. They contain unpaired electrons, whose moments are due to the interactions between neighboring spins, at least partially aligned even when no magnetic field is present. Ferromagnetic substances have an overall net magnetic moment, and they are characterized by a large and positive susceptibility ($0.01\text{-}10^6$) and a large magnetic permeability in the presence of an external magnetic field. Their strong magnetic properties are attributed to the presence of magnetic domains. In these domains, large numbers of atomic moments (10^{12} to 10^{15}) are aligned parallel to the field so that the magnetic force within the domain is strong even in the absence of an applied magnetic field (170; 172; 196).

Besides the ferromagnetic materials, there is a different magnetization state at which the magnetic dipoles or interacting spins of a material are aligned antiparallel in the lattice hence showing a net zero magnetism namely as **antiferromagnetism**. The iron oxide particles such as the magnetite and the maghemite belong to a different magnetization category, the so-called ferrimagnetics. In this class of materials the magnetic moments of the atoms found at different sublattices are opposed, but since those are unequal, a net magnetization value remains.

In **antiferromagnetic** and **ferrimagnetic** materials, the atomic level magnetic dipole moments are similar to those of ferromagnetic materials, however, adjacent dipole moments exist that are not oriented in parallel and effectively cancel or reduce, respectively, the impact of neighboring magnetic dipoles within the material in the absence of an applied field.

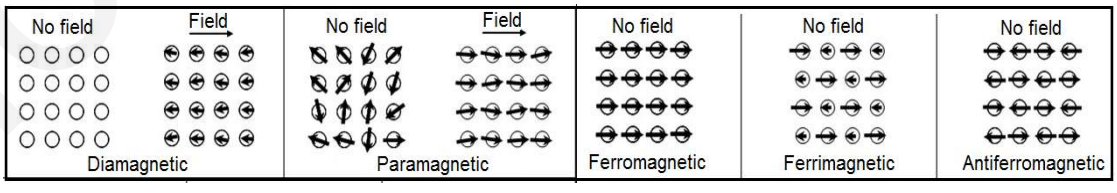

Figure 3.6: *Magnetic dipoles and behavior in the presence and absence of an external magnetic field. Based on the alignment and response of magnetic dipoles, materials are classified as diamagnetic, paramagnetic, ferromagnetic, ferrimagnetic, and antiferromagnetic* **(196)**.

The magnetic properties of the iron oxide particles are closly-related to their size. Particles with diameters of less than 20 nm represent an important class of nanostructured materials (198). It is well-known that the internal ferromagnetism of a ferromagnetic material is no longer maintained as the particle size decreases (199). F Frenkel and J. Dorfman (1930) (200) were the first to predict that a particle of a ferromagnetic material, below a critical size, (<15 nm), would consist of a single magnetic domain (201). When the size of magnetic domain decreases, the effect of thermal fluctuation is not negligible, resulting to the reduction of the remanant magnetization at zero field, whereas the relaxation of the magnetic dipole moments becomes more reversible and fast (199).

Iron oxide, at this scale exhibits a **superparamagnetic** behavior at room temperature with high saturation magnetization (M_s) values (172). That means, when these NPs are placed in an external magnetic field, their magnetic moments align rapidly in the direction of the magnetic field, enhancing the magnetic flux thus the material displays a net magnetization. When the NPs size is around 10-20 nm, each NP becomes a single magnetic domain and shows superparamagnetic behavior (168). Superparamagnetism is caused by thermal effects occurring in the material (202). When the magnetic field is removed, these particles have zero coercivity (the field required to bring the magnetization to zero) and above the blocking temperature (T_B), thermal fluctuations are strong enough to spontaneously demagnetize a previously saturated assembly; therefore superparamagnetic materials have no hysteresis loop (165; 202).

Superparamagnetism occurs when crystal-containing regions of unpaired spins are sufficiently large that they can be regarded as thermodynamically independent, single domains. The net magnetic dipole of these single domains is larger than the sum of their individual unpaired electrons. In the absence of a magnetic field, such magnetic domains are free to rotate due to thermal motion, and are randomly oriented, whereas in the presence of a magnetic field the magnetic dipoles are re-oriented **(figure 3.7)**. After removal of the magnetic field, magnetic domains loose their orientation and the net magnetic moment becomes zero (203). The use of superparamagnetic nanosystems is preferred, especially in biomedical applications, due to their ability to become magnetized upon exposure to a magnetic field whereas no permanent magnetization remains when the field is turned off (202).

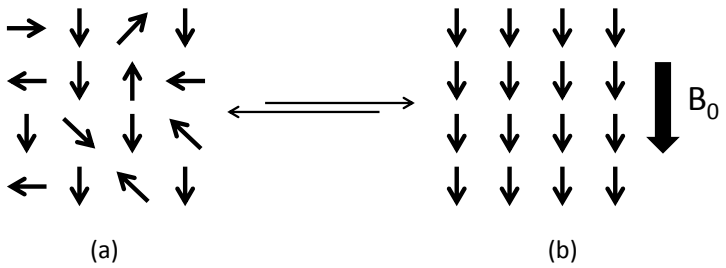

Figure 3.7: (a) *SPIONs single domains are randomly oriented in the absence of an external magnetic field and* ***(b)*** *SPIONs in the presence of an external magnetic field (B_0) are reoriented parallel to the field.*

For magnetic NPs there are three important parameters that describe their strength and magnetization. The first one is the maximum magnetization that can be achieved, known as the saturation magnetization (M_S), and it arises when all the magnetic dipoles are aligned in the direction of an externally applied magnetic field. The second one is the remanent magnetization (M_R), which indicates the residual magnetization after an applied field is removed. The final parameter is the coercive field (H_C), presenting the external field of opposite sign that is required to reduce the magnetization back to zero. **Figure 3.8** shows typical magnetization curves for magnetic NPs exhibiting different magnetic behavior. In contrast to the hysteresis loop which is observed in the case of ferromagnetic NPs (red line), the response of the superparamagnetic NPs under an applied magnetic field, follows a sigmoidal curve without hysteresis (green line). In the same figure the paramagnetic (blue line) and diamagnetic (black line) behaviour are also shown (163; 196).

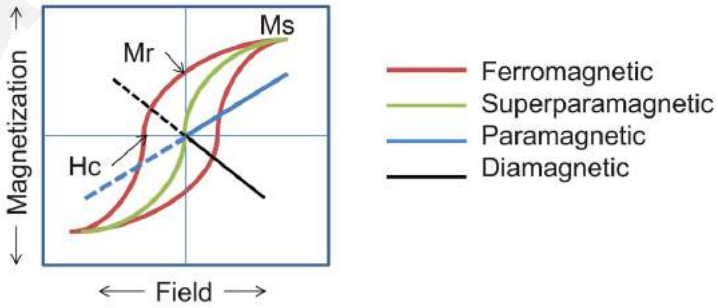

Figure 3.8: *Magnetization versus applied magnetic field strength plots indicating different magnetic responses of the magnetic NPs* **(196)**.

Finally, the magnetic behavior of magnetic NPs is temperature-dependent. As previously mentioned, above the temperature known as the blocking temperature (T_B,), both ferromagnetic and ferrimagnetic NPs exhibit superparamagnetic behavior. More precisely, if the magnetic moment reverses at shorter times than the experimental time scales, the system is found to be in a superparamagnetic state, if not, it is in the so-called blocked state. The temperature, which separates these two regimes, is referred as T_B. T_B depends on the effective anisotropy constant K_u, that determines the energy to be overcome in order to invert the direction of the magnetic dipoles of the material, the size of the particles, the applied magnetic field, and the experimental measuring time (168). While the magnetic dipoles have the tendency to fluctuate randomly and with the temperature rise this phenomenon increases, the moments are not aligned in respect to each other resulting to the reduction of the M_S. Furthermore, at a certain temperature the so-called Curie temperature (T_C), a ferromagnetic material becomes paramagnetic. Néel temperature (T_N) corresponds to the transition temperature of antiferromagnetic or ferrimagnetic behavior to paramagnetic. At these temperatures, the available thermal energy simply overcomes the interaction energy between the spins and the macroscopic magnetic ordering, within the material, is destroyed.

3.2.3. Magnetoactive electrospun polymer-based nanocomposites in biomedical applications

The development of multifunctional magnetic NP-containing systems that present superparamagnetic behavior at room temperature is an ambitious goal, opening new avenues for selective and targeted therapy treatment. Generally NPs are more beneficial compared to microparticles, since they exhibit efficient uptake by a variety of cell types and they are available to a wider range of cellular and intracellular targets due to their smaller size and higher mobility (204). Additionally, when considering the MNP surface chemistry for drug delivery, it is important that magnetic NPs retain sufficient hydrophilicity, and do not exceed 100 nm in size (including the surface coating), so as not to be recognized by the reticuloendothelial system (RES). RES is a class of cells that occur in widely separated parts of the human body, and are phagocytic cells i.e., they can engulf and destroy bacteria, viruses, and other foreign substances (162; 202). As previously noted the stabilization, which is directly linked to the particles' size, is essential for using magnetic NPs in medical applications in water at neutral pH and physiological salinity

(201; 181). Concluding, functionalized magnetic NPs are essential in biomedicine due to their unique magnet properties, higher effective surface areas, lower sedimentation rates and improved tissular difusion (164; 201).

Magnetoresponsive polymer-based fibrous nanocomposites belonging to the broad category of stimuli-responsive materials, is a relatively new class of "soft" composite materials, consisting of magnetic NPs embedded within a polymeric fibrous matrix. The presence of an externally applied magnetic field influences the properties of these materials rendering them useful in numerous biomedical applications including magnetically-triggered drug delivery (205), magnetic cell seeding, magnetic bioseparation (206), hyperthermia cancer treatment (207), contrast enhancement in magnetic resonance imaging (208; 209; 210) and biosensing (211).

All the above emphasize on the importance in the preparation of magnetoactive electrospun fibers (178). The major difficulties during the preparation of such materials include the development of stable dispersions of magnetic NPs, the selection of an appropriate method for fiber preparation and the generation of (nano)fibers with tunable degradation rate depending on the application (212).

Different strategies have been employed to generate electrospun magnetoactive polymer-based (nano)fibers. The main one involves the direct mixing of magnetic NPs with the polymer solution followed by electrospinning. For obtaining homogeneous nanoparticle dispersions in polymer-containing solutions, mechanical stirring and ultrasonication are usually employed (213; 214; 156). As mentioned above, due to their hydrophobicity, high surface area, and the presence of strong magnetic interactions, these MNPs tend to agglomerate. Consequently, inhomogeneous polymer solutions are generated and solution stability issues that disfavor the electrospinning process rise. As a result the magnetic NPs may not be evenly distributed within the produced electrospun nanofibers, whereas such aggregation phenomena may significantly affect the magnetic properties of the final products.

Another approach that has been explored for the production of composite nanofibrous membranes involves the simultaneous electrospinning-electrospraying process. Nanomaterials or nanoparticles are electrosprayed from a different direction to that of electrospinning with a parallel power source and syringe pump as schematically illustrated in **figure 3.9** (86; 215). D. Gupta *et al.* (2009) combined electrospinning and

electrospraying techniques in order to produce a better osteophilic environment for the growth and mineralization of osteoblasts. More precisely, they electrosprayed hydroxypatite (HA) NPs on the surface of electrospun polymeric nanofibers developing in this way a uniform layer (216).

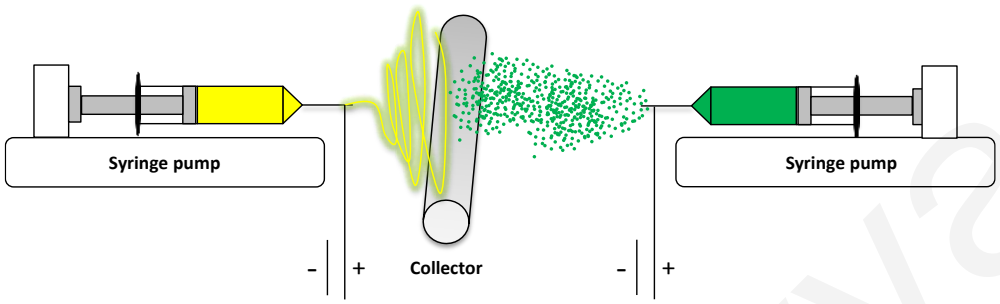

Figure 3.9: *Set-up of simultaneous electrospun-electrospraying.*

Tissue engineering: One of the most important biomedical challenges is the design of an ideal tissue-engineering scaffold. As previously noted the structural features of the tissue-engineering scaffolds affect cell response and must be engineered to mimic the structure and biological functions of ECM, to support cell adhesion, proliferation, migration and also to provide a good environment for the cells ensuring functional neotissue formation. Polymeric nanofibers are gaining increasing popularity because they can serve as tissue-engineering scaffolds, due to their morphological similarities to the native ECM (217; 178).

Magnetic-loaded therapeutic systems have shown promising results in tissue engineering applications. More precisely, it has been demonstrated that magnetoactive tissue engineering scaffolds can be used in the treatment of bone diseases by promoting proliferation and differentiation of osteoblasts, increasing osteointegration, and accelerating new bone formation (218). Based on previous literature reports, the applied static magnetic field promotes cell proliferation thus stimulating bone tissue regeneration (219; 220). The introduction of magnetic nanoparticles results to further enhancement in cell proliferation, demonstrating that the applied magnetic field in combination with magnetic nanoparticles act in a synergistic manner.

However, to the best of our knowledge, very few studies exist so far describing the evaluation of magnetoactive electrospun fibrous membranes as scaffolds for bone regeneration. J. Meng *et al.* (2010) studied cell proliferation, differentiation and ECM

secretion of osteoblast cells in the presence of magnetoactive, electrospun nanofibrous composite mats under a static magnetic field providing a system with promising application potentials (157). They fabricated scaffolds composed of poly(D,L-lactide) (PLA), hydroxyapatite nanoparticles (nHA) and *meso*-2,3-dimercaptosuccinic acid (DMSA)-coated γ-Fe_2O_3 nanoparticles and they showed that when a static magnetic field (0.9-1.0 mT) was applied a significantly higher proliferation rate and faster differentiation of osteoblast cells were displayed **(figure 3.10)** (157).

Moreover, a magnetically-modified extracellular matrix protein (ECM) namely laminin has been attached in a gradient manner onto electrospun nanofibrous scaffolds using an externally-applied magnetic field (221). From all the above it becomes obvious that the combination of electrospun nanofibers with magnetic NPs is expected to lead to new materials with superior properties and functions enabling their high efficacy as advanced tissue engineering scaffolds (222; 163; 84).

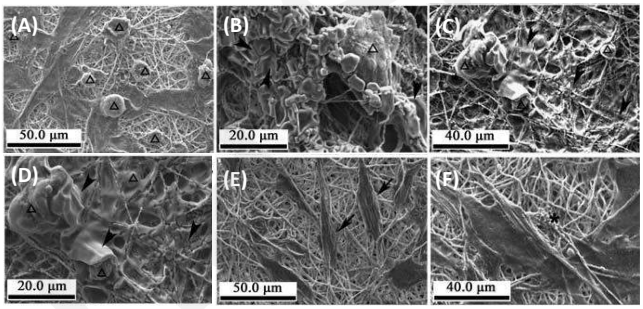

Figure 3.10: *SEM images of the cells on the nanofibrous composite films in the inducible osteogenic supplements for 21 days with applying magnetic fields.* ***A–D:*** *Cells on the γ-Fe_2O_3/nHA/PLA films. E–F: Cells on the nHA/PLA films* **(157)**.

Y. Wei *et al*. (2011) have reported on the fabrication of magnetic biodegradable materials by means of the electrospinning technique, based on native polysaccharide chitosan (CS), polyvinyl alcohol (PVA), and iron oxide (Fe_3O_4) magnetic NPs with potential use in bone regeneration. MG-63 cells were cultured on the Fe_3O_4/CS/PVA nanofibrous membranes to evaluate the cell growth dynamics. The obtained results demonstrated that cell adhesion and proliferation increased in the presence of the magnetic NPs (97).

The performance of magnetoresponsive fibrous mats on bone regeneration was also studied by K. Lai and co-workers (2012) who have reported on the fabrication of fibrous

biocompatible scaffolds consisting of poly(lactic-*co*-glycolic acid) (PLGA) and superparamagnetic Fe_3O_4 NPs with different mass ratios and evaluated their effects on different bone cells in the absence of an external magnetic field (223). The magnetite-containing nanocomposite scaffolds exhibited excellent biocompatibility, enhanced osteoblast cell attachment and proliferation at an early culture time in comparison with the pristine PLGA fibrous analogues.

Drug delivery: Electrospun polymeric fibrous materials have been extensively exploited as drug delivery systems (107; 108), offering some significant medical benefits like large surface area, nontoxic degradation in the human body and the controllable matrix properties such as the diameter, porosity, and morphology by changing the electrospinning processing variables and types of materials.

Of great importance in the design and fabrication of new nanosystems to be used in medical treatment are stimuli-responsive polymer-based biomaterials, exhibiting sensitivity to common triggers, including changes in pH, temperature and magnetic or electrical field. These "smart" nanostructures have demonstrated great potential in the biomedical field as controlled drug delivery systems (224; 225; 226).

Despite the use and future exploitation of MNP-containing electrospun membranes in cell expansion, cell sheet construction, magnetic cell seeding, and cancer hyperthermia treatment (227), those can be also employed in magnetothermally triggered drug delivery (228; 162; 97). The presence of magnetic iron (Fe)-based NPs in a (nano)fibrous drug delivery platform may be proved to be a very promising therapeutic and diagnostic tool in the future, since it may lead to the development of novel and highly effective multifunctional magnetically-triggered drug delivery systems (162).

Generally there are three possible ways of achieving targeted delivery: active, passive, and physical targeting. In active targeting the active agent or the carrier system is attached directly to a tissue- or a cell-specific ligand, whereas passive targeting involves coupling of the active agent to a macromolecule such as a high-molecular-weight polymer that passively reaches the target organ (229; 230). Physical targeting allows distribution of drugs and carrier systems through external influences, such as magnets in the case of MNP or heat (230).

The major disadvantage of most chemotherapies is that they are relatively non-specific. This may have serious negative effects including deleterious side-effects as the drug

attacks normal healthy cells in addition to the target tumour cells. Purposing to the reduction of the drug dosage required, by more efficient and localized targeting, in the late 1970s researchers started to explore the use of magnetic carriers (163). Those structures may be either constructed by MNP coated with a biocompatible polymer or MNP precipitated inside the pores of a porous biocompatible polymer (163; 231; 172).

The effectiveness of the therapy depends on several physical parameters, including the field strength, gradient and volumetric and magnetic properties of the particles. Other ferrofluid parameters such as the particle size, the surface characteristics, the concentration, and the strength of the drug-particle interaction, also influence the infusion route, such as the duration and rate of the injection are very important. Finally, there are physiological parameters such as tissue depth to the target site (e.g. distance from the magnetic field source), reversibility, blood flow, and tumour volume/location (163; 208; 202) that also need to be taken into consideration.

Magnetic drug delivery is currently one of the most active areas in cancer research (208). The first clinical trials in humans with a magnetic drug targeting system were reported by A. S. Lubbe *et al.* (1996), who used ferrofluids (particle size 100 nm) to which the drug epirubicin, which is widely applied for the treatment of solid tumours (232), was chemically bound (233; 234; 235; 236).

Even though large numbers of applications appears dealing with the fabrication of electrospun, polymer-based fibrous (nano)composites comprise polymeric materials and magnetic nanoparticles, only a few studies exist dealing with the investigation of such systems in drug delivery processes. To the best of our knowledge only four reports so far have been focused on the aforementioned application of such polymer-based nanocomposites (178).

L. Wang and co-workers (2012) have reported on the fabrication of electrospun nanofibrous composites based on two cellulose derivatives and Fe_3O_4 magnetite nanoparticles. In those, either indomethacin (IDN) or aspirin have been incorporated as model pharmaceutical compounds and their release profile has been investigated in artificial intestinal juice. Based on their studies they have claimed that the presence of magnetic nanoparticles does not influence the drug release profiles of the nanofibrous devices (237).

In another example, S. T. Tan *et al.* (2005) described the fabrication of superparamagnetic polymer nanofibers consisting of poly(hydroxyethyl methacrylate), PHEMA, poly-L-lactide (PLLA) and magnetite nanoparticles by electrospinning. Their efficiency in drug delivery *via* the incorporation of a fluorescent enzyme namely albumin with dog fluorescein isothiocyanate (ADFI) was investigated. Monitoring the drug release properties of the fluorescent model pharmaceutical compounds has been carried out by means of UV-vis spectrophotometry and fluorescence emission spectroscopy (155).

Finally, in a very recent work by us we have described the fabrication of electrospun magnetoactive polyethylene oxide/poly(L-lactide) (PEO/PLLA) membranes with embedded oleic acid-coated magnetite nanoparticles (OA.Fe_3O_4). Those systems exhibited superparamagnetic behavior at room temperature. The membranes were loaded with a widely used analgesic namely acetaminophen (paracetamol) and its release profile was investigated in a buffer solution and in complete culture media as schematically illustrated in **figure 3.11**. From this investigation in has been demonstrated that the membrane magnetic content as well as the protein content of the release medium are highly influencing factors in the drug release rate (151).

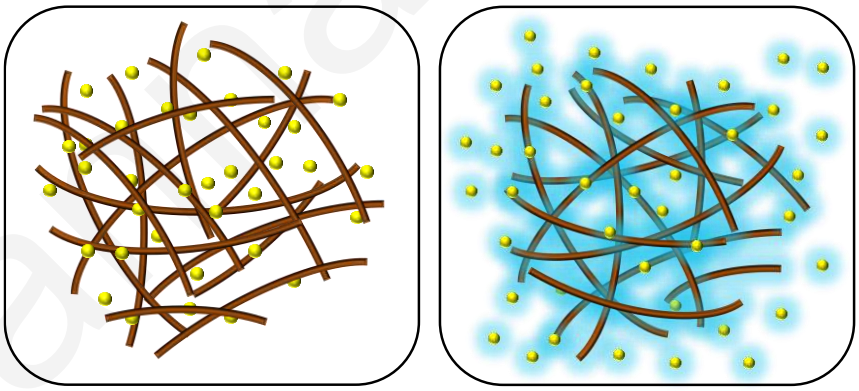

Figure 3.11: *Schematic presentation of the drug release process from drug-loaded magnetoactive electrospun membranes when immersed in an aqueous medium.*

Hyperthermia: Nanoparticles are submicron moieties with diameters ranging from 10 to 100 nm, made of inorganic or organic materials, which have many unique magnetic properties compared with the bulk materials (171). Magnetic NPs are currently the focus of nanotechnology due to their functional and structural properties, including the possibility

to be driven by external magnetic fields, the ability to pass through capillaries without occluding them and to absorb and convert electromagnetic radiation in heat, that are not available from existing molecular or macroscopic agents (238).

The preferential destruction of cancer cells without damaging normal cells has been a desired goal in cancer therapy (208). Cancer cells are destroyed at temperatures higher than 43℃, whereas the optimal temperature for human cells to survive is about 37 °C. Despite the selective damage of cancerous cells due to heating phenomena induced by a magnetic field, magnetic hyperthermia renders cancerous cells more vulnerable to other therapeutic modalities. In hyperthermia treatment external devices are used to transfer energy in the form of heat to tissues either by irradiation with light or *via* electromagnetic waves. Besides magnetic hyperthermia, for hyperthermia induction ultrasound, radiofrequency, microwaves, and infrared radiation are also currently used (207). However, each one of these methods suffers from certain limitations. Based on the above the use of a magnetic field in hyperthermia treatment of malignant tumors has been recognized as a highly promising therapeutic modality in cancer treatment. Magnetic hyperthermia is based on the heat generated at selected sites of the body, due to the presence of magnetic NPs when those are placed in an alternative magnetic field (AMF) (205). The amount of heat generated depends on the nature of magnetic material, the strength of the magnetic field, the frequency of oscillation and the cooling capacity of the blood flow in the tumour site. The magnetic field is not adsorbed by living tissues and it can be applied to deep regions in the living body (172).

MNP-based hyperthermia treatment is advantageous compared to other methods, since it delivers the therapeutic heat directly to the cancer cells rendering the treatment more selective and effective. Selectivity and therapeutic efficiency is enhanced upon anchoring of a cell targetic ligand onto the surface of magnetic NPs. Moreover, the frequencies of oscillating magnetic fields generally pass harmlessly through the body and generate heat only in tissues containing magnetic NPs (207).

Magnetic NPs that are distributed at the targeted tumor site interact with the magnetic field undergoing two different relaxation mechanisms that result to a temperature increase above the physiological body temperature within the range of 41-45℃ (239). More precisely, the Néel relaxation mechanism involves rapid directional changes of the magnetic moments relative to crystal lattice (internal dynamics), whereas in the Brownian relaxation

mechanism heat generation is caused by friction phenomena occurring *via* the physical rotation of the NPs in the medium in which they are dispersed (external dynamics) (207).

Numerous literature examples exist, dealing with the magnetic heating properties of different types of magnetic nanoparticles including iron oxides (Fe_3O_4 and Fe_2O_3) (240), $CoFe_2O_4$ and $MnFe_2O_4$ (241) etc. Nevertheless, the number of reported studies involving the investigation of the applicability of electrospun fibers with embedded magnetic NPs for selective damage of cancerous cells through hyperthermia treatment is very limited **(figure 3.12)**.

In a recent study, electrospun biodegradable chitosan nanofibers with embedded magnetite nanoparticles were explored in regards to their heating capability when exposed to an alternating magnetic field. It was found that the heat produced by the magnetoactive electrospun mats *via* the interaction of the embedded magnetite nanoparticles with the applied alternating magnetic field resulted to a temperature increase in the medium to 45 ^oC, thus demonstrating the potency of these materials in endoscopic treatment of malignant tumors. Moreover, by performing *in vitro* studies, it has been shown that the generated heat causing the aforementioned temperature rise resulted to a significant reduction in the proliferation and growth rate of malignant cells (239).

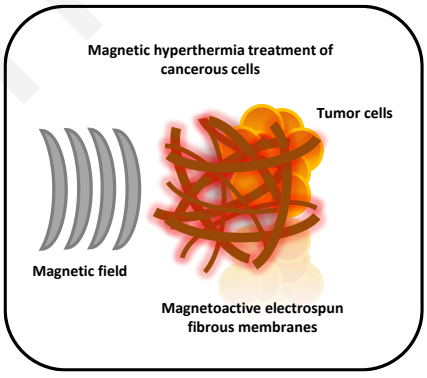

Figure 3.12: *Applicability of magnetoactive electrospun fibrous membranes in hyperthermia cancer treatment.*

In another example, Fe_2O_3 nanoparticles have been incorporated within polyurethane nanofibers by electrospinning, and the resulting fibrous nanocomposite mats have been exposed to an alternating magnetic field. The heating effect was more pronounced upon

increasing the magnetic content within the polymeric nanofibers whereas it had been also demonstrated that the intensity of the applied magnetic field influences the heating capability of the membranes (213).

Although the applicability of polymer-based electrospun magnetoactive fibrous nanocomposites in hyperthermia cancer treatment is new and still unexplored, the first studies provide very promising results, pointing toward their successful use in cancer therapy, either as a stand-alone curing modality or in combination with other therapeutic methods. The immobilization of the magnetic nanoparticles within a solid fibrous polymer matrix is considered to be advantageous for post-surgery hyperthermia treatment at the specific areas of interest resulting to a more effective and targeted therapy.

3.2.4. Catalytic electrospun polymer-based nanocomposites

The acceleration of a chemical reaction of two or more reactants could be achieved by adding a substance known as catalyst, through a process called catalysis. In a catalytic process the reaction rate of a chemical reaction increases by providing a pathway with lower free energy so as for reactants to reach the transition state without changing the position of the equilibrium (242).

Catalysis consists an important field in chemistry since in most chemical reactions a catalyst is involved in least one of their steps (243). Depending on the phase of the substrate related with the phase of the reactants, catalysis can be divided into homogeneous (molecules and enzymes) and heterogeneous. Homogeneous catalytic reactions take place in the liquid phase in which the catalyst and all the other reactants are present. In a heterogeneous catalytic reaction the catalyst is present in a different phase, usually in the solid form, from that of the reactants which are usually present in a liquid state (244). An important benefit of using a heterogeneous catalyst is the relative ease of catalyst separation from the reaction mixture that aids in the creation of continuous chemical processes, and also catalyst recycling. Additionally, in heterogeneous catalysis extreme operating conditions could be used since the catalyst exhibits typically higher tolerance in comparison to its homogeneous analogues. On the other hand, the major drawback of a solid catalyst is that it usually contains a distribution of active sites that are not exactly equivalent. This results to lower selectivity, and difficulties in the determination of the exact catalytic mechanism occurring at the active site (245; 246; 247; 242). Compared to

heterogeneous catalytic systems, homogeneous catalysts do not allow their separation form the reaction mixture after the completion of the reaction. However, they show very attractive selectivity under mild reaction conditions and the reaction mechanism and the nature of the active sites is better understood on a molecular level because the molecular species in a homogeneous catalytic system are easier to identify than those in a heterogeneous one (248; 242; 245; 246; 247).

In homogeneous catalysis, a small active molecule is soluble in a solution reaction, or attached onto the surface by flexible-linker (244). In heterogeneous catalytic reactions, adsorption of reactants from the liquid phase onto a solid surface takes place followed by desorption of the reaction products into the liquid phase as schematically presented in **figure 3.13** (249; 244).

Important types of catalysis are autocatalysis (self-catalysts), biology catalysis (enzyme) and photocatalysis. An autocatalytic reaction takes place in the absence of extra molecules acting as catalysts since the reaction products behave as catalysts for their own formation (250). Throughout photocatalysis a change in the rate of a chemical reaction under the action of light occurs. In this type of catalysis the presence of materials that can adsorb light and participate in the chemical transformation reactions is required (243).

Finally enzymes could act as catalysts for a wide range of organic reactions including redox reactions, carbon-carbon bond formation, and hydrolytic processes. In the past biocatalysis was not the best choice due to several disadvantages involving the limited stability of enzymes under organic reaction conditions, and the low efficiency. However, its improvement in recent years was obvious and enzymes could support numerous examples of organic syntheses (251; 252; 249).

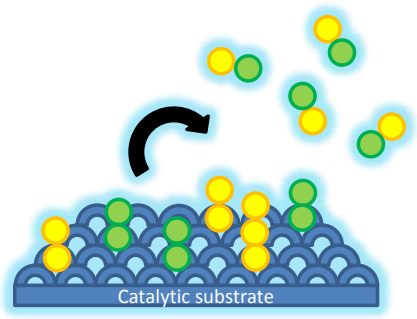

Figure 3.13: *Schematic illustration of heterogeneous catalytic reactions.*

As previously noted an ideal catalyst may be characterized by high activity and selectivity, and also by a high number of product molecules produced per molecule of the catalyst in short time (turnover numbers, TON) (249). Nevertheless, in order to generate an active, selective, and stable catalyst high concentration of catalytically active sites must be available to reagents during catalysis (253). Recently, the development of more efficient and highly active supported catalysts is targeted using nanostructured materials such as nanofibers (254), nanowires (255), carbon nanotubes (256), or metal nanoparticles (257).

Much attention has been focused in metal NPs such as silver (Ag) (258), palladium (Pd) (259; 260), and gold (Au) (261), which exhibit excellent catalytic properties derived by their unique crystalline structures and large specific surface area due to their nanometer scale (262). The combination of the catalytic properties of the aforementioned NPs with electrospun fibrous materials bear a great advantage in terms of high surface-to-volume ratio, high porosity, ease of chemical/physical post-modification processes, recovery, and easy handling. The development of new synthetic/fabrication pathways for further manipulating the architecture and composition of the fibers, may lead to the development of novel, multifunctional hybrid fibrous mats with outstanding catalytic behavior (263; 258; 259; 260; 261). Moreover, the composite catalyst formed by the introduction of NPs on/into solid supports with different nanostructures seems to be the best method to avoid the aggregation of small-sized NPs, thus resulting to a uniform distribution in the substrate retaining their high catalytic activity. Corresponding NP-containing colloidal systems cannot be easily isolated and separated from reaction products after the completion of the reaction, so their recycling is not feasible and their practical applications are limited (264; 265; 266; 258).

There are some literature examples reporting on the incorporation of Pd, Au, and Ag NPs within electrospun polymer fibrous matrices and the evaluation of the resulting fibrous nanocomposites as catalytic supports (267; 268). Pd NPs are well known for their catalytic efficiency and selectivity in carbon-carbon coupling reactions (Heck and Suzuki) (269; 270), in the hydrogenation of dienes and olefins (alkenes) (271), in enamine synthesis (272), in the amination of halopyridines (273) etc.

The Heck reaction **(scheme 3.1)** offers an important tool for the generation of new C-C or C-heteroatom bonds by producing coupling products from olefins with organic moieties bearing a suitable living group such as a halide (binary compound, of a halogen atom and an element or radical that is less electronegative), a triflate (trifluoromethanesulfonate), or

a diazonium (274). Palladium salts and phosphine ligands are the most frequently used catalysts for these reactions. The synthesis of taxol (anticancer drug) (275), of substituted cinnamic acids and corresponding esters, and of octyl 4-methoxycinnamate are some examples of Heck reactions (276; 246; 274).

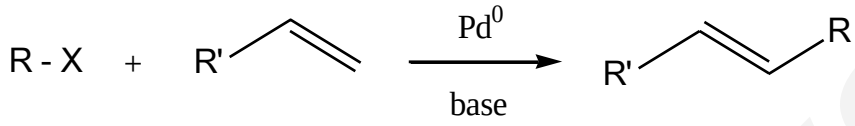

Scheme 3.1: *Schematic illustration of the zero-covalent Pd Heck reaction.*

Although this reaction provides high reaction rates and high turnover numbers and often affords high selectivity and yields, however catalyst recycling is hampered by early precipitation of Pd. This, in combination with the low reactivity of the attractive aryl chlorides limit the use of this process in industrial applications (246; 274).

Among other coupling reactions Suzuki has also gained enormous interest and has become a mainstay of modern synthetic organic chemistry for the preparation of biaryl and heterobiaryl compounds, due to the broad functional group tolerance and the low toxicity associated with boron compounds. It can be further used in coupling of various organic moieties different from aryl compounds, such as alkenes, alkynes, or alkanes (277; 269; 274).

Recently, "click" chemistry has attracted significant attention in materials science. The "click" chemistry concept was established by K. B. Sharpless and co-workers in 2001, as an efficient tool for carrying out polymerizations as well as for performing modifications on macromolecules and solids (278). Well-defined structural polymer-grafted nanoparticles, immobilization of molecules onto the surface of electrospun nanofibers, as well as functional films, hydrogels, carbon nanotubes, and fullerenes have been successfully prepared using click chemistry (279; 280; 281; 282). A well-known example of a click reaction process is the Azide-Alkyne Huisgen Cycloaddition taking place between an azide ($-N_3$) and an alkyne ($\equiv CH$) to form a triazole ring (283; 281). Moreover, the purely thermal 1,3-dipolar cycloaddition reaction between aryl/alkyl azides and strongly activated alkynes, such as acyl- and sulfonyl cyanides as well as acyl-alkynes, was

investigated by K. B. Sharpless and co-workers as a click-type reaction (281). The acceleration of the Huisgen 1,3-dipolar cycloaddition between azides and alkynes even under mild conditions, was published by M. Meldal *et al.* (2002) by using Cu(I) salts, providing product stereoselectivity with high yields, and demonstrating tolerance to oxygen and water (284; 280).

As above-mentioned, NPs may act as effective catalysts in chemistry reactions; consequently, their immobilization on electrospun fibrous membranes could extend the usability and flexibility of the aforementioned reactions (Heck, Suzuki, Click). The incorporation of metal NPs into electrospun nanofibers can be performed *via* the *in situ* generation of the NPs in the fiber. In this synthetic approach the solution containing the polymer and a desired metal salt is electrospun followed by thermal treatment resulting to nanocomposite fibrous mats decorated with metal NPs. An alternative method involves the functionalization of the fibers by the direct deposition of the NPs on the fibers' surfaces (268).

In the literature there are many examples where polymer based nanocomposites containing functional metal NPs have attracted a great deal of attention in regards to their catalytic properties. L. Guo *et al.* (2013) produced Pd NPs/polyvinylpyrrolidone (PVP) composite nanofiberous mats and applied them as heterogeneous catalysts in Heck reaction. Their system provided excellent catalytic activity at low temperature and pressure, stability and reusability (260). L. Gardella *et al.* (2013) fabricated polymer nanofibers based on poly(L-lactic acid) (PLLA) and amino-functionalized polyhedral oligomeric silsesquioxanes (POSS-NH_2) where Pd nanoclusters were homogenously dispersed on their surfaces. The prepared system demonstrated catalytic activity toward the hydrogenation of stilbene into diphenylethane under heterogeneous conditions without Pd leaching during the hydrogenation process (263). X. Fang *et al.* (2011) immobilized gold (Au) NPs into polyethyleneimine (PEI)/polyvinyl alcohol (PVA) nanofibrous mats, which were then crosslinked *via* glutaraldehyde (GA) vapor to render the fibrous mats water-insoluble. The polymer electrospun mat was first used as a nanoreactor to synthesize and immobilize Au NPs. The resulting fibrous nanocomposites demonstrated excellent catalytic activity in the transformation of 4-nitrophenol to 4-aminophenol (261). In 2012 S. Xiao *et al.* tried to immobilize silver (Ag) NPs into electrospun polymer nanofibers rendering them appropriate for the catalytic reduction of 4-nitrophenol to 4-aminophenol. In this approach polymeric mats were prepared by electrospinning followed by crosslinking to yield water-stable polyacrylic acid (PAA)/polyvinyl alcohol (PVA) materials. The Ag NPs were then

immobilized onto the polymeric mats *via* the carboxylic acid groups of PAA capable of complexing the Ag(I) ions and subsequent Ag NP formation by chemical reduction (257).

3.2.5. Electrospun polymer-based nanocomposites for environmental applications

Recently, nanomaterials have been suggested as efficient, cost effective and environmentally friendly candidates for environmental treatment. Several materials have been studied and extensively used for this purpose, such as carbon-based (285; 286; 287), titanium oxide-based (TiO_2) (288), and iron-oxide based nanomaterials (286).

The use of magnetic NPs in environmental remediation processes has received considerable attention. MNP can be used as efficient adsorbents of contaminants from aqueous solutions or gaseous contaminants, due to their nanoscale dimensions, and high surface area-to-volume ratios. Additionally, using a simple magnet the separation of the particles from the medium is feasible, through an efficient, economic, scalable, and nontoxic pathway (289; 290). P. L. Hariani *et al.* (2013) synthesized superparamagnetic Fe_3O_4 by chemical co-precipitation (diameter 5-20 nm) and investigated the ability of the NPs to remove portion dye from water with adsorption capacity 30.503 $mg \cdot g^{-1}$. Portion dyes, including azo dyes are frequently employed in the textile industry (124).

Electrospun fibrous membranes providing high surface area and porous structure constitute beneficial substances for environmental applications offering an attractive and inexpensive option for the efficient removal of various organic contaminants from water. The functionalization of the membranes, or the incorporation of nanoparticles, for example MgO, TiO_2, Al_2O_3, and Fe_3O_4 into electrospun membranes, results to a nanocomposite system which can be effectively used for wastewater purification (291; 292; 287; 124). The appropriate choice of nanofillers usually guide the final properties of the substances, including their mechanical and thermal behavior, hydrophilic/hydrophobic balance, chemical stability, bio-compatibility, optical and/or electronic properties and chemical functionalities. While the surface area as well as the chemical structure has a high impact on the adsorption efficiency of the adsorbent, the incorporation of inorganic nanofillers within electrospun membranes might lead to further optimization of the adsorption efficiency (293). Many publications appear, demonstrating that nanocomposite materials can be used for dye and metal ion removal from wastewater, however only a few examples

have appeared so far on the use of nanocomposite electrospun membranes in water remediation process.

R. Xu *et al.* (2012) synthesized novel mesoporous poly(acrylic acid)/SiO_2 composite electrospun nanofibers (fiber diameter between ~ 300 and ~ 700 nm) modified with vinyl groups and investigated their adsorption efficiency for malachite green (MG). The nanofibers exhibited a high adsorption capacity which was determined using isotherm models and was found to be 220.49 $mg \cdot g^{-1}$ for a 523.84 $m^2 \cdot g^{-1}$ membrane specific surface area (129).

A. R. Keshtkar and co-workers (2013) reported on the fabrication of a novel polyvinyl alcohol/tethra ethyl ortho silicate/aminopropyltriethoxysilane (PVA/TEOS/APTES) nanofibrous membrane, with average fiber diameter of about 197 nm, prepared by sol–gel/electrospinning and its application for the adsorption of uranium (U(VI)) from aqueous solution. The U(VI) adsorption capacity of the membranes reached 168.10 $mg \cdot g^{-1}$. Comparing the aforementioned system with an analogues PVA/TEOS/APTES hybrid film prepared by sol–gel/casting method they showed that the adsorption is less effective in the second case (33.61 $mg \cdot g^{-1}$) (294).

NH_2-functionalized cellulose acetate/silica (CA/silica) composite nanofibrous membranes were successfully prepared *via* the combination of sol-gel and electrospinning technologies by A. A. Taha *et al.* The electrospun membranes, with an average diameter of 100-500 nm, exhibited high adsorption efficiency (19.45 mg/g) for chromium (Cr(VI)) ions (295).

The performance of chitosan/hydroxyapatite (Cs/HAp) composite nanofibrous membrane (fiber diameter ~ 200 nm) prepared by electrospinning for the removal of lead, cobalt and nickel ions from aqueous solution was investigated by M. Aliabadi *et al.* (2013). Their adsorption studies showed that the maximum adsorption capacity of the Cs/HAp composite nanofibrous mats was in order of lead (296.7 $mg \cdot g^{-1}$) > cobalt (213.8 $mg \cdot g^{-1}$) > nickel (180.2 $mg \cdot g^{-1}$) (296).

Another nanocomposite electrospun system has been reported by S. Abbasizadeh and co-workers (2013) who prepared electrospun adsorbents based on polyvinyl alcohol and titanium oxide (PVA/TiO_2) modified with mercapto groups (functional group containing a sulfur atom bonded to a hydrogen atom) for uranium (U(VI)) and thorium (Th(IV)) removal from aqueous solution. Their results showed that the modification of the PVA/TiO_2 nanofibers with the mercapto moieties affected positively the adsorption

capacities, whereas the adsorption capacity was found to be 196.1 $mg \cdot g^{-1}$ and 238.1 $mg \cdot g^{-1}$ for U(VI) and Th(IV) respectively (288).

As mentioned above, nano-sized ferric oxides are used for the removal of organic pollutants and heavy metals from aqueous systems, due to their specific features, including among others excellent thermal and chemical stability, high specific surface area, and magnetic performance (297; 298). Performance toward the removal of lead Pb from water, A. Gholami *et al.* (2013) prepared a composite film by blending polyvinyl chloride, PVC and cellulose acetate, CA with ferric oxides particles followed by solution casting. (141).

S. Qu *et al.* (2008) introduced Fe_2O_3 nanoparticles into multi-walled carbon nanotubes (MWCNTs) *via* a wet chemical method, and employed this system as an adsorbent for the dye contaminates, including methyl blue (MB) and nile red (NR), from water media. The adsorption capacities of MB and NR were found to be 42.3 $mg \cdot g^{-1}$ and 77.5 $mg \cdot g^{-1}$ respectively (286), whereas magnetic separation thus adsorption recovery, was feasible due to the presence of Fe_2O_3 magnetic NPs within the nanotubes.

To the best of our knowledge, there is no previous literature report concerning the use of electrospun polymer-based magnetoactive nanocomposite membranes for the removal of dyes or heavy metal ions from aqueous media. For the first time in the present work magnetoactive polymer-based nanocomposites in the form of electrospun mats have been evaluated as adsorbents for dyes (malachite green) and metal ions (Eu(III)) from aqueous media.

4

Characterization Methods

The characterization of the electrospun, polymer-based membranes prepared in this study was carried out by employing several methods. Gel permeation chromatography (GPC) which is by far the most widely used method for determining average molecular weights and molecular weight distributions was used in the molecular characterization of the random copolymers synthesized by means of free radical polymerization. Proton nuclear magnetic resonance (^{1}H NMR) spectroscopy was employed in order to confirm the expected chemical structures of the copolymers.

For obtaining information on the morphological characteristics of the electrospun fibrous membranes, scanning electron microscopy (SEM) and transmission electron microscopy (TEM) were employed. Differential scanning calorimetry (DSC) and thermal gravimetric analysis (TGA) were used to probe the thermal properties of these materials. Ultraviolet-visible (UV-vis) spectrophotometry was used among others for performing kinetic adsorption studies of various pollutants (metal ions, organic molecules) from aqueous media using the fabricated electrospun membranes as adsorbents, and kinetic drug release studies of paracetamol encapsulated within electrospun polymer and polymer-based nanocomposite mats. Finally, the X-ray diffraction (XRD) spectroscopy and the vibrating

sample magnetometry (VSM) were used for the determination of the nanocrystalline phase and magnetic properties of the membranes containing OA.Fe_3O_4 NPs respectively.

4.1. Molecular characterization

Gel permeation chromatography (GPC), also called size-exclusion chromatography, is the most widely used method for determining polymer molecular weights (M_w) and molecular weight distributions (MWDs). In essence, this process is based on the separation of macromolecules according to their effective size in solution. This method has been used extensively in both biology and polymer chemistry.

Separation is accomplished inside a packed chromatographic column, where the polymer sample is introduced in the mobile phase. The column is filled with a highly porous material that separates the polymer molecules according to size (hydrodynamic volume), a phenomenon often referred to as molecular sieving. The sample is carried by the solvent (mobile phase), through the column and size separation occurs upon exchange of the solute particles between the bulk solvent and the stationary liquid phase within the pores of the packing material. Small molecules are able to diffuse into the pores of the column, and therefore they travel through the column more slowly. Higher molecular weight fractions are thus eluted first as schematically presented in **figure 4.1**.

As previously noted, a chromatographic column is packed with particles that have a specified maximum pore size and a specified pore size distribution. The voids between the particles and the pores are filled with a suitable solvent. The sample is introduced as a dilute solution in the column and the solvent is continually passed through. The solute concentration in the eluent is monitored with a suitable sensitive detector.

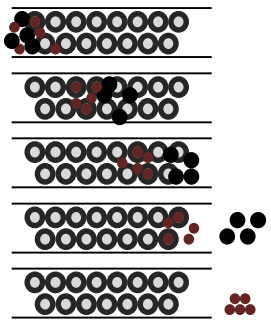

Figure 4.1: *Schematic presentation of the SEC process showing the separation of low and high MW polymers. Smaller molecules diffuse into porous particles, while larger molecules elute in the interstitial regions of the packing material. Therefore, the larger particles elute first and the smaller molecules having access to both interstitial and pore volumes elute later.*

Very large molecules are unable to penetrate the pores of the packing material. Consequently, they are completely excluded from it and are eluted at the volume V_o, corresponding to the volume of the mobile phase. The small molecules have access to all pores and elute at V_t, whereas certain fraction of the pore volume is available for the intermediate-sized solutes eluting at volumes between V_o and V_t.

The chromatographic behavior of solutes separated by SEC can be described by the general chromatographic **equation 4.1**,

$$V_R = V_o + K_d V_i \qquad \textbf{Equation 4.1}$$

Where, V_R is the retention volume of a given solute characterized by a certain value of the volume distribution coefficient K_d, which is a measure of the apparent fractional permeation of the pores by the solute.

In a typical gel permeation chromatogram, the detector's response is plotted against the elution volume or elution time of the diluted polymer solution that passes through the column. To obtain molecular weights at a given retention volume, the chromatogram may be compared with a reference chromatogram obtained with fractions of known average molecular weight in the same solvent and at the same temperature.

The molecular weights as such cannot be determined directly, but only upon calibration of the system. A calibration curve usually plotted as log M *versus* V_R, as shown in **figure 4.2** can be established by determining the elution pattern of a series of well-defined polymers characterized by narrow molecular weight distributions with molecular weights determined by an absolute method (299; 300; 301).

All synthetic polymers consist of a mixture of molecules of the same nature but different size. It is impossible to find a sample of a synthetic polymer in which all chains have exactly the same molecular weight. Consequently the molecular weight can only be defined as an average value.

$$\omega = \sum \omega_i = \sum M_i N_i \qquad \textbf{Equation 4.2}$$

The total weight ω of a polymer sample is the sum of the weights of all the molecular species. N_i is the number of moles of each species i, and the sum can be expressed as $\sum N_i \cdot M_i$ is the molecular weight of each species i, and the sum is presented as $\sum M_i$. By

dividing the total weight of the molecules by their total number we have the number average molecular weight,

$$\overline{M_n} = \frac{\omega}{\sum N_i} = \frac{\sum M_i N_i}{\sum N_i} \qquad \textbf{Equation 4.3}$$

Another way to express the molecular weight average is a weight average. Each molecule in such an average contributes according to the ratio of its particular weight to that of the total,

$$\overline{M_w} = \frac{\sum M_i^2 N_i}{\sum M_i N_i} \qquad \textbf{Equation 4.4}$$

When all molecules are of the same weight, then $\overline{M_w} = \overline{M_n}$. The width of distribution, called the polydispersity index or molecular weight distibution, is determined from the ratio $\overline{M_w} / \overline{M_n}$ (302; 303; 304; 305).

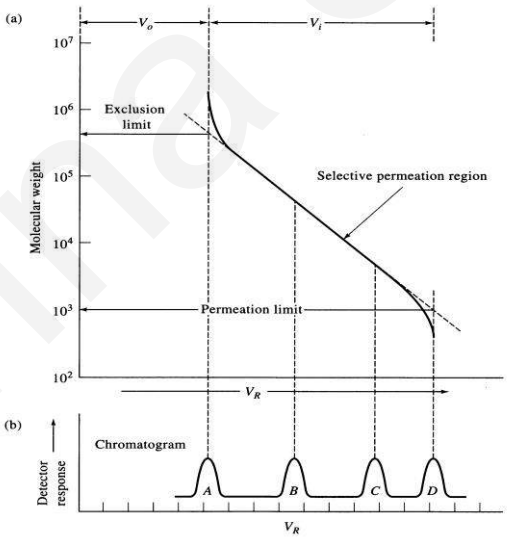

Figure 4.2: *A typical SEC calibration curve showing a plot of log MW versus elution or retention volume of a series of polymer standards of known MW. The total permeation volume of the column V_t, is equal to the exclusion or void volume of the column, V_o, plus the pore volume of the packing within the column V_i. M_o is the extrapolated MW that defines the exclusion limit of the column occurring at V_o, and M_t is the extrapolated MW that defines the total permeation limit of the column occurring at V_t.*

Nuclear magnetic resonance (NMR) spectroscopy became one of the most powerful analytical techniques, used in many different fields of chemistry and also in medicine throughout of NMR imaging (306; 302). The NMR phenomenon is based on the fact that nuclei of atoms have magnetic properties that can be utilized to yield chemical information. Subatomic particles, including protons, neutrons and electrons, have spin. In some atoms, such as ^{12}C, ^{16}O, ^{32}S, these spins are paired and cancel each other out so that the nucleus of the atoms has no overall spin. In contrast, in many atoms, such as ^{1}H, ^{13}C, ^{31}P, ^{15}N, ^{9}F, the nucleus has an overall spin (306).

The number of spin of the nucleus depends on its mass number and atomic number. Nuclei with odd mass numbers have half-integral spin quantum numbers (i.e. 1/2, 3/2, 5/2). Nuclei with an even mass number and an even atomic number have spin quantum numbers equal to zero, and nuclei with an even mass number and an odd atomic number have integral spin quantum numbers (i.e. 1, 2, 3). In the case where the spin quantum numbers equal to zero, the nucleus is NMR inactive, since the existence of nuclear spin is essential (307).

Nuclei behave as magnetic dipoles and their nuclear magnetic moment, μ is defined by the equation:

$$\mu = \frac{\gamma I h}{2\pi}$$ **Equation 4.5**

where, γ is a constant called magnetogyric ratio (for proton γ=26.753 rad s^{-1} $Tesla^{-1}$), I is the spin number and h, is the Plank's constant.

The orientations that a nucleus' magnetic moment can adopt against an external magnetic field (H_o) are not of equal energy. However, in the absence of a magnetic field, the magnetic moments of the protons of a given sample are randomly oriented. When a compound containing hydrogen, and thus protons, is placed in an external magnetic field, its protons may adopt one of the two possible orientations with respect to the external magnetic field.

Spin states which are oriented parallel to the external field are lower in energy than in the absence of an external field. In contrast, spin states whose orientations oppose to the external field are higher in energy than in the absence of an external field. In an NMR spectrometer the energy which is required to "flip" the proton from its lower energy state to its higher energy state, is supplied by electromagnetic radiation in the radiofrequency

region. When energy absorption occurs, the nuclei are said to be in resonance with the electromagnetic radiation.

Nuclear magnetic resonance spectrometers, are designed so that they irradiate the compound with electromagnetic energy of constant frequency while the magnetic field strength is varied or swept. When the magnetic field reaches the correct strength, the nuclei absorb energy, which causes a small electrical current to flow in a receiver coil surrounding the sample, and resonance occurs. The instrument then amplifies this current displaying it as a signal (a peak or series of peaks) on a pre-calibrated chart paper in frequency units, Hz. The result is an NMR spectrum.

Every molecule is influenced by neighboring molecules. In a given molecule, some hydrogen nuclei are found in regions of greater electron density than others. As a result, the nuclei absorb energy at slightly different magnetic field strengths.

Furthermore, the chemical shifts are measured along the bottom of the spectrum on a delta (δ) scale, in units of parts per million and the externally applied magnetic field strength increases from left to right. Signals on the left of the spectrum are said to occur downfield and those on the right are said to be upfield. The signal δ=0 in the spectrum arises from a reference compound, such as tetramethylsilane, TMS ($(CH_3)_4Si$), that is added to the sample to allow calibration of the chemical shift scale. Consequently, the equation for different absorption which can be used is (308; 307; 309; 310),

$$\delta = \frac{observed\ \ shift\ \ from\ \ TMS\ \ in\ \ hertz}{operating\ \ frequency\ \ of\ \ the\ \ instrument\ \ in\ \ hertz} \qquad \textbf{Equation 4.6}$$

4.2. Morphological and structural characterization

A **scanning electron microscope** (**SEM**) is a type of electron microscope that produces images of a sample by scanning it with a focused beam of electrons. The electrons interact with atoms in the sample, producing various signals that can be detected and that contain information about the sample's surface, topography and composition.

Specifically, the electron gun produces a beam of electrons that is attracted through the anode and condensed by the condenser lens and then focused as a very fine point on the specimen by the objective lens. A set of scan coils is located within the objective lens. The

coils are energized by a varying voltage produced by the scan generator, creating a magnetic field that deflects the beam of electrons back and forth in a controlled pattern called a raster. The varying voltage is also applied to a set of deflection coils around the neck of a cathode-ray tube (CRT) and the magnetic field from this coil causes the deflection of a spot of light back and forth on the surface of the CRT. The pattern of deflection of the beam of electrons on the sample is exactly the same as the pattern of deflection of the spot of light on the CRT.

When an incident-beam electron strikes the surface of a sample, a series of complex interactions with the nuclei and the electrons of the atoms of the sample occur. Through these interactions secondary electrons of different energies, X-rays, heat and light are generated. These in turn are used to produce the images of the sample and to collect additional data from the sample.

Secondary electrons (SE), generated from an inelastic interaction (inelastically scattered electron (low angle)), produce the standard SEM images. It is a major advantage of SEM that, beside the backscattered and secondary electrons, a large variety of electron-specimen interactions can be used to form an image and to provide qualitative and quantitative information. SE are produced by the interactions between incident electrons and weakly bound conduction-band electrons in the atoms of the sample, and collected by the detector, converted to a voltage, and amplified. The amplified voltage is then applied to the grid of the CRT and modulates or changes the intensity of the spot on the surface of the CRT.

Finally, all the samples must be of an appropriate size to fit in the specimen chamber and are generally mounted rigidly on a specimen holder called a specimen stub. For conventional imaging in the SEM, specimens must be electrically conductive, at least at the surface, and electrically grounded to prevent the accumulation of electrostatic charge at the surface. Scanning of non-conductive specimens by the electron beam results to surface charging that causes scanning faults and other image artifacts, especially in the secondary electron imaging mode. Therefore such specimens including polymers are usually coated with an ultrathin coating of an electrically conducting material, deposited on the sample's surface (311; 312).

Another basic type of electron microscopy is **transmission electron microscopy (TEM)**, which also produces unique and often complementary images and information. In this microscopy technique, a beam of electrons is transmitted through an ultra-thin specimen.

An image is produced from the interaction of the electrons transmitted through the specimen and it is magnified and focused onto an imaging device, such as a fluorescent screen.

TEM is an important tool in materials science providing information about the morphology, structure of the internal components of a specimen and composition. More specifically, it gives details in relation to the size, shape and arrangement of the particles in the sample. Furthermore, it enables the investigation of the crystal structure including the arrangement of the atoms in an object as well as the quantification of the different compounds comprising the specimen.

A TEM apparatus has a filament assembly at the top of the column, which is connected to the high-voltage supply by an insulated cable in order to emit electrons. Bellow the filament tip and above the anode there is a beam volume called crossover. A beam of monochromatic electrons is produced by an electron gun. This electron beam is focused to a small and thin coherent beam by electromagnetic lenses, and then travels through the condenser-lens system, which is fitted with apertures. Then the focused electron beam strikes the sample which is placed on a concrete base namely grid holder and parts of the beam are transmitted. The transmitted radiation is transformed by the objective lens into an image. After the objective lens, optional objective and selected area metal apertures are placed inside the column where they can restrain the beam by blocking out the high angle diffracted electrons and examine the periodic diffraction of electrons by ordered arrangements of atoms in the sample. The beam passes down the column through the projector lenses, being enlarged all the way. Eventually, the beam strikes the phosphor image screen and light is generated allowing the user to observe the image. The darker areas of the image represent those areas of the sample through which fewer electrons were transmitted and the lighter areas of the image represent those areas of the sample through which more electrons were transmitted.

X-ray diffraction (XRD) spectroscopy is one of the most useful techniques for the analysis of semi-crystalline polymers in the solid state. XRD is a versatile, non-destructive method that gives important information on the most definitive crystallographic structure, including interatomic distances and bond angles, chemical composition and physical properties of a material. As already mentioned in the first chapter, polymers may constitute of both crystalline and amorphous regions. The crystalline region corresponds to the part of the polymer in which the chains are arranged in a regular manner. Among these ordered

regions, polymer chains found in random conformation exist, the so-called amorphous regions. The degree of crystallinity of a polymer can be determined by XRD analysis.

X-rays are electromagnetic radiation with wavelengths in the range 0.5-2.5 Å (same order of magnitude as the interatomic distances in solids), and are produced by bombarding a metal target (usually Cu, Mo) with a beam of electrons emitted from a hot filament (often tungsten). The incident beam ionizes the electrons from the K-shell (1s) of the target and X-rays are emitted as the resultant vacancies are filled by electrons dropping down from the L (2P) or M (3p) levels. This gives rise to Ka and Kb lines.

An X-ray beam impinging on a crystal will be scattered in all directions by the atoms of the crystal. In some directions, an increased intensity is observed due to the constructive interference of the scattered waves. The conditions for constructive interference are easily derived from the simple geometrical picture for the scattering of an X-ray beam by planes of atoms in a crystal, as illustrated in **figure 4.3**. When the X-ray beam of wavelength λ, incidents on the crystal at an angle θ with respect to equidistant hkl lattice-planes, with interplanar distance d_{hkl}, constructive interference will be observed for X-rays that are reflected from the lattice planes at the specular angle, if the path length difference between X-rays scattered from different hkl-planes is an integer times the wavelength. This condition is summarized in the Bragg law **(equation 4.7)**:

$$2d_{hkl} \cdot \sin\theta = n \cdot \lambda \qquad \textbf{Equation 4.7}$$

n is an integer determined by the order given, λ is the X-ray wavelength, d_{hkl} is the distance between the parallel planes of the lattice and Θ is the incident angle.

From the X-ray spectrum and the Scherrer equation **(4.8)** the crystallite size can be calculated:

$$t_{hkl} = \frac{K \cdot \lambda}{f_{whm} \cdot \cos\theta_B} \qquad \textbf{Equation 4.8}$$

where, t is the diameter of the crystallite, K is a constant that depends on the crystallite shape, λ is the X-Ray wavelength, f_{whm} is the full width at half max or integral breadth and Θ_B is the Bragg angle.

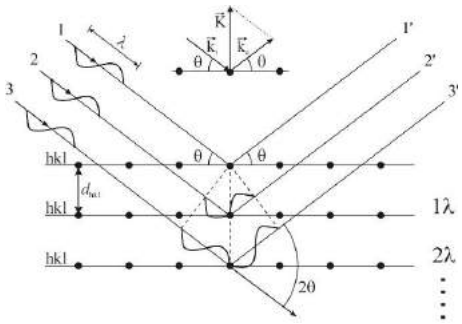

Figure 4.3: *Deriving Bragg's Law using the reflection geometry.*

4.3. Thermal characterization

For more than two decades, **differential scanning calorimetry (DSC)** thermal analysis technique has been used to measure the temperature and heat flow of a material as a function of temperature and time. DSC is primarily used to measure transition temperatures and associated heats of reaction in materials, particularly in polymers. Quantitative and qualitative information about physical and chemical changes that involve endothermic or exothermic processes, or changes in heat capacity, are provided by DSC (313).

In DSC, a polymer sample and an inert reference are heated, usually under nitrogen atmosphere, and thermal transitions in the sample are detected and measured. The sample holder most commonly used is a very small aluminum cup, and the reference is either an empty cup or a cup containing an inert material in the temperature range of interest.

The heat flux DSC and the power compensation DSC, are the two distinguished types of differential scanning calorimeters. In power-compensation DSC the temperatures of the sample and reference are controlled independently using separate, identical furnaces. The temperature is the same both in the sample and the reference. However, there is a difference in the thermal power of the two furnaces. The enthalpy or heat capacity change in the sample, relative to the furnace, is the energy which is measured by the thermal power changes, required to maintain them at the same temperature. Heat capacity C_p, is the amount of heat required to acquire a certain temperature increase in a material and it is obtained by dividing the heat supplied by the temperature increase according to **equation 4.9**.

$$C_p = \frac{q}{\Delta T}$$ **Equation 4.9**

In a heat flux DSC, the sample and the reference, which are enclosed in a single furnace, are placed on a thermoplastic disc with a low-resistance heat-flow path. The furnace is heated at a linear heating rate and the heat is transferred to the sample and reference pan through a thermoelectric disk. Due to the temperature difference between the sample and the reference, enthalpy or heat capacity exists and measured. Consequently, the heat flow is determined by the thermal equivalent of Ohm's law **(equation 4.10)**.

$$q = \frac{\Delta T}{R}$$ **Equation 4.10**

where, q is the sample heat flow, ΔT is the temperature difference between the sample and the reference, and R is the resistance of the thermoelectric disk.

Furthermore, the data of temperature increase (ΔT) are plotted against the difference in heat output of the two heaters at a given temperature or time, i.e. heating rates (heat/time). Characteristic plots obtained, correspond to thermal transitions such as melting (T_m) and crystallization (T_c) transition temperatures of a crystalline sample, and glass transition (T_g) temperatures. It is important to recognize that polymers with both crystalline and amorphous domains will provide T_g, T_c, and also T_m. T_m and T_c features can be only obtained for polymers that can form crystals. Completely amorphous polymers exhibit only T_g (314; 315).

As previously noted, thermal analysis refers to a variety of techniques in which a physical property of a sample is continuously measured as a function of temperature. Another important and useful tool that is usually applied to characterize the thermal behavior of materials is **thermal gravimetric analysis (TGA)**.

Thermal gravimetric analysis is used to determine physical and chemical changes that result in changes in mass when a material is heated. Specifically, it is based on the measurements of the amount of weight change of a material, either as a function of increasing temperature, isothermally as a function of time, or under different environment conditions that may be created within the apparatus. Inorganic materials, metals, polymers, ceramics, glasses and composite materials can be analyzed by this technique.

The TGA experiments are carried out in an atmosphere of nitrogen, helium, under air, etc. or they can be also performed in vacuum, at a temperature range from 25 °C to 900 °C. The maximum temperature is 1000 °C. The sample -usually a few milligrams in weight- is heated at a constant rate and has constant weight until it begins to decompose at a certain temperature. The temperature depends on variables, such as the heating rate, the nature of the solid and the atmosphere in which the sample is heated.

Assuredly, TGA is an essential technique for characterizing polymeric materials. Through this method thermal stability, composition, sample purity and other properties of the original sample can be determined (314; 315).

4.4. Optical characterization

Electronic spectroscopy is often called spectroscopy in the ultraviolet (UV), visible (vis) and near infrared (NIR) region of the electromagnetic spectrum because electrons are transferred from low-energy to high-energy atomic or molecular orbitals when the material is irradiated with light. The energy hv of the photon must be exactly the same as the difference between the two orbital energy levels according to **equation 4.11**,

$$\Delta E = h\nu = \frac{hc}{\lambda} \qquad \textbf{Equation 4.11}$$

where, h is Plank's constant, ν is frequency in Hz, c is the velocity of radiation in vacuum and λ is wavelength in nm.

Specifically, **ultraviolet-visible (UV-vis) spectroscopy** is very useful as an analytical technique due to the fact that it can be used to identify some functional groups in molecules and also, it can be used for determining the content of the different compounds. Furthermore, organic chemists use UV-vis spectroscopy mainly for detecting the presence, and elucidating the nature of the conjugated multiple bonds or aromatic rings.

The ultraviolent region extends from 10 to 400 nm, where the vacuum ultraviolet region extends from 10 to 200 nm and the ultraviolet region from 200 to 400 nm. The visible region extends from 400 to 800 nm as clearly shown in the electromagnetic spectrum provided in **figure 4.4**.

A UV-vis spectrometer records a spectrum as a plot of wavelengths of absorbed radiation *versus* the intensity of absorption. The correct absorption value is called "molar absorptivity" or "molar extinction coefficient" ε, which is defined, according to the Beer-Lambert law, by the **equation 4.12**,

$$A = \log \frac{I_0}{I} = \varepsilon l c \qquad \textbf{Equation 4.12}$$

where, I_0 is the intensity of the incident radiation, I is the intensity of the transmitted radiation, ε is the molar absorption coefficient, l is the path length of the absorbing solution, and c is the concentration of the absorbing species.

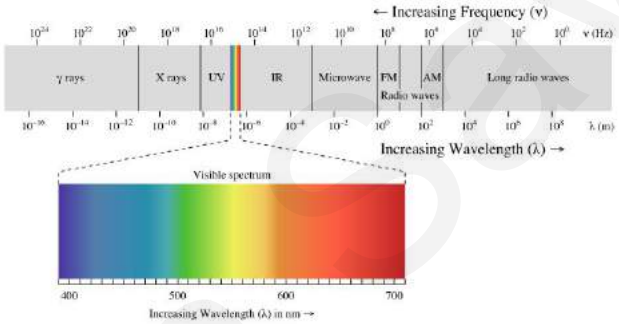

Figure 4.4: *The electromagnetic spectrum in which the UV-vis region is indicated.*

According to the theory of molecular orbitals, when two atoms are combined to form a chemical bond, electrons from both atoms take part to this bond and occupy a new orbital, a molecular orbital. The atomic orbitals of two bounded atoms are combined to form a "bonded" low energy molecular orbital and an "antibonded" molecular orbital of high energy.

Specifically, valence electrons are found in three types of electron orbitals: single or σ bonding orbitals, double or trible π bonding orbitals and non-bonding orbitals, the n orbitals, which do not take part in the chemical bonds. Sigma (σ) bonding orbitals tend to be lower in energy than π bonding orbitals, which in turn are lower in energy than the non-bonding orbitals.

As a result, an electron transition occurs from one of these orbitals to an empty orbital, when electromagnetic radiation of the approximate frequency is absorbed, usually to an antibonding orbital, σ^* or π^* as shown in **figure 4.5**. Particularly, absorption of UV-vis

radiation produces the electronic transitions $\sigma \rightarrow \sigma^*$, $\eta \rightarrow \sigma^*$, $\eta \rightarrow \pi^*$, $\pi \rightarrow \pi^*$, where the energy ΔE of these transitions follows the order $\eta \rightarrow \pi^* < \pi \rightarrow \pi^* < \eta \rightarrow \sigma^* << \sigma \rightarrow \sigma^*$.

The most common electronic transitions are observed in π bond-containing structures, where the systems absorb UV-vis irradiation and the excitation of electron involves the transfer from the highest-energy occupied bonding molecular orbital or the HOMO orbital, into the lowest-energy unoccupied antibonding molecular orbital or the LUMO orbital (316; 317).

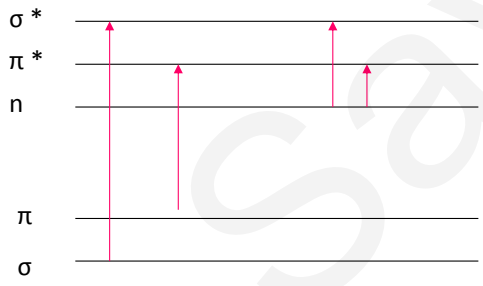

Figure 4.5: *Electronic transitions occurring after the absorption of UV-vis irradiation.*

4.5. Magnetic characterization

Vibrating sample magnetometry (VSM) was used in the present study to determine the magnetic properties of the magnetoactive electrospun nanocomposites membranes. A vibrating sample magnetometer (VSM) operates on Faraday's Law of induction, according to which, a changing magnetic field produces an electric field. This electric field is measurable and can provide information about the changing magnetic field.

Initially, the sample to be analysed is placed in a constant magnetic field. If the sample is magnetic, this constant magnetic field will magnetize the sample by aligning the magnetic domains, or the individual magnetic spins, with the field. The stronger the constant field is, the larger the magnetization will be. The magnetic dipole moment of the sample will create a magnetic field around the sample. As the sample vibrates moving up and down, this magnetic field changes relative to time and can be sensed by a set of pick-up coils **(figure 4.5)**.

The alternating magnetic field will cause an electric field in the pick-up coils according to Faraday's Law. This current will be proportional to the magnetization of the material. The higher the magnetization is, the greater the induced current will be. The instrument is connected to a computer and the software provides data on the change of the magnetization of a sample relative to the strength of the externally applied magnetic field.

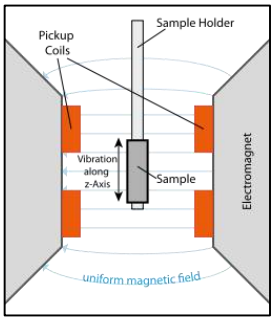

Figure 4.6: *Schematic diagram of a vibrating sample magnetometer.*

The hysteresis loop measurement is the most common magnetic experiment. The parameters extracted from this experiment are used to characterize the magnetic properties of a material such as the saturation magnetization M_s, the remanence M_r and the coercivity H_c. By applying an external magnetic field starting from a maximum value (positive or negative) the magnetometer measures the magnetization of the material at each point. The presence of a hysteresis loop is typical for ferromagnetic and ferrimagnetic materials whereas superparamagnetic materials exhibit no hysteresis.

5

Experimental Section

5.1. Solvents and reagents

Monomers: The monomer 2-(acetoacetoxy) ethyl methacrylate (AEMA, $C_{10}H_{14}O_5$, M_w=214.22 g·mol^{-1}, 95%) was purchased from Sigma-Aldrich, benzyl methacrylate (BzMA, $C_{11}H_{12}O_2$, M_w=176.21 g·mol^{-1}, 96%) was purchased from Merck/Sigma-Aldrich, and methyl methacrylate (MMA, $C_5H_8O_2$, M_w=100.12 g·mol^{-1}, 99%) was purchased from Fluka. While MMA was used without further purification, AEMA and BzMA were passed through alumina (aluminum oxide, 98%, Sigma-Aldrich) prior to polymerization reactions.

Homopolymers: The three homopolymers poly(vinyl pyrrolidone), (PVP, $\overline{M}_n$=1 300 000 g·mol^{-1}), poly(ethylene oxide), (PEO, $\overline{M}_n$=600 000 g·mol^{-1}), and poly(L-lactide) (PLLA, $\overline{M}_n$= 99 000 g·mol^{-1}), were purchased from Sigma-Aldrich and used as received from the manufacturer.

Other reagents: The radical initiator 2,2'-azobis(isobutyronitrile) (AIBN, 95%) was purchased from Sigma-Aldrich and was re-crystallized twice from ethanol prior to use. Iron sulfate (II) heptahydrate (97%) and iron chloride (III) tetrahydrate (99%) were purchased from Sigma-Aldrich. Palladium (II) acetate ($Pd(OCOCH_3)_2$, M_w=224.51 g·mol^{-}

[1], 98%) and copper (II) acetate monohydrate ($Cu(CO_2CH_3)_2 \cdot H_2O$, M_w=199.65 g·mol^{-1}, 98% ACS reagent) were also purchased from Sigma-Aldrich. Sodium hydroxide pellets (NaOH) were purchased from Scharlau. N-acetyl-p-aminophenol (acetaminophen) was kindly provided by Aegis Ltd, Cyprus. Malachite green oxalate (N-methylated diaminotriphenylmethane dye, MG, $C_{52}H_{54}N_4O_{12}$, M_w=927.02 g·mol^{-1}) was purchased from Scharlau, metronidazole (MET, $C_6H_9N_3O_3$ M_w=171.15 g·mol^{-1}) was purchased from Fluka and 1,2, dichlorobenzene (DCB, $C_6H_4Cl_2$ M_w=147.00 g·mol^{-1}, 99 % reagent plus) was purchased from Sigma-Aldrich. Oleic acid (99%) was purchased from Merck. All reagents were used as provided by the manufacturer without further purification. Benzyl azide was prepared from benzyl bromide and sodium azide according to the literature (318).

Solvents: Chloroform ($CHCl_3$), ethanol (EtOH, ≥99.9%), hydrochloric acid (HCl, 37%) tetrahydrofuran (THF, HPLC grade), methanol (MeOH, Analytical grade, ACS reagent), and n-hexane (96%) were purchased from Scharlau. Ethyl acetate (EtOAc (EA), 99.8%) was purchased from Fluka. The above-mentioned solvents were used as provided by the manufacturer without further purification. Concerning deuterated solvents, deuterated chloroform ($CDCl_3$, 99.8%) was used in proton nuclear magnetic resonance (^{1}H NMR) studies.

Solutions: Dulbecco's phosphate buffered saline (DPBS) solution (pH 7.2) was purchased from Sigma-Aldrich. Dulbecco's modified eagles medium (DMEM), inactivated fetal calf serum (FCS) and antibiotics/antimycotic solution antibiotics (Penicillin/Streptomycin/ Amphotericin) were purchased from Invitrogen.

Uranium (U(VI)) and thorium (Th(IV)) stock solutions were prepared by dissolution of $UO_2(NO_3)_2x6H_2O$ and $Th(NO_3)_4x5H_2O$ respectively which were purchased from Merck in aqueous media. Europium (Eu(III)) stock solution was prepared by dissolution of $Eu(NO_3).5H_2O$ that was purchased from Sigma-Aldrich in aqueous media. The metal ions concentration in the solution was determined by using Arsenazo(III) ($C_{22}H_{18}As_2N_4O_{14}S_2$) according to a previously described method (319; 320) which was purchased from Sigma-Aldrich. For the pH adjustments, sodium hydroxide (NaOH) and perchloric acid ($HClO_4$) were used, which were purchased from Sigma-Aldrich. As background electrolytes for ionic strength adjustments sodium perchlorate ($NaClO_4$) solutions were used. All metal ion adsorption experiments were performed under normal atmospheric conditions ($p(CO_2)=10^{-3.5}$ atm and 25℃).

5.2. Instrumentation

Fabrication: All **electrospinning** experiments were performed at room temperature. Equipment included a controlled-flow, four channel volumetric microdialysis pump (KD Scientific, Model: 789252), syringes with specially connected spinneret needle electrodes, that were connected to the anode, a high-voltage power source (10-30 KV) and a custom-designed, grounded target collector, covered with aluminum foil, which was connected to the cathode. All equipment was placed inside an interlocked Faraday enclosure safety cabinet.

Molecular characterization: Proton nuclear magnetic resonance (^{1}H NMR) spectroscopy was used for confirming the expected structure of the polymers prepared in the present work. ^{1}H NMR spectra were recorded in $CDCl_3$ using an Avance Brucker 300 MHz and 500 MHz spectrometer equipped with an Ultrashield magnet. The $CDCl_3$ contained traces of tetramethylsilane (TMS), which was used as an internal reference. The average molecular weights and polydispersity indices of the polymers were determined by **size exclusion chromatography** (SEC). All measurements were carried out at room temperature using Styragel HR 3 and Styragel HR 4 columns. The mobile phase was THF, delivered at a flow rate 1 mL min^{-1} using a Waters 515 isocratic pump. The refractive index was measured with a Waters 2414 refractive index detector. The instrumentation was calibrated using poly(methyl methacrylate) (PMMA) standards with narrow polydispersity indices (MWs of 102, 450, 670, 1580, 4200, 14400, 31000, 65000, 126000, 270000, 446000, 739000 g mol^{-1}) supplied by Polymer Standards Service (PSS).

Morphological characterization: Transmission electron microscopy (TEM) measurements were performed on a 1010 JEOL microscope (200 kV). **High resolution transmission electron microscopy** (HRTEM) analysis was performed by using a TECNAI F30 G2 S-TWIN microscope operating at 300 kV equipped with energy dispersive X-ray spectrometer (EDX). Both, TEM and HRTEM/EDX analysis were prepared by Dr. E. Vasile at the University Politehnica of Bucharest (Faculty of Applied Chemistry and Materials Science, Department of Bioengineering and Biotechnology), and V. Eugenia at the University Politehnica of Bucharest (Faculty of Medical Engineering, Department of Bioengineering and Biotechnology). Samples (nanocomposite membranes) were placed onto double copper grid (oyster) to be visualized by TEM. The morphological characteristics of the fibrous membranes obtained in the absence and presence of inorganic NPs, were determined by **scanning electron microscopy (SEM)** (Vega TS5136LS-

Tescan). The samples were gold-sputtered (~15 nm) (sputtering system: K575X Turbo Sputter Coater – Emitech, Bal-tec SCD 500) prior to SEM inspection.

Thermal analysis: Thermal gravimetric analysis (TGA) measurements were carried out with a Q500 TA Instruments. Samples (6±0.2 mg) were placed in ceramic crucibles. An empty ceramic crucible was used as a reference. Samples were heated from ambient temperature to 600 °C in a 50 $mL \cdot min^{-1}$ flow of argon (Ar) with a heating rate of 10 $°C \cdot min^{-1}$. **Differential scanning calorimetry (DSC)** was used to measure the glass transition temperatures T_gs of the fibrous polymer membranes using the Q100 TA Instrument with a heating rate of 10 $°C \cdot min^{-1}$. Each sample was scanned twice between 0 °C and +180 °C. The second run (heat) was used for data analysis.

Structural analysis: X-ray powder diffraction patterns were obtained using Rigaku (30 kV, 25 mA) with λ=1.5405 Å (Cu)) in the range of 20-80° and at a scanning rate of 1°/min.

Optical analysis: Ultraviolet-visible spectrophotometer (UV-vis) Jasco V-630 was used to carry out the drug release kinetic measurements and UV 2401 PC Shimadzu was used for the determination of the metal ion concentration in aqueous media.

Magnetic characterization: The magnetic properties of the magnetic nanocomposite fibrous membranes prepared in this work were measured with a **vibrating sample magnetometer (VSM)**, model 880 from ADE technologies USA at 300 K. These measurements were carried out in the research group of Prof. L. Vekas (Center of fundamental and advanced technical research, Romania Academy, Timisoara Branch, Timisoara, Romania).

5.3. Membrane fabrication and applications

5.3.1. PEO/PLLA and PEO/PLLA/OA.Fe_3O_4 electrospun membranes

Microfibrous pristine and magnetoactive nanocomposite membranes, based on the water soluble and biocompatible poly(ethylene oxide) (PEO), the biocompatible and biodegradable poly(L-lactide) (PLLA), and pre-formed oleic acid-coated magnetic nanoparticles (OA.Fe_3O_4 NPs), were fabricated by electrospinning and evaluated for the first time as drug delivery systems and as adsobants for the removal of radioactive metal ions and organic water-soluble dyes from aqueous media.

Synthesis of oleic acid-coated iron oxide magnetic nanoparticles: The OA.Fe_3O_4 NPs were prepared at the Center for Fundamental and Advanced Technical Research, Romanian Academy, Timisoara branch, Romania in the research group of the Prof. L. Vekas by following an experimental procedure developed by Bica *et al*. (321; 180; 322). Briefly, magnetite NPs, Fe_3O_4, were obtained by the co-precipitation in aqueous solution of Fe^{2+} and Fe^{3+} ions (salts $FeSO_4.7H_2O$; $FeCl_3.4H_2O$) in the presence of NH_4OH, at 80–82 °C. Subsequently, oleic acid was added in a significant excess (about 30 vol %) to the system right after the co-precipitation had started, which resulted in the chemisorption of the acid on the magnetite surface. This was followed by a washing process with distilled water with magnetic decantation and filtration to remove aggregated particles. Then, flocculation (acetone) was used to extract magnetite particles coated with a single surfactant layer from the solution of residual salts and free surfactant. The dried powder was redispersed in light hydrocarbon. This flocculation/re-dispersion procedure was performed several times to ensure that the presence of free surfactant in the final solution was negligible.

Membrane fabrication: The PEO/PLLA-based nanofibers were fabricated by electrospinning according to the following procedure. Firstly, an appropriate amount of commercially available homopolymers was dissolved in $CHCl_3$, with polymer-solution concentrations 2.5 and 4% w/v and weight percentage proportion of PEO/PLLA:70/30 respectively. This specific weight ratio was chosen so as for the membrane to exhibit high stability and retain its integrity when immersed in aqueous solutions (*via* the incorporation of the hydrophobic PLLA) whereas at the same time presenting good water wettability properties (*via* the introduction of the hydrophilic PEO). The prepared solution was loaded into a glass syringe (10 mL volume) and then electrospun. Systematic parametric studies were carried out by varying the applied voltage, the distance from the tip of the needle to the collector, the needle inner diameter, and the solution flow rate, which was controlled with the aid of a syringe pump.

The same procedure was followed in the presence of OA.Fe_3O_4 NPs. The PEO/PLLA solutions were mixed with different amounts of OA.Fe_3O_4 NPs (5, 10, 20, 37, 50 and 70% wt. in respect to the total polymer mass) in $CHCl_3$ solution at room temperature. In all cases, the polymer-solution concentration was kept constant (2.5 and 4% w/v respectively) and only the concentration of the OA.Fe_3O_4 varied.

For the kinetic release study of acetaminophen the PEO/PLLA/acetaminophen system, consisting of PEO/PLLA (polymer-solution concentration: 2.5% w/v; weight percentage proportion PEO/PLLA:70/30 respectively) and acetaminophen (0.25 $g \cdot L^{-1}$) was prepared in $CHCl_3$. PEO/PLLA/OA.Fe_3O_4/acetaminophen systems, consisting of PEO/PLLA (polymer-solution concentration: 2.5% w/v; weight percentage proportion PEO/PLLA:70/30 respectively), acetaminophen (0.25 $g \cdot L^{-1}$), and OA.Fe_3O_4 NPs (20% and 70% wt. in respect to the amount of PEO/PLLA) were also prepared in $CHCl_3$ **(Table 5.1 (I))**.

For the adsorption studies of heavy metal ions, including europium (Eu(III)), uranium (U(VI)), and thorium (Th(IV)), as well as the adsorption experiments carry out with malachite green (MG) organic dye, solutions of PEO/PLLA and PEO/PLLA/OA.Fe_3O_4 (polymer-solution concentration: 4% w/v; weight percentage proportion of PEO/PLLA:70/30 respectively, 37 and 50% wt. OA.Fe_3O_4 in respect to the total polymer mass) were prepared in $CHCl_3$, followed by electrospinning to obtained the corresponding fibrous mats **(Table 5.1 (II, III))**.

The quantities of the reactants used for the preparation of all the above-mentioned series of membranes are summarized in **table 5.1**.

Table 5.1: *Quantities of the reactants used for the preparation of PEO/PLLA and PEO/PLLA/OA.Fe_3O_4-based electrospun membranes.*

(I) Membranes for drug delivery						
a/a	**Sample**	**$CHCl_3$ (mL)**	**PEO (g)**	**PLLA (g)**	**OA.Fe_3O_4 (g)**	**acetaminophen (g)**
1	PEO	10	0.25	-	-	-
2	PEO/PLLA	10	0.175	0.075	-	-
3	PEO/PLLA/OA.Fe_3O_4 (5% wt.)	10	0.175	0.075	0.0526	-
4	PEO/PLLA/OA.Fe_3O_4 (10% wt.)	10	0.175	0.075	0.0556	-
5	PEO/PLLA/OA.Fe_3O_4 (20% wt.)	10	0.175	0.075	0.0625	-
6	PEO/PLLA/OA.Fe_3O_4 (50% wt.)	10	0.175	0.075	0.250	-
7	PEO/PLLA/acetaminophen	10	0.175	0.075	-	0.0025
8	PEO/PLLA/OA.Fe_3O_4 (20% wt.)/acetaminophen	10	0.175	0.075	0.0625	0.0025
9	PEO/PLLA/OA.Fe_3O_4 (70% wt.)/acetaminophen	10	0.175	0.075	0.6256	0.0025
(II) Membranes for the removal of heavy metal ions from aqueous media						
a/a	**Sample**	**$CHCl_3$ (mL)**		**PEO (g)**	**PLLA (g)**	**OA.Fe_3O_4 (g)**
1	PEO/PLLA	10		0.28	0.12	-
(III) Membranes for the removal of MG organic dye from aqueous media						
a/a	**Sample**	**$CHCl_3$ (mL)**		**PEO (g)**	**PLLA (g)**	**OA.Fe_3O_4 (g)**
1	PEO/PLLA	10		0.28	0.12	-
2	PEO/PLLA/OA.Fe_3O_4 (37% wt.)	10		0.28	0.12	0.235
3	PEO/PLLA/OA.Fe_3O_4 (50% wt.)	10		0.28	0.12	0.400

Drug release studies: Acetaminophen has been encapsulated within the PEO/PLLA-based electrospun membranes aiming toward the investigation of the drug release profile in Dulbecco's Phosphate-Buffered Saline (DPBS) solution (pH 7.2) and in tissue culture media. Single pieces (10 mg, sample dimensions: ~ 2 cm x 2 cm) of the PEO/PLLA/acetaminophen and the PEO/PLLA/OA.Fe_3O_4/acetaminophen (20 and 70% wt. OA.Fe_3O_4) membranes in dry form were immersed in DPBS solution (5 mL) and the release of acetaminophen from the membranes was followed kinetically by recording the UV-vis spectra of the solution at different time intervals. Kinetic studies were repeated for three times and the average values were determined.

In order to assess release kinetics in an environment mimicking tissue culture conditions the PEO/PLLA/OA.Fe_3O_4 20% wt./acetaminophen system was placed separately in a vial containing 10 mL of complete culture media consisting of Dulbecco's Modified Eagles Medium (DMEM) supplemented with 10% Fetal Calf Serum (FCS) and 1% antibiotic-antimycotic (Penicillin/Streptomycin/Amphotericin), maintained at 37 °C, 5% CO_2 and 95% humidity for the indicated time interval. Solution aliquots were taken out at specific time intervals and analysed by UV-vis spectrophotometry. The drug release studies performed in complete culture media were carried out in collaboration with Dr. A. Odysseos (EPOS-Iasis, R&D, Nicosia, Cyprus).

Magnetic hyperthermia: The magnetic hyperthermia studies were carried out by Dr. G. Sarigiannis at the University of Patras (Departments of Materials Science) as follows: The magnetoactive membranes were dispersed in 1 mL of de-ionized water in glass vial at a concentration of 10, 20, 40 and 100 $mg \cdot mL^{-1}$ in magnetic material (Fe_3O_4). Magnetic heating was performed using a hyperthermia system, by placing the suspension at the center of a multiturn copper coil at a frequency (f) of 110 kHz and amplitude (H_o) of 25 mT (19.9 $kA \cdot m^{-1}$) respectively. Temperature rise was recorded by using a sensitive thermocouple (with accuracy ±0.1°C) for 300s.

Adsorption studies for the removal of Eu (III), U(VI), and Th(IV) heavy metal ions from aqueous media: These studies were performed together with the Ph.D candidate M. Efstathiou, from the research group of Dr. I. Pashalides of the Department of Chemistry, University of Cyprus.

Batch experiments in polyethylene (PE) screw-cap bottles containing a certain amount of the PEO/PLLA membrane (10 mg) in contact with 3 mL of an aqueous Eu(III), U(VI) or

Th(IV) solution of known total metal concentration ($1 \cdot 10^{-5}$, $1 \cdot 10^{-3}$ and $7 \cdot 10^{-6}$ M respectively) were conducted. The pH was adjusted by addition of 0.1 M NaOH or 0.1 M $HClO_4$. Following equilibration time (24 hours), pH was measured using a glass electrode (Hanna Instruments pH 211) and the analytical metal ion concentration in solution was determined by recording the UV-vis spectra of the solution by means of arsenazo-III (Arz(III)). Arsenazo(III) is a chromogenic reagent capable of forming stable complexes with the above-mentioned ions. Prior to concentration determination, the solutions were ultra-filtrated using 0.45 μm membrane filters to remove any solid phase particulates from the solution.

To investigate the effect of various parameters (e.g. pH, initial metal ion concentration and ionic strength) on the Eu(III), U(VI) and Th(IV) adsorption, three different classes of experiments were conducted. In these experiments the parameter under investigation was varied while the other experimental parameters were kept constant. The effect of pH was studied in an adsorption system with pre-weigh amount of adsorbent (10 mg) and 3 mL of the test solution (I=0.1 M) in which pH was varied between 1 and 10 for the Eu(III) and U(VI) and 0 and 3 for the Th(IV) by addition of $HclO_4$ or NaOH. For studying the effect of the initial metal ion concentration, the latter was varied between $1 \cdot 10^{-3}$and $7 \cdot 10^{-6}$ M, at a prefixed amount of adsorbent (10 mg), I=0.1 M and the optimum pH, which was ~ 6.5 for the Eu(III), ~ 6 for the U(VI), and ~ 3 for the Th(IV). Finally, the ionic strength (I) effect was studied for I=0.01, 0.1 and 1 M at a prefixed amount of adsorbent (10 mg) and constant metal ion concentration ($1 \cdot 10^{-3}$ and $7 \cdot 10^{-6}$ M for U(VI) and Th(VI) respectively).

Adsorption studies for the removal of MG organic dye from aqueous media: Adsorption studies were conducted by means of batch experiments in PE screw-cap tubes containing a certain amount of the membrane immersed in malachite green (MG) solution (prepared in de-ionized water) of known concentration for 24 hours. After equilibrium UV-vis spectrophotometry was used to determine the residual dye concentration in the supernatant at the MG maximum absorption wavelength (618 nm). The amount of MG adsorbed on the membranes (q_e) and % removal efficiency (% q_e) were calculated.

In order to investigate the effect of the initial dye concentration on the adsorption process, a highly concentrated MG stock solution was initially prepared ($1 \cdot 10^{-4}$ M) and used for the preparation of MG solutions of various concentrations ranging from $1 \cdot 10^{-6}$ M to $1 \cdot 10^{-5}$ M. The effect of pH on the dye removal by the PEO/PLLA and PEO/PLLA/OA.Fe_3O_4 membranes was studied by placing a pre-fixed amount of the adsorbent in the MG solution

of known concentration in which pH was adjusted at different pH values ranging between 3 and 9. The pH values of MG solutions were adjusted by using NaOH or HCl aqueous solutions (0.1-1 M) while the dye concentration remained constant ($6 \cdot 10^{-6}$ M).

For determining the thermodynamic parameters related to the adsorption process the above-mentioned procedure was repeated at 318 K and 338 K. Pieces of membranes were placed in MG solution of known concentration ($1.13 \cdot 10^{-5}$ M) for 24 hours prior to UV-vis analysis.

Kinetic adsorption studies were performed by immersing a specific amount of either PEO/PLLA or PEO/PLLA/OA.Fe_3O_4 membrane (10 mg) in different plastic tubes containing MG solution (3 mL, $C_0=1 \cdot 10^{-5}$ M (0.0927 $g \cdot L^{-1}$)), and recording the UV-vis spectra of the supernatant solution at different time intervals.

All experiments were performed at room temperature (298 K) and in all cases the total volume of the solution (3 mL) and the mass of the adsorbent (10 mg) were retained the same.

Finally for the regeneration and recycling studies of the membranes, the MG-loaded PEO/PLLA and PEO/PLLA/OA.Fe_3O_4 membranes were removed from aqueous solutions and were immersed in ethanol (EtOH) solution (3 mL). After 5 min the membranes were removed from the alcohol solution and re-immersed in another MG solution of the same initial concentration ($C_0=1 \cdot 10^{-5}$ M). The UV-vis spectrum of the supernatant was recorded after 24 hours for determining the amount of the adsorbed dye. The aforementioned adsorption-desorption cycle was repeated three times.

5.3.2. MMA-*co*-AEMA, MMA-*co*-AEMA/OA.Fe_3O_4-based electrospun membranes

Microfibrous pristine and magnetoactive nanocomposite membranes, consisting of methacrylic random copolymers based on methyl mehacrylate (MMA) and 2-(acetoacetoxy)ethyl methacrylate (AEMA) (MMA-*co*-AEMA) and preformed oleic acid-coated magnetic NPs (OA.Fe_3O_4 NPs), were fabricated by electrospinning and evaluated as adsorbents for the removal of heavy metal ions from aqueous solution.

Random copolymer synthesis: Conventional free radical polymerization (FRP) was employed for the synthesis of the MMA-*co*-AEMA random copolymers. To a round-

bottomed flask (50 mL) equipped with a stirring bar and fitted with a rubber septum, the monomers MMA (2.1 mL, 19.6 mmol) and AEMA (4.3 mL, 22.5 mmol) were added. AIBN (2.5 mg, $1.52 \cdot 10^{-5}$ mol) was dissolved in THF (21 mL) and was added to the flask with the aid of a syringe. After dissolution, the reaction mixture was placed in an oil bath at 65 °C for 10 hours under inert (nitrogen) atmosphere. Polymerization was terminated by cooling the reaction down to room temperature. The produced MMA-*co*-AEMA random copolymer was retrieved by precipitation in n-hexane (polymer solution to n-hexane in volume ratio 1:10) and was left to dry in a vacuum oven at room temperature for a few hours. The same procedure was followed for synthesizing a series of random copolymers of the type MMA-*co*-AEMA in various chemical compositions.

Table 5.2 summarizes the quantities of the reactants used for the synthesis of the MMA-*co*-AEMA random copolymers.

Table 5.2: *Quantities of the reactants used for the synthesis of the MMA-co-AEMA random copolymers.*

a/a	Sample	Solvent (mL)	MMA (mL)	AEMA (mL)	MMA-*co*-AEMA molar ratio	AIBN (10^{-3} mol)
1	MMA-*co*-AEMA	21 (THF)	2.1	4.3	1:1.15	0.015
2	MMA-*co*-AEMA	54 (EA)	8.4	7.6	1:0.5	0.10
3	MMA-*co*-AEMA	40 (EA)	4.2	7.6	1:1	0.08
4	MMA-*co*-AEMA	20 (EA)	2.0	4.3	1:2	0.39
5	MMA-*co*-AEMA	8 (EA)	5.0	3.0	1:3	0.31
6	MMA-*co*-AEMA	32 (EA)	20.0	12.0	1:3	1.26

Membrane fabrication: MMA-*co*-AEMA-based fibrous mats were fabricated by electrospinning. An appropriate amount of the in house synthesized random copolymers was initially dissolved in THF with polymer solution concentration of 6% w/v. However this concentration was not the optimum one to obtain uniform fibers. Consequently new polymer solutions of higher concentrations (30% w/v) were prepared whereas THF was also replaced by $CHCl_3$. This particular solvent was found to be more appropriate since it promoted the complete solubilization of OA.Fe_3O_4. The prepared solution was loaded into a glass syringe (10 mL volume) and then electrospun. Systematic parametric studies were carried out by varying the applied voltage, the distance from the tip of the needle to the collector, the needle inner diameter and the solution flow rate.

The same procedure was followed in the presence of OA.Fe_3O_4 NPs. The MMA-*co*-AEMA solutions were mixed with different amounts of OA.Fe_3O_4 NPs (2, 4, 10, 30, and 70% wt.

in respect to the total polymer mass) in THF at room temperature. In all cases, the polymer concentration was kept constant (6% w/v) and only the concentration of the OA.Fe_3O_4 NPs varied.

For the adsorption studies of radioactive Eu(III) metal ions from aqueous media, homogeneous solutions of PEO/MMA-*co*-AEMA and PEO/MMA-*co*-AEMA/OA.Fe_3O_4 (polymer-solution concentration: 4% w/v; weight percentage proportion of PEO/MMA-*co*-AEMA:70/30 respectively, 37% wt. OA.Fe_3O_4 in respect to the total polymer mass) were prepared in $CHCl_3$, and were further electrospun to yield the corresponding fibrous mats.

The quantities of the reactants used for the preparation of all the above-mentioned systems are summarized in **table 5.3**.

Table 5.3: *Quantities of the reactants used for the preparation of the pristine MMA-co-AEMA and the MMA-co-AEMA/OA.Fe_3O_4-based electrospun membranes.*

a/a	Sample	Polymer-solution concentration (w/v)	Solvent (mL)	PEO (g)	MMA-*co*-AEMA (g)	OA.Fe_3O_4 (g)
1	MMA-*co*-AEMA	6	10 (THF)	-	0.6	-
2	MMA-*co*-AEMA/OA.Fe_3O_4 (2% wt.)	6	10 (THF)	-	0.6	0.012
3	MMA-*co*-AEMA/OA.Fe_3O_4 (4% wt.)	6	10 (THF)	-	0.6	0.025
4	MMA-*co*-AEMA/OA.Fe_3O_4 (10% wt.)	6	10 (THF)	-	0.6	0.067
5	MMA-*co*-AEMA/OA.Fe_3O_4 (30% wt.)	6	10 (THF)	-	0.6	0.257
6	MMA-*co*-AEMA/OA.Fe_3O_4 (70% wt.)	6	10 (THF)	-	0.6	1.400
7	MMA-*co*-AEMA	30	10 ($CHCl_3$)	-	0.6, 3	-
8	PEO/MMA-*co*-AEMA	4	10 ($CHCl_3$)	0.28	0.12	-
9	PEO/MMA-*co*-AEMA/OA.Fe_3O_4 (37% wt.)	4	10 ($CHCl_3$)	0.28	0.12	0.235

Adsorption studies for the removal of Eu(III) heavy metal ions from aqueous media: The adsorption studies were performed together with the Ph.D candidate M. Efstathiou, from the research group of Dr. I. Pashalides of the Department of Chemistry, University of Cyprus.

Batch experiments were carried out in polyethylene (PE) screw-cap bottles containing a certain amount of membrane (adsorbent dosage=10 mg per 3 mL) in contact with 3 mL of an aqueous Eu(III) solution of known total metal ion concentration. For studying the effect of the initial metal ion concentration, a pre-fixed amount of the adsorbent (10 mg) was placed in the aqueous Eu(III) solutions (3 mL) of known concentration ($1 \cdot 10^{-4}$ to $7 \cdot 10^{-6}$ M), I=0.1 M and optimum pH 6.5. The effect of pH was studied in an adsorption system with pre-weigh amount of adsorbent (10 mg) and 3 mL of the test solution (I=0.1 M) in

which pH was varied between 1 and 10. pH was adjusted by adding of 0.1 M NaOH or 0.1 M $HClO_4$.

Following equilibration time (24 hours), pH was measured using a glass electrode and the analytical metal ion concentration in solution was determined by recording the UV-vis spectra of the solution by means of Arz-III. Prior to concentration determination, the test solution was ultra-filtrated using 0.45 μm membrane filters to remove any solid phase particulates from the solution.

5.3.3. MMA-*co*-BzMA-based electrospun membranes

Fibrous membranes, consisting of methacrylic random copolymers based on benzyl methacrylate (BzMA) and methyl methacrylate (MMA) (MMA-*co*-BzMA) were fabricated by electrospinning and evaluated as substrates for the removal of organic water-soluble pollutants, including metronidazole, and 1,2 dichlorobenzene.

Random copolymers synthesis: Conventional free radical polymerization (FRP) was employed for the synthesis of the MMA-*co*-BzMA random copolymers. To a round-bottomed flask (50 mL) equipped with a stirring bar and fitted with a rubber septum, the monomers MMA (5 mL, 4.71 mmol) and BzMA (4.3 mL, 22.5 mmol) were added. AIBN (7.8 mg, 0.471 mmol) was dissolved in EA (13 mL) and was added to the flask with the aid of a syringe. The reaction mixture was stirred rapidly at room temperature and heated at 65 °C for 10 hours. After dissolution, the reaction mixture was placed in an oil bath at 65 °C for 10 h under inert (nitrogen) atmosphere. Polymerization was terminated by cooling the reaction down to room temperature. The produced MMA-*co*-BzMA random copolymer was retrieved by precipitation in n-hexane (polymer solution to n-hexane in volume ratio 1:10) and was left to dry in a vacuum oven at room temperature for a few hours.

Table 5.4 summarizes the quantities of the reactants used for the synthesis of two MMA-*co*-BzMA random copolymers.

Table 5.4: *Quantities of the reactants used for the synthesized of a series MMA-co-BzMA random copolymers.*

a/a	Sample	EA (mL)	MMA (mL)	BzMA (mL)	MMA-*co*-BzMA molar ratio	AIBN (mmol)
1	MMA-*co*-BzMA	13	5.0	8.0	1:1	0.471
2	MMA-*co*-BzMA	25	9.4	15.0	1:1	0.885

Membrane fabrication: MMA-*co*-BzMA and PEO/MMA-*co*-BzMA fibrous mats were prepared by electrospinning. Appropriate amounts of the in house synthesized random copolymer were dissolved in $CHCl_3$ with polymer polymer-solution concentrations 10, 30 and 50% w/v. In the case of the PEO/MMA-*co*-BzMA, a 52% w/v solution was prepared containing a weight percentage proportion PEO/MMA-*co*-BzMA:4/96. The prepared homogeneous solution was loaded into a glass syringe (10 mL volume) and then electrospun. Systematic parametric studies were carried out by varying the applied voltage, the distance from the tip of the needle to the collector, the needle inner diameter, and the solution flow rate.

The quantities of the reactants used for the preparation of all the above-mentioned systems are summarized in **table 5.5**.

Table 5.5: *Quantities of the reactants used for the preparation of the MMA-co-BzMA electrospun membranes.*

a/a	Sample	$CHCl_3$ (mL)	PEO (g)	MMA-*co*-BzMA (g)
1	MMA-*co*-BzMA	10	-	5
2	PEO/MMA-*co*-BzMA	10	0.2	5

Adsorption studies for the removal of dichlorobenzene and metronidazole from aqueous media: Single pieces (10 mg) of electrospun membranes consisting of MMA-*co*-BzMA in dry form, were immersed in both 1,2 dichlorobenzene (5 mL) and metronidazole (5 mL) aqueous solutions at known concentration 0.1 $mg \cdot mL^{-1}$ ($8.88 \cdot 10^{-4}$ $mol \cdot L^{-1}$) and 0.02 $mg \cdot mL^{-1}$ ($1.17 \cdot 10^{-4}$ $mol \cdot L^{-1}$) respectively. The adsorption of the pollutants from the membranes was followed kinetically by recording the UV-vis spectra of the supernatant solution at the different time intervals.

5.3.4. PVP, PVP/PLLA and PVP/PLLA/OA.Fe_3O_4 electrospun membranes

The fabrication of fibrous membranes based on poly(vinyl pyrrolidone) (PVP), poly(L-lactide) (PLLA) and pre-formed oleic acid coated magnetite NPs (OA.Fe_3O_4) was carried out by means of the electrospinning technique.

Membrane fabrication: Electrospun membranes comprised of the commercially available homopolymers PVP and PLLA and preformed OA.Fe_3O_4 NPs were fabricated. Initially, solutions of PVP (polymer-solution concentrations: 3, 5, 10 and 15% w/v) and solutions of PVP/PLLA (polymer-solution concentration: 10% w/v; weight percentage proportion PVP/PLLA:70/30 respectively) were prepared in $CHCl_3$. The PVP/PLLA solutions were then mixed with different amounts of OA.Fe_3O_4 NPs (5, 10 and 20% wt. in respect to the total polymer mass) at room temperature. In all cases, the polymer concentration in solution was kept constant (10% w/v) and only the concentration of the OA.Fe_3O_4 varied.

The quantities of the reactants used for the preparation of a series of PVP, PVP/PLLA and PVP/PLLA/OA.Fe_3O_4 solutions are summarized in **table 5.6**.

Table 5.6: *Quantities of the reactants used for the preparation of the PVP, PVP/PLLA and PVP/PLLA/OA.Fe_3O_4 solutions in $CHCl_3$.*

a/a	Sample	Polymer-solution concentration (w/v)	$CHCl_3$ (mL)	PVP (g)	PLLA (g)	OA.Fe_3O_4 (g)
1	PVP	3	10	0.3	-	-
2	PVP	5	10	0.5	-	-
3	PVP	10	10	1.0	-	-
4	PVP	15	10	1.5	-	-
5	PVP/PLLA	10	10	0.7	0.3	-
6	PVP/PLLA/OA.Fe_3O_4 (5% wt.)	10	10	0.7	0.3	0.053
7	PVP/PLLA/OA.Fe_3O_4 (10% wt.)	10	10	0.7	0.3	0.111
8	PVP/PLLA/OA.Fe_3O_4 (20% wt.)	10	10	0.7	0.3	0.250

5.3.5. PVP/metal nanoparticles

PVP-Pd and PVP-Cu_2O electrospun fibrous nanocomposite membranes were prepared and evaluated as heterogeneous catalytic supports in Heck, Suzuki and click chemistry reactions.

Synthesis of PVP-Pd colloidal nanohybrids: The PVP-Pd colloidal nanohybrids (mols vinyl pyridine (VP) units/mols palladium salt ($Pd(OCOCH_3)_2$) = 20:1 were prepared as follows: (323) In a round bottom flask equipped with a magnetic stirrer, PVP (1.0 g, 9

mmol of vinylpyrridine units) was dissolved in MeOH (10 mL). Subsequently, palladium acetate (100 mg, 0.45 mmol) was added to the polymer solution and the reaction mixture was heated at reflux (65 °C) for 2 hours. During this period, the colour of the solution changed from yellow to dark brown indicating the formation of Pd NPs. After the completion of the reaction, the brown coloured solution was allowed to cool down at room temperature and it was then stored in sealed glass vials. The solutions were stable and no precipitation was observed even after several months.

Synthesis of PVP-Cu colloidal nanohybrids: The PVP-Cu colloidal nanohybrids (mols vinyl pyridine (VP) units/mols copper salt ($Cu(CO_2CH_3)_2 \cdot H_2O$) = 3.6:1 were prepared as follows: In a vial equipped with a magnetic stirrer, PVP (1.0 g, 9 mmol of vinylpyrridine units) was dissolved in MeOH (7.5 mL). Subsequently, copper acetate monohydrate (500 mg, 2.5 mmol) was added to the polymer solution and the mixture was left to stir overnight at (~ 20 °C). During this period, the colour of the solution changed from colourless to blue. Afterwards, hydrazine monohydrate (972 μL, 20.0 mmol) was added and the colour of the solution became dark red, indicating the formation of Cu NPs. Air exposure of the colloidal solution led to a colour change from red to light blue, indicative of the oxidation of the Cu NPs to Cu_2O (324). The final PVP-capped Cu_2O NPs exhibited high stability in methanol MeOH and no agglomeration/ destabilization phenomena were observed even after several months.

Membrane fabrication: The PVP-Pd and PVP-Cu_2O colloidal solutions were used for the fabrication of Pd and Cu_2O-containing PVP fibrous membranes by means of the electrospinning technique. Systematic parametric studies were carried out by varying the applied voltage between to the needle-to-collector distance, the needle inner diameter, and the flow rate so as to determine the optimum experimental conditions for obtaining fibrous materials.

Membrane crosslinking: Water-insoluble PVP-Pd and PVP-Cu_2O fibrous nanocomposites were obtained *via* thermal crosslinking of the as prepared corresponding electrospun fibers. More precisely, the electrospun PVP-Pd and PVP-Cu_2O membranes were placed in an oven and heated at 180 °C for 5 hours.

Catalysis: The catalytic experiments were performed in the research group of Dr. P. A. Koutentis by Dr. A. Kalogirou at the Department of Chemistry, University of Cyprus.

Heck reaction: To a stirred solution of iodobenzene (22 μL, 0.20 mmol) in dry DMF (1 mL) at 20 °C, was added n-butyl acrylate (43 μL, 0.30 mmol), Et_3N (75 μL, 0.54 mmol) and the PVP-Pd 20:1 electrospun membrane (11 mg, 2.4 mol %). The mixture was heated to 125 °C in a sealed tube until complete consumption of iodobenzene. The mixture was then cooled to 20 °C and t-BuOMe (10 mL) was added. The polymer precipitate was filtered and washed with t-BuOMe (10 mL), then dried under vacuum. The membrane was reused in subsequent reactions without further treatment. The organic washings were washed with H_2O (2×10 mL), combined, dried (Na_2SO_4) and evaporated to give after column chromatography (n-hexane/DCM, 1:1) n-butyl cinnamate (36 mg, 88%) as a yellow oil.

^{1}H NMR δ: (500 MHz; $CDCl_3$) 7.69 (1H, d, J 16.0, =CH), 7.53-7.51 (2H, m, Ar H), 7.39-7.36 (3H, m, Ar H), 6.45 (1H, d, J 16.0, =CH), 4.21 (2H, t, J 6.7, OCH_2), 1.72-1.66 (2H, m, CH_2), 1.48-1.40 (2H, m, CH_2), 0.97 (3H, t, J 7.4, CH_3).

Suzuki reaction: To a stirred solution of 4-iodoanisole (117 mg, 0.50 mmol) in THF (0.8 mL) and H_2O (0.4 mL) at 20 °C was added phenyl boronic acid (91 mg, 0.75 mmol), powdered K_2CO_3 (138 mg, 1.00 mmol) and the crosslinked PVP-Pd 20:1 membrane (20 mg, 1.6 mol %) and the mixture was heated to 80 °C in a sealed tube until compete consumption of the starting material. The mixture was then cooled to 20 °C and t-BuOMe (10 mL) was added. The polymer precipitate was filtered and washed with t-BuOMe (10 mL), then dried under vacuum. The membrane was reused in subsequent reactions without further treatment. The organic washings were washed with H_2O (2×10 mL), combined, dried (Na_2SO_4) and evaporated to give 4-methoxybiphenyl (90 mg, 98%) as colourless needles, mp 81-83 °C (from EtOH/H_2O, 80-82 °C (325));

^{1}H NMR δ: (500 MHz; $CDCl_3$) 7.56 (2H, d, J 7.9, Ar H), 7.54 (2H, d, J 8.7, Ar H), 7.42 (2H, dd, J 7.6, 7.6 Ar H), 7.38 (1H, dd, J 7.4, 7.4 Ar H), 6.99 (2H, d, J 8.7, Ar H), 3.86 (3H, s, CH_3);

Click chemistry: To a stirred solution of benzyl azide, synthesized according to the literature (318), (67 mg, 0.50 mmol) in dioxane (1 mL) at 20 °C was added phenylacetylene (60 μL, 0.55 mmol), followed by Et_3N (77 μL, 0.55 mmol) and the crosslinked PVP-Cu_2O 3.6:1 membrane (11.6 mg, 5.0 mol % Cu). The mixture was heated to 60 °C in a sealed tube until compete consumption of the starting material. The mixture was then cooled to 20 °C and t-BuOMe (10 mL) was added. The polymer precipitate was

filtered and washed with t-BuOMe (10 mL), then dried under vacuum. The membrane was reused in subsequent reactions without further treatment. The organic washings were evaporated to give 1-benzyl-4- phenyl-1H-1,2,3-triazol (102 mg, 87%) as colourless needles, mp 121-123 °C (from c-hexane,123-125 °C (326));

^{1}H NMR δ: (500 MHz; CDCl3) 7.80 (2H, d, J 7.3, Ar H), 7.68 (1H, s, Ar H), 7.41- 7.35 (5H, m, Ar H), 7.32-7.29 (3H, m, Ar H), 5.55 (2H, s, CH_2);

6

Results and Discussion

6.1. PEO/PLLA and PEO/PLLA/OA.Fe_3O_4 electrospun membranes: Fabrication, characterization and applications

Fibrous polymer-based nanocomposite membranes consisting of the hydrophilic, biocompatible and thermoresponsive polyethylene oxide (PEO), the hydrophobic, biocompatible and biodegradable poly(L-lactide) (PLLA), and preformed oleic acid-coated magnetic nanoparticles (OA.Fe_3O_4 NPs) were successfully fabricated by electrospinning, characterized in regards to their morphology, composition, thermal and magnetic properties and evaluated for the first time in drug delivery and hyperthermia applications (151) as well as in water remediation processes as adsorbents for the removal of heavy metal ions and organic water-soluble dyes from aqueous media (327).

6.1.1. Membrane fabrication

Initially, homogeneous solutions of PEO, PEO/PLLA and PEO/PLLA/OA.Fe_3O_4 were prepared in $CHCl_3$. The polymer-solution concentration was set at either 2.5 % w/v **(table 6.1 (I))** or at 4% w/v **(table 6.1 (II, III))**, whereas the PEO/PLLA weight percentage was

maintained at 70/30 respectively. The chemical structures of the PEO and the PLLA homopolymers and of the preformed OA.Fe_3O_4 are illustrated in **figure 6.1**. The obtained solutions were then electrospun under specific electrospinning conditions to yield fibrous electrospun mats as shown in **figure 6.1.** In the case of the magnetoactive electrospun membranes the magnetic content varied from 5% - 70% wt.

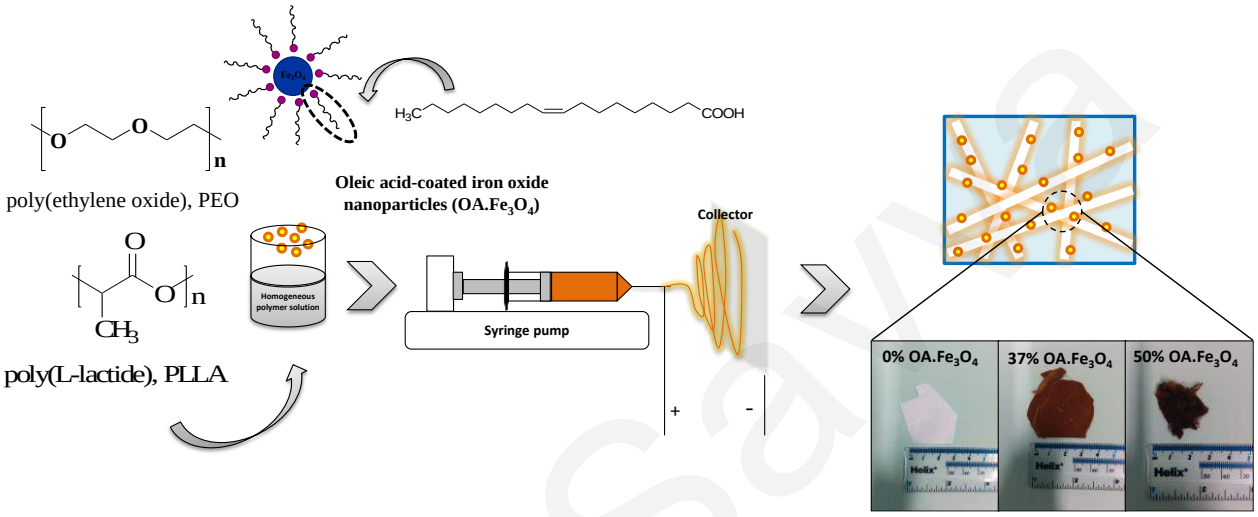

Figure 6.1: *Chemical structures and names of the main reagents used for the preparation of PEO, PEO/PLLA, and PEO/PLLA/OA.Fe_3O_4 fibrous membranes by electrospinning (Photographs provided correspond to the PEO/PLLA fibrous mats containing 0, 37 and 50% wt. OA.Fe_3O_4).*

Besides the incorporation of magnetic NPs within PEO/PLLA electrospun mats, a pharmaceutical compound namely acetaminophen (also known as paracetamol) has been also introduced within the membranes **(table 6.1 (I)**, **entries 7-9**) aiming toward the evaluation of the drug-loaded electrospun mats in drug delivery applications as described in a following subchapter **(6.1.3.1.)**.

The successful generation of fibrous membranes requires the determination of the optimal processing parameters that include the concentration of the polymeric solution (which significantly affects the solution viscosity), the applied voltage, the delivery rate of the solution toward the collector, the diameter of the needle, and the distance between the tip of the needle and the collector.

Experimental parametric studies were carried out for the PEO and the PEO/PLLA systems both in the absence and presence of the magnetic NPs in order to define the optimum parameters for the production of electrospun fibrous membranes. **Table 6.1** summarizes

the optimum experimental electrospinning conditions followed for the successful generation of the fibrous membranes.

Table 6.1: *Optimum experimental conditions employed for the fabrication of the PEO, PEO/PLLA and PEO/PLLA/OA.Fe_3O_4-based membranes.*

(I) Membranes for drug delivery					
a/a	**Sample**	**Needle (G)**	**Flow rate ($mL \cdot h^{-1}$)**	**Voltage (kV)**	**Needle-to-collector distance (cm)**
1	PEO	16	3	10	15
2	PEO/PLLA	16	3	10	30
3	PEO/PLLA/OA.Fe_3O_4 (5% wt.)	16	4	20	25
4	PEO/PLLA/OA.Fe_3O_4 (10% wt.)	16	4	20	25
5	PEO/PLLA/OA.Fe_3O_4 (20% wt.)	16	4	23	25
6	PEO/PLLA/OA.Fe_3O_4 (50% wt.)	16	4.5	25	25
7	PEO/PLLA/acetaminophen	16	3	25	25
8	PEO/PLLA/OA.Fe_3O_4 (20% wt.)/acetaminophen	16	4	25	25
9	PEO/PLLA/OA.Fe_3O_4 (70% wt.)/acetaminophen	16	5	25	25
(II) Membranes for the removal of heavy metal ions from aqueous media					
a/a	**Sample**	**Needle (G)**	**Flow rate ($mL \cdot h^{-1}$)**	**Voltage (kV)**	**Needle-to-collector distance (cm)**
1	PEO/PLLA	16	4	25	25
(III) Membranes for the removal of malachite green (MG) from aqueous media					
a/a	**Sample**	**Needle (G)**	**Flow rate ($mL \cdot h^{-1}$)**	**Voltage (kV)**	**Needle-to-collector distance (cm)**
1	PEO/PLLA	16	4	25	25
2	PEO/PLLA/OA.Fe_3O_4 (37% wt.)	16	4.5	25	25
3	PEO/PLLA/OA.Fe_3O_4 (50% wt.)	16, 18, 22	4.5	25	25

6.1.2. Membrane characterization

Morphological characterization: The morphological characteristics of the membranes were determined by SEM. **Figure 6.2** provides the SEM images in different magnifications of **(a)** the PEO homopolymer **(b)** the PEO/PLLA (polymer-solution concentration: 2.5% w/v), **(c)** the drug-loaded PEO/PLLA/acetaminophen (polymer-solution concentration: 2.5% w/v) and **(d)** the PEO/PLLA (polymer-solution concentration: 4% w/v). The PEO membranes exhibited a multimodal diameter distribution ranging between 1 and 3 μm, whereas in the presence of PLLA the obtained fibers were characterized by higher homogeneity. This phenomenon is probably attributed to the low Tg of the PEO (around -50 ^oC) allowing for fiber merging in ambient conditions and thus broader fiber diameter distribution, whereas in the presence of PLLA exhibiting high Tg values (around 60 ^oC) this merging process is prevented. Upon increasing the concentration from 2.5 to 4% w/v, the fibers exhibited cylindrical, highly homogeneous and larger diameters ranging between 3 and 4 μm. This observation is in line with other literature examples supporting that upon

increasing the solution concentration the diameter of the obtained continuous electrospun fibers increases (45; 52; 53). Moreover, as seen in **figure 6.2 (c)** the incorporation of acetaminophen within the PEO/PLLA membranes did not significantly affect the morphological characteristics of the membranes.

(a) PEO, polymer-solution concentration: 2.5%w/v in $CHCl_3$

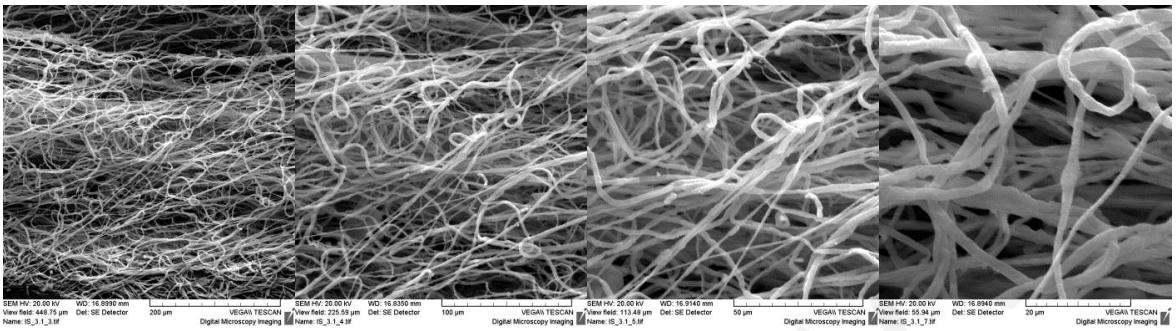

(b) PEO/PLLA, polymer-solution concentration: 2.5% w/v in $CHCl_3$

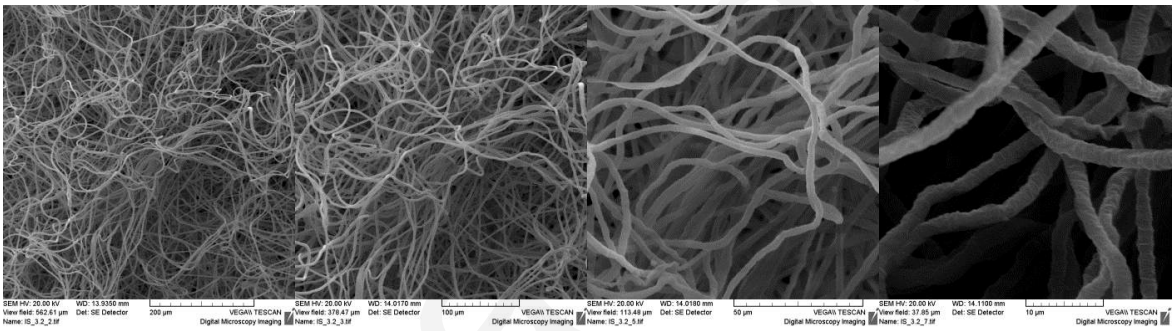

(c) PEO/PLLA/acetaminophen, polymer-solution concentration: 2.5% w/v in $CHCl_3$

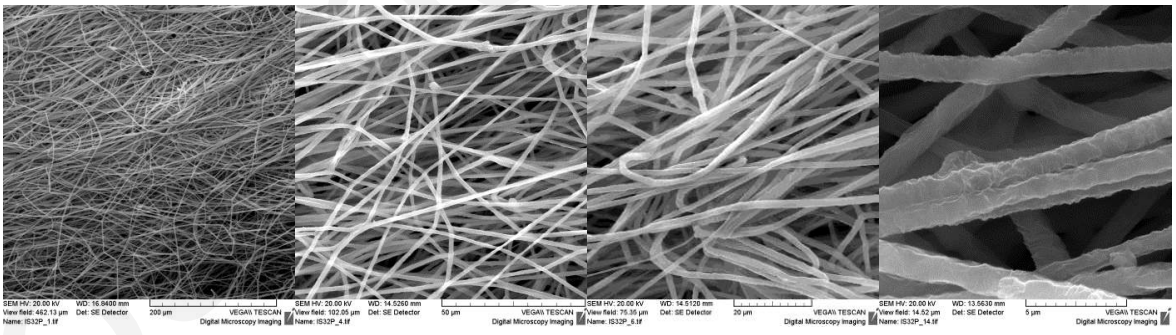

PEO/PLLA, polymer-solution concentration: 4% w/v in $CHCl_3$

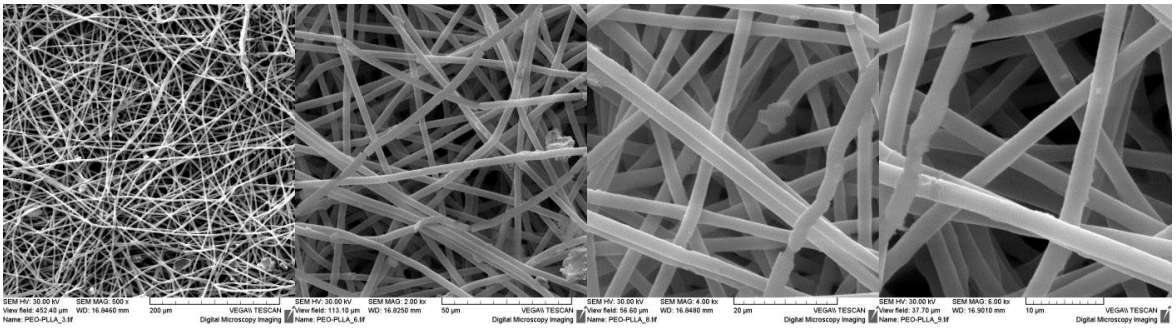

Figure 6.2: *SEM images of the PEO, PEO/PLLA and PEO/PLLA/acetaminophen electrospun membranes.*

In **figure 6.3** the SEM images of the magnetoactive PEO/PLLA/OA.Fe_3O_4 membranes containing **(a)** 5, **(b)** 10, **(c)** 20, **(d)** 50% wt. OA.Fe_3O_4 and of the drug-loaded magnetoactive membranes PEO/PLLA/OA.Fe_3O_4 (**(e)** 20 and **(f)** 70% wt.)/acetaminophen systems prepared starting from homogeneous $CHCl_3$ solutions of polymer concentration 2.5% w/v are provided. In addition, magnetoactive membranes containing 37 and 50 % wt. OA.Fe_3O_4 **(figure 6.3**, images **(g)** and **(h)** respectively**)** generated from $CHCl_3$ solutions of 4% w/v polymer concentration are also shown.

By comparing the SEM micrographs of the magnetoactive fibrous membranes with 50% wt. magnetic content obtained starting from two different polymer-solution concentrations (i.e. 2.5% w/v and 4% w/v, **figure 6.3 (d)** and **(h)** respectively) whereas all other processing parameters were kept the same, it was concluded that upon increasing the concentration of the solution, fewer beaded structures along the nanofibers were generated. SEM revealed the presence of a multimodal diameter distribution ranging between 1 and 3 μm.

From the SEM analyses it was also observed that the presence of the magnetic NPs within the membranes did not significantly affect the morphological characteristics of the fibers. As seen in **figure 6.3 (a-d)** upon increasing the magnetic content within the membranes from 2.5 up to 50% wt. the fibers retain their continuity and cylindrical morphology, whereas no significant diameter variations or extensive beaded structures are observed. This is somehow expected due to the very small nanometer-sized particles. Similarly, SEM has shown that the incorporation of acetaminophen within the PEO/PLLA/OA.Fe_3O_4 membranes did not influence the morphological characteristics of the membranes (**figure 6.3 (e) and (f)**).

(a) PEO/PLLA/OA.Fe_3O_4 5% wt., polymer-solution concentration: 2.5% w/v in $CHCl_3$

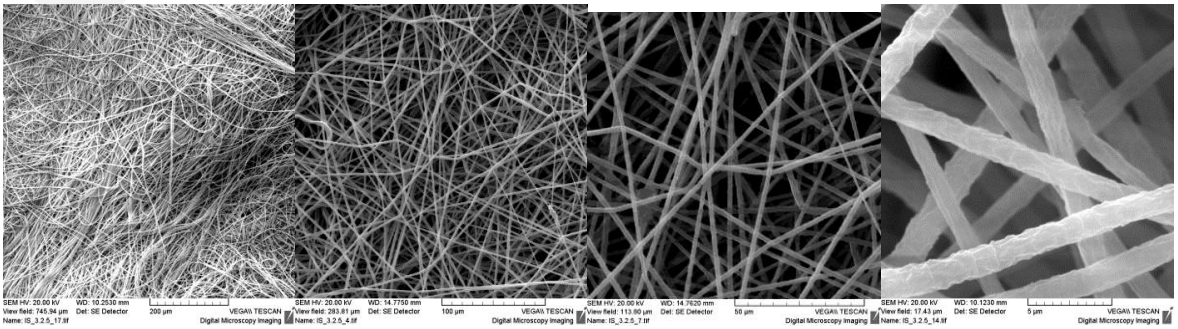

(b) PEO/PLLA/OA.Fe_3O_4 10% wt., polymer-solution concentration: 2.5% w/v in $CHCl_3$

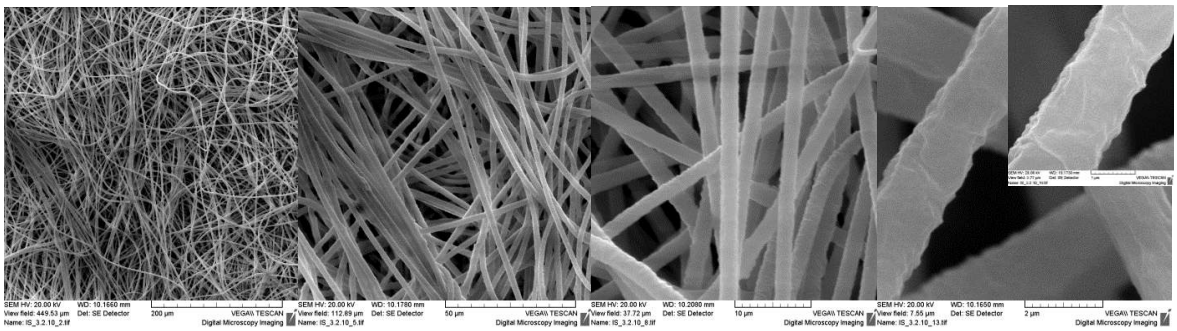

(c) PEO/PLLA/OA.Fe_3O_4 20% wt., polymer-solution concentration: 2.5% w/v in $CHCl_3$

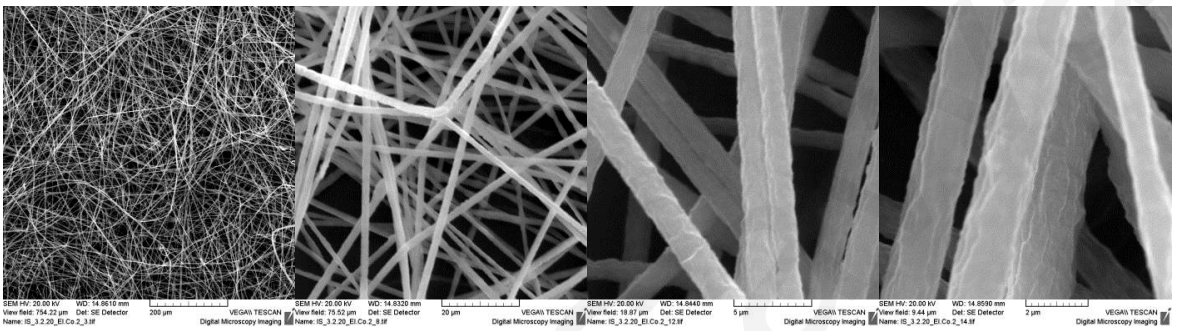

(d) PEO/PLLA/OA.Fe_3O_4 50% wt., polymer-solution concentration: 2.5% w/v in $CHCl_3$

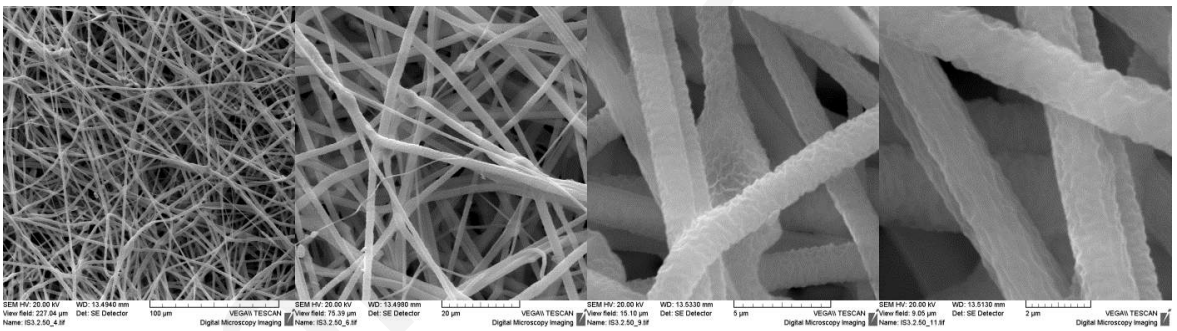

(e) PEO/PLLA/OA.Fe_3O_4 20% wt./acetaminophen, polymer-solution concentration: 2.5% w/v in $CHCl_3$

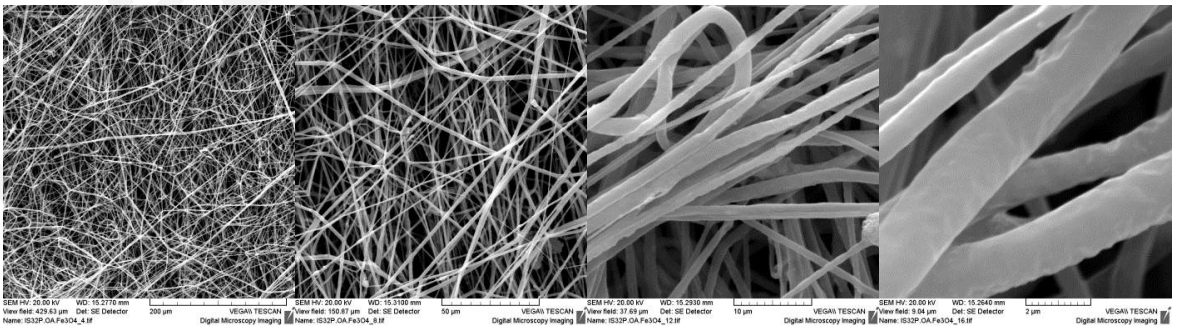

(f) PEO/PLLA/OA.Fe_3O_4 70% wt./acetaminophen, polymer-solution concentration: 2.5% w/v in $CHCl_3$

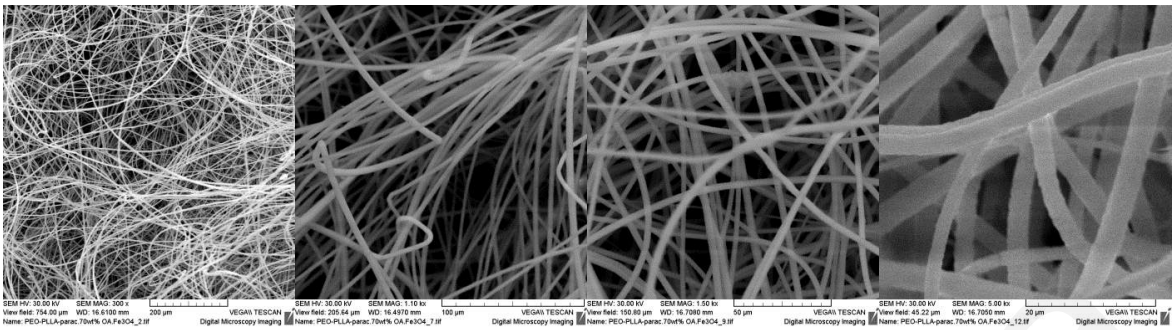

(g) PEO/PLLA/OA.Fe_3O_4 37% wt., polymer-solution concentration: 4% w/v in $CHCl_3$

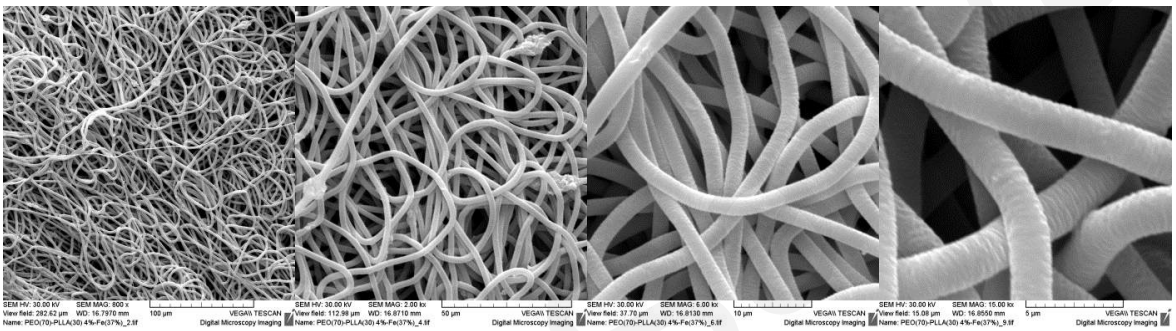

(h) PEO/PLLA/OA.Fe_3O_4 50% wt., polymer-solution concentration: 4% w/v in $CHCl_3$

16G

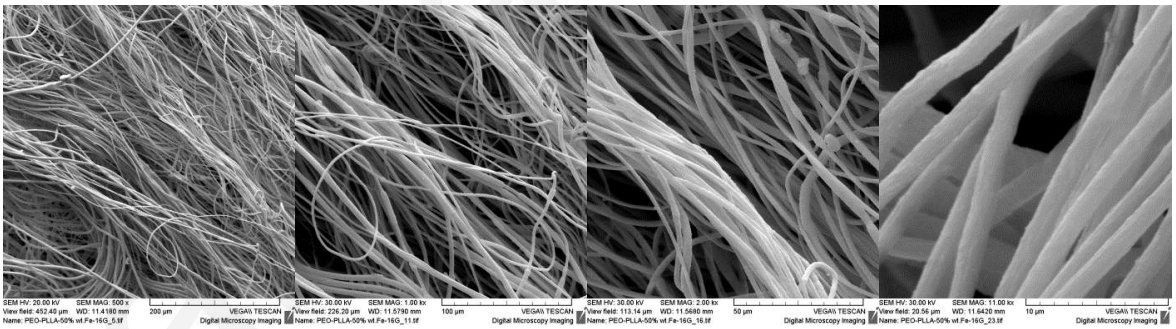

18G

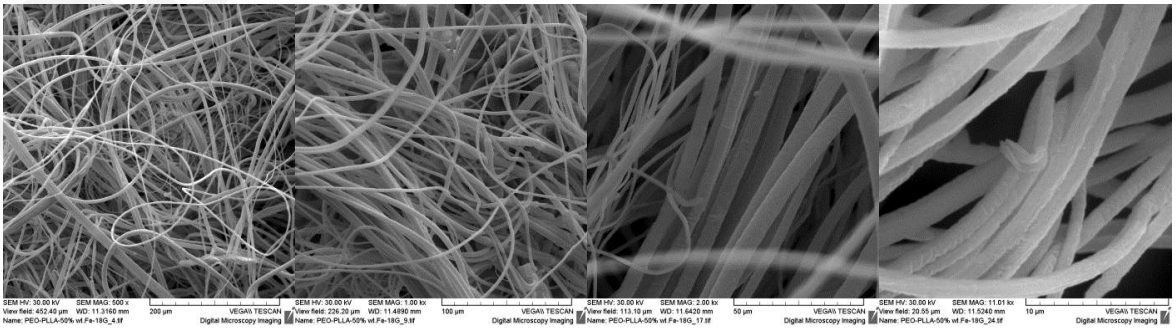

22G

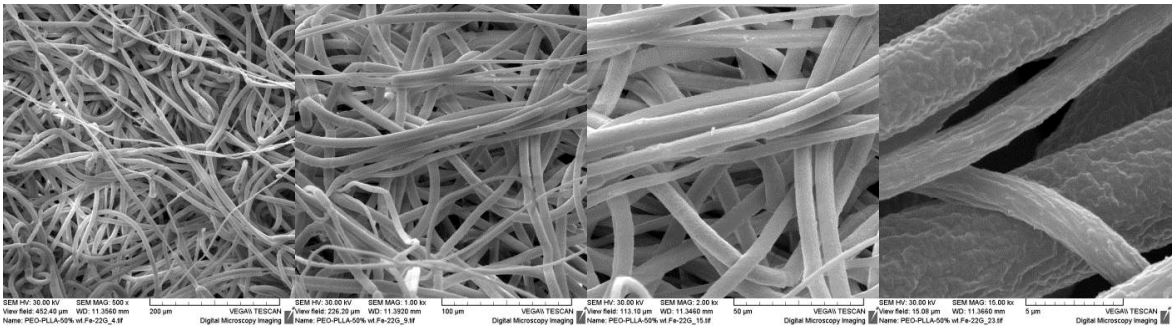

Figure 6.3: *SEM images of the PEO/PLLA/OA.Fe_3O_4 and the drug-loaded PEO/PLLA/OA.Fe_3O_4/acetaminophen magnetoactive electrospun nanocomposite membranes.*

The PEO/PLLA/OA.Fe_3O_4 membranes were also visualized by HRTEM. **Figure 6.4** depicts transmission electron micrographs of the membrane containing OA.Fe_3O_4 20% wt. magnetic NPs. From the TEM bright field images **(figure 6.4 (a)** and **(b))** it can be clearly seen that the magnetic Fe_3O_4 NPs embedded within the membranes are spherical in shape with average diameters of approximately 5 nm. Moreover, a distinct dispersion of the NPs in the PEO/PLLA matrix resulting in high homogeneity can be observed. By comparing the size distribution of the pre-formed OA.Fe_3O_4 NPs (328) with the mean diameters of the OA.Fe_3O_4 NPs embedded within the polymer fibers it can be concluded that no nanoparticle agglomeration phenomena occur during the electrospinning process since the dimensions of the embedded NPs are retained within the same range. NPs are nanocrystals and HRTEM imaging **(figure 6.4 (c))** discloses the crystalline planes (311) of Fe_3O_4 with 2.51 Å characteristic interplanar distances.

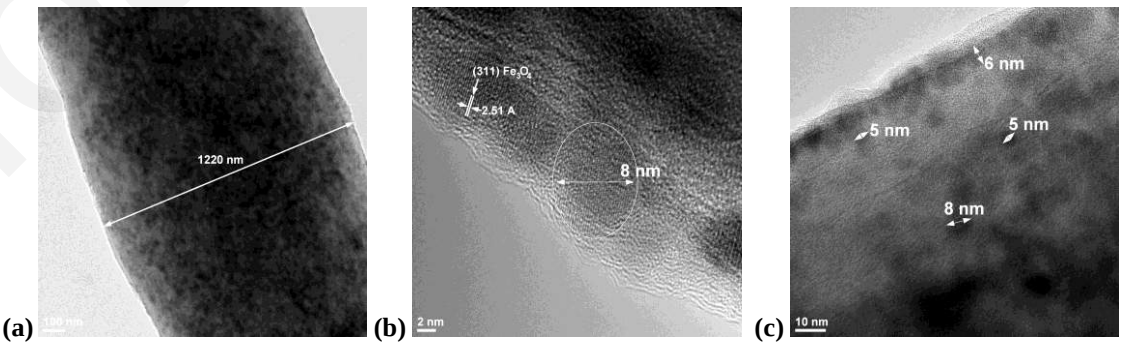

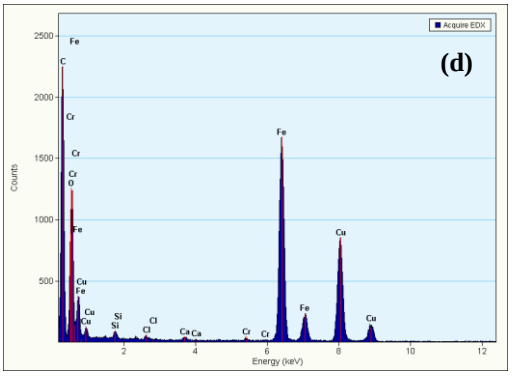

Figure 6.4: (a, b) *TEM bright field,* ***(c)*** *HRTEM images and* ***(d)*** *corresponding EDX spectrum of the PEO/PLLA/OA.Fe_3O_4 polymeric membranes in the presence of OA.Fe_3O_4 NPs 20% wt.*

The EDX spectrum (**figure 6.4 (d))** shows the presence of Fe, O and C as the major elements in the sample (element Cu comes from the copper grid). The presence of minor elements Ca, Si, Cl, Cr is attributed to mild sample contamination during the preparation process for TEM investigations.

Thermal characterization: The degradation temperatures of the resulting PEO/PLLA-based polymeric membranes (polymer-solution concentration: 2.5% w/v) were determined by TGA measurements. The modulation of the decomposition temperature of the membranes by the embedded OA.Fe_3O_4 was determined by this method **(figure 6.5)**. In the case of the pure OA.Fe_3O_4 a weight loss is observed at lower temperatures (below 300 °C), which is attributed to the decomposition of the organic oleic acid coating (329). The magnetite-free polymer membrane begins to decompose at a temperature lower than ~ 300 °C at which the nanocomposite PEO/PLLA/OA.Fe_3O_4 membrane starts to decompose, suggesting that the magnetic NPs affect favorably in the thermal stability of the membranes, acting as heat barriers due to the nanoparticle-polymer interactions (330). This finding is in line with the report that poly(methyl methacrylate)/Fe_3O_4 composite nanofibrous membranes present a higher degradation temperature in comparison to the pristine PMMA fibers (331). The remaining residue observed in the case of the magnetite-containing membrane at higher temperatures (T > 430 °C) corresponds to the inorganic (Fe_3O_4) content.

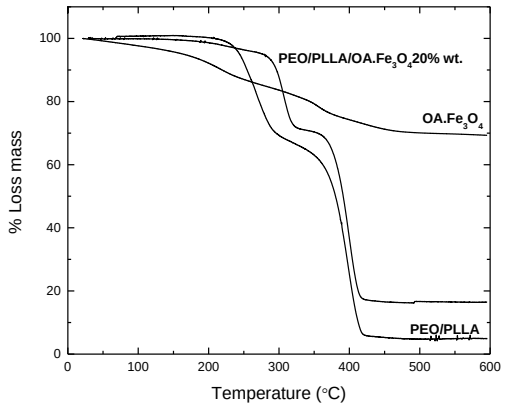

Figure 6.5: *TGA thermograms of the pure OA.Fe_3O_4 NPs, the PEO/PLLA and the PEO/PLLA/OA.Fe_3O_4 20% wt. electrospun membranes.*

The TGA traces of the PEO/PLLA-based polymeric membranes (polymer-solution concentration: 4% w/v) both in the absence and presence of OA.Fe_3O_4 NPs are provided in **figure 6.6**. As seen in the thermograms, a similar thermal decomposition profile as the one described above is observed with the pristine polymer membrane starting to decompose at a lower temperature compared to the nanocomposite membrane analogue, while at ~ 420 °C, it decomposes completely losing all of its weight. The remaining residue observed in the case of the magnetite-containing membrane at higher temperatures (T > 430 °C) corresponds to the inorganic (Fe_3O_4) content.

The characteristic melting points corresponding to the PEO and the PLLA crystalline domains in the absence and presence of the magnetic NPs are seen in the DSC thermal curves of the PEO/PLLA and the PEO/PLLA/OA.Fe_3O_4 50% wt. provided in **figure 6.7**. The characteristic melting point of the PEO homopolymer was observed at around 65 °C and the one corresponding to the PLLA at around 170 °C in agreement with previous literature reports (332; 333). In the presence of magnetite, a significant decrease in the melting enthalpy of both the PEO and the PLLA domains was observed, confirming the reduction of crystallinity caused by the incorporation of the OA.Fe_3O_4 within the membranes. The relative degree of crystallinity of PEO in the PEO/PLLA membranes in the presence and absence of magnetic NPs is calculated from the melting enthalpy values obtained from the area of the melting curves for PEO in DSC thermograms and using the following **equation 6.1**:

$$Degree\ of\ crystallinity = \left(\frac{\Delta H_m}{\Delta H_m^{\circ}}\right) \cdot 100\% \qquad \textbf{Equation 6.1}$$

where, ΔH_m is the melting enthalpy of PEO in the PEO/PLLA samples and $\Delta H°_m$ is the melting enthalpy of 100% crystalline PEO that is equal to 213.7 J/g.

Based on the above the degree of crystallinity of PEO in the PEO/PLLA and PEO/PLLA/OA.Fe_3O_4 was calculated to be 38% and 24% respectively.

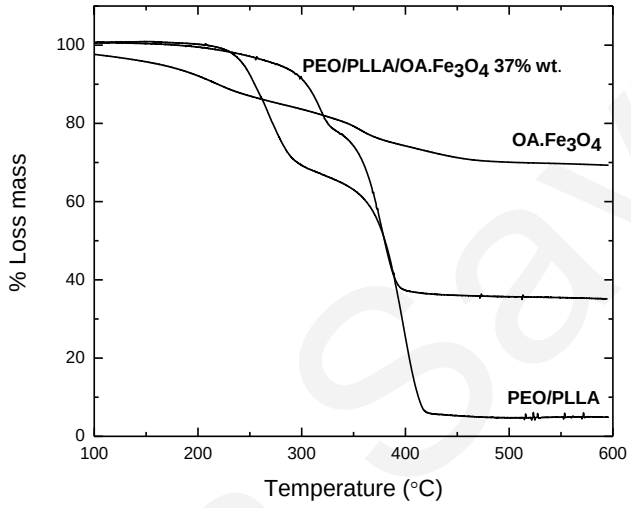

Figure 6.6: *TGA thermograms of the pure OA.Fe_3O_4 NPs, the PEO/PLLA and the PEO/PLLA/OA.Fe_3O_4 37% wt. electrospun membranes.*

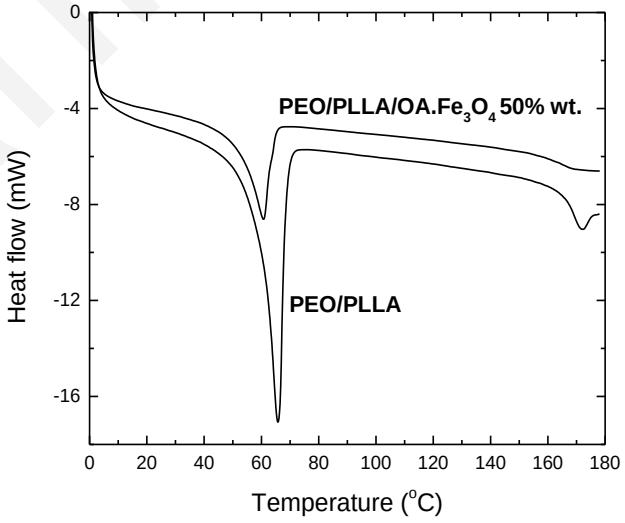

Figure 6.7: *DSC thermograms of the PEO/PLLA and the PEO/PLLA/OA.Fe_3O_4 50% wt. fibrous membranes.*

Nanocrystalline phase characterization: The nanocrystalline phase adopted by the OA.Fe_3O_4 NPs embedded within the nanocomposite membranes, was investigated by XRD. The powder XRD diffraction pattern of the membrane PEO/PLLA/OA.Fe_3O_4 with 37 and 50% wt. of magnetic content (OA.Fe_3O_4) is provided in **figure 6.8**, together with the pattern corresponding to pure OA.Fe_3O_4 NPs for comparison. The diffractogram displays six board peaks appearing at 2θ ~ 30°, 36°, 43°, 54, 58° and 63°, verifying the presence of magnetite (Fe_3O_4) within these materials (334; 335; 336).

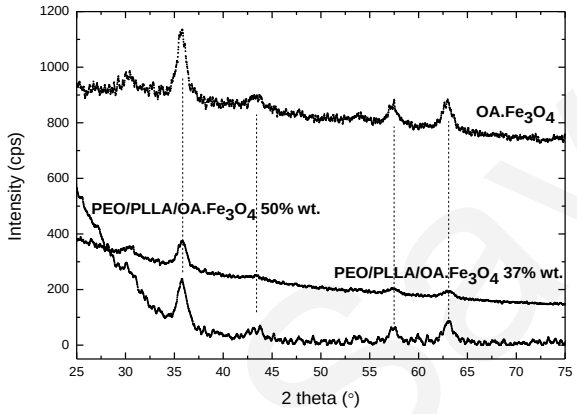

Figure 6.8: *X-ray diffraction patterns of the pure OA.Fe_3O_4 NPs and the PEO/PLLA/OA.Fe_3O_4 nanocomposite membranes containing OA.Fe_3O_4 37 and 50% wt.*

Magnetic characterization: Investigation of the magnetic properties of the PEO/PLLA/ OA.Fe_3O_4 nanocomposite membranes was carried out by VSM at 300K. **Figure 6.9** shows the magnetization *versus* applied magnetic field strength plots (M=*f*(H)) corresponding to nanocomposite membranes loaded with different amounts of OA.Fe_3O_4. The sigmoidal shape of these plots and the lack of a hysteresis loop demonstrate the superparamagnetic behavior of these materials at ambient temperature. Furthermore, magnetization plots showed that upon increasing the magnetic content within the membranes, the saturation magnetization (M_s) increases, while the superparamagnetic properties are retained. The nanocomposite membranes exhibit much lower magnetization values in comparison to the M_s of the pure Fe_3O_4 NPs (~ 45 emu·g^{-1}). Based on literature reports, the saturation magnetization of the bulk (uncoated) Fe_3O_4 NPs is approximately (~ 92 emu·g^{-1}) (337). The oleic-acid coated magnetite NPs exhibit lower saturation magnetization (~ 40 emu·g^{-1}) due to the presence of the organic, non-magnetic oleic acid coating giving further credence to the notion that the presence of a non-magnetic coating (oleic acid) (336) or a stabilizing

surfactant (338), affects the magnetization due to quenching of surface effect. The incorporation of the OA.Fe_3O_4 within the PEO/PLLA fibrous membranes results to a further decrease of the M_s owing to the existence of the non-magnetic polymers (337; 338; 339).

In **figure 6.9 (a)** the magnetization plots of the electrospun PEO/PLLA-based magnetoactive membranes with 5, 10, and 50% wt. OA/Fe_3O_4 obtained from solutions with polymer-solution concentration of 2.5% w/v are provided. **Figure 6.9 (b)** shows the magnetization plots of the PEO/PLLA-based magnetoactive membranes containing 37 and 50% wt. OA/Fe_3O_4 obtained from solutions with 4% w/v polymer-solution concentration. The photographs in **figure 6.9 (c)** show the PEO/PLLA/OA.Fe_3O_4 magnetoactive membranes with 20 and 50% wt. of magnetic content, attached on a permanent magnet.

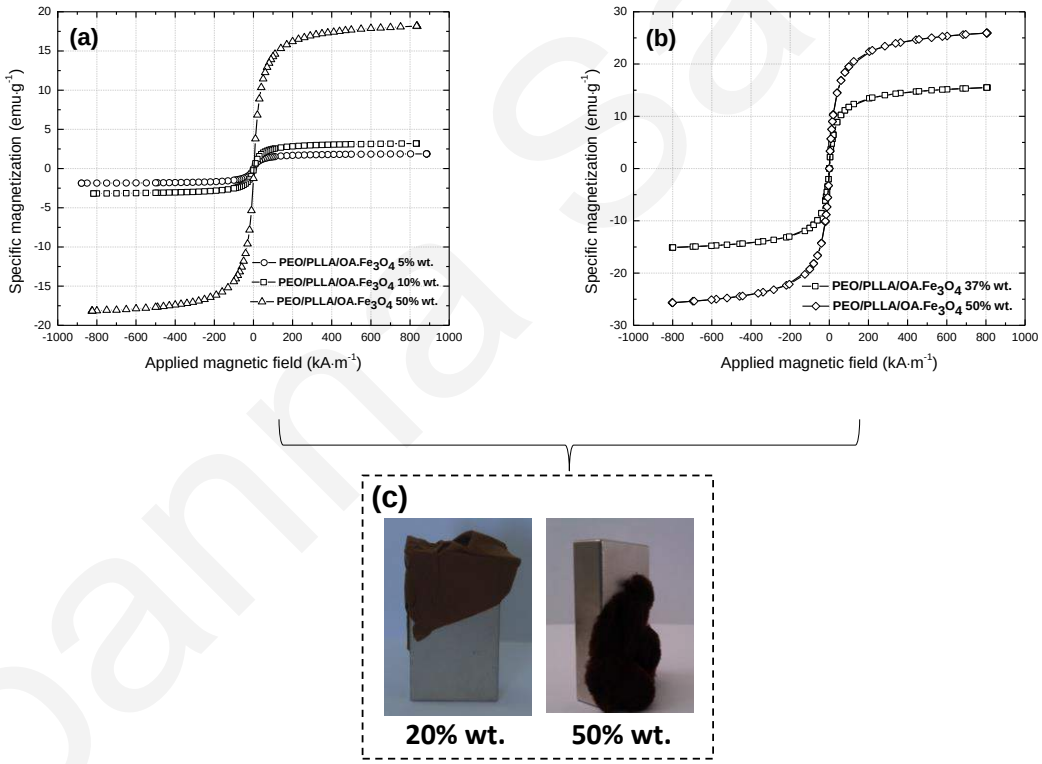

Figure 6.9: *PEO/PLLA-based magnetoactive membranes consisting of* ***(a)*** *OA/Fe_3O_4 with 5, 10, and 50% wt. prepared from solution with polymer-solution concentration of 2.5% w/v,* ***(b)*** *OA/Fe_3O_4 with 37 and 50% wt. prepared from solution with polymer-solution concentration of 4% w/v, measured at 300K, and* ***(c)*** *photographs show magnetoactive membranes with 50% wt. OA.Fe_3O_4 attached on a permanent magnet.*

6.1.3. Membrane applications

6.1.3.1. Biomedical applications

Drug delivery: Acetaminophen or paracetamol is a widely available analgetic and antipyretic drug soluble in organic solvents such as methanol and ethanol and slightly soluble in water. Its characteristics render it a very suitable compound for use in proof-of-principle drug release studies involving nanometric therapeutic platforms.

The drug release profile of acetaminophen was investigated in DPBS solution (pH 7.2), by means of UV-vis spectrophotometry, by recording the characteristic maximum absorption signal of the released drug appearing at ~ 243 nm at different time intervals. **Figure 6.10** depicts the UV-vis spectra **(figure 6.10 (a))** and the corresponding average absorption (at λ_{max} ~ 243 nm) *versus* time (A=*f*(t)) plot **(figure 6.10 (b))** for the PEO/PLLA/acetaminophen system after being immersed in DPBS aqueous solution. Upon immersing the membrane in the aforementioned solution and recording the UV-vis spectra of the solution at the indicated time intervals, a systematic increase in the absorption signal appearing at ~ 243 nm corresponding to the acetaminophen molecules released from the membrane has been observed. The absorption signal reached a plateau (~ 1 a.u.) after approximately 3 hours. By measuring the absorption of acetaminophen in DPBS aqueous solutions of known concentrations at the maximum absorption wavelength (~ 243 nm), and calculating the corresponding acetaminophen solution-concentration by following the Lambert-Beer Law **(equation 6.2)**,

$$A = \varepsilon \cdot l \cdot C \qquad \textbf{Equation 6.2}$$

where, A is the absorbance, ε is the molar extinction coefficient (absorbtivity) ($L \cdot mol^{-1} \cdot cm^{-1}$), l is the path length of the sample-that is, the path length of the cuvette in which the sample is contained (cm), and C is the concentration of the compound in solution ($mol \cdot L^{-1}$). It is possible to quantify the results presented in **figure 6.10 (c)** i.e. determine the exact concentration of the released drug at certain time, *via* the construction of the absorption *versus* concentration calibration curve (ε=81.4 $L \cdot g^{-1} \cdot cm^{-1}$). Based on the calibration curve, the concentration of the acetaminophen released at different time intervals was calculated and the corresponding concentration *versus* time plot is provided in **figure 6.10 (c)**.

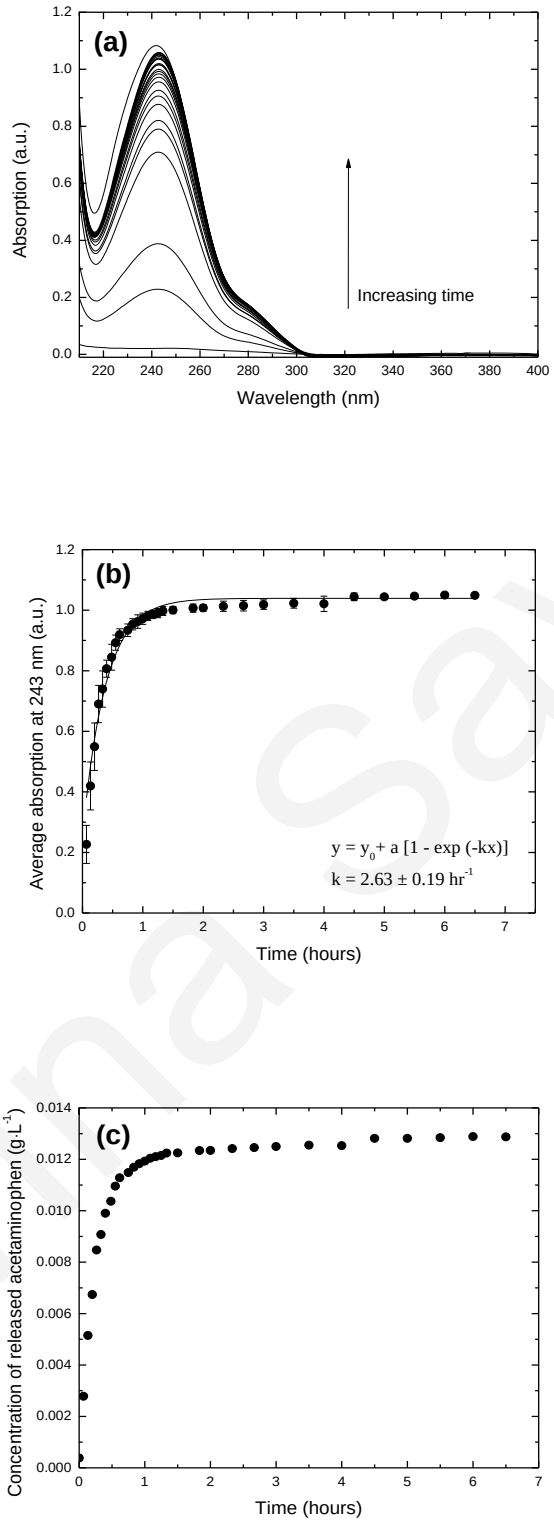

Figure 6.10: *Kinetic release studies of acetaminophen from the PEO/PLLA/acetaminophen membrane in DPBS solution (pH 7.2), at room temperature:* ***(a)*** *UV-vis spectra,* ***(b)*** *average absorption (at λ_{max} ~ 243 nm) versus time kinetic plot and* ***(c)*** *concentration versus time kinetic plot.*

According to the previous literature findings, upon blending the hydrophilic PEO with hydrophobic/biodegradable polymers such as PLLA, polycaprolactone (PCL) and poly(D,L-lactic-co-glycolic acid) (PLGA) of lower molecular weight (MW) compared to PEO, phase separation occurs between the hydrophilic and the hydrophobic domains (340). As a result, encapsulated pharmaceutical compounds are expected to be diffused out of the membranes upon dissolution of the PEO hydrophilic domains when the membranes are immersed in an aqueous medium. Additionally, the membrane erosion profile and consequently the drug release rate profile could be tuned accordingly, by varying the hydrophilic to the hydrophobic content within the membranes.

Figure 6.11 shows the SEM images of the drug-loaded PEO/PLLA membranes after a 3 months period of immersion in aqueous media. As revealed from the images, the presence of the highly water-soluble PEO within these materials resulted to significant morphological changes of the fibers upon hydration due to the dissolution of the PEO polymer chains.

PEO/PLLA/acetaminophen after being immersed in aqueous media

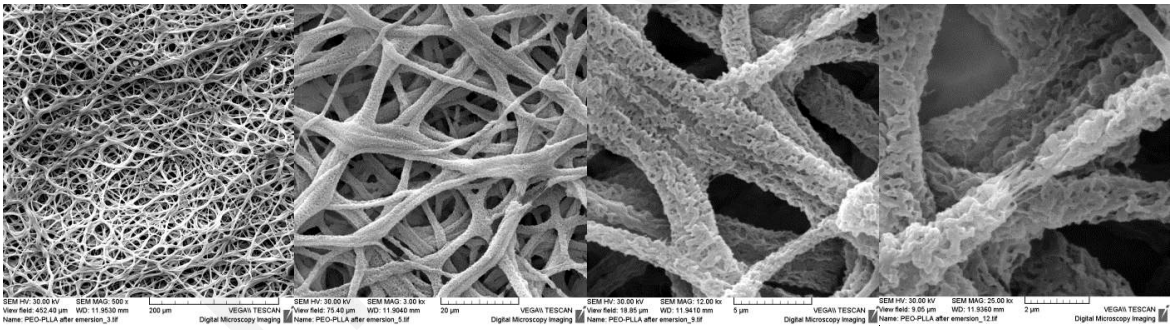

Figure 6.11: *SEM images of the PEO/PLLA/acetaminophen electrospun membrane after being immersed in DPBS aqueous solution for 3 months.*

The drug release profile was also investigated in the presence of magnetic OA.Fe_3O_4 NPs i.e. by using the PEO/PLLA/OA.Fe_3O_4/acetaminophen membranes as drug delivery platforms. A schematic presentation of the drug release process from the magnetoactive membranes, as well as the UV-vis spectra and corresponding average absorption and concentration *versus* time plots for the PEO/PLLA/OA.Fe_3O_4/acetaminophen systems are provided in **figure 6.12**. Moreover representative SEM images of the aforementioned systems recorded after 3 months of membrane immersion in DPBS aqueous solution are also provided. As in the case of the magnetite-free membranes, the presence of the highly

water-soluble PEO within these materials caused significant morphological changes of the membranes upon hydration **(figure 6.12 (b))**. Although such changes were more pronounced in the case of the magnetite-free PEO/PLLA analogues **(figure 6.11)**, the presence of magnetite rendered the membranes more fragile.

As in the case of the OA.Fe_3O_4-free PEO/PLLA membranes, the intensity of the characteristic absorption signal of acetaminophen appearing at ~ 243 nm increased with time, indicating drug release from the magnetoactive nanocomposite membranes. However, kinetic constants for the PEO/PLLA/acetaminophen ($k=2.63\pm0.19$ hr^{-1}) and the PEO/PLLA/OA.Fe_3O_4/ acetaminophen systems containing OA.Fe_3O_4 20 and 70% wt. ($k=1.68\pm0.07$ hr^{-1} and 0.92 ± 0.02 hr^{-1} respectively) revealed slower release rate in the presence of magnetite NPs. This negative effect on release kinetics may be attributed to the fact that the membrane becomes more hydrophobic due to the hydrophobic nature of the Fe_3O_4 surface at pH values below 8 (341) as well as the presence of the hydrophobic oleic acid chains, resulting to the deceleration of the hydration and thus dissolution of the PEO hydrophilic domains, and consequently to slower drug diffusion. To the best of our knowledge limited examples exist in literature, reporting on the use of polymer-based magnetoactive fibrous membranes as drug delivery systems. In those studies it has been concluded that the presence of the magnetic NPs within the membranes does not affect the drug release process and it is basically governed by the properties of the polymers matrix (342).

The fractional drug release was determined as the ratio of the actual concentration of the drug released as determined experimentally from **figures 6.10 (d)** and **6.12 (d)**, to the acetaminophen concentration considering complete drug release in solution. In the absence of magnetite, a relatively high drug percentage (~ 35 %) is retained within the PLLA insoluble phase of the membrane. This percentage was found to significantly decrease by increasing the magnetic content reaching ~ 5 % in the PEO/PLLA/OA.Fe_3O_4 membrane with the highest magnetic content (70% wt.). These results strongly suggest that in the absence of magnetite, reinforcement of hydrophobic interactions between acetaminophen and the PLLA regions of the membrane occurs resulting to a higher partition coefficient for acetaminophen with the PLLA fibers. On the contrary, in the presence of high magnetite content (which is retained within the PLLA fibrous areas, demonstrated by the absence of magnetite leaching in solution, as illustrated in photograph provided in **figure 6.12 (a)**), the PLLA-OA.Fe_3O_4 act competitively to the PLLA-acetaminophen hydrophobic interactions, causing the exclusion of the drug from the PLLA phase and therefore its

almost complete release. Moreover, these results may be explained in terms of reduced crystallinity of PLLA with the increase of the OA.Fe_3O_4 fraction (**figure 6.7)**, facilitating the drug diffusion, which is otherwise very slow due to its entrapment in the PLLA crystalline domains.

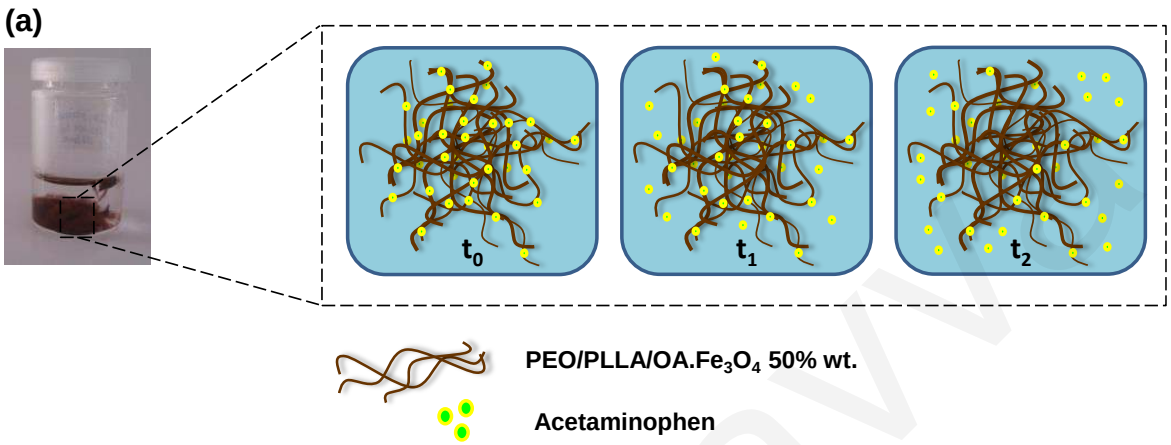

(b) PEO/PLLA/OA.Fe_3O_4 20% wt./acetaminophen after being immersed in aqueous media

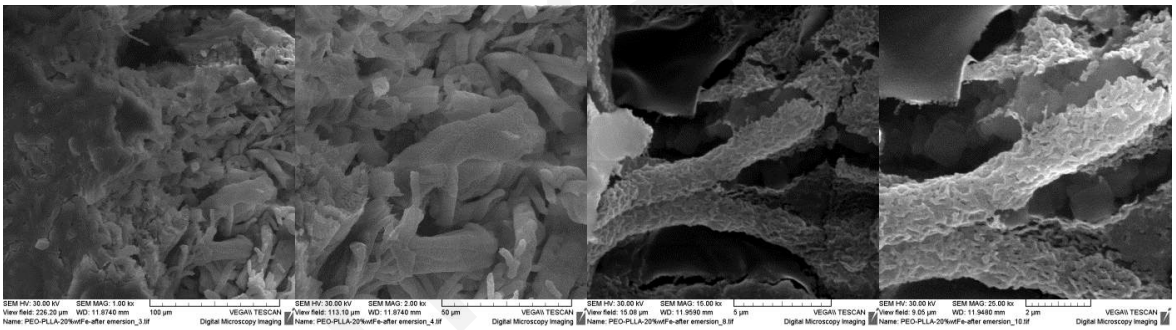

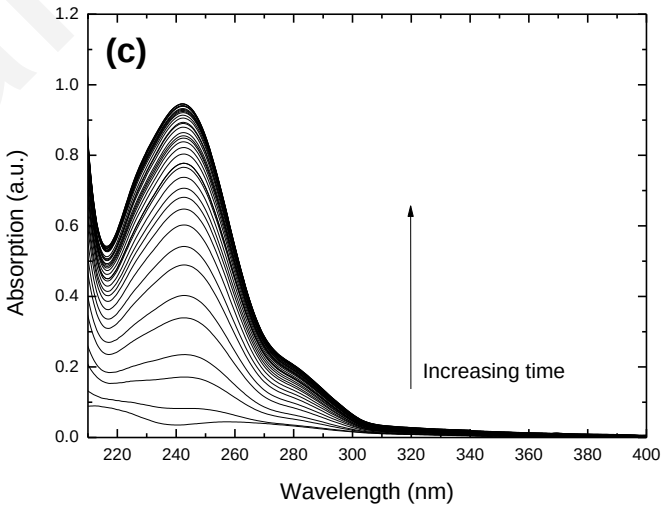

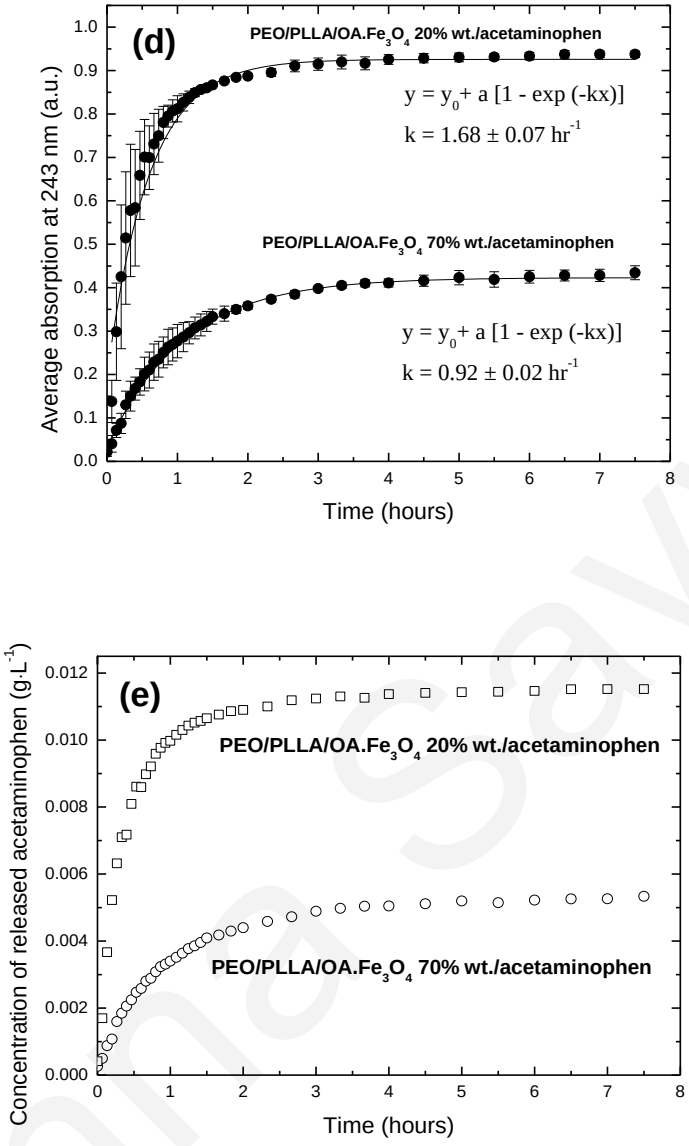

Figure 6.12: *Kinetic release studies of acetaminophen from the PEO/PLLA/OA.Fe_3O_4/acetaminophen membranes immersed in DPBS solution (pH 7.2), at room temperature:* ***(a)*** *Schematic presentation of the drug release process and photograph of the drug-loaded PEO/PLLA/OA.Fe_3O_4/acetaminophen membrane immersed in DPBS aqueous solution,* ***(b)*** *SEM images of the drug-loaded PEO/PLLA/OA.Fe_3O_4/acetaminophen membrane recorded after being immersed for 3 months in DPBS aqueous solution,* ***(c)*** *UV-vis spectra recorded at different time intervals upon immersing the PEO/PLLA/OA.Fe_3O_4 20% wt./acetaminophen membrane in DPBS aqueous solution,* ***(d)*** *corresponding average absorption (at λ_{max} ~ 243 nm) and* ***(e)*** *concentration versus time kinetic plots for the nanocomposite membranes containing OA.Fe_3O_4 20 and 70% wt.*

Figure 6.13 summarizes the drug release profiles demonstrated as A_t/A_∞ *versus* time normalized plots for the aforementioned release studies performed in DPBS. A_t denotes the

average absorption of the released drug at time t, and A_∞ the absorption corresponding to the maximum amount of the released drug.

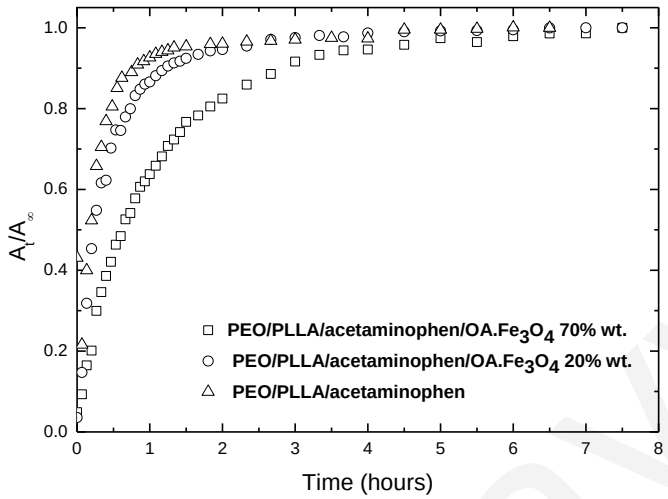

Figure 6.13: *Normalized A_t/A_∞ versus time plots of acetaminophen release studies performed in DPBS: PEO/PLLA/acetaminophen and PEO/PLLA/OA.Fe_3O_4/acetaminophen containing OA.Fe_3O_4 20 and 70% wt.*

The effectiveness of the PEO/PLLA/OA.Fe_3O_4 fibrous membranes as drug delivery systems was also assessed with acetaminophen release kinetics performed in complete culture media mimicking tissue culture conditions. **Figure 6.14** shows **(a)** the UV-vis spectra of all components of the media and **(b)** the absorption (recorded at ~ 243 nm) *versus* time (A=*f*(t)) plot corresponding to the release profile of acetaminophen from the nanocomposite membrane into the media. **Figure 6.15** summarizes the drug release profiles demonstrated as A_t/A_∞ *versus* time normalized plots for the PEO/PLLA/OA.Fe_3O_4 20% wt./acetaminophen recorded in DPBS and in MEDIA.

The kinetic constant determined for the release rate in the complete media (k=0.93±0.007 hr^{-1}) has been statistically lower than the release rate in DPBS solution. The high concentration of protein in the FCS present in complete media is expected to form a well-defined corona around the magnetite NPs. Direct interaction of protein, antibiotics and additives of complete media with the drug phase could further contribute to this finding. Media pH throughout the measurements was 7.5, which is very close to the pH of the DPBS solution. Therefore, it is not expected that this small difference would affect release

kinetics especially since acetaminophen remains neutral (free of charge) in the pH range 1-8 and becomes ionized (its phenol group -OH) and more hydrophilic at higher pHs.

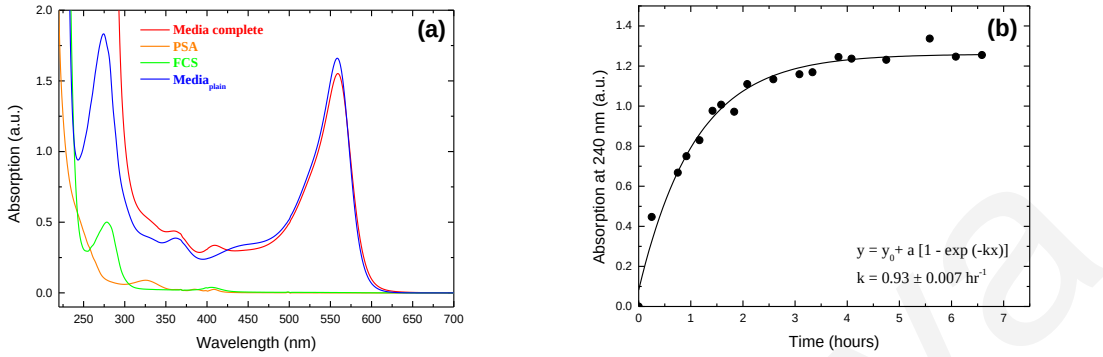

Figure 6.14: (a) *UV-vis Spectra of MEDIA$_{complete}$ consisting of 10% FCS and 1% PSA, DMEM$_{plain}$, FSC, and PSA dissolved in PBS* ***(b)*** *kinetic release study of acetaminophen from the PEO/PLLA/OA.Fe$_3$O$_4$ 20%wt. acetaminophen membrane in complete media at room temperature.*

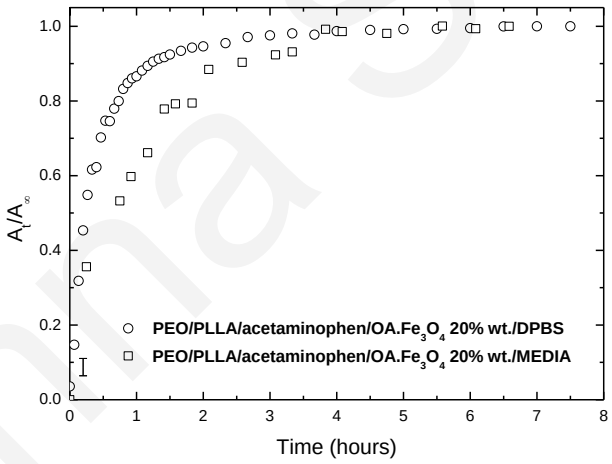

Figure 6.15: *Normalized A_t/A_∞ versus time plots of the PEO/PLLA/OA.Fe$_3$O$_4$ 20% wt./acetaminophen recorded in DPBS and in MEDIA.*

Magnetic hyperthermia: The PEO/PLLA/OA.Fe_3O_4 magnetoactive nanocomposite membranes were also evaluated toward their ability to release heat when subjected to an alternating (AC) magnetic field. The heating ability of the magnetoactive membranes is expressed in terms of specific adsorption rate (SAR), and it is calculated using the **equation 6.3**:

$$SAR = \frac{\left[C_{water} \cdot V_s \cdot \frac{dT}{dt}\right]}{m_{Fe_3O_4}}$$ **Equation 6.3**

where, C_{water} is the specific heat capacity of water (4.185 $J \cdot L^{-1} \cdot K^{-1}$), V_s the volume of the sample (1 mL), m_{Fe3O4} is the mass of the magnetic material in the studied sample (mg) and (dT/dt) is the temperature ramp rate in $K \cdot min^{-1}$. The SAR values (Watts per gram of magnetic material Fe_3O_4) were obtained by fitting the experimental heating curves (temperature *versus* time).

In general, the heating ability of the magnetic NPs depends on the nature and morphology of the particles and their volume fraction. SAR reflects the magnitude of heat dissipation from magnetic NPs to the surrounding medium, which depends not only on the properties of the particles themselves, but also on external factors such as the magnitude (H) and frequency (ν) of the AC magnetic field as shown in **equation 6.4** (206):

$$SAR = 4.1868\ \pi\ {\mu_0}^2\ \frac{\varphi M_s V}{1000kT}\ {H_0}^2 \nu\ \frac{2\pi\nu\tau}{(1+2\pi\nu\tau)^2}$$ **Equation 6.4**

where, φ is the volume fraction of the superparamagnetic material, M_s the specific magnetization, ν is the frequency of the oscillating magnetic field, H_o is the magnetic field intensity, μ_o the vacuum permeability and τ is the relaxation time (Néel and Brownian) of the magnetic NPs. In an attempt to compare results performed under different magnetic field intensity and frequency, another index has been recently proposed (343; 344) to compare several commercially available magnetic NPs, namely intrinsic loss power (ILP). ILP can be easily calculated according to the **equation 6.5**,

$$ILP = \frac{SAR}{H^2 \cdot \nu}$$ **Equation 6.5**

where, SAR is measured in $W \cdot Kg^{-1}$, field strength H in $kA \cdot m^{-1}$ and the frequency ν in kHz.

Figure 6.16 displays the temperature rise over time whereas the calculated SAR and ILP values of the magnetoactive membranes in concentrations of 10, 20, 40 and 100 $mg \cdot mL^{-1}$ in magnetic material (Fe_3O_4) are provided in **table 6.2**. The observed heating of the magnetoactive membranes at a frequency of 110 kHz (magnetic field of 25 mT) was relatively low, even at high concentrations of 100 $mg \cdot mL^{-1}$ in magnetic material. ILP values for commercial ferrofluids have been reported (343) in the range 0.2-3.1 $nHm^2 \cdot Kg^{-1}$. The current membranes display relatively low ILP in comparison to the commercial

ferrofluids. These findings correspond well with the theoretical and experimental data reported by Fortin *et al*. relating small nanocrystallite size to low ILP values (345). It appears that the very small diameter of the NPs (5 nm) and their low M_s determined by VSM result to lower SAR values. It should be also emphasized at this point that the inclusion of the magnetic NPs within the fibrous polymer matrix, prevents them from relaxing through Brownian motion. Therefore, the term $2\pi\nu\tau/(1+2\pi\nu\tau)^2$ in equation (6.2) decreases, leading to smaller SAR values.

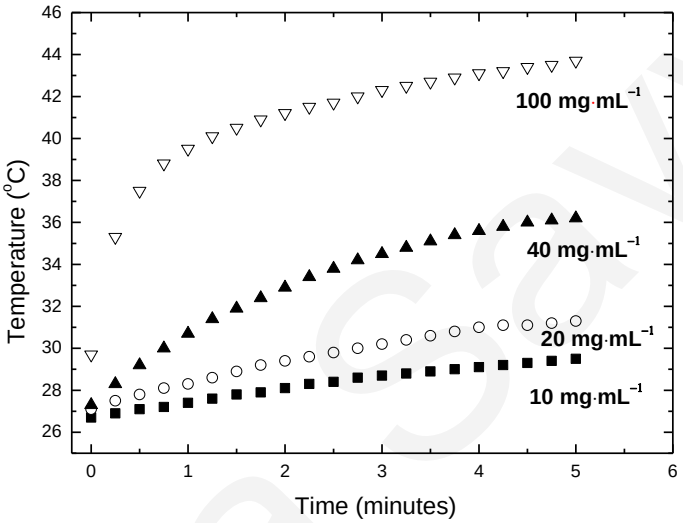

Figure 6.16: *Time – dependent temperature curves of the magnetoactive membranes at various concentrations of magnetic material (Fe_3O_4) at 110 kHz frequency and 25 mT magnetic field.*

Table 6.2: *SAR and ILP values as a function of concentration of magnetic material Fe_3O_4.*

Concentration ($mg \cdot mL^{-1}$)	**SAR ($W \cdot g^{-1}_{Fe3O4}$) [($W \cdot g^{-1}_{Fe}$)]**	**ILP ($nHm^2 \cdot kg^{-1}_{Fe3O4}$) [($nHm^2 \cdot kg^{-1}_{Fe}$)]**
10	5.58[8.50]	0.128[0.20]
20	5.58[8.50]	0.128[0.20]
40	6.98[10.64]	0.160[0.26]
100	15.62[23.80]	0.369[0.56]

In summary, the novel PEO/PLLA/OA.Fe_3O_4 electrospun fibrous membranes demonstrating tunable superparamagnetic behavior at temperatures suitable for biological applications, have been evaluated in drug delivery and magnetic hyperthermia processes.

Drug release kinetic profiles of the widely used phenolic pharmaceutical acetaminophen disclosed the presence of OA.Fe_3O_4 and the protein content of the release medium as critical parameters for the drug release rate. The above-mentioned magnetoactive fibrous nanocomposites were also successfully tested for the induction of hyperthermia through AC magnetic field.

The tunability of the degradation time window endowed by the different combinations of biocompatible and biodegradable polymers can enable the achievement of the desirable release profile of specific pharmaceuticals for pre-defined therapeutic applications. Additionally, in combination with a profound superparamagnetic potential, these platforms provide promising tools for future exploitation in hyperthermia treatment and in magnetothermally triggered drug delivery.

6.1.3.2. Environmental applications

Adsorption studies for the removal of Eu(III), Th(IV), and U(VI) heavy metal ions from aqueous media: Europium (Eu) belongs to the lanthanide series with electron configuration $1s^2\ 2s^2\ 2p^6\ 3s^2\ 3p^6\ 4s^2\ 3d^{10}\ 4p^6\ 5s^2\ 4d^{10}\ 5p^6\ 6s^2\ 4f^7$ ([Xe] $6s^2\ 4f^7$). Europium has no significant biological role and is relatively non-toxic compared to other heavy metals. Uranium (U) and Thorium (Th) are silvery-white metallic, naturally occurring radioactive chemical elements in the actinide series of the periodic table with electron configuration $1s^2\ 2s^2\ 2p^6\ 3s^2\ 3p^6\ 4s^2\ 3d^{10}\ 4p^6\ 5s^2\ 4d^{10}\ 5p^6\ 6s^2\ 4f^{14}\ 5d^{10}\ 6p^6\ 7p^2\ 5f^4$ ([Rn] $5f^3\ 6d^1\ 7s^2$) and $1s^2\ 2s^2\ 2p^6\ 3s^2\ 3p^6\ 4s^2\ 3d^{10}\ 4p^6\ 5s^2\ 4d^{10}\ 5p^6\ 6s^2\ 4f^{14}\ 5d^{10}\ 6p^6\ 6d^2\ 7s^2$ ([Rn] $6d^2\ 7s^2$) for the U and Th respectively.

Europium-based systems are of special interest for optical excitation and emission studies because they exhibit high luminescent quantum efficiencies (346). The principal hydrolytic complex in acidic solutions of Eu^{3+} is thought to be $[Eu(OH)]^{2+}$, although the cation appears to resist hydrolysis when the pH remains below 5-6. A precipitate of $Eu(OH)CO_3^-$ or $Eu(OH)_3$, generally forms when the pH of solutions containing Eu(III) ions exceeds ~ 6 (347; 348; 349). The chemical behaviour of uranium in aqueous solutions, particularly of hexavalent uranium, is governed by hydrolysis, complexation with naturally occurring ligands, colloid generation and solid phase formation (350). Thorium exists only in the tetravalent state and is capable of forming both monomeric and polymeric hydrolysis products, which govern the chemical behavior of Th(IV) in aqueous

solutions. Th(IV) hydrolysis starts at pH 2 and results eventually in the formation of the very stable $Th(OH)_{4(s)}$ species that limits the thorium(IV) solubility even in the acidic pH range.

Because of their toxicity, radionuclides such as uranium and thorium even at trace levels are considered to be a major public health concern. Therefore the selective and effective removal of such elements from contaminated environmental compartments (e.g. soils, waters), is of great interest, particularly for the nuclear technology. Nanoscale fibers exhibit a large surface area, which results in high separation efficiency. Very recently, electrospun membranes have been successfully used for the removal of heavy metal ions from aqueous solutions (294). In addition, efficient recovery of rare earth elements (REE) from large quantities of processing solutions and industrial wastewaters is of particular importance to protect the environment and cover the continuously increasing global demand for REE, which find wide application in green and sustainable products for energy and manufacturing uses.

For the first time in the present work, fibrous PEO/PLLA-based electrospun membranes have been evaluated as substrates for the adsorption of trivalent europium (Eu(III)), tetravalent thorium (Th(IV)), and hexavalent uranium (U(VI)) (351). Experiments on the effect of pH, ionic strength and initial metal ion concentration on the separation efficiency were performed to investigate possible pH-triggered selectivity, understand possible interaction mechanisms and evaluate the adsorption capacity of the membranes.

Regarding the morphological characteristics of the membranes prior to their immersion in the metal ion-containing aqueous media, the PEO/PLLA electrospun mats exhibited a cylindrical shape and a relatively high homogeneity with mean diameters of approximately 3 μm **(figure 6.2 (d))**, while after immersion some morphological changes were observed as seen in **figure 6.17 (a)** due to membrane hydration resulting to the dissolution of the highly hydrophilic PEO polymer chains.

(a) PEO/PLLA after being immersed in U(VI)-containing aqueous media at different pHs

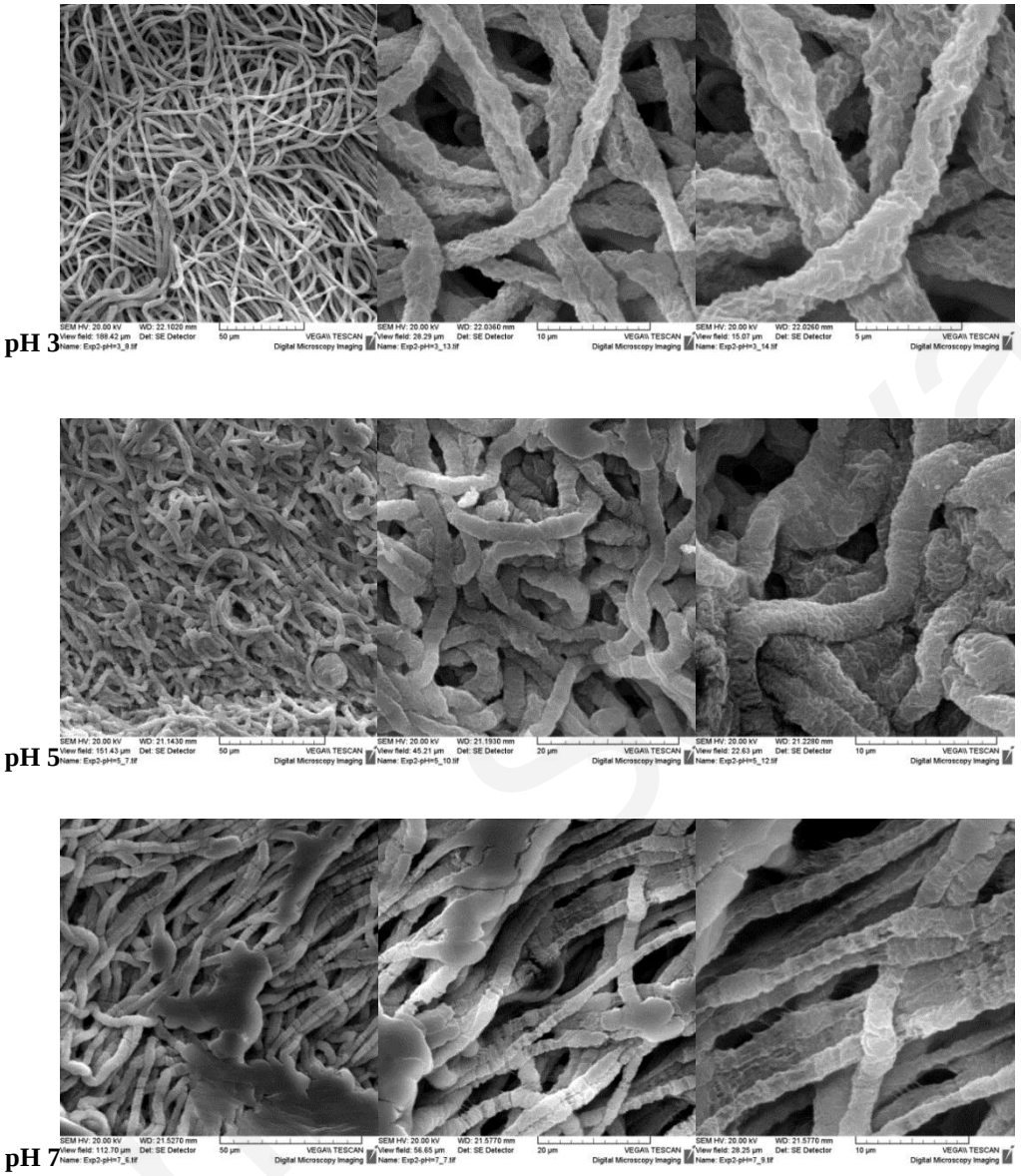

(b) PEO/PLLA after being immersed in Eu(III)-containing aqueous media

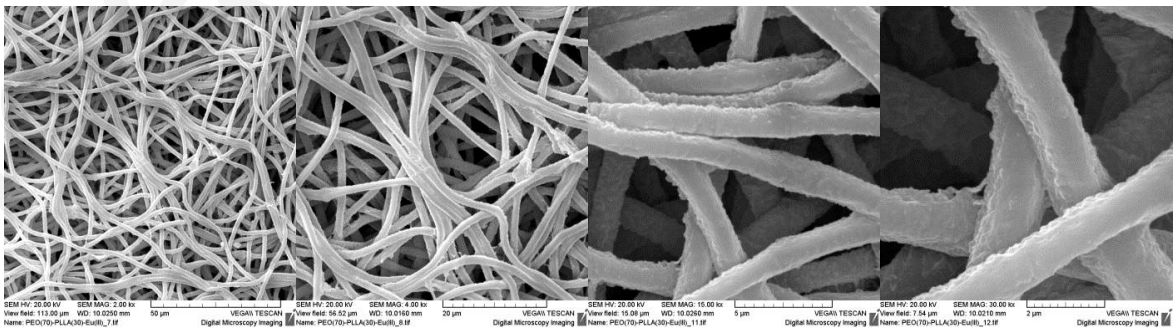

Figure 6.17: (a) *PEO/PLLA fibrous electrospun membranes after being immersed in aqueous/electrolyte uranium media with final pH 3, 5, and 7,* ***(b)*** *PEO/PLLA fibrous electrospun membranes after being immersed in aqueous/electrolyte europium media.*

With known parameters including the mass of the adsorbent, ($m_{adsorbent}$=10 mg), the solution volume (V_{sln}=3 mL), the metal ion initial solution concentration ($C_{0(Eu(III))}=1\cdot10^{-5}$, $C_{0(Th(IV))}=7\cdot10^{-6}$, $C_{0(U(VI))}=1\cdot10^{-3}$M), the temperature (T=25 °C), the time (t=24 hours) and the ionic strength (I=0.1 M), the remaining metal ion concentration in solution at equilibrium (C_e) was determined, by recording the UV-vis absorption spectra of the supernatant and calculating the corresponding metal ion solution concentration by following the Lambert-Beer Law **(equation 6.2)**, *via* the construction of the absorption (at 650 nm) *versus* metal ion solution concentration calibration curve.

The molar extinction coefficient ε of the Eu(III)-Arz(III), U(VI)-Arz(III) and Th(IV)-Arz(III) complex at 650 nm determined from the corresponding calibration curves was $\varepsilon_{Eu(III)}$=(87500±500), $\varepsilon_{U(VI)}$=(48000±300) and $\varepsilon_{Th(IV)}$=(28500±100) $L\cdot mol^{-1}\cdot cm^{-1}$, respectively. **Figure 6.18** shows the UV-vis spectra of the three aforementioned metal ion-Arz(III) complexes.

The amount of metal ions adsorbed on the membranes (q_e) and the % removal efficiency (% q_e) were calculated using **equations 6.6 and 6.7**.

$$q_e = \frac{(C_0 - C_e)}{W} \cdot V \qquad \textbf{Equation 6.6}$$

$$\%q_e = \frac{(C_0 - C_e)}{C_0} \cdot 100 \qquad \textbf{Equation 6.7}$$

q_e ($mol\cdot Kg^{-1}$) is the amount of metal ion adsorbed onto the unit amount of the adsorbent, C_0 ($mol\cdot L^{-1}$) is the initial metal ion concentration, C_e ($mol\cdot L^{-1}$) corresponds to the equilibrium concentration of metal ions in solution, V (L) is the solution volume and W (g) is the adsorbent (membrane) mass.

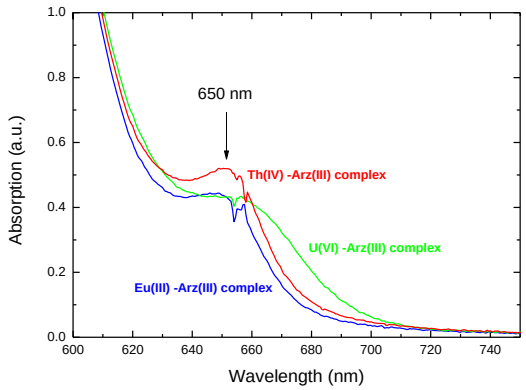

Figure 6.18: *UV-vis spectra of the Eu(III)-Arz(III), U(VI)-Arz(III), and Th(IV)-Arz(III) complexes.*

As previously noted the effect of the initial concentration, pH, and ionic strength on the metal ion adsorption efficiency of the membranes was studied. The effect of pH on the relative adsorption of Eu(III), Th(IV), and U(VI) by the PEO/PLLA fibrous membranes is shown in **figure 6.19.**

For Th(IV) the investigations have been performed up to pH 3 because above this pH hydrolysis results in precipitation, which becomes predominant and interferes with adsorption. In order to focus on adsorption and have a well-defined system with unambiguous data evaluation, the adsorption of Th(IV) on the fibrous membrane has been studied for pH $\leq$ 3. According to the graph presented in **figure 6.19**, the relative adsorption of Th(IV) increases with increasing pH and reaches a value of 90±10% at pH 3. This is a relatively high value, which is (to the best our knowledge) for the first time described for Th(IV) adsorption at such low pH and can be attributed to the high affinity of the PEO/PLLA membrane for Th(IV). A schematic illustration of the Th(IV) binding by the membrane active moieties is provided in **scheme 6.1**. The proposed binding mode of Th(IV) by the ester groups is based on literature data (352; 353).

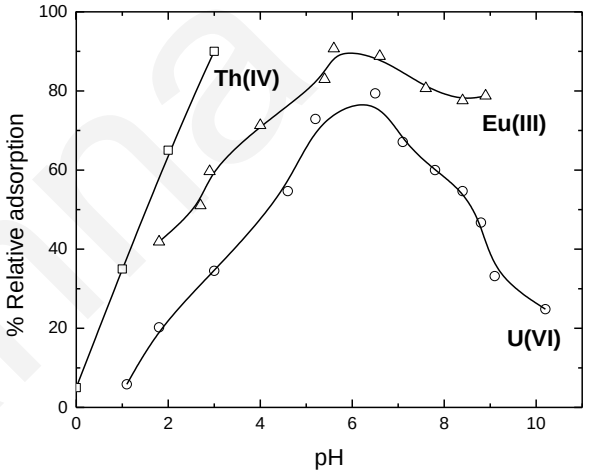

Figure 6.19: *The effect of pH on the relative adsorption of Eu(III), Th(IV), and U(VI) by the PEO/PLLA fibrous membrane.*

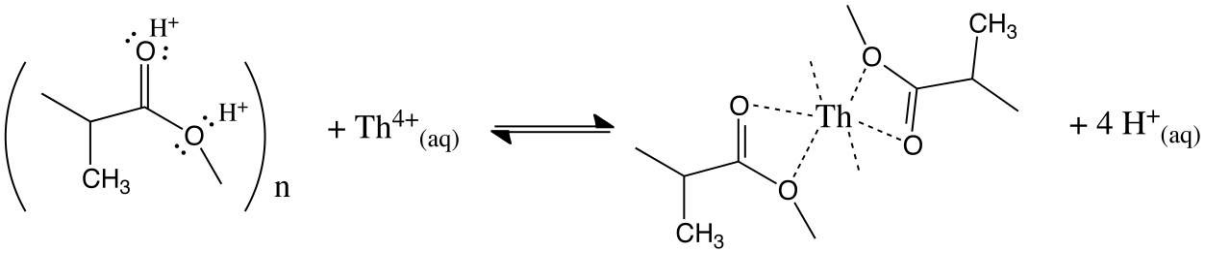

Scheme 6.1: *Th(IV) binding by the membrane active ester moieties present on the PLLA chains.*

The relative adsorption of U(VI) increases with increasing pH and reaches a maximum value (80±10%) at pH ~ 6. Above pH 6 the relative adsorption of U(VI) decreases reaching a value of ~ 20 % at pH 10. For pH values below 6 the relative adsorption decreases with pH decreasing. For pH < 6 the hydrogen ion concentration increases steadily and the hydrogen ions compete effectively the adsorption of the U(VI) species by the active moieties of the membrane, resulting in a lower adsorption efficiency. At concentration below 10^{-5} M and in the acidic pH range UO_2^{2+} and UO_2OH^+ are the dominating U(VI) species in solution (354; 350). The proposed binding mode of U(VI) by the membrane is shown in **scheme 6.2** (355).

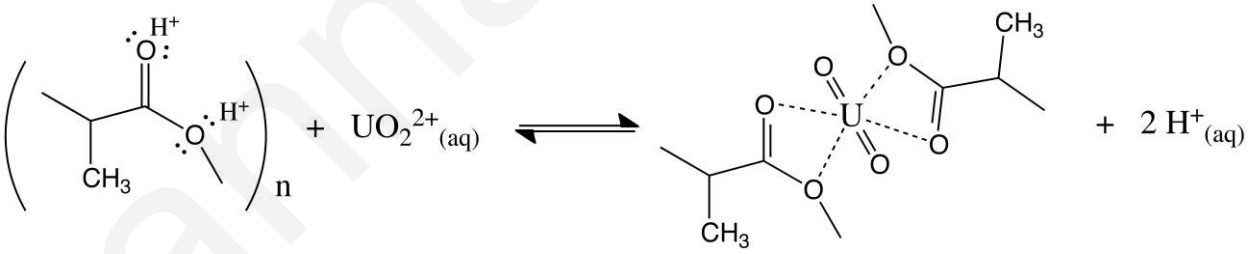

Scheme 6.2: *U(VI) binding by the membrane active ester moieties present on the PLLA chains.*

Above pH 6, carbonate concentration in solution increases dramatically favouring the formation of U(VI) carbonate complexes (e.g $UO_2(CO_3)_2^{2-}$), which stabilize U(VI) in solution and result in the destabilization of surface adsorbed species (**scheme 6.3**). Similar trends have been also reported by other researchers (356; 357; 358). The proposed biding mode of Eu(III) ion by the membrane is illustrated in **scheme 6.4**.

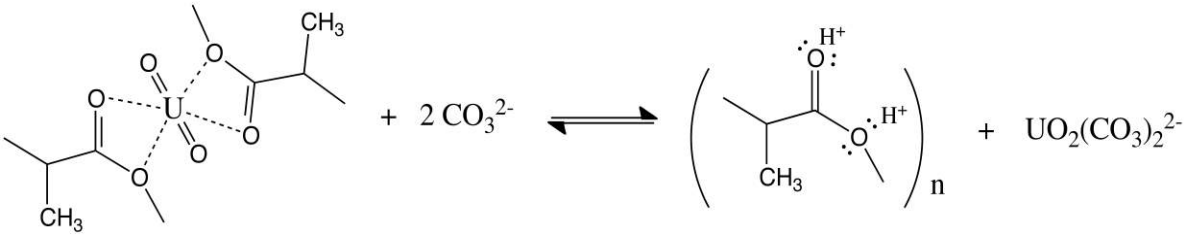

Scheme 6.3: *The formation of the U(VI) carbonate complexes.*

The relative adsorption of Eu(III) increases with increasing pH and reaches a maximum value (90±10%) at pH ~ 6. Above pH 6 the relative adsorption of Eu(III) decreases slightly reaching a value of ~ 80 % at pH 7 where it remains stable. For pH above 6.5 carbonate concentration in solution increases dramatically favouring the formation of Eu(III) carbonate complexes (e.g. $EuCO_3^+$, $Eu(CO_3)_2^-$), which stabilize Eu(III) in solution (359). The complex formation between the ester group of PLLA and Eu(III) is shown in **scheme 6.4**.

The high affinity of the PEO/PLLA electrospun membrane for Th(IV) at pH 3 and the significantly lower adsorption efficiency of the membrane for Eu(III) and U(VI) at the same pH could be utilized for a pH-triggered, selective removal of Th(IV) from acidic process solutions, containing those free elements.

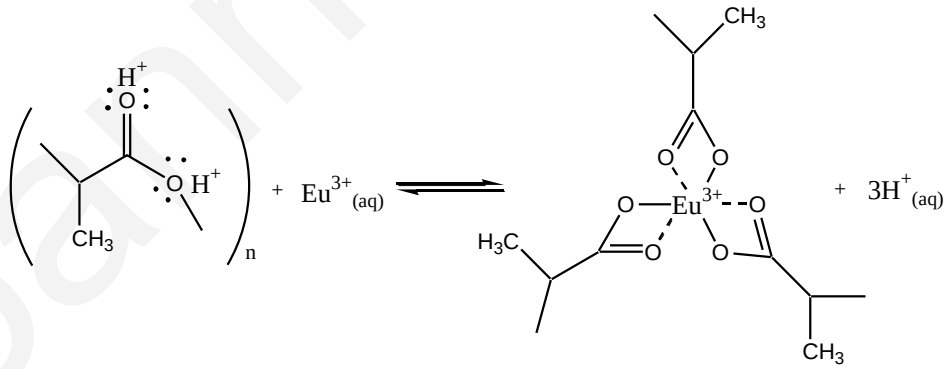

Scheme 6.4: *Eu(III) binding by the membrane active ester moieties present on the PLLA chains.*

Figure 6.20 shows the effect of ionic strength (I = 0.01, 0.1 and 1 M) on the relative adsorption efficiency of the fibrous membranes for Th(IV), and U(VI) at pH 3. A comparison of the data obtained from experiments at different ionic strength does not show any significant effect of this parameter on the adsorption efficiency of the membrane

for both actinide ions, indicating the development of specific interactions between the actinide ions and the active moieties of the membrane that eventually result in the formation of inner-sphere complexes (360; 355). This result is of particular interest since the membrane may also bind selectively the actinide ions in saline media.

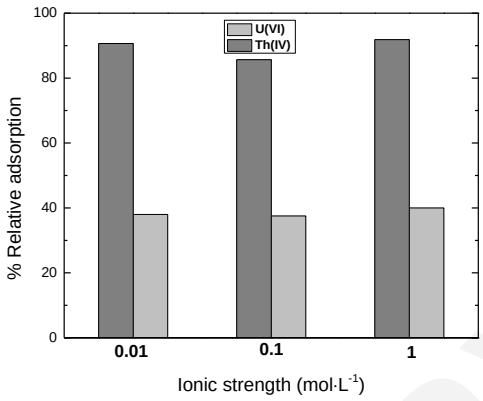

Figure 6.20: *The effect of ionic strength on the relative adsorption of Th(IV) and U(VI) by the fibrous PEO/PLLA electrospun membranes.*

Finally, in order to evaluate the maximum adsorption capacity (q_{max}) of the electrospun membranes, adsorption experiments with various Eu(III), Th(IV), and U(VI) initial solution concentrations have been performed at optimum pH (3 for Th(IV), 6.5 for Eu(III) and 6 for U(VI)) retaining the other parameters the same ($m_{adsorbent}$=10 mg, V_{sln}=3 mL, T=25 °C, t=24 hours, I=0.1 M). The corresponding experimental data, which are graphically shown in **figure 6.21** are well-fitted by the Langmuir isotherm. This empirical model assumes that the adsorption takes place at a finite number of homogeneous sites on the surface of the adsorbent until monolayer formation (361).

The Langmuir isotherm model is described by the following equations:

$$q_e = \frac{q_{max} \cdot K_d \cdot C_e}{1 + K_d \cdot C_e} \qquad \textbf{Equation 6.8}$$

$$\frac{1}{q_e} = \frac{1}{q_{max} \cdot K_d \cdot C_e} + \frac{1}{q_{max}} \qquad \textbf{Equation 6.9}$$

where, C_e ($mg \cdot L^{-1}$) is the equilibrium concentration, q_e ($mg \cdot g^{-1}$) is the amount of metal ions adsorbed at equilibrium per unit mass of adsorbent, q_{max} ($mg \cdot g^{-1}$) is the maximum

adsorption at monolayer coverage and K_d ($L \cdot mg^{-1}$) is the Langmuir adsorption equilibrium constant that reflects the adsorption energy.

The Langmuir adsorption isotherms expressing the relationship between q_e *versus* the remaining metal ion concentration in solution at equilibrium (C_e), as well as the linearized $1/q_e$ *versus* $1/C_e$ isotherms corresponding to the Eu(III), Th(IV), and U(VI) metal ion adsorption by the PEO/PLLA membranes are provided in **figure 6.21 (a)** and **(b)** respectively. q_e was calculated using **equation 6.8**, whereas q_{max} and K_d could be calculated from the slope ($1/q_{max} \cdot K_d$) and the intercept ($1/q_{max}$) (**equation 6.9)** of the linearized plots. The experimental results support the formation of inner-sphere complexes with a q_{max} value of ~ 6.5, ~ 10.5, and ~ 4.5 $mmol \cdot kg^{-1}$ for Eu(III), Th(IV) and U(VI), respectively.

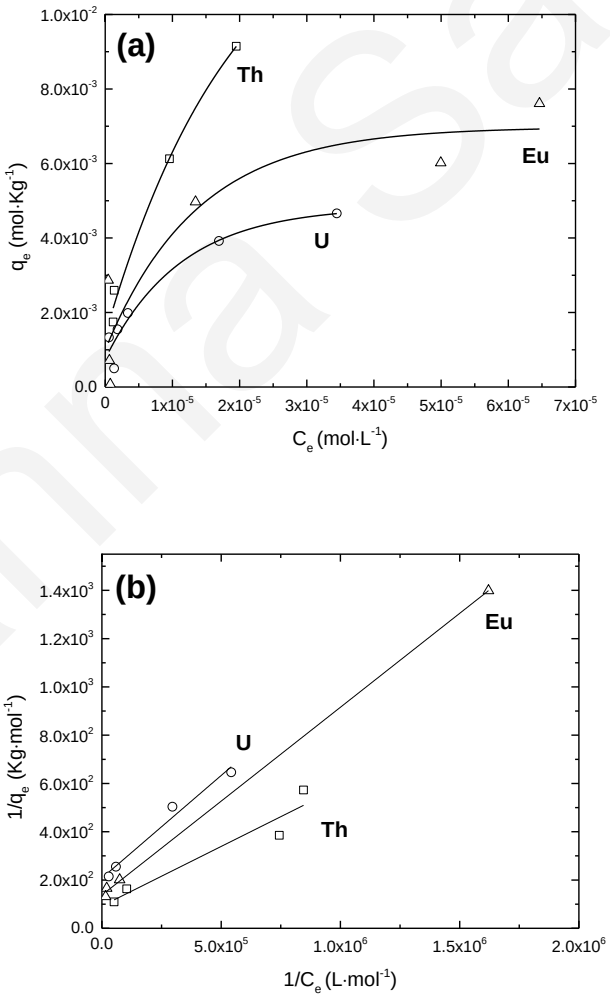

Figure 6.21: (a) *q_e versus C_e and* ***(b)*** *linearized $1/q_e$ versus $1/C_e$ Langmuir isotherms corresponding to the Eu(III), Th(IV), and U(VI) metal ion adsorption by the PEO/PLLA membranes.*

Adsorption studies for the removal of malachite green (MG) from aqueous media: Microfibrous electrospun membranes of the type PEO/PLLA and PEO/PLLA/OA.Fe_3O_4 were further evaluated as adsorbents for one of the most common synthetic organic dyes namely malachite green (MG) (***N*-methylated diaminotriphenylmethane dye**) **(figure 6.22)** from aqueous media (362). MG is widely used in the textile, paper, paint and ink industries. However, despite its wide use, MG represents a risk to human health due to its adverse effects on the immune and reproductive systems, carcinogenic, genotoxic, mutagenic and teratogenic properties (363).

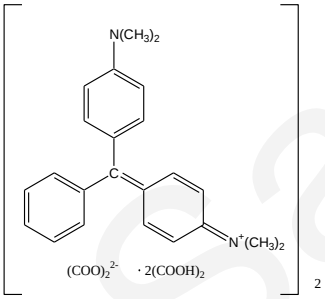

Figure 6.22: *Chemical structure of malachite green oxalate:* ***N-methylated diaminotriphenylmethane dye.***

An in-depth investigation of the membrane efficacy for the removal of MG from aqueous solutions was carried out. More precisely, the effect of various parameters including the pH, the initial dye concentration and the membrane magnetic content on the adsorption capacity of the membranes has been investigated in the absence and presence of magnetite NPs. Moreover, the change in free energy (ΔG^0), enthalpy (ΔH^0) and entropy (ΔS^0) were determined from adsorption experiments carried out at different temperatures.

Regarding the morphological characteristics of the membranes prior to immersion in aqueous MG solution, the PEO/PLLA magnetite-free **(figure 6.2 (d))** and nanocomposite **(figure 6.3 (h))** fibers exhibited a cylindrical shape and a relatively high homogeneity with mean diameters of approximately 3 μm. After immersion some morphological changes occurred as seen in **figure 6.23.** Notably, due to hydration/degradation phenomena after a year the magnetite-free fibers appeared to be thinner in diameter while retaining their cylindrical morphology (**figure 6.23 (b)**). On the other hand, the magnetite-containing analogues exhibited higher resistance to hydration/degradation (**figure 6.23 (c)**). This

phenomenon is probably attributed to the fact that the OA.Fe_3O_4-containing (50% wt.) membranes are more hydrophobic in nature, due to the hydrophobicity of the Fe_3O_4 surface at pH values below 8 (341) as well as the presence of the hydrophobic oleic acid chains surrounding the Fe_3O_4 NPs. Consequently, membrane hydration is prohibited or a least decelerated in the presence of OA.Fe_3O_4 (151). However, it has been observed that the magnetite-containing membranes with magnetic content exceeding 50% wt. demonstrated inferior mechanical properties compared to the magnetite-free analogues after immersion as seen in **figure 6.23 (a).** This may be attributed to the fact that upon increasing the nanoparticle content their dispersion in the polymer matrix is worsened whereas nanoparticle agglomeration phenomena may be promoted, resulting to the generation of stress concentration points that in turn lead to reduced mechanical properties.

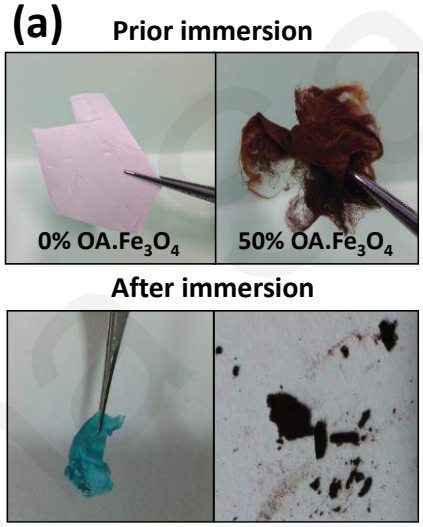

(b) PEO/PLLA after being immersed in aqueous MG media

After a month

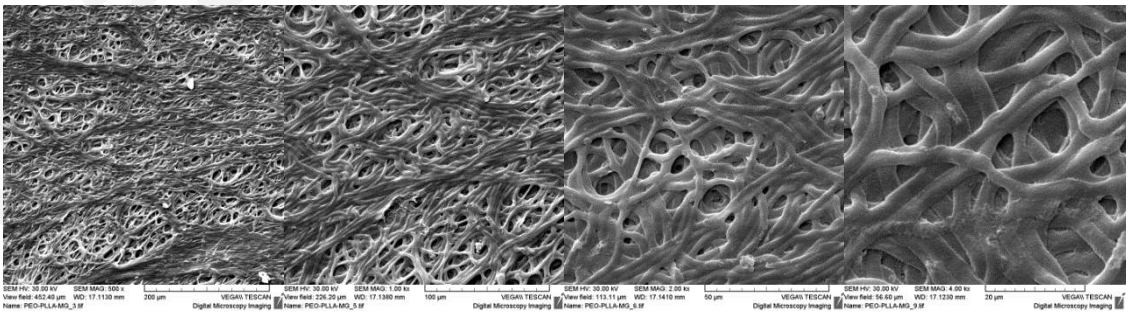

After a year

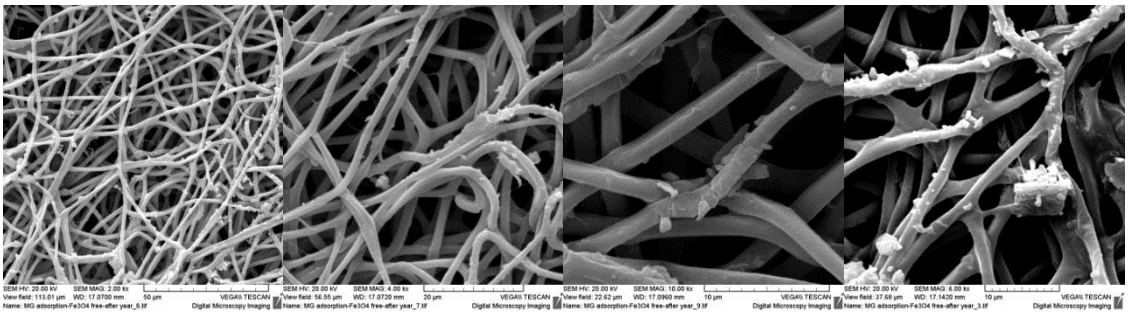

(c) PEO/PLLA/OA.Fe_3O_4 50% wt. after being immersed in aqueous MG media

After a month

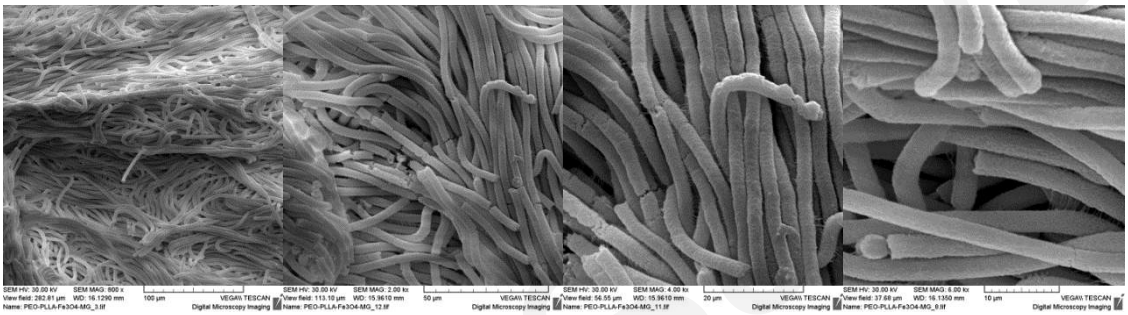

After a year

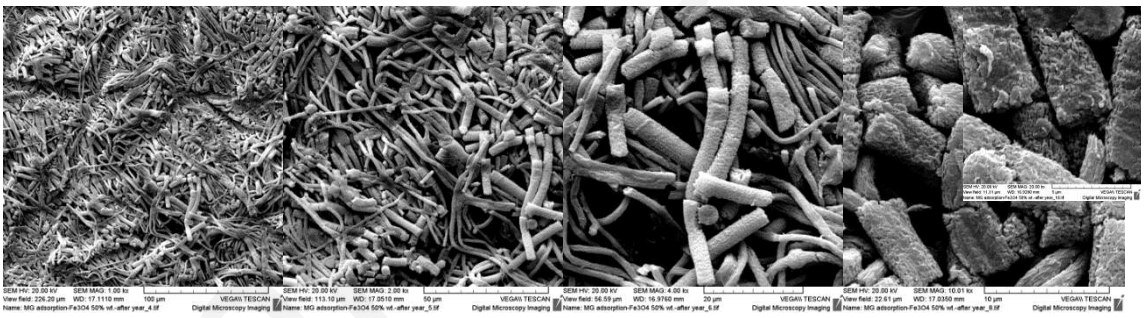

Figure 6.23: (a) *Photographs of the membranes prior and after immersion in MG media,* ***(b)*** *PEO/PLLA and* ***(c)*** *PEO/PLLA/OA.Fe_3O_4 50% wt. fibrous membranes after being immersed in aqueous MG media.*

In order to investigate the effect of contact time on membrane adsorption efficiency, the MG kinetic adsorption profile was recorded upon immersing the PEO/PLLA and the PEO/PLLA/OA.Fe_3O_4 membranes in a MG aqueous solution of known concentration ($C_0=1\cdot10^{-5}$ M) and recording the UV-vis spectrum of the supernatant at different time intervals.

Figure 6.24 provides a schematic presentation of the MG adsorption process by the membranes and photographs of the MG aqueous solutions in which the PEO/PLLA **(a)** and the PEO/PLLA/OA.Fe_3O_4 **(b)** dye adsorbents were immersed. As seen in the photographs,

the MG-containing wastewater changed to be almost colorless in the case where the PEO/PLLA membrane was used as an adsorbent, whereas fading of the color was also observed when the OA.Fe_3O_4-containing membrane was introduced instead. These results demonstrated that both, the PEO/PLLA and the PEO/PLLA/OA.Fe_3O_4 microfibrous materials could act as effective adsorbents (to a different extent) of MG from water.

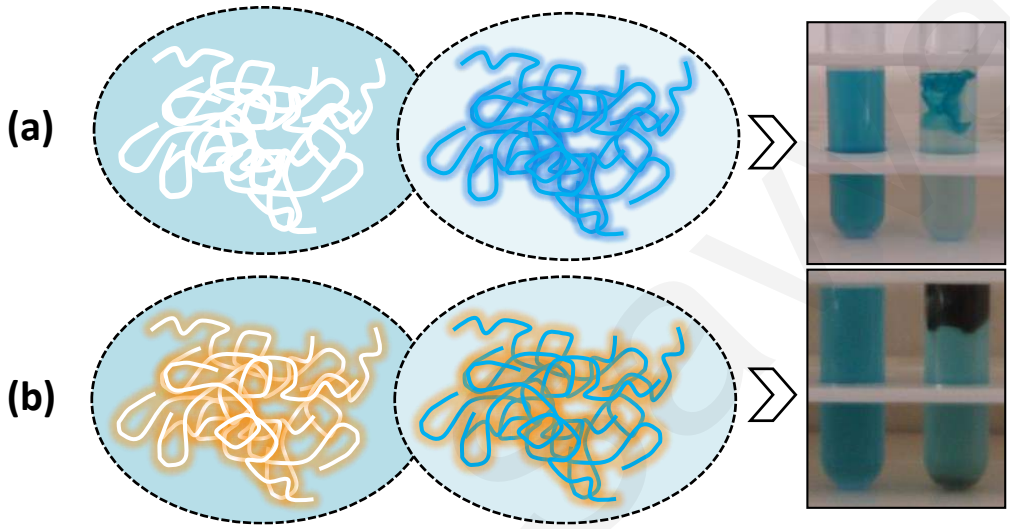

Figure 6.24: *Schematic presentation of the removal of MG by the microfibrous membranes and photographs of the process using* ***(a)*** *the PEO/PLLA and* ***(b)*** *the PEO/PLLA/OA.Fe_3O_4 electrospun membranes as dye adsorbents. Photographs were taken 24 hours after membrane immersion in the MG aqueous solution.*

Figure 6.25 provides the absorption of the remaining in solution MG and related adsorption percentage *versus* time plots corresponding to the adsorption profile of MG from the PEO/PLLA **(figure 6.25 (a))** and the PEO/PLLA/OA.Fe_3O_4 (37 and 50% wt.) **(figure 6.25 (b))** microfibrous membranes. Upon immersing the membranes in the MG aqueous solution and recording the UV-vis spectra of the solution at the indicated times, a systematic decrease in the MG absorption signal corresponding to the unbound MG molecules (appearing at ~ 618 nm) was clearly observed.

With the other parameters known ($m_{adsorbent}$=10 mg, V_{sln}=3 mL, $C_0=10^{-5}$ M, T=25 °C, t=24 hours) the remaining MG concentration in solution at equilibrium C_e could be determined by recording the UV-vis absorption spectra of the supernatant at certain time intervals (C_t) and calculating the corresponding MG solution concentration by following the Lambert-Beer Law (**equation 6.2**), *via* the construction of the absorption (at 618 nm) *versus* MG

concentration calibration curve (ε=141749.41±3673.45 $L \cdot mol^{-1} \cdot cm^{-1}$). Adsorption kinetic constants corresponding to the magnetite-free PEO/PLLA ($k=3.336 \cdot 10^{-2} \pm 3.488 \cdot 10^{-4}$ min^{-1}) and the magnetoactive PEO/PLLA/OA.Fe_3O_4 systems with 37% wt. OA.Fe_3O_4 ($k=1.338 \cdot 10^{-2} \pm 3.417 \cdot 10^{-4}$ min^{-1}) and 50% wt. OA.Fe_3O_4 ($k=2.785 \cdot 10^{-2} \pm 1.1665 \cdot 10^{-3}$ min^{-1}) revealed slower adsorption rates in the case of the Fe_3O_4-containing membranes whereas lower adsorption percentages were also observed in the presence of magnetite (~ 70% compared to ~ 95% determined in the absence of Fe_3O_4).

This phenomenon may be interconnected to the altering of the surface area of the membranes due to the incorporation of the magnetic nanoparticles. Preliminary results obtained by BET measurements have shown that upon increasing the magnetic content the surface area of the membranes decreases resulting to the reduction of the membrane adsorption efficiency.

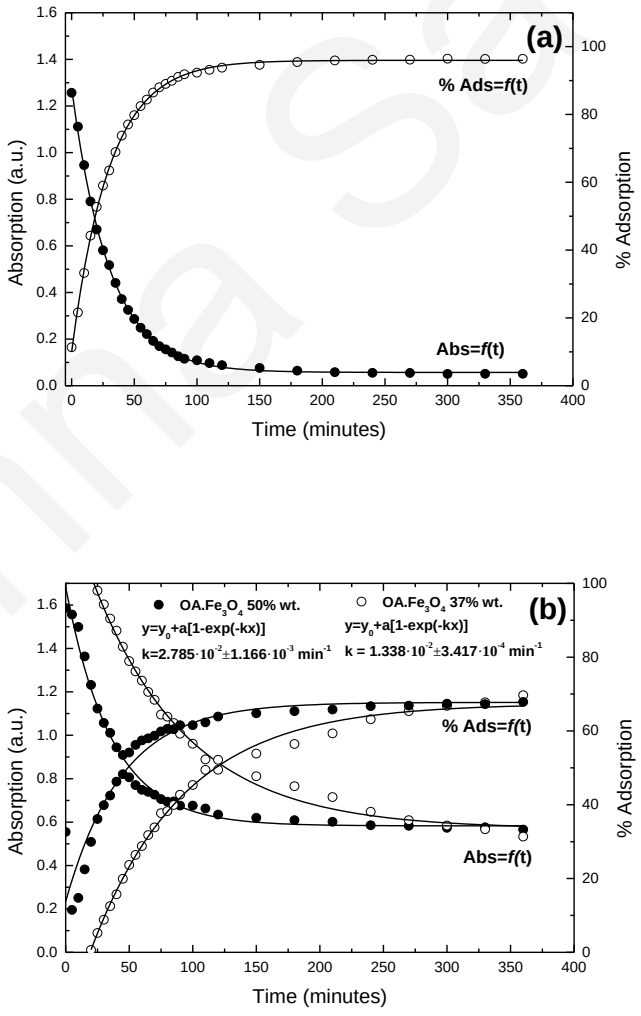

Figure 6.25: *Kinetic adsorption studies of MG from aqueous solutions at room temperature using:* ***(a)*** *PEO/PLLA and* ***(b)*** *PEO/PLLA/OA.Fe_3O_4 (with OA.Fe_3O_4 37 and 50% wt.) microfibrous membranes as adsorbents.*

Figure 6.26 summarizes the MG adsorption profiles demonstrated as A_t/A_0 *versus* time normalized plots for the above-mentioned adsorption studies performed in water. A_t denotes the absorption of the MG molecules found free in solution at time t, and A_0 corresponds to the initial absorption (at t=0) of the MG molecules found free in solution.

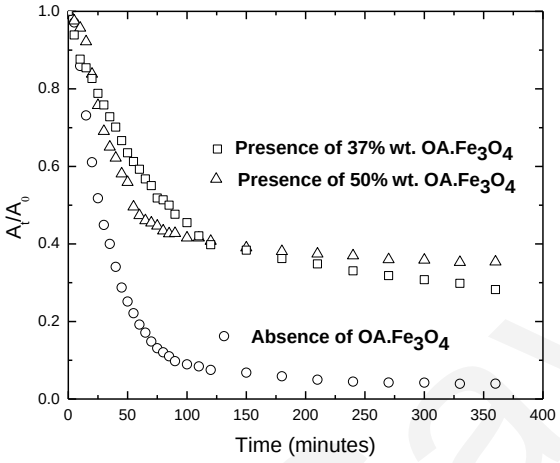

Figure 6.26: *Normalized A_t/A_0 versus time plots corresponding to the PEO/PLLA and PEO/PLLA/OA.Fe_3O_4 in the presence of OA.Fe_3O_4 37 and 50% wt. microfibrous membranes, employed as adsorbents of MG in aqueous solutions at room temperature.*

pH is also an important parameter which affects the capacity of an adsorbent in wastewater treatment. Specifically in the case of MG, the pH effect on the adsorption process is more pronounced since this particular dye undergoes structural changes depending on the pH (134). Due to the chromatic changes of MG at different pHs, the UV-vis spectrophotometry can only be used in the analysis of the MG adsorption efficacy by different adsorbents, based on absorption measurements at the MG characteristic wavelength of 618 nm within a certain pH range (between ~ 3-6) (363; 134). Specifically, in acidic pH (pH < 2) the deep green MG^+ (having three distinct absorption signals appearing at 317 nm, 427 nm and 618 nm) turns into protonated cyan MGH^+ whereas in alkaline conditions (pH > 8) it turns into a colorless carbinol base MGOH as seen in **figure 6.27**. **Figure 6.28 (a)** shows the UV-vis spectra of MG solutions recorded at different pHs prior to membrane immersion whereas in **figure 6.28 (b)** a variation curve of the MG adsorption percentage onto the PEO/PLLA/OA.Fe_3O_4 50% wt. membrane as a function of pH determined upon recording the MG absorption at 618 nm is provided. The effect of pH

on MG adsorption by the PEO/PLLA/OA.Fe_3O_4 microfibrous nanocomposite adsorbent was investigated at specific MG concentration ($6 \cdot 10^{-6}$ M) and contact time (24 hours).

The reduced adsorption percentage of MG at lower pH values may be attributed to repulsive phenomena developed between the MGH^+, and the positive charges generated on the magnetite surfaces at pH < 8. Similar observations (i.e. reduced adsorption efficacy for MG at low pH values) have been also reported by other groups (364; 127) and have been attributed to two reasons: (a) electrostatic repulsive effects existing between the sorbent and MG owing to the development of positive charges on both, the sorbent and MG under those conditions, inhibiting the MG sorption and (b) competing adsorption effects between the positively charged dye molecules and excess H^+ ions that are present in solution. At a pH range of 3-6, such phenomena still exist since MG is found in its protonated form (MG^+) (middle chemical structure, **figure 6.27**) and magnetite still possesses positive charges on its surface, but they are less pronounced. At pH > 8 the magnetite surface becomes negatively charged and hydrophilic resulting to an increase of the adsorption efficiency of MG that is found in its carbinol base form possessing –OH polar groups.

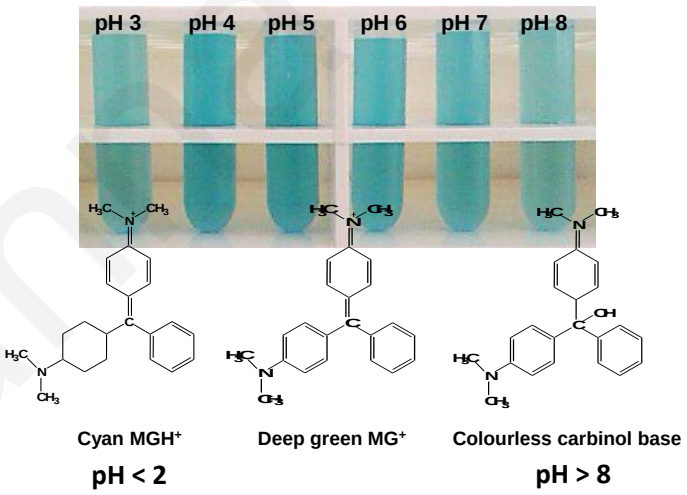

Figure 6.27: *Chemical structures of the different MG structures (MGH^+, MG^+ and carbinol base) exhibiting colour variations in aqueous solutions, associated with changes in solution pH.*

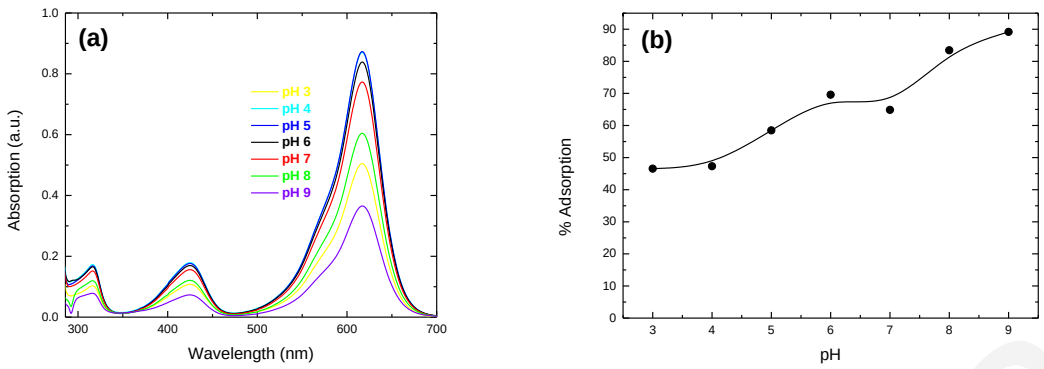

Figure 6.28: (a) *UV-vis spectra of MG recorded at different pHs prior to membrane immersion and* ***(b)*** *MG adsorption percentage onto the PEO/PLLA/50% wt. OA.Fe_3O_4 membrane as a function of pH, determined upon recording the MG absorption at 618 nm by UV-vis spectrophotometry.*

In order to evaluate the maximum membrane adsorption capacity (q_{max} ($mg \cdot g^{-1}$)) through the effect of initial MG solution concentration ($m_{adsorbent}$=10 mg, V_{sln}=3 mL, $C_0=1 \cdot 10^{-6}$ M to $1 \cdot 10^{-5}$), adsorption experiments have been performed at room temperature (298 K) for 24 hours using different MG initial solution concentrations. The Langmuir isotherm model **(equation 6.8)** was employed in order to analyze the data obtained from the adsorption experiments.

As previously mentioned, by constructing the absorption *versus* MG concentration calibration curve, it is possible to determine the exact remaining MG concentration in solution C_e ($mg \cdot g^{-1}$) and the amount of MG adsorbed q_e ($mg \cdot g^{-1}$) at equilibrium by recording the UV-vis absorption spectra of the supernatant. From the $1/q_e$ *versus* $1/C_e$ linearized plots, q_{max} and K_d could be calculated from the slope ($1/q_{max} \cdot K_d$) and the intercept ($1/q_{max}$) respectively **(table 6.3)**.

Table 6.3: *Experimental Langmuir parameters for MG adsorption determined using electrospun PEO/PLLA and PEO/PLLA/OA.Fe_3O_4 membranes as adsorbents.*

Sample Code	q_{max} ($mg \cdot g^{-1}$)	K_d ($L \cdot mg^{-1}$)	R^2
0% wt. OA.Fe_3O_4	8.809	0.399	0.90929
37% wt. OA.Fe_3O_4	1.473	0.376	0.86443
50% wt. OA.Fe_3O_4	1.684	0.404	0.95665

The UV-vis spectra of MG aqueous solutions of various initial concentrations, the Langmuir adsorption isotherms expressing the relationship between q_e *versus* the remaining MG concentration in solution at equilibrium (24 hours), C_e, as well as the linearized $1/q_e$ *versus* $1/C_e$ isotherms corresponding to the MG adsorption by the PEO/PLLA and PEO/PLLA/OA.Fe_3O_4 membranes are provided in **figure 6.29 (a)**, **(b)** and **(c)** respectively. q_e was determined by using **equation 6.5**.

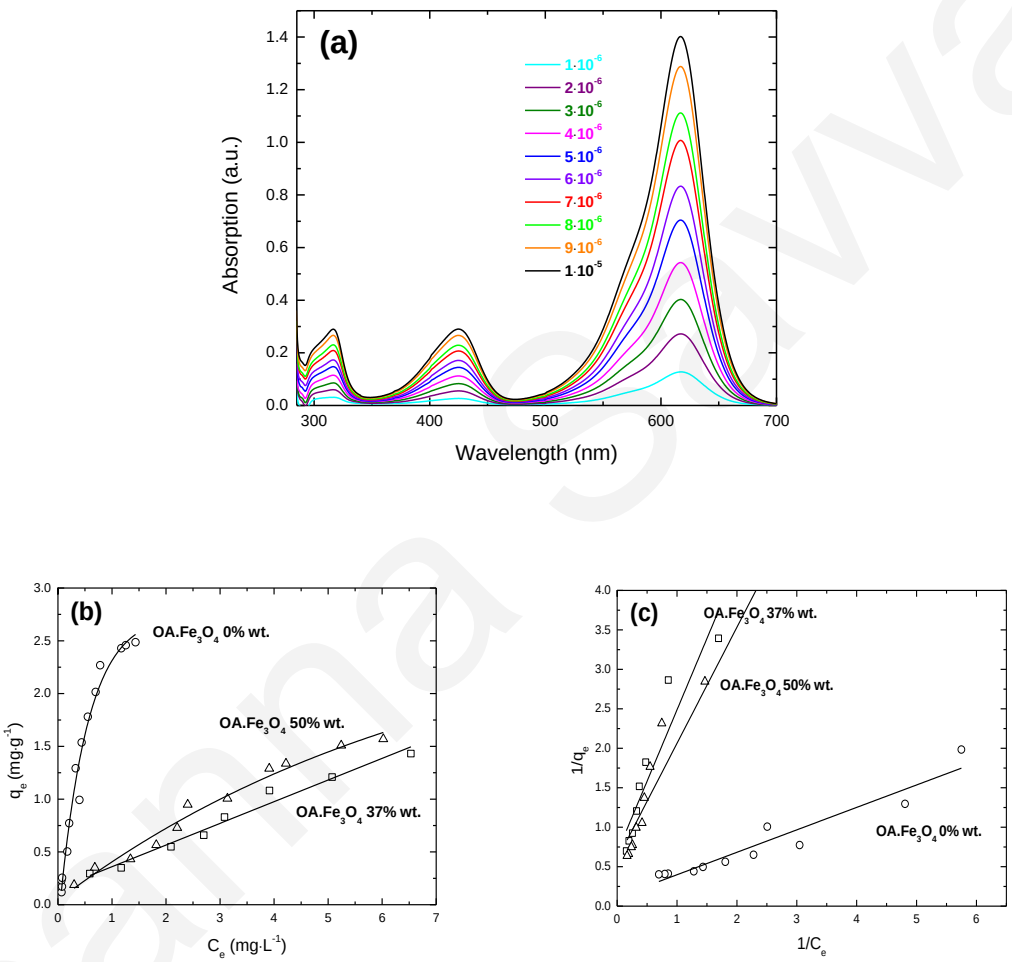

Figure 6.29: (a) *UV-vis absorption spectra of MG aqueous solutions of various initial solution concentrations,* ***(b)*** *q_e vs C_e Langmuir adsorption isotherms, and* ***(c)*** *linearized ($1/q_e$ vs $1/C_e$) Langmuir adsorption isotherms corresponding to the MG adsorption by the PEO/PLLA membranes in the absence and presence of 37 and 50% wt. OA.Fe_3O_4 NPs.*

The results provided in **table 6.3** suggest that the presence of magnetite within the membranes reduces the amount of the dye adsorbed. A possible explanation for this phenomenon might be the hydrophobic and cationic nature of the surface of the magnetite NPs at pH values below 8 (341), that disfavour the incorporation of MG found in its

positively charged form (MG^+) within the membranes, due to the development of electrostatic repulsive forces. Moreover, repulsive phenomena may be also promoted due to the presence of the hydrophobic oleic acid chains employed as steric stabilizers onto the Fe_3O_4 surfaces. Those experimental findings are in line with the aforementioned experimental results related to the effect of contact time adsorption values (q_{max}) that were found to decrease in the case of the Fe_3O_4-loaded systems.

The influence of temperature on the MG adsorption onto the pristine and nanocomposite electrospun membranes was investigated so as to determine the thermodynamic parameters (enthalpy (ΔH^0), entropy (ΔS^0) and change in free energy (ΔG^0)) related to the adsorption process. The only variable in the experiments performed was temperature (298, 318, 338 K), whereas the initial MG concentration ($1.13 \cdot 10^{-5}$ M) and contact time (24 hours) remained the same. By constructing the $\ln K_d$ *versus* 1/T plot provided in **figure 6.30**, ΔH^0 and ΔS^0 were calculated from the slope ($\Delta H^0/R$) and the intercept ($\Delta S^0/R$) respectively according to Van't Hoff **equation 6.10**. K_d is calculated as C_{ads}/C_e, where C_e ($mol \cdot L^{-1}$) is the equilibrium concentration, C_{ads} ($mol \cdot L^{-1}$) is the concentration of the amount of MG adsorbed at equilibrium, R (8.314 $J \cdot K^{-1} \cdot mol^{-1}$) is the gas constant and T (K) is the temperature.

$$lnKd = \frac{\Delta S^0}{R} - \frac{\Delta H^0}{RT} \qquad \textbf{Equation 6.10}$$

The Gibbs free energy change ΔG^0 is calculated from **equation 6.11**.

$$\Delta G^0 = -RT\ lnKd \qquad \textbf{Equation 6.11}$$

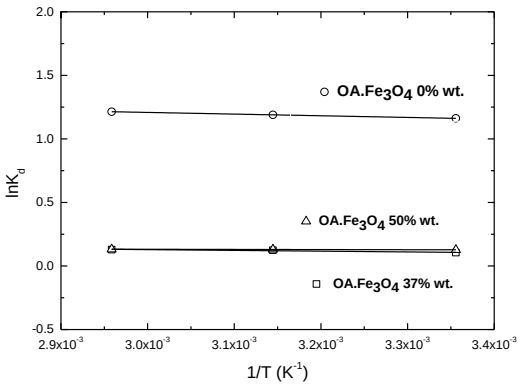

Figure 6.30: *Plots of $\ln K_d$ versus 1/T for MG adsorption onto the PEO/PLLA and the PEO/PLLA/OA.Fe_3O_4 electrospun membranes.*

Table 6.4 summarizes the calculated values of the thermodynamic parameters ΔG^0, ΔH^0 and ΔS^0 related to the adsorption process. Negative ΔG^0 values are obtained in all cases, indicating that the adsorption onto the Fe_3O_4-free and the Fe_3O_4-containing membranes is feasible and spontaneous. Moreover, the positive ΔH^0 values as well as the increase of K_d with increasing temperature (365) indicate the endothermic nature of the adsorption process. A comparison of the ΔG^0 values corresponding to the pristine and Fe_3O_4-loaded adsorbents shows that the adsorption process is thermodynamically less favored in the latter case. This is in line with the above-discussed experimental results that demonstrated the reduced adsorption efficiency of the membranes in the presence of Fe_3O_4 NPs. Moreover, the decrease of the ΔS^0 values upon temperature increase suggests that the adsorption process is further promoted at higher temperatures.

Table 6.4: *Thermodynamic parameters of MG adsorption onto the PEO/PLLA electrospun fibrous membranes in the absence and presence of magnetic NPs.*

Sample code	Temperature (K)	ΔH° (KJ·mol^{-1})	ΔS° (KJ·mol^{-1}·K^{-1})	ΔG° (KJ·mol^{-1})
OA.Fe_3O_4 0% wt.	298	1.0902	0.0134	-2.8785
	318			-3.1447
	338			-3.4112
OA.Fe_3O_4 37% wt.	298	0.4986	0.0026	-0.2612
	318			-0.3285
	338			-0.3625
OA.Fe_3O_4 50% wt.	298	0.0944	0.0014	-0.3156
	318			-0.3447
	338			-0.3705

The regeneration ability of the electrospun PEO/PLLA and PEO/PLLA/OA.Fe_3O_4 37% wt. dye adsorbents was examined by removing the MG-loaded membranes from the aqueous solution and immersing them in ethanol. An immediate coloration of the alcohol solution was observed, clearly indicating the desorption of MG from the membranes and its transfer into the alcohol media. Subsequently, the membranes were re-immersed in a freshly prepared MG solution (of the same initial concentration as that used during the first adsorption step) and the whole desorption/re-adsorption process was repeated for 2 more times. In **figure 6.31**, the removal efficiency of MG is presented as % adsorption *versus* number of cycles plot. After three adsorption-desorption cycles, the adsorption capacity was ~ 90% in the case of the PEO/PLLA membrane and ~ 40% in the case of the Fe_3O_4-containing system, a result that is important for practical applications.

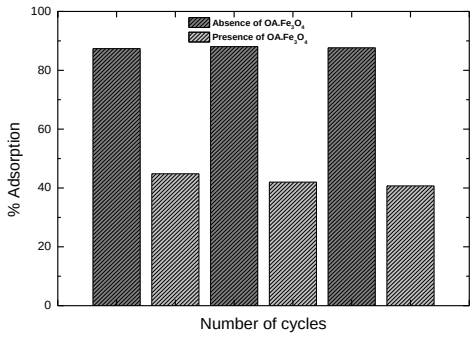

Figure 6.31: *Regeneration (MG adsorption-desorption) cycles performed using the pristine and the Fe_3O_4-containing microfibrous membranes as adsorbents.*

In conclusion, PEO/PLLA and magnetoactive (superparamagnetic) PEO/PLLA/OA.Fe_3O_4 membranes were evaluated for the first time as adsorbents for the removal of MG from aqueous solutions. The obtained results showed that the adsorption process follows the Langmuir isotherm model, suggesting monolayer adsorption on a homogeneous surface. Most importantly, it was found that the presence of Fe_3O_4 NPs within the membranes seems to disfavor the adsorption process. In addition the obtained results demonstrated that adsorption also depends on operating variables including initial MG concentration and solution pH. The thermodynamic parameters determined from temperature dependent adsorption measurements suggested that the adsorption of MG onto the Fe_3O_4-free and the Fe_3O_4-containing membranes is spontaneous and endothermic. Finally, regeneration/re-use cycles demonstrated the recyclability of these systems. Consequently, the ability of these materials to act as effective adsorbents for MG combined with the possibility of their recovery from aqueous solutions upon applying an external magnetic field and their recyclability provides a promising tool for the future development of highly efficient, stimuli (magneto)-responsive adsorbents for the removal of hazardous materials from wastewater.

6.2. Methacrylate-based electrospun membranes: Fabrication, characterization and environmental applications

Electrospun microfibrous membranes based on functional methacrylate-based polymers and pre-formed oleic acid-coated magnetic NPs (OA.Fe_3O_4 NPs) were successfully fabricated and employed for the first time in water remediation processes as adsorbents for heavy metal ions (Eu(III)) and selective organic pollutants (metronidazole, 1,2-dichlorobenzene).

6.2.1. MMA-*co*-AEMA-based electrospun membranes

In an effort to develop novel electrospun membranes with functionalities that would assist the development of specific interactions with heavy metal ions that are present in wastewater, random copolymers containing *β*-ketoester metal ion chelating moieties have been in house synthesized and further used in membrane fabrication. In addition, from our previous studies it has been demonstrated that the *β*-ketoester groups can bind effectively onto the inorganic iron oxide surfaces providing an improved stabilization (339; 176).

6.2.1.1. Synthesis and molecular characterization

Copolymer synthesis: Conventional free radical polymerization was employed for the synthesis of the methyl methacrylate-*co*-2-(acetoacetoxy)ethyl methacrylate) (MMA-*co*-AEMA) random copolymers as illustrated in **scheme 6.5**. More precisely, the synthesis of random copolymers consisting of the hydrophobic MMA and the hydrophobic/metal ion binding AEMA monomers was performed in EA or THF in the presence of 2,2'-azobis-(isobutylnitrile) (AIBN), that served as the radical source.

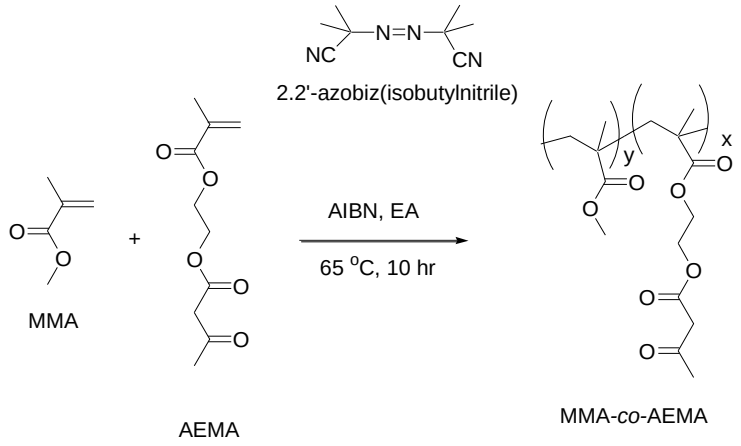

Scheme 6.5: *Synthetic methodology followed for the preparation of the MMA-co-AEMA random copolymers.*

Molecular characterization: The molecular characteristics of the MMA-*co*-AEMA random copolymers were determined by SEC and ^{1}H NMR. **Table 6.5** summarizes the chemical structures of the copolymers prepared in this study along with their average molecular weight ($\overline{M_w}$) and composition characteristics. As expected, the use of a non-controlled radical polymerization process led to the generation of polymeric materials characterized by relatively high polydispersity indices (PDI) ranging between ~ 1.8 and 3.3. In **figure 6.32** the SEC traces of selective MMA-*co*-AEMA random copolymers prepared in the present study are displayed.

Table 6.5: *Chemical structures of the copolymers, average molecular weights, and polydispersity indices.*

a/a	Chemical Structures[1]	$\overline{M_n}$ [2] (g·mol^{-1})	$\overline{M_w}$ [3] (g·mol^{-1})	PDI
1	$MMA_{1.0}$-*co*-$AEMA_{1.0}$	133560	348740	2.61
2	$MMA_{1.0}$-*co*-$AEMA_{1.07}$	119720	275890	2.30
3	$MMA_{1.0}$-*co*-$AEMA_{0.72}$	106830	189380	1.77
4	$MMA_{1.0}$-*co*-$AEMA_{2.2}$	104200	237540	2.28
5	$MMA_{1.0}$-*co*-$AEMA_{3}$	96794	315760	3.26
6	$MMA_{1.0}$-*co*-$AEMA_{3}$	99842	244720	2.45

[1]the molar ratios between the MMA and AEMA moieties were determined by ^{1}H NMR

[2] M_n = Number average molecular weight

[3] M_w = Weight average molecular weight

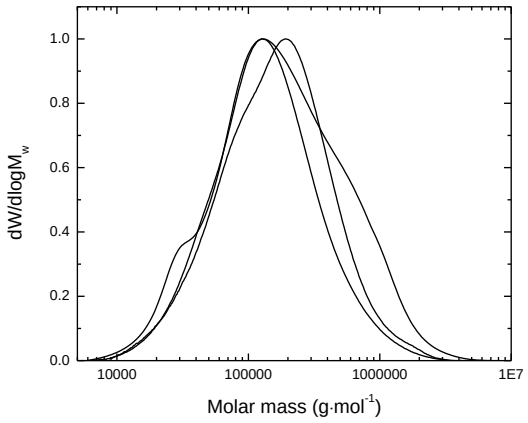

Figure 6.32: *SEC eluograms of selected MMA-co-AEMA random copolymers.*

The expected chemical structure of the MMA-*co*-AEMA random copolymers was confirmed by ^{1}H NMR spectroscopy. **Figure 6.33** exemplarily shows the ^{1}H NMR spectrum of the $MMA_{1.0}$-*co*-$AEMA_{2.2}$ random copolymer. The peak assignments are shown in the spectrum. The MMA:AEMA comonomer compositions **(table 6.5)** were determined from the ratio of the areas under the characteristic signals of the AEMA and the MMA, appearing at 4.17 (CH_2, d) and 3.59 (CH_3, f) respectively, after subtracting from the latter the area corresponding to the –CH_2 groups of AEMA (f).

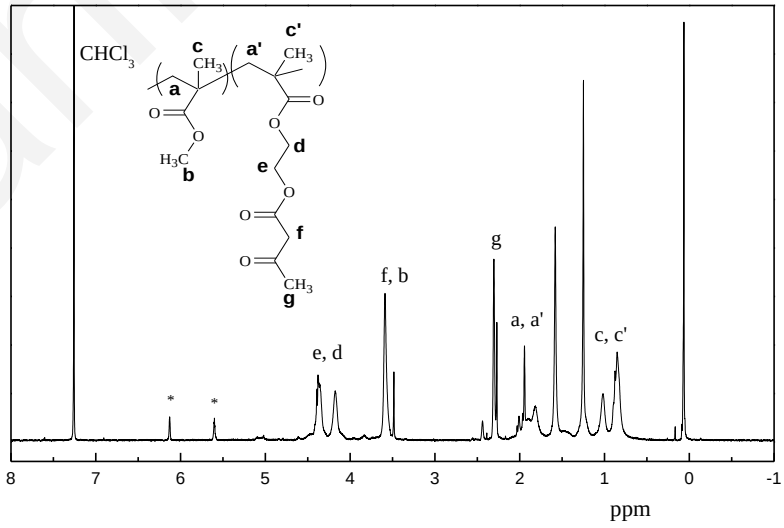

Figure 6.33: *^{1}H NMR spectrum of the $MMA_{1.0}$-co-$AEMA_{2.2}$ random copolymer. *Residual monomer.*

6.2.1.2. Membrane fabrication

Fibrous membranes comprised of MMA-*co*-AEMA random copolymers and OA.Fe_3O_4 magnetic NPs were fabricated by electrospinning, starting from solutions prepared in THF and $CHCl_3$, with concentrations 6 and 30% w/v respectively. In order to improve the wettability of the completely hydrophobic MMA-*co*-AEMA fibrous membranes, the PEO homopolymer was mixed together with the random copolymer in $CHCl_3$ to yield polymer blends, with polymer-solution concentration 4% w/v and weight percentage PEO/MMA-*co*-AEMA:4/96 respectively.

By employing specific experimental conditions, fibrous membranes were successfully fabricated. Experimental parametric studies were carried out for the MMA-*co*-AEMA and the PEO/MMA-*co*-AEMA systems in the presence and absence of magnetite NPs, in order to define the optimum parameters for the production of electrospun fibrous membranes. **Table 6.6** summarizes the optimum experimental electrospinning conditions followed for the successful generation of the fibrous membranes. Photographs of the prepared electrospun fibrous membranes are illustrated in **figure 6.34**.

Table 6.6: *Optimum experimental conditions employed for the fabrication of the MMA-co-AEMA and PEO/MMA-co-AEMA electrospun membranes, both in the absence and presence of OA.Fe_3O_4 magnetic NPs.*

a/a	Sample	Polymer solution concentration (w/v)/Solvent	Needle (G)	Flow rate ($mL \cdot h^{-1}$)	Voltage (kV)	Needle-to-collector distance (cm)
1	MMA-*co*-AEMA	6/THF	16	3	10	30
2	MMA-*co*-AEMA/OA.Fe_3O_4 (2% wt.)	6/THF	16	1.8	15	25
3	MMA-*co*-AEMA/OA.Fe_3O_4 (4% wt.)	6/THF	16	1.8	15	25
4	MMA-*co*-AEMA/OA.Fe_3O_4 (10% wt.)	6/THF	16	1.2	15	25
5	MMA-*co*-AEMA/OA.Fe_3O_4 (30% wt.)	6/THF	16	0.3	25	20
6	MMA-*co*-AEMA/OA.Fe_3O_4 (70% wt.)	6/THF	16	0.6	25	20
7	MMA-*co*-AEMA	30/$CHCl_3$	18	0.3	10	20
8	PEO/MMA-*co*-AEMA	4/$CHCl_3$	18	2	20	25
9	PEO/MMA-*co*-AEMA/OA.Fe_3O_4 (37% wt.)	4/$CHCl_3$	18	2	20	25

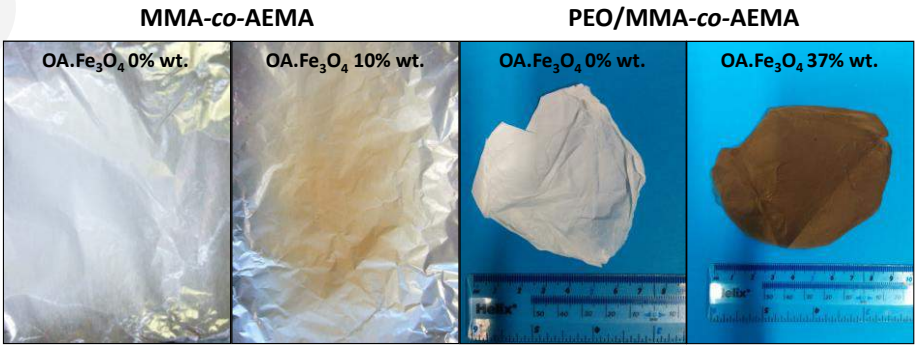

Figure 6.34: *Photographs of the as-prepared MMA-co-AEMA and PEO/MMA-co-AEMA electrospun fibrous membranes*

6.2.1.3. Membrane characterization

Morphological characterization: The morphological characteristics of the membranes were determined by SEM. **Figure 6.35 (a)** provides the SEM images of the pristine MMA-*co*-AEMA fibrous membrane obtained in the absence of the OA.Fe_3O_4 magnetic NPs starting from a polymer solution prepared in THF. The fibers produced are partially separated from each other whereas fiber bundles and junctions can be also observed. Moreover, the SEM images reveal the presence of a multimodal diameter distribution ranging between ~ 1 to ~ 2 μm. This phenomenon has been previously observed by other groups and it has been attributed to the splitting of the electrospinning jet during the process (34).

The fabrication of magnetoactive, electrospun MMA-*co*-AEMA-based fibrous membranes involved the incorporation of the pre-formed OA.Fe_3O_4 magnetic NPs of various concentrations into the polymer solutions prior to the electrospinning process. Upon mixing different amounts of OA.Fe_3O_4 with the polymer in THF, highly viscous solutions containing both, the magnetic NPs and the polymer were obtained and were further electrospun aiming to obtain magnetoactive fibrous membranes. **Figure 6.35** provides the SEM micrographs of the MMA-*co*-AEMA/OA.Fe_3O_4 electrospun membranes containing OA.Fe_3O_4 **(b)** 2 **(c)** 4, **(d)** 10**, (e)** 30, **(f)** 70% wt.

As seen from the images no significant changes were observed in the morphological characteristics of the fibers upon increasing the magnetic content in the range of 2-10% wt. Similar observations were reported by X. Xua *et al*. (366) for electrospun PVP-Fe(0) nanocomposite fibers in which the Fe(0) inorganic content ranged between 1.25-10% wt. However, upon significantly increasing the magnetic content (i.e. 30 and 70% wt.) while maintaining the electrospinning conditions relatively unchanged, a morphological change from fibers to bead-like structures has been induced. A possible explanation for this morphological transition might be the influence of the OA.Fe_3O_4 found at high concentrations in solution on different parameters affecting the electrospinning process. According to Fong *et al.* the formation of beads may be strongly influenced by the viscoelasticity of the solution, the charge density carried by the jet, and the surface tension of the solution which are closely related with the solvent (57; 58; 59; 367). Moreover, fibers obtained from low concentration solutions tend to be shorter and finer, compared to the fibers generated from more viscous solutions (45; 52; 53). Consequently, upon

increasing the polymer-solution concentration from 6 to 30 % w/v and replacing THF with $CHCl_3$, more homogeneous and thicker fibers were obtained **(figure 6.35 (g))**.

As previously mentioned, the membrane wettability in aqueous media is an important parameter in systems destined for use in water remediation processes. For this purpose, the hydrophilic PEO was mixed together with the MMA-*co*-AEMA random copolymer to yield blended PEO/MMA-*co*-AEMA fibrous membranes that contained or not magnetic NPs. The addition of PEO in the MMA-*co*-AEMA-based polymeric solution prepared in $CHCl_3$ followed by electrospinning, resulted to fibrous membranes consisting of cylindrical homogeneous fibers with diameters ranging between 2 and 3 μm. In contrast to the MMA-*co*-AEMA/OA.Fe_3O_4 systems with relatively high magnetic content prepared starting from THF solutions, SEM demonstrated that the incorporation of OA.Fe_3O_4 magnetic NPs within the PEO/MMA-*co*-AEMA membranes even at percentages as high as 37% wt. did not significantly affect the morphological characteristics of the membranes. This difference may be attributed to the fact that the OA.Fe_3O_4 exhibit higher solubility in $CHCl_3$ than in THF, resulting to polymer/OA.Fe_3O_4 solutions of higher homogeneity thus avoiding NP aggregation phenomena during the process that may in turn affect significantly the morphological characteristics of the obtained electrospun mats.

(a) MMA-*co*-AEMA, polymer-solution concentration: 6%w/v in THF

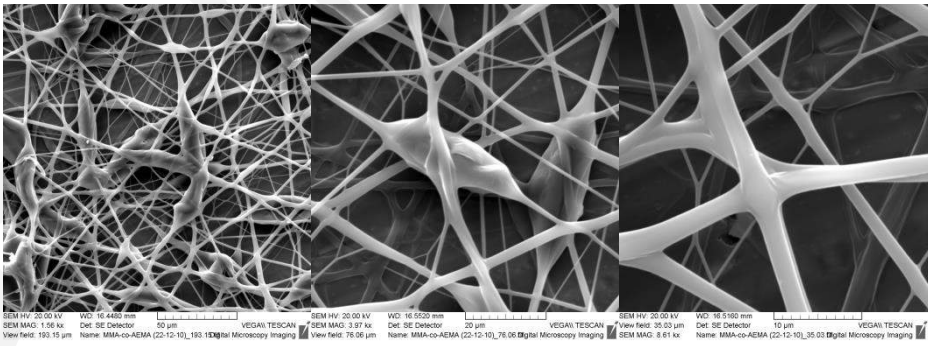

(b) MMA-*co*-AEMA/OA.Fe_3O_4 2% wt., polymer-solution concentration: 6%w/v in THF

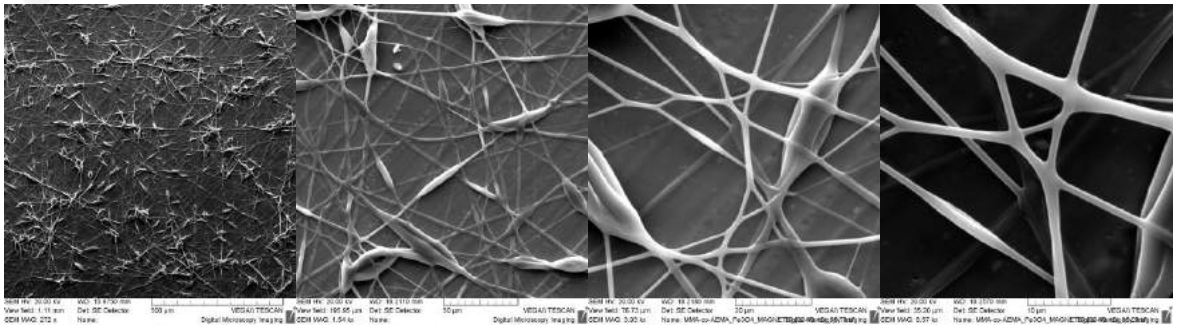

(c) MMA-*co*-AEMA/OA.Fe_3O_4 4% wt., polymer-solution concentration: 6%w/v in THF

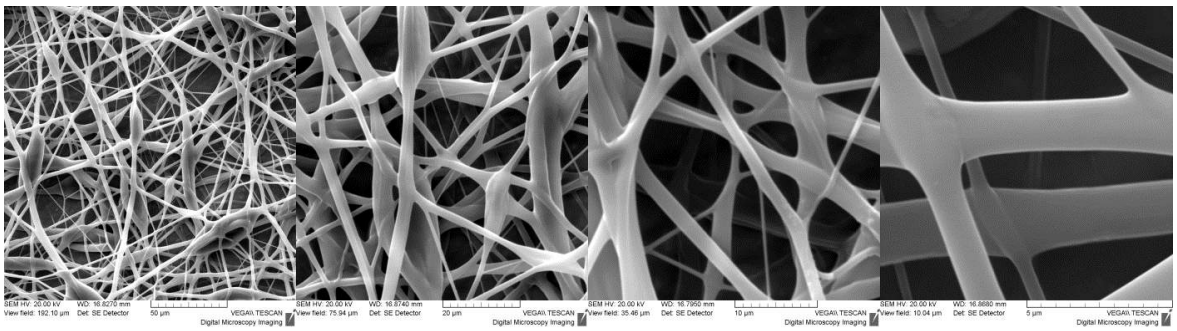

(d) MMA-*co*-AEMA/OA.Fe_3O_4 10% wt., polymer-solution concentration: 6%w/v in THF

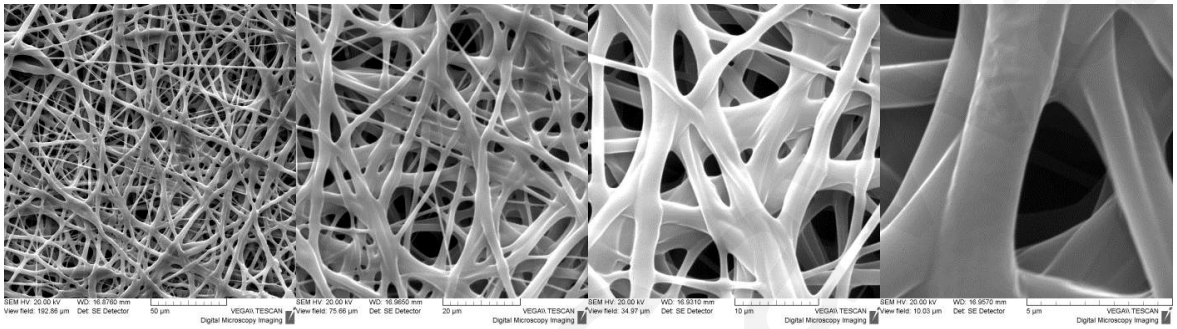

(e) MMA-*co*-AEMA/OA.Fe_3O_4 30% wt., polymer-solution concentration: 6%w/v in THF

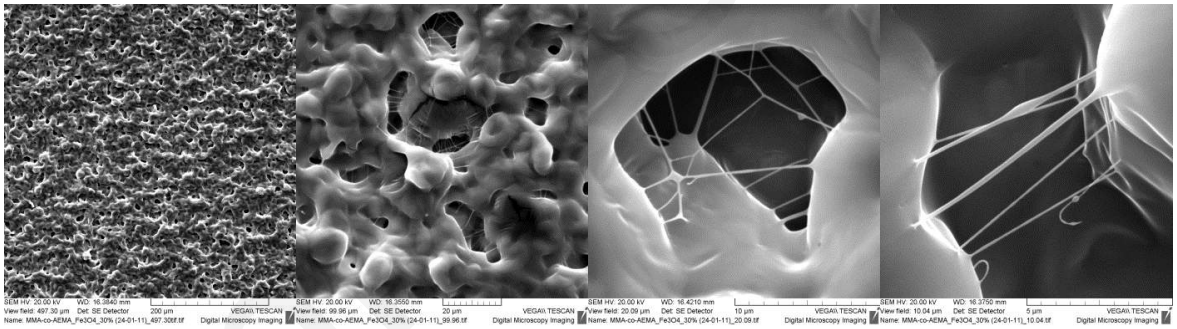

(f) MMA-*co*-AEMA/OA.Fe_3O_4 70% wt., polymer-solution concentration: 6%w/v in THF

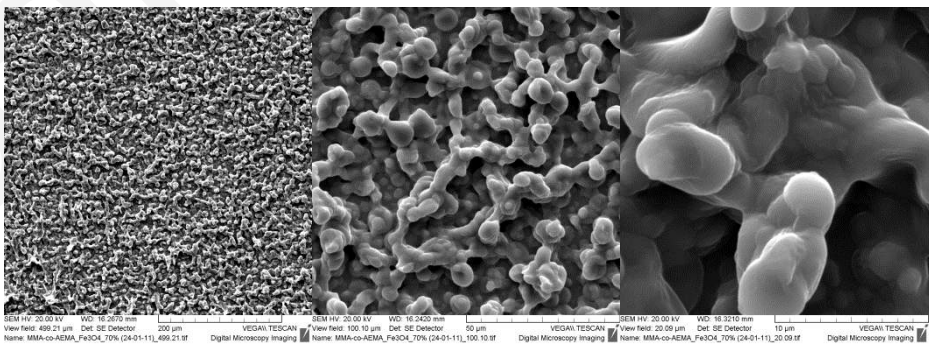

(g) MMA-*co*-AEMA, polymer-solution concentration: 30%w/v in $CHCl_3$

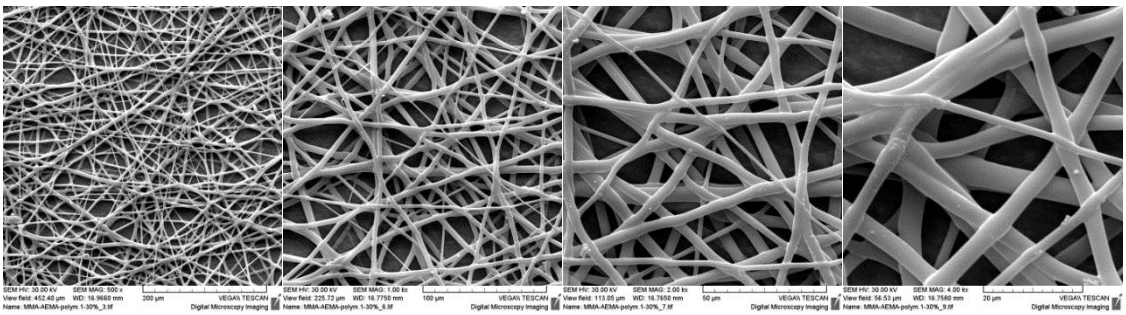

(h) PEO/MMA-*co*-AEMA, polymer-solution concentration: 4%w/v in $CHCl_3$

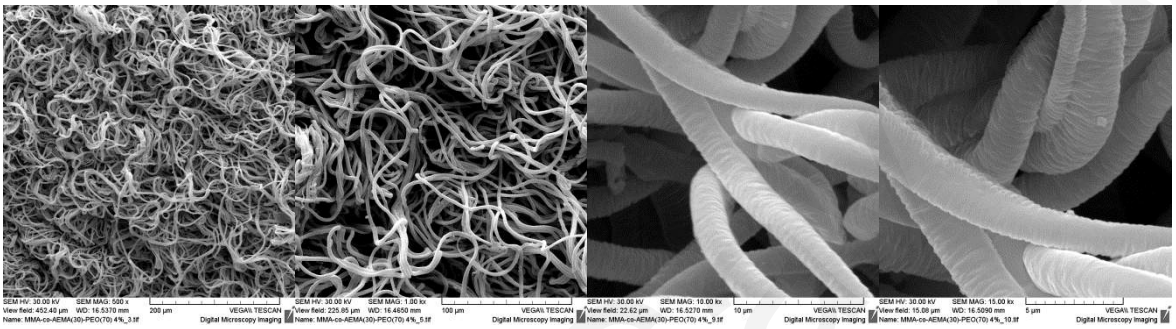

(d) PEO/MMA-*co*-AEMA/OA.Fe_3O_4 37% wt., polymer-solution concentration: 4%w/v in $CHCl_3$

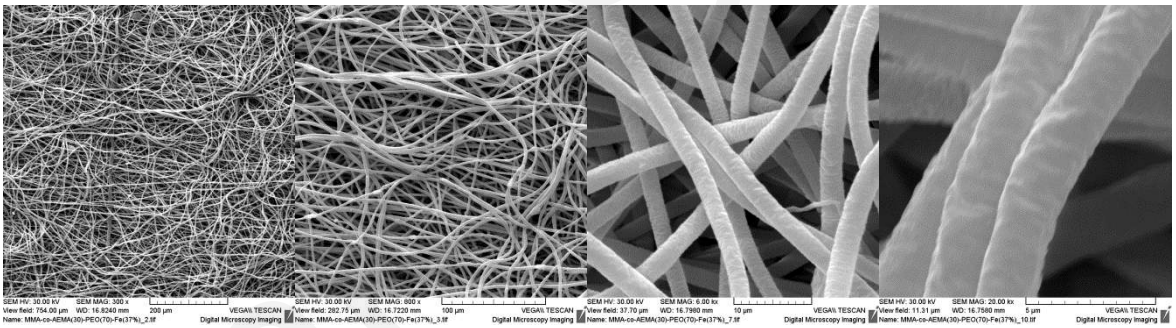

Figure 6.35: *SEM images of the MMA-co-AEMA and the PEO/MMA-co-AEMA electrospun fibrous membranes and of their magnetoactive analogues obtained in the presence of OA.Fe_3O_4 magnetic NPs.*

Thermal properties: The degradation temperature of the resulting fibrous membranes was determined by TGA measurements. The TGA traces of the membranes both in the absence and presence of OA.Fe_3O_4 NPs are provided in **figure 6.36**. As seen in the thermograms, the fibrous PEO/MMA-*co*-AEMA blended membranes begin to decompose at ~ 400 °C compared to the membranes consisting of only MMA-*co*-AEMA that begin to decompose at a lower temperature, ~ 200 °C. Moreover, the PEO/MMA-*co*-AEMA membrane start to decompose at a slightly lower temperature (~ 350 °C) compared to the nanocomposite analogue with OA.Fe_3O_4 37% wt. (~ 380 °C), while at ~ 420 °C, it decomposes completely losing all of its weight. Similarly, the MMA-*co*-AEMA fibrous membranes start to

decompose at ~ 200 °C, while the nanocomposite (OA.Fe_3O_4 10% wt.) analogue begins to decompose at a higher temperature (~ 250 °C). At ~ 430 °C the magnetite-free MMA-*co*-AEMA membrane decomposes completely losing all of its weight. The remaining residue observed in the case of the magnetite-containing membrane at higher temperatures (T > 430 °C) corresponds to the inorganic (Fe_3O_4) content.

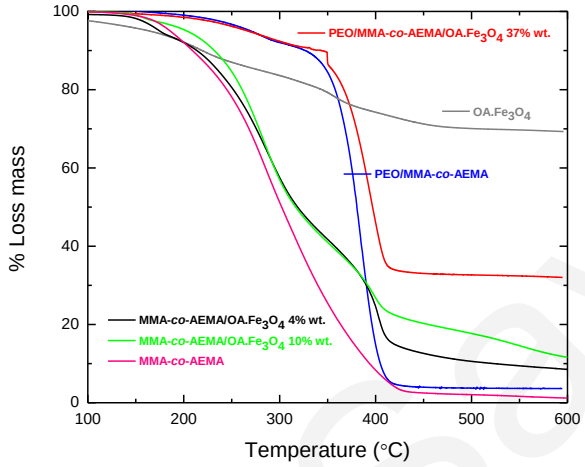

Figure 6.36: *TGA thermograms of the MMA-co-AEMA and PEO/MMA-co-AEMA electrospun membranes in the absence and presence of OA.Fe_3O_4 magnetic NPs (4, 10, and 37% wt.).The TGA thermogram of the as-prepared OA.Fe_3O_4 is also given for comparison.*

Nanocrystalline phase characterization: The nanocrystalline phase adopted by the OA.Fe_3O_4 NPs embedded within the nanocomposite membranes was investigated by X-ray diffraction (XRD) spectroscopy. **Figure 6.37** provides the powder XRD diffraction pattern of the PEO/MMA-*co*-AEMA/OA.Fe_3O_4 electrospun membrane with 37% wt. of magnetic content and the XRD pattern corresponding to pure OA.Fe_3O_4 for comparison. The diffractogram of the membrane displays six broad peaks appearing at 2θ ~ 30˚, 36˚, 43˚, 54˚, 58˚, and 63˚, verifying the presence of magnetite (OA.Fe_3O_4) within this system (336; 335; 334).

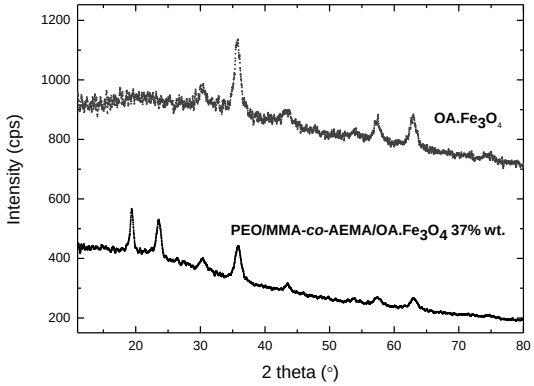

Figure 6.37: *X-ray diffraction patterns of the as-prepared OA.Fe_3O_4 NPs and the PEO/MMA-co-AEMA/OA.Fe_3O_4 37% wt. nanocomposite fibrous membranes.*

Magnetic properties: The magnetic behavior of the nanocomposite membranes was investigated by VSM at 300K. **Figure 6.38** exemplarily shows the magnetization *versus* applied magnetic field strength plot (M=*f*(H)) corresponding to the MMA-*co*-AEMA and the PEO/MMA-*co*-AEMA nanocomposite membranes loaded with OA.Fe_3O_4 4 and 37% wt. respectively. The sigmoidal shape of the plots and the lack of a hysteresis loop demonstrate the superparamagnetic behaviour of both systems at ambient temperature. Moreover, from the magnetization plots it becomes obvious that upon increasing the magnetic content within the membranes, the saturation magnetization (M_s) increases as expected, while the superparamagnetic properties are retained.

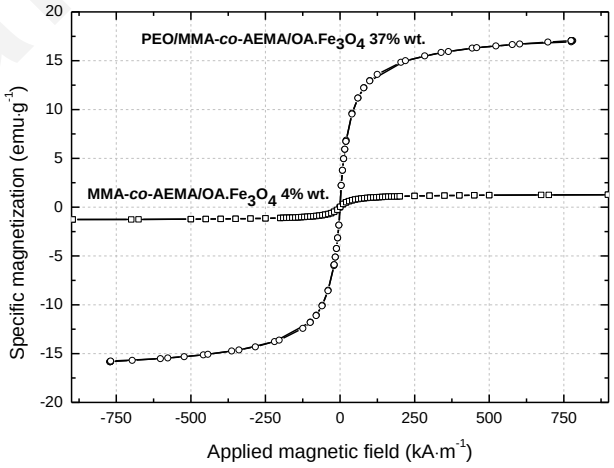

Figure 6.38: *Magnetization curves of the MMA-co-AEMA/OA.Fe_3O_4 and PEO/MMA-co-AEMA OA.Fe_3O_4 nanocomposite fibrous membranes containing 4 and 37% wt. OA.Fe_3O_4 respectively.*

6.2.1.4. Membrane application as adsorbent for heavy metal ions

Adsorption studies for the removal of Eu(III) heavy metal ions from aqueous media: The effectiveness of the PEO/MMA-*co*-AEMA (70:30) 4% w/v systems in removing europium from aqueous solutions was investigated by carrying out experiments on the effect of pH, initial metal ion concentration and membrane magnetic content (327). The incorporation of magnetic NPs within the membranes targeted towards the enhancement of the adsorption efficiency and the recovery of the adsorbent by using a simple magnet (289).

A pre-fixed amount of the adsorbent was placed in an aqueous Eu(III) solution of a known concentration and the UV-vis spectrum of the supernatant was recorded after 24 hours for determining the amount of the adsorbed Eu(III) ions. A schematic presentation of the adsorption process and related photographs of the membranes immersed in europium aqueous solutions are illustrated in **figure 6.39**. The results were compared to those obtained using the PEO/PLLA membrane as adsorbent instead (see section **6.1.3.2.**).

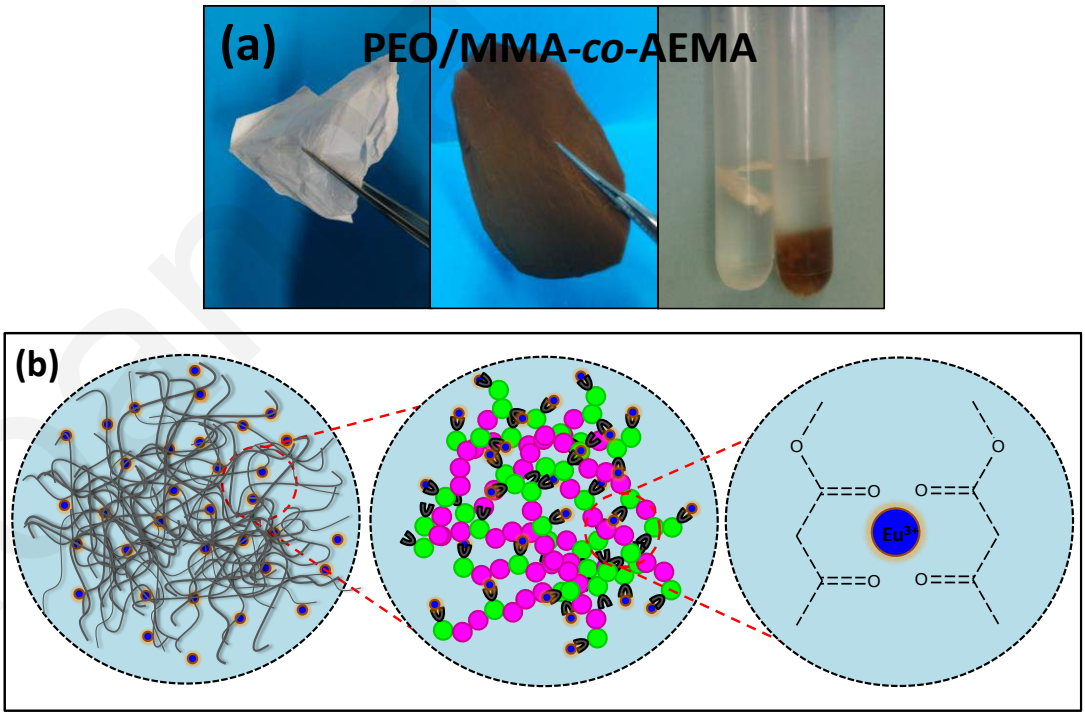

Figure 6.39: (a) *Photographs of the PEO/MMA-co-AEMA fibrous membranes in the absence and presence of OA.Fe_3O_4 magnetic NPs 37% wt., and* ***(b)*** *schematic illustration of the Eu(III) metal ion adsorption process realized via complexation of the β-ketoester groups with the Eu(III) ions.*

The morphological characteristics of the membranes after immersion in an aqueous solution containing Eu(III) ions were determined by SEM. **Figure 6.40** shows characteristic SEM micrographs of both, the magnetite-free and the magnetite-containing nanocomposite membranes after immersion.

(a) PEO/MMA-*co*-AEMA after being immersed in Eu(III)-containing aqueous media

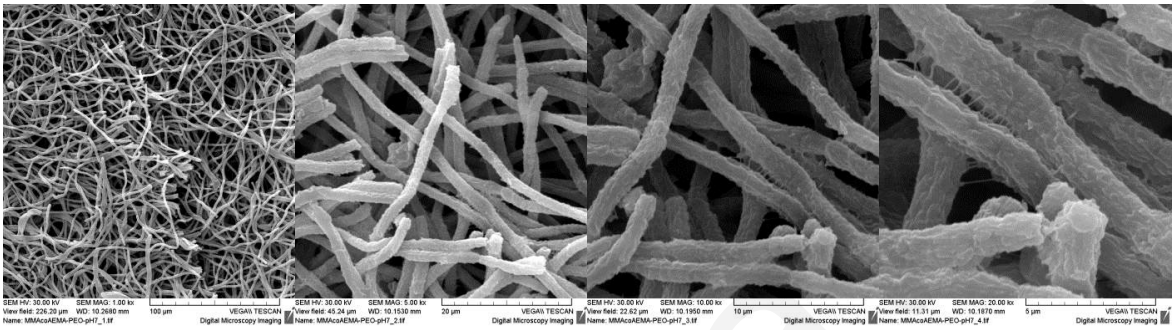

(b) PEO/MMA-*co*-AEMA/OA.Fe_3O_4 37% wt. after being immersed in Eu(III)-containing aqueous media

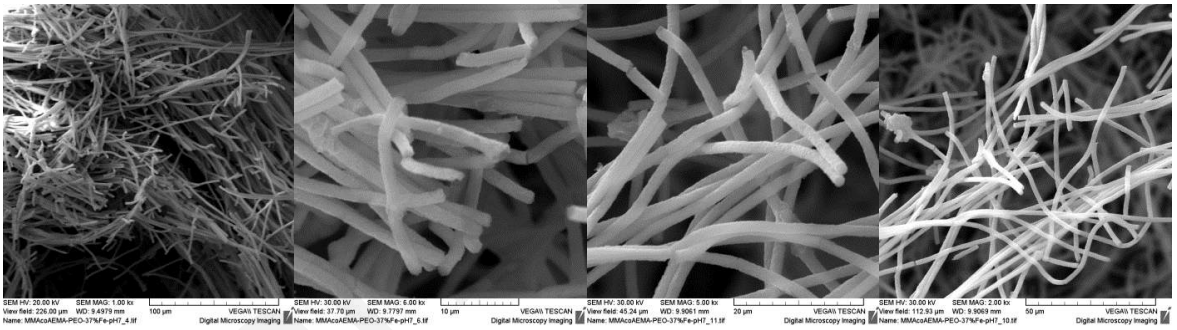

Figure 6.40: *SEM images of* ***(a)*** *PEO/MMA-co-AEMA fibrous membranes and* ***(b)*** *PEO/MMA-co-AEMA/OA.Fe_3O_4 37% wt. nanocomposite fibrous membranes after being immersed in aqueous media containing Eu(III) ions.*

As already discussed in previous sections (see section **6.1.3.2.**), pH is a very important parameter which affects the capacity of an adsorbent in wastewater treatment processes. The effect of pH on the europium sorption onto the PEO/MMA-*co*-AEMA electrospun membranes and their magnetoactive nanocomposite analogues was investigated and the corresponding variation curves of the metal ions adsorption percentage as a function of pH are provided in **figure 6.41**. The experiments have been performed up to pH 8 since above this value the formation of Eu(III) carbonate complexes, $EuCO_3^+$ and $Eu(CO_3)_2^-$, occurs. As seen in the figure, the relative adsorption of Eu(III) on both systems, increases with

increasing pH, reaching a maximum value of ~ 80% and ~ 95% at pH 6.5 for the PEO/MMA-*co*-AEMA and the PEO/MMA-*co*-AEMA/OA.Fe_3O_4 systems respectively.

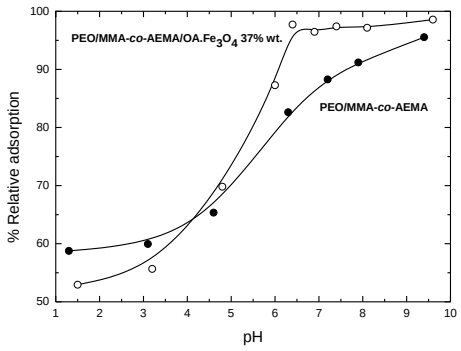

Figure 6.41: *The effect of pH on the relative adsorption of Eu(III) metal ions by the PEO/MMA-co-AEMA fibrous membrane in the absence and presence of OA.Fe_3O_4 magnetic NPs..*

In order to evaluate the maximum membrane adsorption capacity (q_{max} ($mg \cdot g^{-1}$)) through the effect of initial metal ion solution concentration, adsorption experiments using metal ion solutions of different concentrations ($1 \cdot 10^{-6}$ to $1 \cdot 10^{-4}$ M) have been performed at the optimum pH (pH 6.5) at room temperature. The Langmuir isotherm model was employed to fit the equilibrium experimental data of Eu(III) sorption onto the membranes. **Figure 6.42 (a)** shows the obtained q_e ($mol \cdot Kg^{-1}$) *versus* C_e ($mol \cdot L^{-1}$) plots as well as **(b)** the linearized $1/q_e$ *versus* $1/C_e$ isotherms. The maximum adsorption capacity of europium onto electrospun membranes was found to be ~ 14 and ~ 17 $mmol \cdot Kg^{-1}$ for the OA.Fe_3O_4-free and nanocomposite fibrous membranes respectively.

This small difference may be attributed to the fact that the Fe_3O_4 NPs may weakly interact with the paramagnetic Eu(III) ions *via* dipole-dipole interactions due to the fact that Fe_3O_4 exhibit permanent magnetic moment (368). Another possibility might be the complex formation between the free hydroxyl groups that may be present onto the surfaces of the Fe_3O_4 nanoparticles located on the outer surfaces of the fibers and the Eu(III) ions.

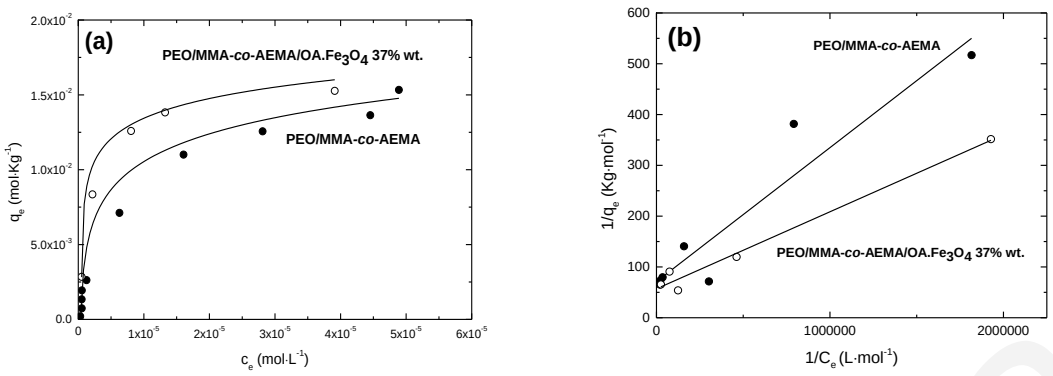

Figure 6.42: (a) *Langmuir adsorption isotherms and* ***(b)*** *linearized Langmuir adsorption isotherms plots corresponding to the Eu(III) adsorption by the PEO/MMA-co-AEMA and the PEO/MMA-co-AEMA/OA.Fe_3O_4 nanocomposite fibrous membranes containing OA.Fe_3O_4 37% wt.*

A comparison of the adsorption efficiency of the PEO/PLLA and the PEO/MMA-*co*-AEMA electrospun fibrous membranes **(figure 6.43)** demonstrated that the latter act as more effective adsorbents for Eu(III) ions. More precisely the PEO/PLLA system reaches a q_{max} at ~ 6 mmol·Kg^{-1} whereas the PEO/PMMA-*co*-AEMA membrane exhibits a significantly higher value ~ 14 mmol·Kg^{-1}. Those findings verify our initial hypothesis that the presence of the *β*-ketoester metal binding groups within the membranes may assist favourably the sorption process.

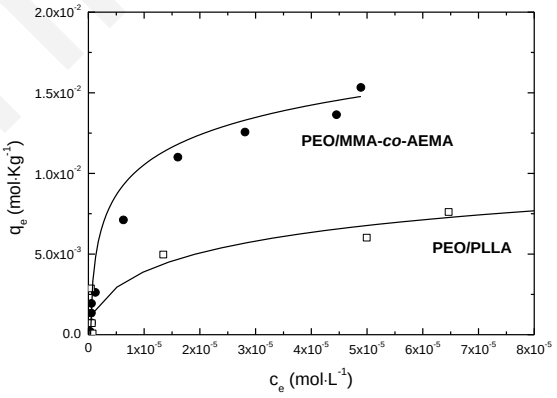

Figure 6.43: *Langmuir adsorption isotherms plots corresponding to the Eu(III) adsorption by the PEO/MMA-co-AEMA and the PEO/PLLA fibrous membranes.*

6.2.2. MMA-*co*-BzMA-based electrospun membranes

Electrospun fibrous membranes, consisting of methacrylic random copolymers based on benzyl methacrylate (BzMA) and methyl methacrylate (MMA) were successfully fabricated and characterized, aiming toward the removal of two organic water-soluble pollutants namely metronidazole and 1,2 dichlorobenzene.

6.2.2.1. Synthesis and molecular characterization

Copolymer synthesis: Conventional free radical polymerization was employed for the synthesis of the methyl methacrylate-*co*-benzyl methacrylate (MMA-*co*-BzMA) random copolymers. The polymerization reaction scheme is illustrated in **scheme 6.6.**

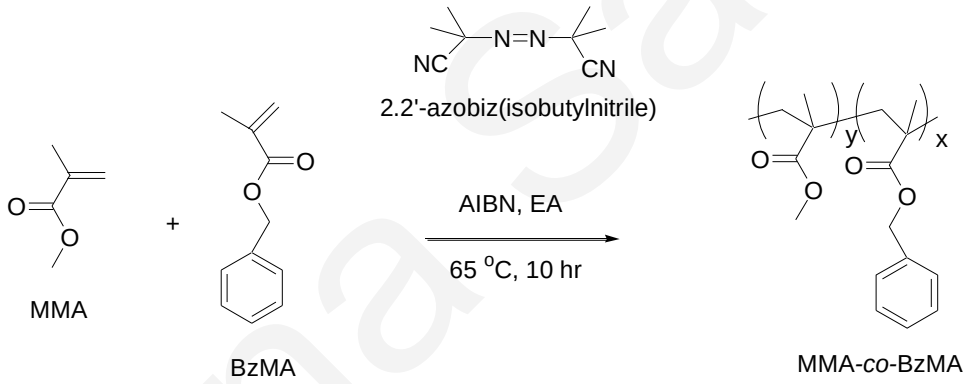

Scheme 6.6: *Synthetic scheme followed for the preparation of the MMA-co-BzMA random copolymers.*

Molecular characterization: The molecular characteristics of the MMA-*co*-BzMA random copolymers obtained by free radical polymerization were determined by SEC and ^{1}H NMR. **Table 6.7** summarizes the chemical structures of the copolymers prepared in this study along with their average molecular weights and composition characteristics. As expected, the use of a non-controlled radical polymerization process led to the generation of polymeric materials characterized by relatively high polydispersity indices (PDI) ~ 2.0. In **figure 6.44** the SEC traces of two MMA-*co*-AEMA random copolymers are displayed.

Table 6.7: *Average molecular weights, polydispersity indices and polymerization yields of the MMA-co-BzMA random copolymers.*

a/a	Chemical Structures[1]	$\overline{M_n}$ [2] (g·mol^{-1})	$\overline{M_w}$ [3] (g·mol^{-1})	PDI	Yield (%)
1	$MMA_{1.0}$-*co*-$BzMA_{1.03}$	41641	90400	2.17	63
2	$MMA_{1.0}$-*co*-$BzMA_{1.0}$	43501	88333	2.03	45

[1]the molar ratios between the MMA and BzMA moieties were determined by ^{1}H NMR

[2] M_n = Number average molecular weight

[3] M_w = Weight average molecular weight

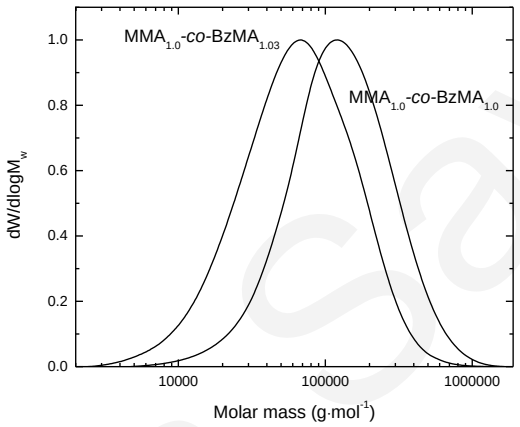

Figure 6.44: *SEC eluograms of the MMA-co-BzMA random copolymers.*

The expected chemical structure of the MMA-*co*-BzMA random copolymers was confirmed by ^{1}H NMR spectroscopy. **Figure 6.45** exemplarily shows the ^{1}H NMR spectrum of the $MMA_{1.0}$-*co*-$BzMA_{1.03}$. The peak assignments are shown in the spectrum. The MMA:BzMA comonomer compositions **(table 6.7)** were determined from the ratio of the areas under the characteristic signals of the MMA and the BzMA, appearing at 3.54 (CH_3, b) and 4.97 (CH_2, d) respectively.

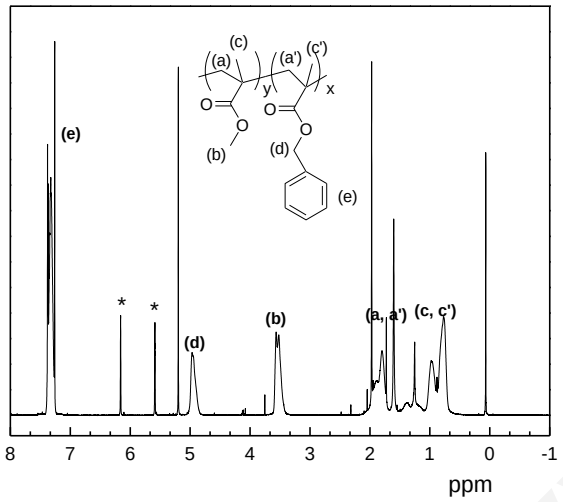

Figure 6.45: *^{1}H NMR spectrum of the $MMA_{1.0}$-co-$BzMA_{1.03}$ random copolymer. *Residual monomer.*

6.2.2.2. Membrane fabrication

Electrospun fibrous membranes comprised of MMA-*co*-BzMA random copolymers were fabricated starting from homogeneous polymer solutions prepared in $CHCl_3$, with concentrations 10, 30, and 50% w/v. As previously noted, the successful generation of fibrous membranes requires the determination of the optimal processing parameters. Experimental parametric studies were carried out for the MMA-*co*-BzMA systems, and optimum parameters for the production of electrospun fibrous membranes were obtained. **Table 6.8** summarizes the optimum experimental electrospinning conditions followed for the successful generation of the fibrous membranes. In order to improve the wettability of the completely hydrophobic fibrous membranes, the PEO homopolymer was mixed with the random copolymer in $CHCl_3$ in a 4/96 weight percentage respectively and electrospun to yield blended PEO/MMA-*co*-BzMA fibrous membranes. Photographs of the as-prepared membranes are illustrated in **figure 6.46**.

Table 6.8: *Optimum experimental conditions employed for the fabrication of the MMA-co-BzMA-based electrospun fibrous membranes.*

a/a	Sample	Polymer-solution concentration (w/v)	Needle (G)	Flow rate ($mL \cdot h^{-1}$)	Voltage (kV)	Needle-to-collector distance (cm)
1	MMA-*co*-BzMA	10	18	1.0	20	20
2	MMA-*co*-BzMA	30	18	0.2	25	10
3	MMA-*co*-BzMA	50	16, 18	0.8	25	20
4	PEO/MMA-*co*-BzMA (4/96)	52	16	3.5	25	25

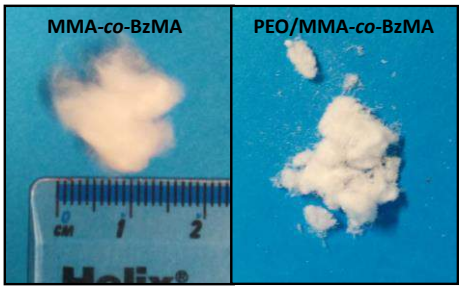

Figure 6.46: *Photographs of the as-prepared electrospun MMA-co-BzMA-based fibrous membranes.*

6.2.2.3. Membrane characterization

Morphological characterization: The morphological characteristics of the membranes were determined by SEM. **Figure 6.47** provides the SEM images of the MMA-*co*-BzMA electrospun fibers obtained from solutions with various concentrations as well as images of the PEO/MMA-*co*-BzMA system. At the lowest concentration **(figure 6.47 (a))** polymer microbeads with an irregular shape were obtained instead of continuous fibers. Upon increasing the polymer-solution concentration from 10 to 30% w/v, in addition to polymer beads, some limited fiber formation occurred in the form of thin fibers (54; 367; 17). It is noteworthy to mention at this point that the formation of the beaded fibers is governed by several process and solution parameters including viscosity/concentration/molecular weight and surface tension (367).

At higher polymer-solution concentration (50% w/v) continuous polymer fibers with diameters ranging between 3 to 5 μm were observed **(figure 6.47 (c))**. In the case of the PEO/MMA-*co*-BzMA blended membranes, SEM revealed the presence of fibers. However, in comparison to the MMA-*co*-BzMA systems, the blended analogues were characterized by much less homogeneity in terms of fiber diameters as seen in **figure 6.46 (d)**.

(a) MMA-*co*-BzMA, polymer-solution concentration: 10%w/v in $CHCl_3$

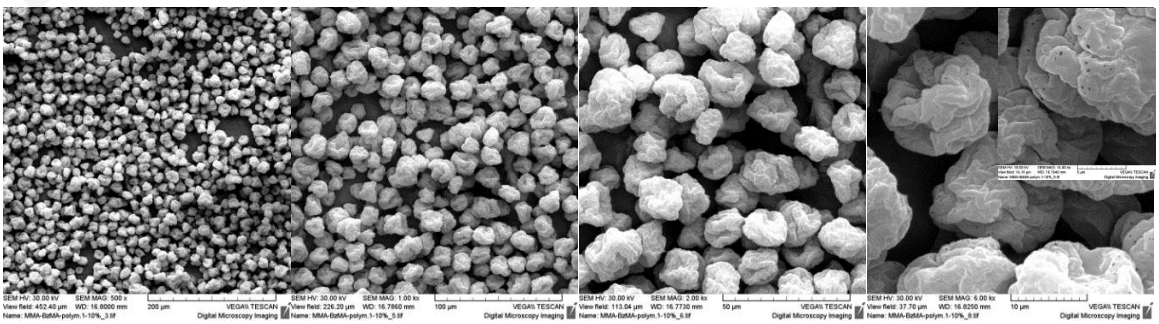

(b) MMA-*co*-BzMA, polymer-solution concentration: 30%w/v in $CHCl_3$

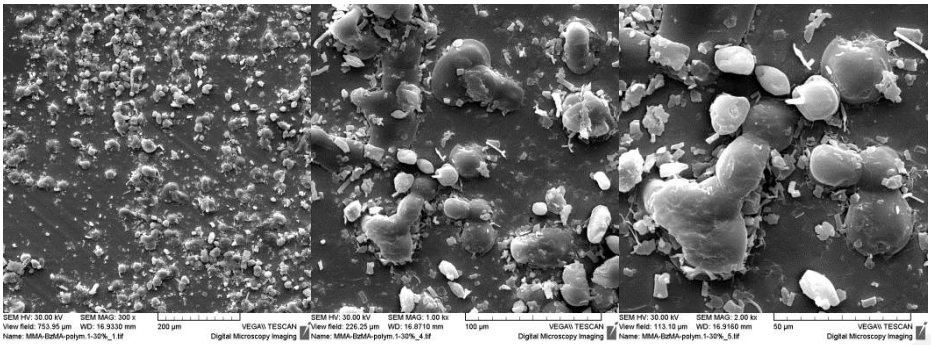

(c) MMA-*co*-BzMA, polymer-solution concentration: 50%w/v in $CHCl_3$

16G

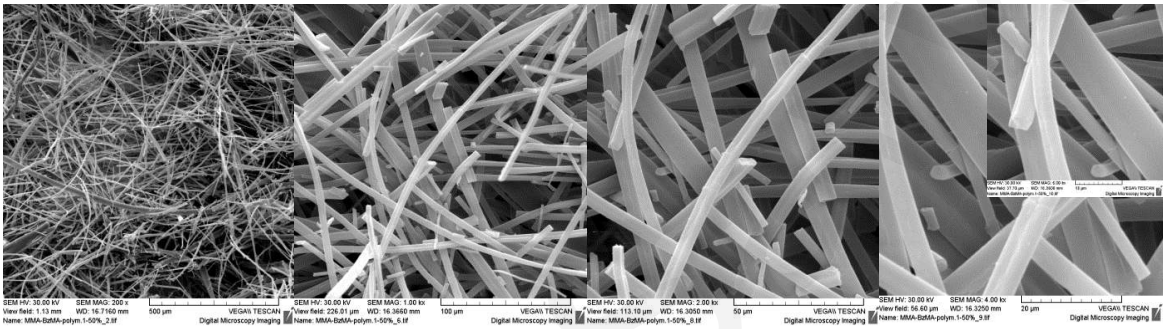

18G

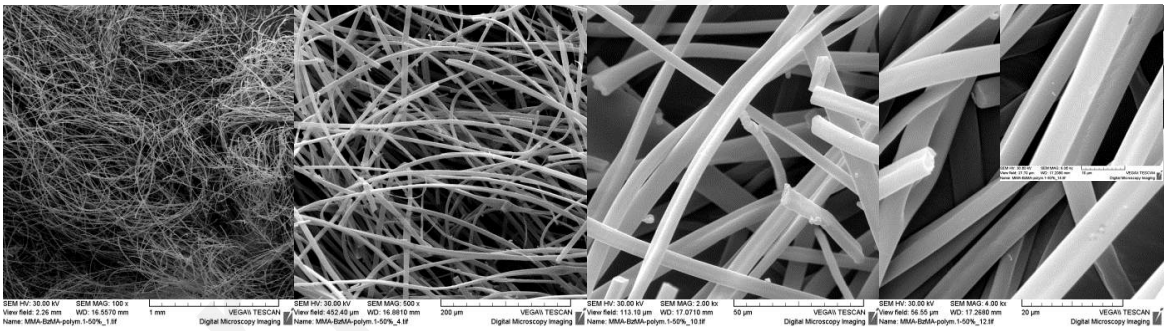

(d) PEO/MMA-*co*-BzMA, polymer-solution concentration: 52%w/v in $CHCl_3$

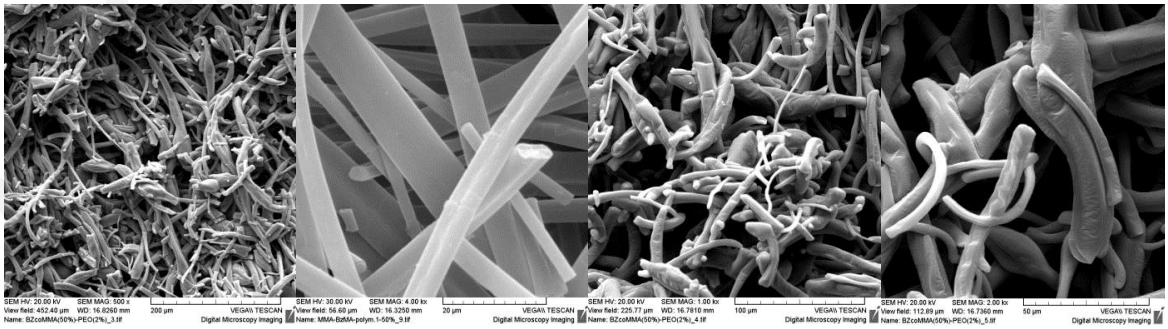

Figure 6.47: *SEM images of the MMA-co-BzMA-based electrospun fibrous membranes.*

Thermal properties: The degradation temperature of the resulting fibrous membranes was determined by TGA measurements. The TGA trace of the MMA-*co*-BzMA membrane is provided in **figure 6.48**. As seen in the thermogram, the membrane begins to decompose at ~ 250 °C while at ~ 400 °C, is decomposes completely losing all of its weight.

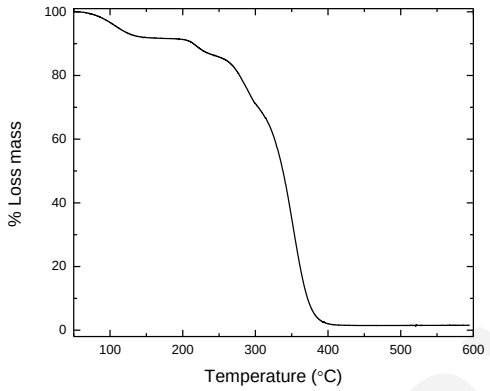

Figure 6.48: *TGA thermogram of MMA-co-BzMA fibrous membrane.*

6.2.2.4. Membrane evaluation as adsorbent of organic pollutants

Adsorption studies for the removal of 1,2 dichlorobenzene and metronidazole from aqueous media: The methacrylate-based electrospun membranes were used in the recovery of two organic pollutants namely 1,2 dichlorobenzene and metronidazole (MET) from aqueous media. MET, the structure of which is presented in **figure 6.49** is a nitroimidazole antiprotozoal agent with a powerful antibacterial activity against anaerobics (369). However this antibiotic when released in aqueous media acts as a contaminant due to its limited biodegrability (370; 371) .

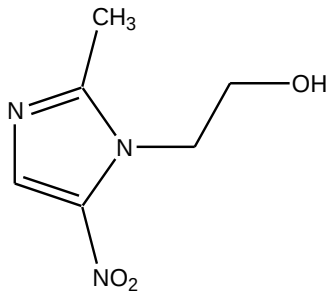

Figure 6.49: *Chemical structure of metronidazole.*

1,2 dichlorobenzene (DCB), the structure of which is presented in **figure 6.50** is a manufactured organohalogen compound used as a solvent for degreasing hides and wool. It also serves as a synthetic reagent for dye manufacture. It is chemically stable and its photochemical degradation in soil and aquatic environments is limited. DCB exhibits very low solubility in water; it only dissolves at very low concentrations.

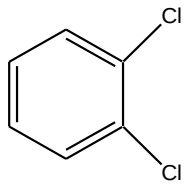

Figure 6.50: *Chemical structure of 1,2 dichlorobenzene.*

The investigation of the effect of contact time between the pollutants dissolved in water and the fibrous membranes was studied upon immersing small membrane pieces in MET and DCB aqueous solutions of known concentrations and recording the UV-vis spectra of the supernatant at different time intervals.

Figure 6.51 provides the UV-vis spectra obtained at different times intervals for **(a)** the MET and **(b)** the DCB aqueous supernatant solutions as well as the normalized absorption *versus* time plots (A_t/A_0 *vs* t, where A_t denotes the absorption of the MET or DCB molecules found free in solution at time t, and A_0 corresponds to the initial absorption (at t=0) of the MET o DCB molecules found free in solution) for **(c)** MET and **(d)** DCB. The concentration of the non-adsorbed pollutant was determined at λ_{max} (MET at ~ 320 nm and DCB at ~ 216.5 nm) of the recording UV-vis absorption spectra using the UV-vis calibration curves (ε=60.55385±1.24702 $mL \cdot mg^{-1} \cdot cm^{-1}$ or 0.3537±7.28·10^{-3} $L \cdot mol^{-1} \cdot cm^{-1}$ for MET and ε=3.43187±0.16994 $mL \cdot mg^{-1} \cdot cm^{-1}$ or 6.8·10^{-3}±9.31645·10^{-19} $L \cdot mol^{-1} \cdot cm^{-1}$ for DCB), as in the other adsorption-related experiments.

As seen from the UV-vis plots **(figure 6.51 (a))** the intensity of the characteristic absorption signal of DCB appearing at ~ 217 nm reduced with time, indicating pollutant adsorption from the MMA-*co*-BzMA fibrous membranes reaching 20% in 150 min (kinetic constant k=3.429·10^{-2}±3.522·10^{-3} min^{-1}). Nevertheless, in the case of MET **(figure 6.50 (b))** the absorption intensity remained relatively unchanged indicating the disfavorable adsorption of MET from the fibrous membrane reaching only 6% in 150 min (kinetic

constant $k=7.898\cdot10^{-2}\pm2.04\cdot10^{-3}$ min^{-1}). The preferential adsorption of DCB over MET by the membrane may be attributed to the development of π-π interactions between the aromatic rings existing in the DCB and in the BzMA moieties of the copolymer MMA-*co*-BzMA.

Hydrophobic interactions play an important role in the adsorption of pollutants from aqueous media. However, a highly hydrophobic adsorbent may exhibit wetting difficulties when placed in an aqueous environment that in turn may reduce its active surface area. The incorporation of PEO within the PEO/MMA-*co*-BzMA blended membranes was found to significantly improve the adsorption efficiency of the membranes (75% kinetic constant: $k=4.333\cdot10^{-2}\pm5.279\cdot10^{-3}$ min^{-1}) (**figure 51 (d)**). A possible explanation is that the dissolution of the PEO chains upon immersing the membrane in water increases the number of voids between the fibers facilitating the diffusion of the aqueous solution within the membrane.

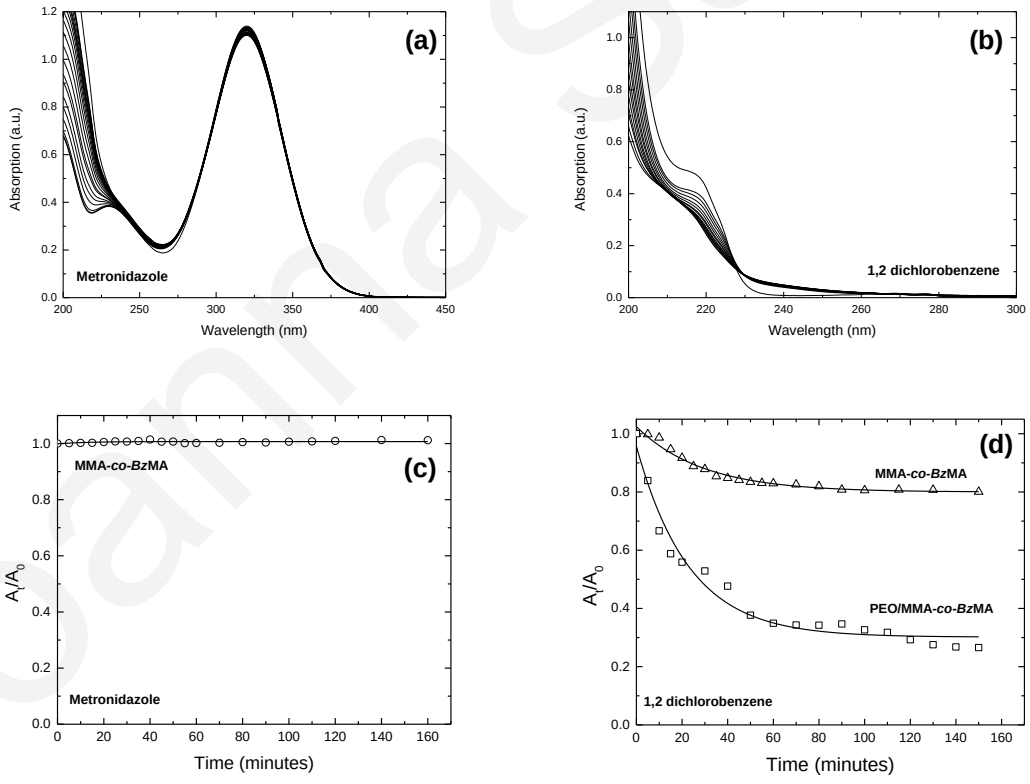

Figure 6.51: *UV-vis spectra of* ***(a)*** *MET and* ***(b)*** *DCB supernatant solutions recorded at different time intervals. Normalized A_t/A_0 versus time plots, corresponding to the adsorption profile of* ***(c)*** *MET, and* ***(d)*** *DCB by the MMA-co-BzMA and PEO/MMA-co-BzMA membranes.*

6.3. PVP-based electrospun membranes: Fabrication, characterization and catalytic applications

The fabrication and characterization of electrospun membranes based on the hydrophilic and biocompatible poly(vinyl pyrrolidone) (PVP) **(figure 6.52)** (44) is described in this section.

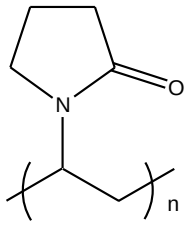

Figure 6.52: Chemical structure of poly(vinyl pyrrolidone) (PVP).

6.3.1. PVP, PVP/PLLA and PVP/PLLA/OA.Fe_3O_4 electrospun membranes

Initially PVP was combined with the hydrophobic and biodegradable poly(L-lactide) (PLLA) and pre-formed oleic acid-coated iron oxide NPs (OA.Fe_3O_4), allowing the development of PVP/PLLA/OA.Fe_3O_4 magnetoactive fibrous nanocomposites (174).

6.3.1.1. Membrane fabrication

Fibrous membranes comprised of PVP **(figure 6.52)**, PVP/PLLA and PVP/PLLA/OA.Fe_3O_4 were prepared by electrospinning. For determining the optimum electrospinning conditions to obtain fibrous (nanocomposite) membranes, different experimental parameters were systematically varied while maintaining the rest relatively unchanged. Experimental parametric studies were carried out for the PVP (polymer-solution concentration: 3, 5, 10, 15% w/v) and the PVP/PLLA (weight percentage proportion:70/30, polymer-solution concentration: 10% w/v) systems in the absence and presence of the magnetic NPs prepared in $CHCl_3$ solution. Under specific experimental conditions, fibrous PVP and PVP/PLLA membranes, as well as magnetite-containing membranes with different magnetic loading (OA.Fe_3O_4 5, 10, and 20% wt.) were

successfully obtained by electrospinning. **Table 6.9** summarizes the optimum experimental electrospinning conditions employed for the fabrication of the above-mentioned systems.

Table 6.9: *Optimum experimental conditions employed for the fabrication of the PVP and PVP/PLLA fibrous membranes in the absence and presence of OA.Fe_3O_4.*

a/a	Sample code	Polymer-solution concentration (w/v)	Needle (G)	Flow rate ($mL \cdot h^{-1}$)	Voltage (kV)	Needle-to-collector distance (cm)
1	PVP	3	16	20	15	25
2	PVP	5	20	15	15	25
3	PVP	10	22	10	20	30
4	PVP	15	20	10	20	25
5	PVP/PLLA	10	20	10	25	30
7	PVP/PLLA/OA.Fe_3O_4 5% wt.	10	20	10	15	25
8	PVP/PLLA /OA.Fe_3O_4 10% wt.	10	20	10	10	25
9	PVP/PLLA /OA.Fe_3O_4 20% wt.	10	20	10	10	25

6.3.1.2. Membrane characterization

Morphological characterization: The morphological characteristics of the membranes were determined by SEM. Initially, parametric studies were carried out for the PVP homopolymer upon systematically increasing the polymer-solution concentration from 3 to 15% w/v. As already mentioned variations in polymer polymer-solution concentration significantly influence the size and morphology of the fibers (57; 58; 59; 367; 138). According to literature reports (43; 37; 39) it is expected that at lower polymer polymer-solution concentrations, fragmentation of the charged jet occurs leading to the generation of droplets as a result of the applied voltage and the solution's surface tension (57). As the concentration of the polymer solution increases, a mixture of fibers and beads is obtained, while a further increase causes the morphological transition of the beads from spherical to ellipsoidal and finally to continuous fibers, owing to chain entanglement effects arising in concentrated solutions.

Indeed as shown in **figure 6.53 (a)**, starting from the low concentration solutions (3 and 5% w/v), the co-existence of fibrous and beaded structures is observed with the latter being the dominant ones, whereas upon increasing the polymer-solution concentration the fibrous morphology dominates. As seen in the figure, an increase of the polymer-solution concentration to 15% w/v leads to the disappearance of the beaded structures and the generation of continuous fibers with mean diameters of ~ 7-8 μm.

The SEM images of the produced PVP/PLLA membranes and of the nanocomposite PVP/PLLA/OA.Fe_3O_4 membranes containing OA.Fe_3O_4 in concentration 5, 10 and 20% wt. are also provided in **figures 6.53 (b)** and **(c)** respectively. In all cases the polymer-solution concentration was maintained at 10 % w/v since at this concentration continuous fibers were obtained with mean diameters in the range of ~ 5.5 μm – 8.5 μm. Upon increasing the magnetic content from 5 to 20% wt., no significant changes were observed in the morphological characteristics of the fibers in line with previously reported results (151).

(a) PVP, polymer-solution concentration: 3, 5, 10, and 15% w/v in $CHCl_3$

3% **5%** **10%** **15%**

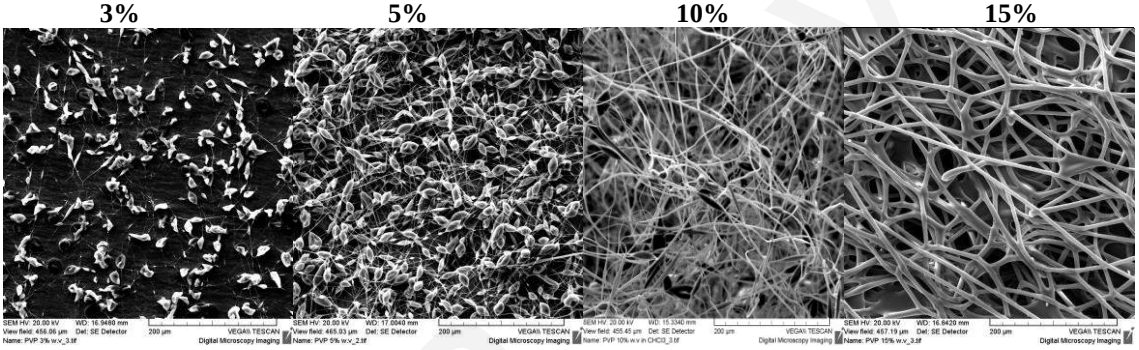

(b) PVP/PLLA, polymer-solution concentration: 10 w/v in $CHCl_3$

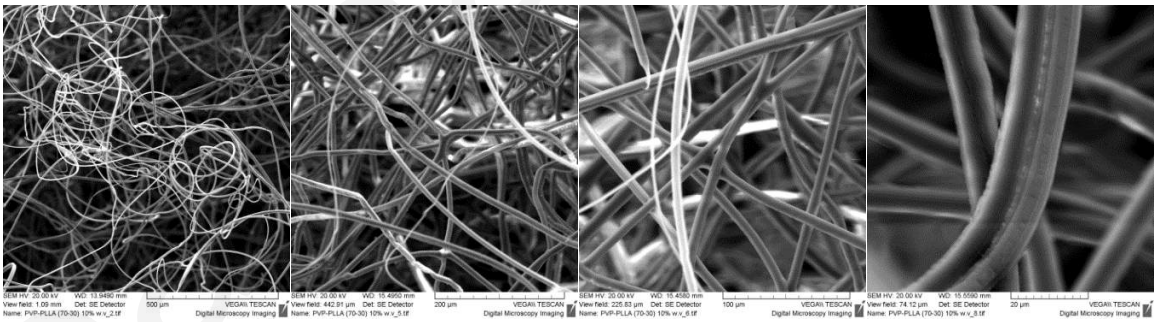

(c) PVP/PLLA/OA.Fe_3O_4 (5, 10, and 20% wt.), polymer-solution concentration: 10 w/v in $CHCl_3$

5%

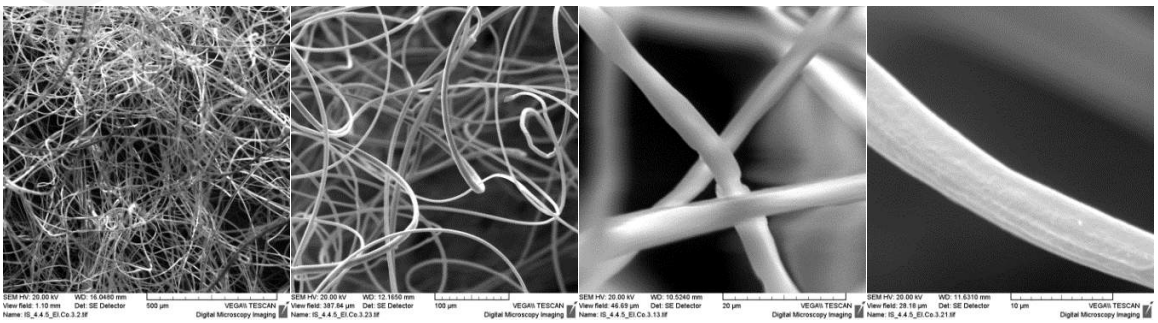

10%

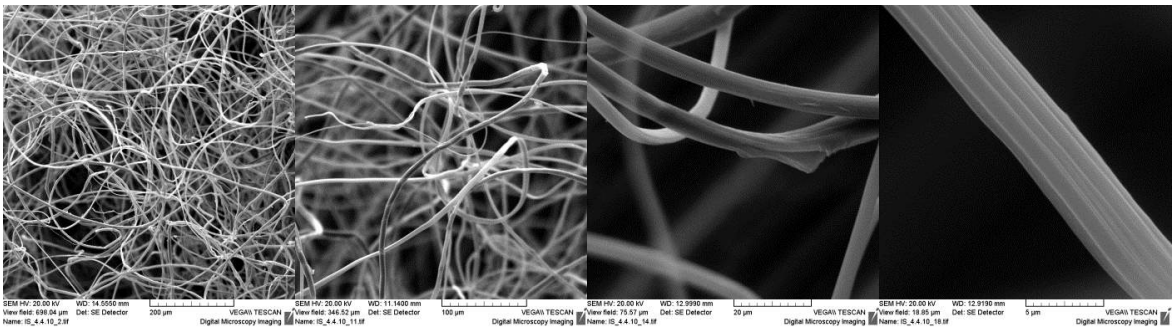

20%

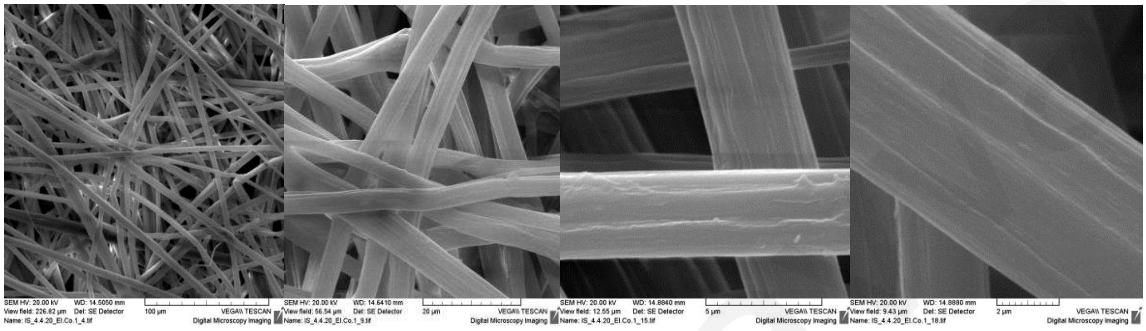

Figure 6.53: *SEM images of the pristine **(a)** PVP and **(b)** PVP/PLLA electrospun polymer membranes as well as **(c)** of the magnetoactive PVP/PLLA/OA.Fe_3O_4 analogues obtained in the presence of OA.Fe_3O_4 NPs 5, 10 and 20% wt.*

TEM was also employed for visualizing the PVP/PLLA/OA.Fe_3O_4 systems. In **figure 6.54** transmission electron micrographs of the PVP/PLLA/OA.Fe_3O_4 nanocomposite fibrous membranes containing OA.Fe_3O_4 20% wt. NPs are depicted. From the TEM bright field images **(figure 6.54 (a)**, **(b)**, and **(c))** it can be clearly seen that the magnetic Fe_3O_4 NPs embedded within the membranes are spherical with average diameters of approximately 5 nm. By comparing the TEM images and size distribution of the as-prepared OA.Fe_3O_4 NPs provided in a recent publication (328) with the mean diameters of the NPs embedded within the PVP/PLLA fibers, it can be concluded that no significant agglomeration phenomena occur during the electrospinning process since the dimensions of the embedded NPs are retained within the same range.

Moreover, the magnetic NPs are uniformly dispersed in the PVP/PLLA matrix resulting in high homogeneity. The HRTEM image presented in **figure 6.54 (d)** showed that the NPs are nanocrystals, disclosing the crystalline planes (311) of Fe_3O_4 with 2.51 Å characteristic interplanar distance.

The EDX spectrum presented in **figure 6.54 (e)** shows the presence of Fe, O and C as the major elements in the sample (element Cu comes from the copper grid). The presence of minor elements such as Si and Cl may be attributed to mild sample contamination during the preparation process for TEM investigations.

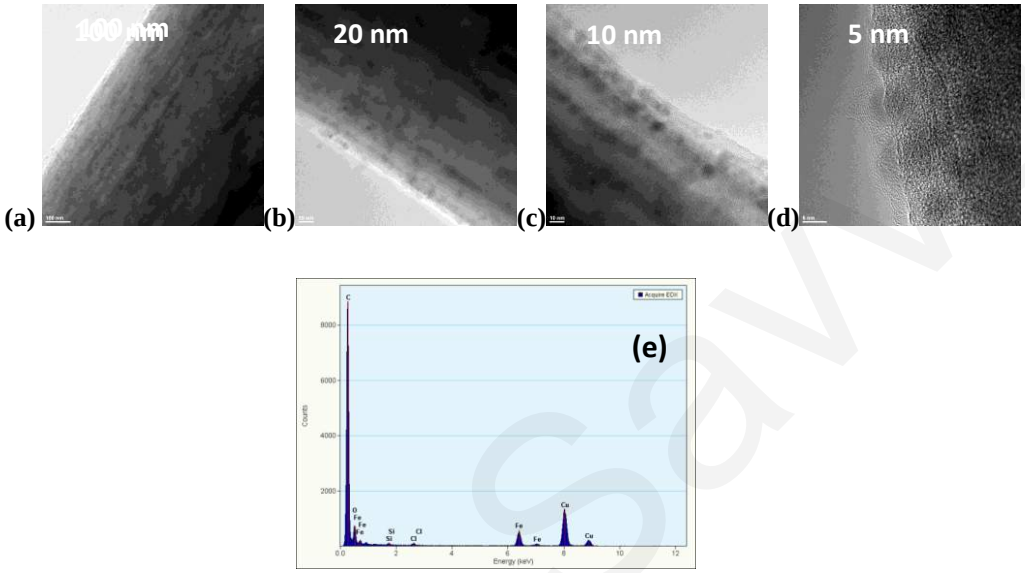

Figure 6.54: (a, b, c) *TEM bright field and* ***(d)*** *HRTEM images and* ***(e)*** *corresponding EDX spectrum of the PVP/PLLA/OA.Fe_3O_4 polymeric membranes in the presence of OA.Fe_3O_4 NPs 20% wt.*

Thermal properties: The thermal stability of the PVP/PLLA membranes was determined in the presence and absence of OA.Fe_3O_4 NPs by means of TGA. The degradation profiles of the pure OA.Fe_3O_4, the pristine PVP/PLLA and the nanocomposite PVP/PLLA/OA.Fe_3O_4 fibrous membranes are provided in **figure 6.55**. In the case of the pure OA.Fe_3O_4 the weight loss observed at temperatures below 300 °C, is attributed to the decomposition of the organic stabilizing layer (oleic acid) (329). Two-step decomposition profile is observed in the case of the PVP/PLLA membranes. The first degradation step is observed at around 320 °C, and it is attributed to the decomposition temperature of PLLA in agreement with previously reports (372; 373). PVP degradates at a higher temperature (~ 470 °C) in line with previously reported findings (374). The remaining residue observed in the case of the magnetite-containing membrane at higher temperatures (T > 400 °C), corresponds to the inorganic (Fe_3O_4) content.

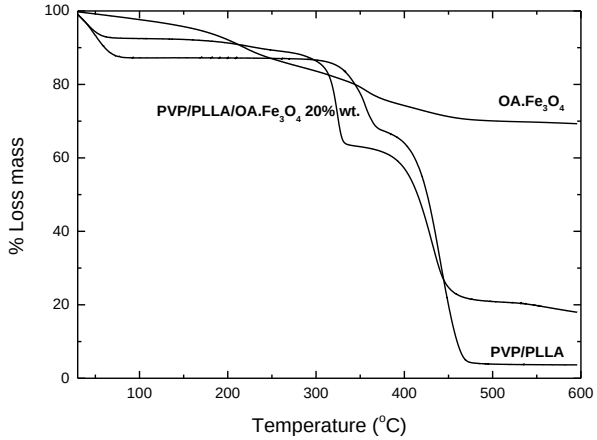

Figure 6.55: *TGA thermograms of OA.Fe_3O_4 NPs, PVP/PLLA and PVP/PLLA/OA.Fe_3O_4 20% wt.*

Magnetic properties: Investigation of the magnetic properties of the PVP/PLLA/OA.Fe_3O_4 nanocomposite fibrous membranes was carried out by VSM at 300 K. **Figure 6.5** shows the magnetization *versus* applied magnetic field strength plots (M=*f*(H)) corresponding to nanocomposite membranes loaded with different amounts of OA.Fe_3O_4 (5 and 10% wt.). The sigmoidal shape of these plots and the lack of a hysteresis loop demonstrates the superparamagnetic behavior of these materials at ambient temperature. Moreover tunability of the saturation magnetization (M_s) is possible upon varying the magnetic content within the membranes, retaining at the same time the superparamagnetic response.

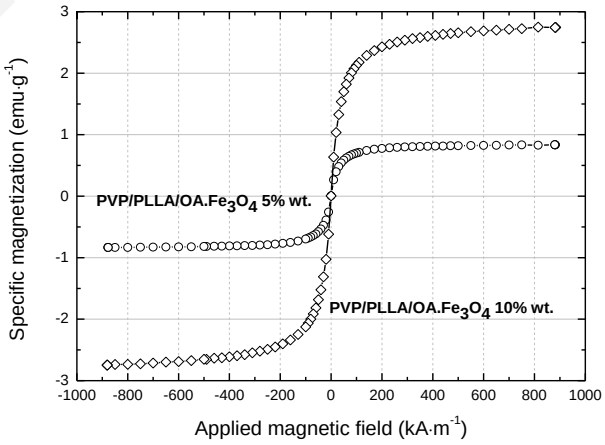

Figure 6.56: *Magnetization curves of the PVP/PLLA/OA.Fe_3O_4 nanocomposite membranes containing OA.Fe_3O_4 5 and 10% wt. measured at 300 K.*

These novel magnetoactive PVP/PLLA/OA.Fe_3O_4 fibrous nanocomposite membranes consisting of microfibers with embedded, uniformly dispersed magnetite NPs could be further crosslinked either *via* UV-irradiation (photo-crosslinking) or thermally for the development of fibrous materials exhibiting high stability in aqueous media that could be further employed in biomedical and environmental applications.

6.3.2. PVP/Pd and PVP/Cu_2O electrospun nanocomposite membranes

PVP-based microfibrous nanocomposite membranes with embedded palladium (Pd) and copper (I) oxide (Cu_2O) NPs were prepared and evaluated as heterogeneous catalytic supports in Heck, Suzuki and click chemistry reactions. While two recent reports describe the evaluation of PVP-Pd electrospun fibers in Heck reaction processes (259; 260), no other couplings have appeared in the literature using this type of polymer-based catalytic support. In addition, to the best of our knowledge there are no reports on the fabrication and characterization of Cu_2O NP immobilized on electrospun PVP fibrous matrices that have been evaluated as catalytic supports in click chemistry reaction processes (375).

6.3.2.1. Preparation and characterization of PVP-Pd, PVP-Cu and PVP-Cu_2O colloidal solutions

The PVP-coated Pd and Cu metal NPs have been prepared in the form of stable colloidal solutions by following previously reported synthetic methods (376; 377) as already described in the experimental section. The reaction process involved the reduction of Pd(II) ions into metallic Pd(0) NP in refluxing MeOH that functions as both, solvent and reducing agent in the presence of PVP acting as a steric stabilizer, whereas in the case of the Cu(II) ions, hydrazine monohydrate was introduced as a reducing agent for generating metallic PVP-capped Cu(0) NPs as shown in **figure 6.57**.

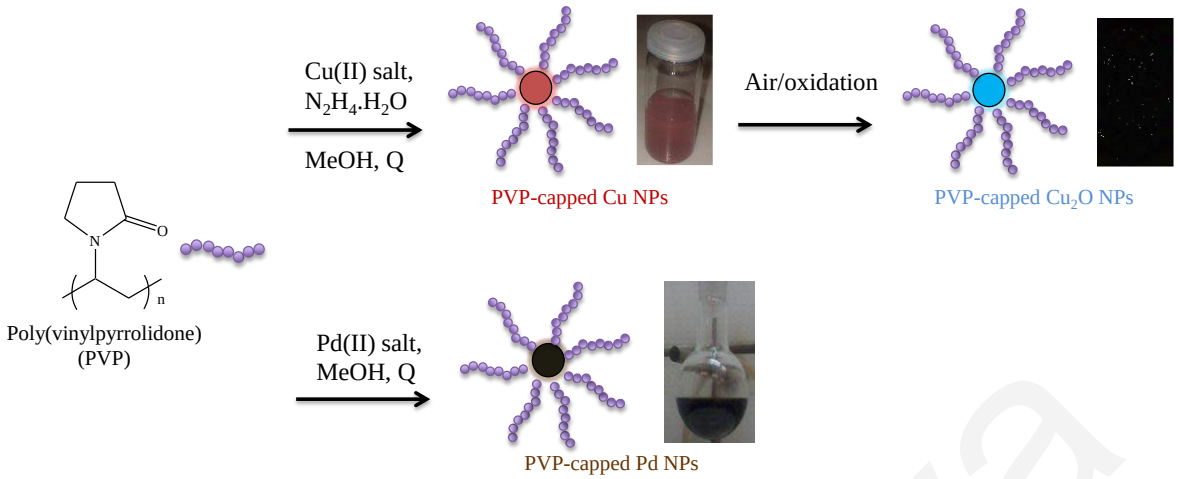

Figure 6.57: *Schematic presentation of the synthetic pathways followed for the generation of the PVP-Pd, PVP-Cu and PVP-Cu_2O colloidal solutions stabilized in MeOH and corresponding photographs.*

The PVP, PVP-Pd and PVP-Cu MeOH solutions were characterised by UV-vis spectrophotometry and the related spectra are provided in **figure 6.58**. The broad absorption tail appearing between 300 – 800 nm is typical for Pd metal NP colloidal systems (378; 379) whereas in the case of the Cu-containing solutions the characteristic surface plasmon resonance (SPR) signal appears at around 580 nm, indicating the existence of Cu MNP in solution (380). When the freshly prepared PVP-Cu colloidal solution was exposed to air, a gradual colour change of the colloidal solution from red to light blue (see related photographs in **figure 6.57**) was observed, indicating the oxidation of the Cu NP to Cu_2O NP. Similar solution colour change observations (i.e. from red to light blue) were previously reported for oleyamine-coated Cu NPs that have been transformed into Cu_2O NPs (381).

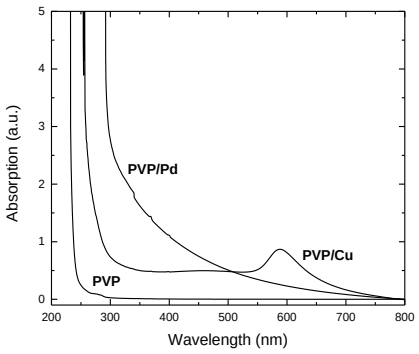

Figure 6.58: *UV-vis spectra of the pristine PVP MeOH solution and the PVP-Pd and PVP-Cu hybrid colloidal solutions (recorded upon appropriate dilution of the as-prepared colloidal solutions).*

6.3.2.2. Membrane fabrication

Fibrous membranes comprised of PVP and either Pd or Cu_2O NPs were prepared by electrospinning as schematically depicted in **figure 6.59**.

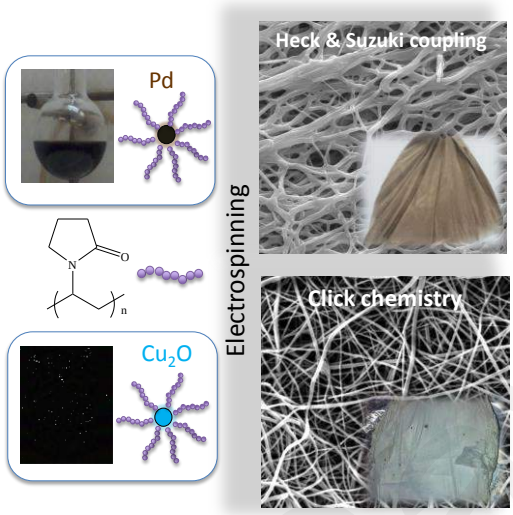

Figure 6.59: *Schematic presentation of the process used for the fabrication of the PVP-Pd and the PVP-Cu_2O nanocomposite membranes starting from colloidal nanohybrid solutions. Photographs show the solutions and the corresponding electrospun nanocomposite membranes.*

Systematic parametric studies involved varying the polymer-solution concentration, the applied voltage, the delivery rate of the solution, the diameter of the needle and the needle-to-collector distance, so as to determine the optimum experimental conditions for the production of fibrous polymer-metal or metal oxide NP nanocomposite membranes. In **table 6.10** the optimum electrospinning parameters used for the production of fibrous PVP-Pd and PVP-Cu_2O electrospun membranes are provided.

Table 6.10: *Optimum experimental parameters employed for the fabrication of the nanocomposite PVP-Pd and PVP-Cu_2O electrospun fibrous membranes.*

a/a	Sample Code	Needle (G)	Flow rate ($mL \cdot h^{-1}$)	Voltage (kV)	Needle-to-Collector Distance (cm)
1	PVP	18	3.0	20	20
2	PVP-Pd (20:1)*	16	5.0	15	20
3	PVP-Cu_2O (3.6:1)*	16	2.5	20	10

**Mole ratio of VP units to the metal ion salt*

6.3.2.3. Membrane characterization

The morphological characteristics of the membranes were determined by SEM and TEM. As seen in the SEM images presented in **figure 6.60**, in all cases continuous, beaded-free cylindrical fibers were obtained under the optimum electrospinning conditions employed. Moreover, no significant changes were observed in the morphology of the fibers in the presence of the embedded Pd and Cu_2O NPs.

(a) PVP

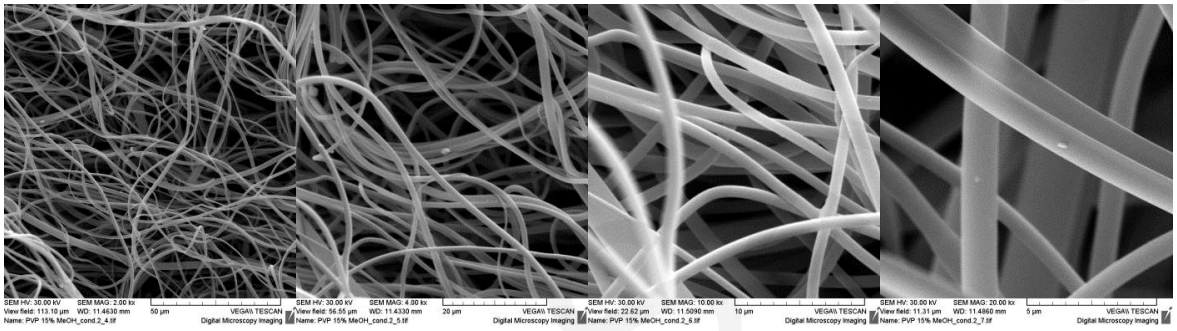

(b) PVP-Pd

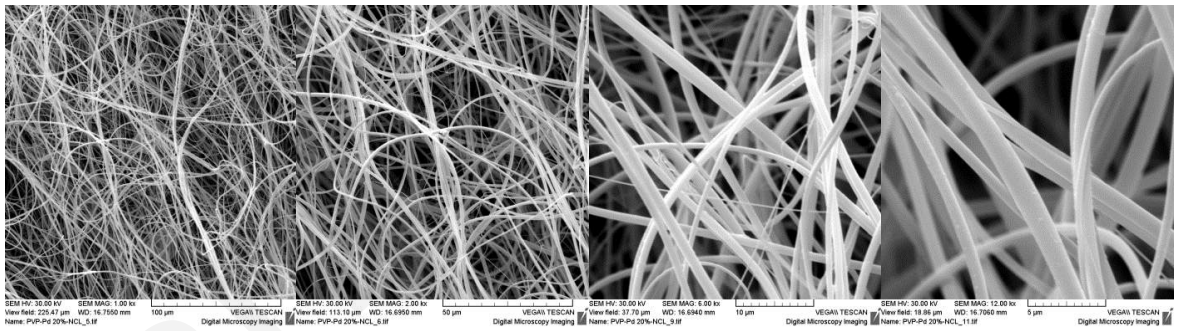

(c) PVP-Cu_2O

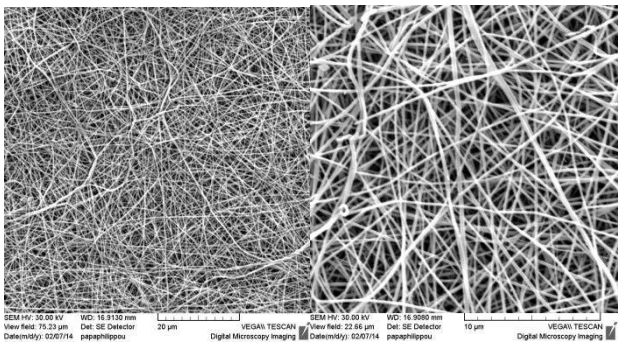

Figure 6.60: *SEM images of **(a)** the pristine PVP, **(b)** the PVP-Pd and **(c)** the PVP-Cu_2O nanocomposite electrospun fibrous membranes.*

The as-prepared Pd- and Cu_2O-containing fibrous nanocomposites were also visualized by TEM **(figure 6.61)**. From the TEM bright field images **(figure 6.61 (a), (b), (f-h))** it can be clearly seen that the inorganic NPs embedded within the membranes are spherical in shape with average diameters of ~ 5 nm. Moreover, a distinct dispersion of the NP in the PVP fibrous matrix resulting in high homogeneity can be observed in both cases. HRTEM analysis was only feasible in the case of the PVP-Pd membranes whereas the PVP-Cu_2O system exhibited high instability in the electron beam. The Pd NPs embedded within the fibrous PVP matrix are nanocrystals and HRTEM imaging **(figure 6.61 (c-d))** discloses the crystalline planes (111) and (200) of Pd NP with characteristic interplanar distances of 2.27 and 1.97 Å, respectively. In addition, the EDX spectrum corresponding to the PVP-Pd system **(figure 6.61 (e))** shows the presence of Pd and O as the major elements in the sample. The presence of Cu is attributed to the Cu grid employed in TEM investigations. In the case of the PVP-Cu_2O, the EDX analysis cannot provide any useful information since Cu grid is employed during sample analysis and the expected oxygen can be found both in the polymer matrix and in the Cu_2O NPs.

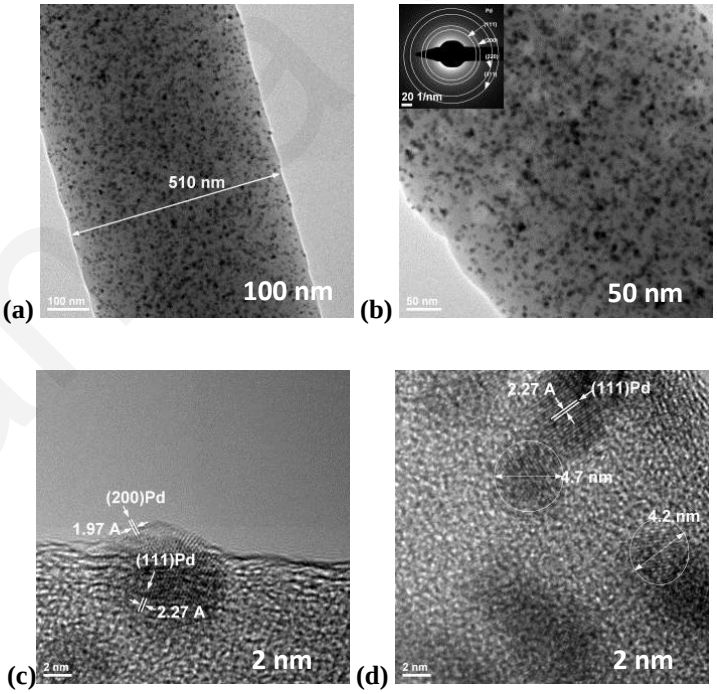

(a) **(b)** **(c)** **(d)**

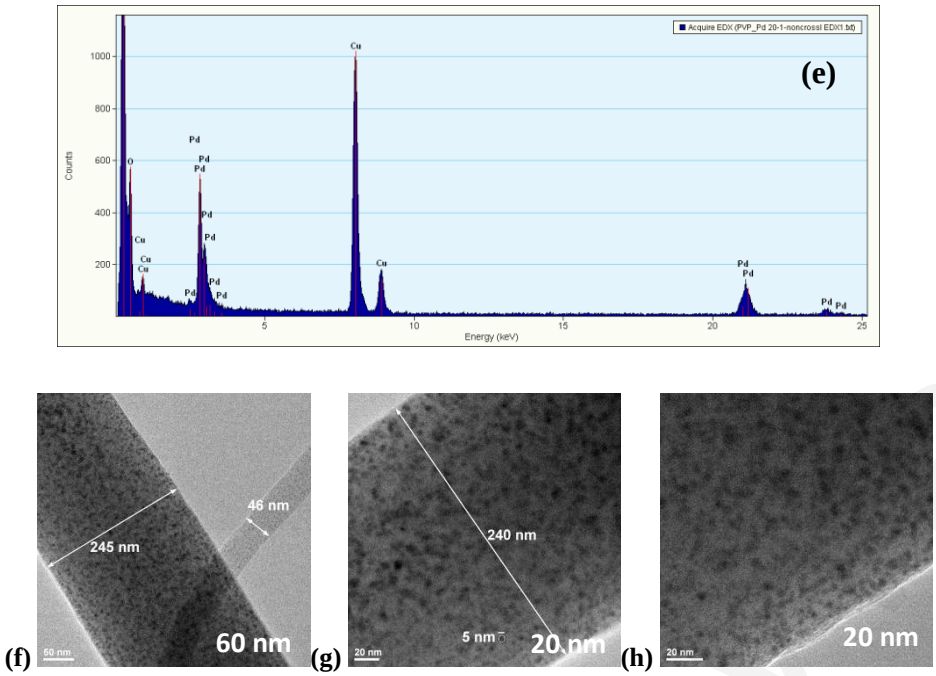

Figure 6.61: ***(a, b)*** *TEM bright field and* ***(c, d)*** *HRTEM images of the as-prepared PVP-Pd nanocomposite electrospun membranes.* ***(f-h)*** *TEM bright field images of the as-prepared PVP-Cu_2O membranes.* ***(e)*** *EDX spectrum of the PVP-Pd electrospun membrane.*

For preventing membrane dissolution and consequently NP leaching in the organic media used for performing selected organic reactions by introducing the aforementioned materials as heterogeneous catalytic supports, thermal crosslinking of the membranes was carried out. The morphology and compositional characteristics of the nanocomposite fibers after thermal treatment were determined by means of SEM and TEM/EDX analysis.

SEM images of the thermally-induced crosslinked PVP-Pd and PVP-Cu_2O electrospun nanocomposite membranes **(figure 6.62 (a)** and **(b))** indicate that the membranes maintained their cylindrical shape and that no significant morphology changes were observed compared to the non-crosslinked systems. After thermal treatment the membranes were immersed in an aqueous solution where no membrane dissolution was observed (as in the case of the non-crosslinked analogues that are water-soluble due to the hydrophilic character of PVP) **(figure 6.62 (c))** indicating that the crosslinking process was successful.

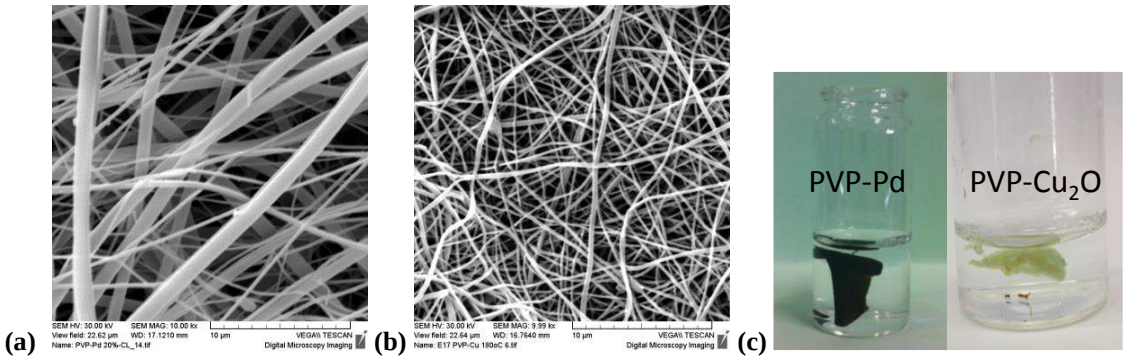

Figure 6.62: ***(a)*** *SEM images of the PVP-Pd and* ***(b)*** *PVP-Cu_2O crosslinked nanocomposite membranes (before reactions).* ***(c)*** *Photographs of the PVP-Pd and the PVP-Cu_2O membranes immersed in water after crosslinking.*

In **figure 6.63** the corresponding TEM images accompanied by EDX analysis spectra are provided. Owing to the superior stability of the crosslinked materials compared to the non-crosslinked ones, it was possible to perform HRTEM analysis on both systems that confirmed the existence of Cu_2O NP within the PVP-Cu_2O membranes. As in the case of the non-crosslinked PVP-Pd electrospun membranes, spherical Pd nanocrystals embedded within the crosslinked PVP matrix can be visualized in the bright field TEM images provided in **figure 6.63 (a), (b)** while HRTEM discloses the characteristic crystalline planes of Pd NP **(figure 6.63 (c), (d))**. The presence of the Pd NP within the crosslinked membranes has been also verified by EDX analysis **(figure 6.63 (e))**. HRTEM confirmed the existence of Cu_2O NP in the PVP-Cu_2O crosslinked membranes **(figure 6.63 (i))** since the characteristic crystalline planes (110) and (111) of Cu_2O NP with respective 3.02 and 3.47 Å interplanar distances can be clearly seen.

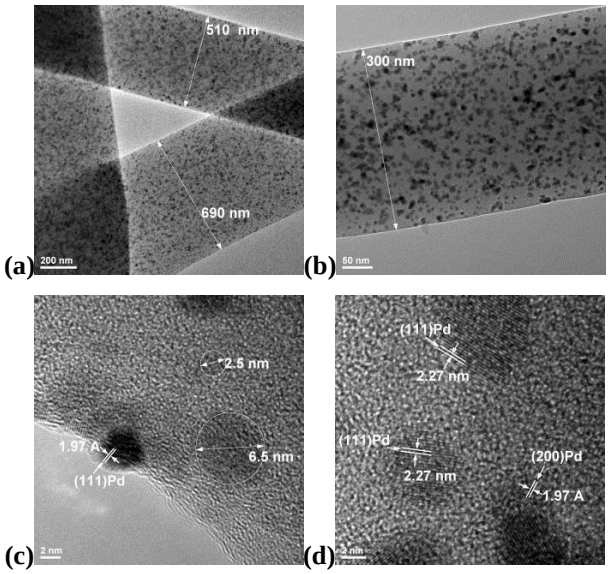

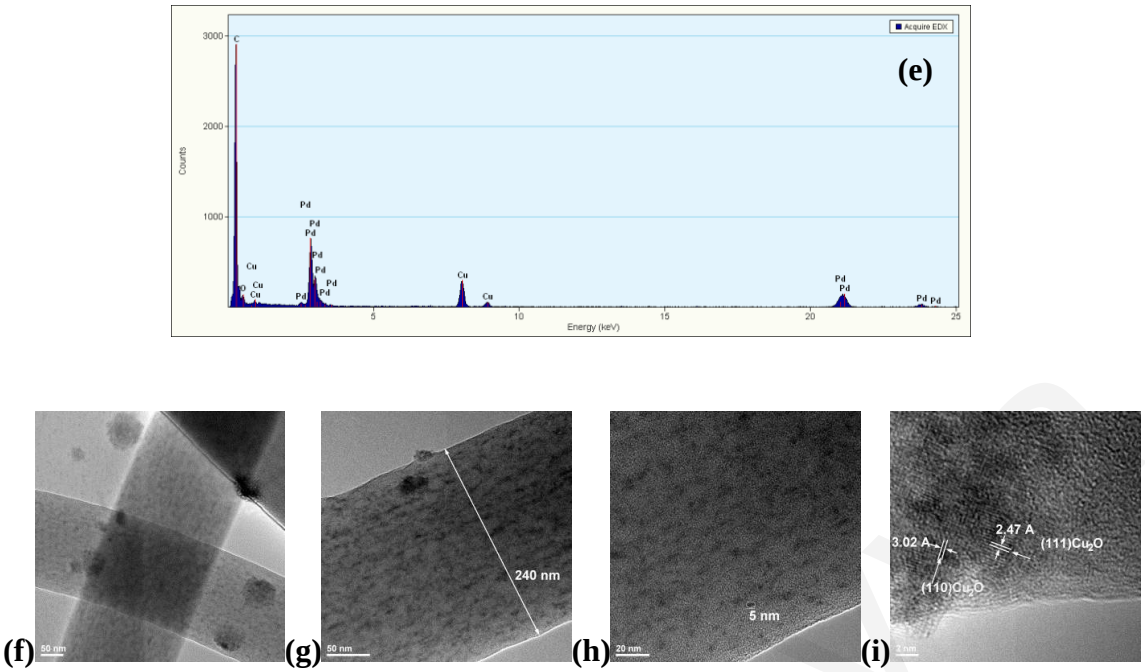

Figure 6.63: ***(a, b)*** *Bright field and* ***(c)*** *high resolution TEM images, and* ***(d)*** *corresponding EDX spectrum of the PVP-Pd crosslinked electrospun nanocomposite membrane.* ***(e, f)*** *Bright field and* ***(g)*** *high resolution TEM images of the PVP-Cu_2O crosslinked electrospun nanocomposite membrane.*

6.3.2.4. Membrane application in heterogeneous catalysis

Heck reactions: In the course of our current research, the use of electrospun PVP-Pd membranes in performing a Heck coupling reaction was first reported by Bai and co-workers (259). As such, we used identical reaction conditions to perform the reaction of phenyl iodide with butyl acrylate. The authors performed the reaction of phenyl iodide with butyl acrylate in DMF with 7.4 mol % Pd and obtained a 99% conversion of acrylate **1** (**scheme 6.7**) after 23 h reaction time. Moreover, they could recover their catalyst and use it repeatedly without loss of activity after washing several times with EtOH and water.

Having in our hands both a crosslinked and a non-crosslinked membrane containing Pd NPs, we performed the same Heck reaction, using 1.5 equivalent of the acrylate, 2.7 equivalent of Et_3N and 7.4 mol % Pd from the either crosslinked or non-crosslinked material. After 14 h we observed complete consumption of the starting iodide and the formation of product **1** in 88% yield (isolated yield) with both catalysts used **(scheme 6.7)**. Under these conditions the non-crosslinked membrane dissolved to give a dark brown coloured solution as expected. The crosslinked membrane demonstrated higher tolerance in the reaction conditions employed (DMF, 125 °C, reaction time: 14 hr). An attempt to

isolate the polymer catalysts by filtration upon completion of the reaction led to low recoveries of up to ~ 60%.

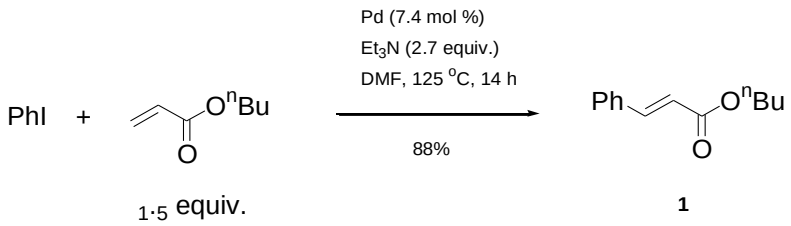

Scheme 6.7: *Heck reaction between iodobenzene and n-Butyl acrylate using the PVP-Pd electrospun membrane as heterogeneous catalytic support.*

A better way to isolate the catalyst was required, as well as a reduction of catalyst loading that would prove the usability of the method. Using a lower loading of Pd (2.4 mol %) and reducing the reaction temperature to 100 °C the reaction was successful with both the crosslinked and the non-crosslinked polymer systems, giving good yields of product **(table 6.11)**. Most importantly, a change in reaction work-up allowed the recovery and reuse of the colloidal PVP-Pd nanocatalyst generated *via* dissolution of the membranes under the reaction conditions employed. In order to verify whether the catalysts could be reused and whether there was any notable difference between the two catalytic systems, the reaction was repeated up to three times. Gratifyingly, both catalysts were active even during the 3rd run and gave consistent high yields of product.

Table 6.11: *Heck reaction with PVP-Pd electrospun membranes.*

Heck reaction with PVP-Pd electrospun membranes

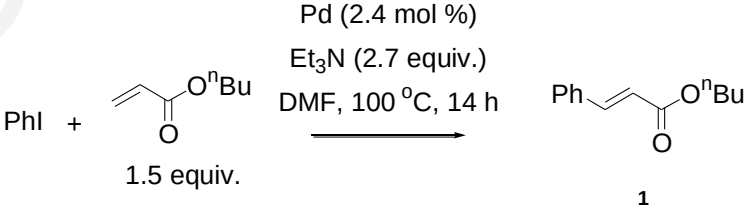

Reaction run	Electrospun membrane	Yield of **1** (%)
1	Crosslinked	97
2	"	88
3	"	89
1	Non-Crosslinked	98
2	"	96
3	"	95

The reactions involving the crosslinked material showed a marked drop in product yield (from 97% in run 1 to 88 and 89% in runs 2 and 3), however, a similar drop was not observed with the non-crosslinked membrane. This phenomenon may be due to a partial destruction of the membrane morphology under the reaction conditions employed that may have led to a reduction in its active surface area and consequently to a decrease in its catalytic efficacy. To verify this hypothesis SEM analysis was performed on the crosslinked PVP-Pd membrane recovered after 3 consecutive reaction runs. Indeed, as seen in the SEM images provided in **figure 6.64 (b)**, cylindrical fibers with larger mean diameters compared to the as-prepared crosslinked analogue **(figure 6.64 (a))** were obtained after 3 reaction runs. The above-mentioned problem may be overcome by performing the Heck reaction in different organic solvents or under milder reaction conditions.

(a) 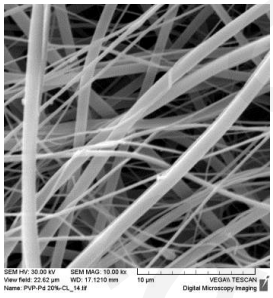 **(b)** 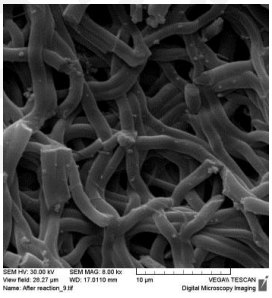

Figure 6.64: *SEM images of **(a)** the as-prepared PVP-Pd crosslinked membrane and **(b)** the crosslinked PVP-Pd membrane recovered after 3 reaction runs.*

Suzuki reaction: To further evaluate the versatility of the crosslinked PVP-Pd electrospun fibers as coupling agents, a classical Suzuki reaction was then attempted. The Suzuki reaction between phenylboronic acid and 4-iodoanisole was successful in the absence of a phosphine ligand, using THF and water as the reaction solvents. Furthermore, the reusability of the catalyst was briefly investigated with up to 3 consecutive coupling reaction runs being effective. Interestingly, after three reaction cycles a gradual increase of the reaction time was observed indicating a drop in the reactivity of the catalyst. However, even in this case the obtained yields of the product (4-methoxybiphenyl, **2** – **scheme 6.8**) were still high (> 92%)**.**

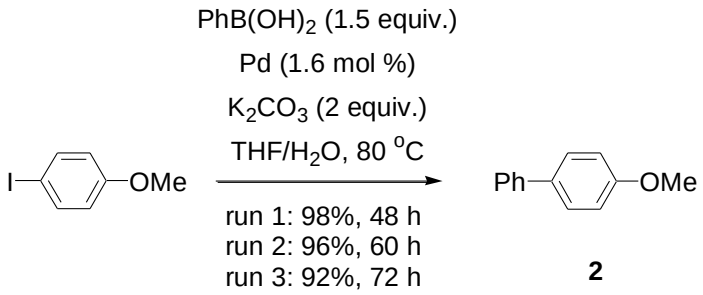

Scheme 6.8: *Suzuki reaction between 4-iodoanisole and phenylboronic acid performed in the presence of the crosslinked PVP-Pd membrane.*

Click chemistry: The well-known click chemistry is used to afford inert triazole units from Huisgen [3+2] cycloadditions between organic azides and terminal alkynes and it is catalysed by copper(I) salts (382). Some of the click reaction strategies that have been developed involve apart from the introduction of Cu(I) salts, their generation *in situ* from Cu(II) in the presence of a reducing agent as well as from metallic copper oxidized *in situ* by air (383). An improvement to this procedure has been the use of solid supported copper NPs which results in reusable catalysts and reduces both the amount of copper needed in catalysis and also copper contamination of the products (384). This first use of electrospun PVP-Cu_2O NPs expands the usability and flexibility of this reaction.

The click reaction between benzyl azide and phenylacetylene in the presence of Et_3N and PVP-Cu_2O electrospun nanocomposite membranes (crosslinked) was investigated. The reaction was successful with the starting materials been consumed within 2 h and the product 1-benzyl-4-phenyl-1*H*-1,2,3-triazole (**3**) was isolated in 87% yield (**scheme 6.9**). The polymer catalyst was reused in three consecutive reaction runs, and a small drop in product yield was observed indicating a gradual loss of catalyst reactivity over consecutive runs **(scheme 6.9)**. SEM characterisation of the crosslinked PVP-Cu_2O membranes after 3 runs revealed that although the fibers retain their cylindrical shape they tend to merge **(figure 6.65)**, in line with the above-discussed results on the PVP-Pd crosslinked membrane employed in the Heck reaction processes.

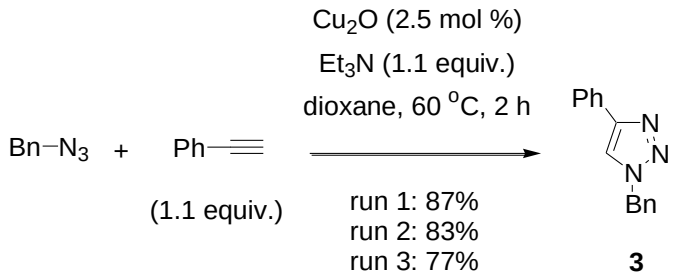

Scheme 6.9: *Click reaction between benzyl azide and phenylacetylene performed in the presence of the crosslinked PVP-Cu_2O electrospun nanocomposite membrane.*

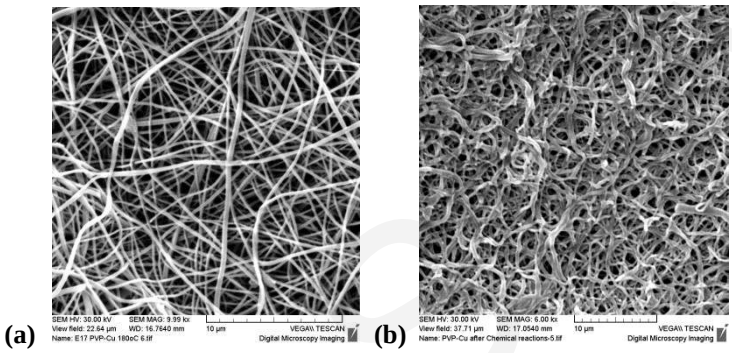

Figure 6.65: *SEM images of the **(a)** as-prepared PVP-Cu_2O crosslinked electrospun membrane and **(b)** the crosslinked PVP-Cu_2O membrane upon completion of the click reactions (after 3 reaction cycles).*

In conclusion, catalytic Pd and Cu_2O NP have been immobilized into electrospun PVP crosslinked mats and the resulting fibrous nanocomposites were evaluated as heterogeneous catalytic supports in Heck, Suzuki (PVP-Pd) and click chemistry (PVP-Cu_2O) reactions. By employing a new recovery protocol, the crosslinked membranes can be easily recovered and re-used as demonstrated by the fact that they remained catalytically active even after 3 consecutive reaction runs exhibiting high catalytic efficiencies in all cases. The high versatility of PVP to act as effective steric stabiliser for various NPs in organic solvents (including Ag, Au, Cu, Pd, Cu_2O etc.) allowing for their intermixing within a single electrospun fibrous membrane, creates new prospects for the future development of multifunctional electrospun catalytic supports.

7

Conclusions

In the present work, novel electrospun fibrous membranes comprised of polymers with specific functionalities combined or not with inorganic nanoparticulate systems were fabricated, characterized and evaluated in drug delivery, environmental, and catalytic applications. These polymer-based fibers were successfully generated by means of the electrospinning technique.

Firstly, multi-responsive polymer-based nanocomposite membranes consisting of biocompatible and biodegradable polymers and magnetite nanoparticles were fabricated, characterized by various techniques and evaluated as drug delivery and hyperthermia-induced materials. More precisely, electrospun magnetoactive fibrous nanocomposite membranes based on the water soluble and biocompatible poly(ethylene oxide) (PEO), the biocompatible and biodegradable poly(L-lactide) (PLLA) and pre-formed oleic acid-coated magnetite NPs (OA.Fe_3O_4) have been fabricated and characterized by different methods to obtain information on their morphological characteristics, composition, thermal and magnetic properties. These magnetoactive fibrous membranes, exhibited tunable superparamagnetic behavior in the presence of the magnetic field at temperatures suitable for biological applications.

Moreover, the widely used phenolic pharmaceutical N-acetyl-p-aminophenol (acetaminophen (paracetamol)) has been encapsulated within the membranes and the resulting drug loaded electrospun mats were evaluated in controlled drug delivery. Our findings suggested that the presence and the presence of OA.Fe_3O_4 and the protein content of the release are critical parameters for the drug release rate. In the absence of magnetite, a relatively high drug percentage (~ 35%) is retained within the PLLA insoluble phase of the membrane. This percentage was found to significantly decrease by increasing the magnetic content reaching ~ 5% in the PEO/PLLA/OA.Fe_3O_4 membrane with the highest magnetic content (70% wt.). The high concentration of protein in the fetal calf serum (FCS) present in complete media caused further reduction of the release rate. Such changes could be attributed to intermolecular interactions between serum proteins, acetaminophen and polymeric fibers. The heating ability of the magnetoactive fibrous nanocomposites was also successfully tested for hyperthermia remote induction through AC magnetic field.

The above-mentioned system was also evaluated for the first time as a substrate for the removal of metal ions belonging to the lanthanides and actinides including trivalent europium Eu(III), tetravalent thorium Th(IV), and hexavalent uranium U(VI) from aqueous media. The experimental data indicated increased affinity of the membrane for the metal ions, which was pH dependent and reached maximum values (>90 %) for Eu(III), Th(IV) and U(VI) at pH 6, pH 3 and pH 6, respectively. The maximum adsorption capacity (q_{max}) at optimum conditions was evaluated from the Langmuir isotherm and was found to amount ~ 6.5, ~ 10.5, and ~ 4.5 mmol·kg^{-1} for Eu(III), Th(IV) and U(VI), respectively. In addition, studies on the effect of ionic strength on the adsorption efficiency, no significant effect was observed indicating that the adsorption of Th(IV) and U(VI) on the membrane was most probably based on specific interactions and the formation of inner-sphere surface complexes. The significantly higher adsorption efficiency of the membrane for Th(IV) in acidic media (pH ≤ 3) could be utilized for a pH-triggered, selective separation of Th(IV) from Eu(III) and U(VI) from aqueous media.

The prepared PEO/PLLA and magnetoactive PEO/PLLA/OA.Fe_3O_4 membranes were also evaluated for the first time for the removal of MG from aqueous solutions. An in-depth investigation of the efficacy of the (Malachite Green) MG removal from aqueous solutions was carried out, recording experiments on the effect of pH, initial dye concentration (adsorption capacity of the membranes), and membrane magnetic content. Moreover, changes in free energy (ΔG^0), enthalpy (ΔH^0) and entropy (ΔS^0) were determined from adsorption experiments carried out at different temperatures. Most importantly, it was

found that the presence of Fe_3O_4 NPs within the membranes seems to disfavor the adsorption process. In addition the obtained results showed that adsorption also depends on operating variables including initial MG concentration and solution pH. The thermodynamic parameters determined from temperature dependent adsorption measurements suggest that the adsorption of MG onto the Fe_3O_4-free and the Fe_3O_4-containing membranes is spontaneous and endothermic.

In conclusion, the demonstration of the ability of these materials to act as effective adsorbents for MG and harmful metal ions combined with the possibility of their recovery from aqueous solutions upon applying an external magnetic field and their recyclability, provides a promising tool for the future development of highly efficient, stimuli (magneto)-responsive adsorbents for the removal of hazardous materials from wastewater.

Methacrylate-based random copolymers that were in house synthesized were used for fabricating functional electrospun fibrous membranes that were further evaluated in water remediation processes. More precisely, methacrylic random copolymers based on methyl methacrylate (MMA) and 2-(acetoacetoxy)ethyl methacrylate (AEMA) (MMA-*co*-AEMA) were synthesized by free radical polymerization and further combined with pre-formed oleic acid-coated magnetite (OA.Fe_3O_4) nanoparticles for the generation of magnetoactive, electrospun microfibrous nanocomposite membranes. A series of well-defined nanocomposite membranes was fabricated and characterized. The incorporation of pre-formed oleic acid (OA)-coated magnetite NPs within the membranes, resulting to a superparamagnetic response combined with the presence of *β*-ketoester metal binding functionalities that were present on the polymer chains allowed for their evaluation as adsorbants for the removal of Eu(III) metal ions from aqueous media. The resulting membranes were further characterized in term of their morphological and thermal properties. The maximum adsorption capacity of europium onto electrospun membranes was found to be ~ 14 and ~ 17 $mmol \cdot Kg^{-1}$ for the OA.Fe_3O_4-free and nanocomposite fibrous membranes respectively. A comparison of the adsorption efficiency of the PEO/PLLA and the PEO/MMA-*co*-AEMA electrospun fibrous membranes demonstrated that the latter act as more effective adsorbents for Eu(III) ions. More precisely the PEO/PLLA system reaches a q_{max} at ~ 6 $mmol \cdot Kg^{-1}$ whereas the PEO/PMMA-*co*-AEMA membrane exhibits a significantly higher value ~ 14 $mmol \cdot Kg^{-1}$. Those findings verify our initial hypothesis that the presence of the *β*-ketoester metal binding groups within the membranes may assist favourably the sorption process.

Additionally, polymethacrylate-based fibrous membranes, consisting of benzyl methacrylate (BzMA) and methyl methacrylate (MMA), in the form of MMA-*co*-BzMA random copolymers, were also prepared and used as adsorbents for the removal of organic water-soluble pollutants from aqueous solutions including metronidazole and 1,2 dichlorobenzene. The adsorption affinity studies showed that the MMA-*co*-BzMA-based fibrous membranes demonstrated sorption only for the organic pollutant 1,2 dichlorobenzene.

In an effort to further expand the polymer-based magnetoactive electrospun membrane families, prepared in this Thesis, the fabrication and characterization of electrospun membranes consisting of the hydrophilic and biocompatible poly(vinyl pyrrolidone) (PVP) the hydrophobic and biodegradable poly(L-lactide) (PLLA) and pre-formed oleic acid-coated iron oxide nanoparticles (OA.Fe_3O_4) has been also carried out. The fabricated fibrous membranes were characterized in terms of their morphology providing information on the fiber diameters, which were strongly affected by the solution properties, as well as the morphological/dimensional characteristics of the embedded OA.Fe_3O_4 NPs. The nanocomposite microfibrous membranes, with uniformly dispersed of magnetic NPs within the fibers, exhibited superparamagnetic behavior at room temperature that can be tuned depending on the magnetic content. The additional ability of PVP for self-crosslinking when exposed to UV irradiation or upon thermal treatment allows for the future development of highly stable in aqueous media PVP-based crosslinked fibrous magnetoactive nanocomposites, with potential use in the biomedical and environmental fields.

Finally, metal NP-containing electrospun polymer-based nanocomposite fibrous membranes were successfully prepared upon the incorporation of inorganic metal NPs within polymeric (PVP) fibers enabling the production of materials with special functionalities and unique properties. Specifically, electrospun fibrous membranes containing Pd and Cu_2O NPs were fabricated aiming toward the investigation of their catalytic performance in organic reactions. Following synthetic protocols appearing in the literature stable colloidal solutions of PVP-capped Pd and Cu NPs were prepared. Subsequently, electrospinning was employed under specific processing conditions resulting to metal NP-containing fibrous membranes, which then crosslinked *via* thermal treatment. The resulting nanocomposite fibrous membranes were evaluated as heterogeneous catalytic supports in Heck, Suzuki (PVP-Pd), and click chemistry (PVP-Cu_2O) reactions. By employing a new recovery protocol, the crosslinked membranes can

be easily recovered and re-used as demonstrated by the fact that they remained catalytically active even after 3 consecutive reaction runs exhibiting high catalytic efficiencies in all cases. The high versatility of PVP to act as effective steric stabiliser for various nanoparticles in organic solvents (including Ag, Au, Cu, Pd, Cu_2O etc) allowing for their intermixing within a single electrospun fibrous mat, creates new prospects for the future development of multifunctional electrospun catalytic supports.

References

1. F. W. Harris. Intoduction to polymer chemistry. Journal of Chemical Education, 1981, Vol. 58, pp. 837-843.
2. H. R. Allcock, F. W. Lampe, J. E. Mark. The scope of polymer chemistry (Chapter 1). *Contemporary polymer chemistry.* Pearson Education, 2003, pp. 1-26.
3. A. Ravve. Physical properties and physical chemistry of polymers (Chapter 2). *Principles of polymer chemistry.* Springer, 2000, pp. 17-67.
4. D. W. Van Krevelen, K. Te Nijenhuis. Typology of polymers (Chapter 2). *Properties of Polymers.* Elsevier, 2009, pp. 7-47.
5. G. Moad, E. Rizzardo, S. H. Thang. Living radical polymerization by the RAFT process. Australian Journal of Chemistry, 2005, Vol. 58, pp. 379-410.
6. N. Hadjichristidis, S. Pispas, G. A. Floudas. *Block copolymers-syntehtic strategies, physical properties, and applications.* Wiley-Interscience, 2003.
7. S. F. Sun. *Physical chemistry of macromolecules: Basic principles and issues.* John Wiley, 1994.
8. K. A. Aamer, G. N. Tew. Raft polymerization of anovel activated ester monomer and conversion to a terpyridine-containing homopolymer. Journal of Polymer Science, 2007, Vol. 45, pp. 5618-5625.
9. X. L. Sun, WEI-DONG HE, J. Li, L. Y. Li, B. Y. Zhang, T. T. Pan. RAFT cryopolymerizations of N,N-dimethylacrylamide and N-isopropylacrylamide in moderately frozen aqueous solution. Journal of Polymer Science, 2009, Vol. 47, pp. 6863-6872.
10. D. A. Shipp. Living radical polymerization: Controlling molecular size and chemical functionality in vinyl polymers. Journal of Macromolecular Science, 2005, Vol. 45, pp. 171-194.
11. J. Zeleny. The electrical discharge from liquid points, and a hydrostatic method of measuring the electric intensity at their surfaces. Physical Review, 1914, Vol. 3, pp. 69-91.
12. A. Formhals. Process and apparatus for preparing artificial threads. US Patent 1-975-504, 1934.
13. J. K. Hong, S. V. Madihally. Next generation of electrosprayed fibers for tissue regeneration. Tissue Engineering: Part B, 2011, Vol. 17, pp. 125-141.
14. A. Formhals. Method and apparatus for spinning. US Patent 2-349-950, 1939.
15. G. Taylor. Electrically driven jets. Proceeding the Royal of Society, 1969, Vol. 313, pp. 453-475 .
16. J. Doshi, D. H. Renker. Electrospinning process and applications of electrospun fibers. Journal of Electrostatics, 1995, Vol. 35, pp. 151-160.
17. D. H. Reneker, I. Chun. Nanometer diameter fibers of polymer, produced by electrospinning. Nanotechnology, 1996, Vol. 7, pp. 216-223.
18. T. Subbiah, G. S. Bhat, R. W. Tock, S. Parameswaran, S. S. Ramkumar. Electrospinning of nanofibers. Journal of Applied Polymer Science, 2005, Vol. 96, pp. 557-569.
19. T. Joachim, C. Ondarcuhu. Drawing a single nanofiber over hundreds of microns. Europhysics Letters, 1998, Vol. 42, pp. 215-220.
20. G. M. Grzybowski, B. Whitesides. Self-assembly at all scales. Science, 2002, Vol. 295, pp. 2418-2421.
21. L. A. Smith, P. X. Ma. Nano-fibrous scaffolds for tissue engineering. Colloids and Surfaces B: Biointerfaces, 2004, Vol. 39, pp. 125–131.
22. J. C. Ellison, A. Phatak, D. W. Giles. Melt blown nanofibers: Fiber diameter distributions and onset of fiber breakup. Polymer, 2007, Vol. 48, pp. 3306-3316.

23. M. Charlesr. Template synthesis of electronically conductive polymer nanostructures. Accounts Chemicals Research, 1995, Vol. 28, pp. 61-68.
24. W. E. Teo, S. Ramakrishna. A review on electrospinning design and nanofibre assemblies. Nanotechnology, 2006, Vol. 17, pp. R89-R106.
25. Z. M. Huang, Y. Z. Zhang, M. Kotaki, S. Ramakrishna. A review on polymer nanofibers by electrospinning and their applications in nanocompisites. Composites Science and Technology, 2003, Vol. 63, pp. 2223-2253.
26. J. Venugopal, Y. Z. Zhang, S. Ramakrishna. Electrospun nanofibers: Biomedical applications. Part N: Journal of Nanoengineering and Nanosystems, 2005, Vol. 218, pp. 35-45.
27. J. Yang, S. Zhan, N. Wang, X. Wang, Y. Li, Y. Li, W. Ma, H. Yu. A mini review: Electrospun hierarchical nanofibers. Journal of Dispersion Science and Technology, 2010, Vol. 31, pp. 760-769.
28. H. S. Wang, G. D. Fu, X. S. Li. Functional polymeric nanofibers from electrospinning. 2009, Vol. 3, pp. 21-31.
29. A. L. Yarin, S. Koombhongse, D. H. Reneker. Taylor cone and jetting from liquid droplets in electrospinning of nanofibers. Journal of Applied Physics, 2001, Vol. 90, pp. 4836-4846.
30. D. H. Reneker, A. L. Yarin, H. Fong, S. Koombhongse. Bendinginstability of electrically charged jets of polymer solutions in electrospinning. Journal of Applied Physics, 2000, Vol. 87, pp. 4531-4547.
31. M. M. Hohman, M. Shin, G. Rutledge, M. P. Brenner. Electrospinning and electrically forced jets. I. Stability theory. Physics of Fluids, 2001, Vol. 13, pp. 2201-2220.
32. D. Li, Y. Xia. Electrospinning of nanofibers: Reinventing the wheel. Advanced Materials, 2004, Vol. 16, pp. 1151-1170.
33. N. Khan. Applications of electrospun nanofibers in the biomedical field. Studies by Undergraduate Researchers at Guelph, 2012, Vol. 5, pp. 63-73.
34. K. Garg, G. L. Bowlin. Electrospinning jets and nanofibrous structures. Biomicrofluidics, 2011, Vol. 5, pp. 1-19.
35. A. Frenot, I. S. Chronakis. Polymer nanofibers assempled by electrospinning. Current Opinion in Colloid and Interface science, 2003, Vol. 8, pp. 64-75.
36. J. Lin, X. Wang, B. Ding, J. Yu, G. Sun, M. Wang. Biomimicry via electrospinning. Critical Reviews in Solid State and Materials Sciences, 2012, Vol. 37, pp. 94-114.
37. N. Bhardwaj, S. C. Kundu. Electrospinning: A fascinationg fiber fabrication technique. Biotechnology Advances, 2010, Vol. 28, pp. 325-347.
38. Z. Li, C. Wang. One-dimensional nanostructures electrospinning technique and unique nanofibers. Springer Briefs in Materials, 2013.
39. V. Pillay, C. Dott, Y. E. Choonara, C. Tyagi, L. Tomar, P. Kumar, L. C. du Toit, V. M. K. Ndesendo. A review of the effect of processing variables on the fabrication of electrospun nanofibers for drug delivery applications. Journal of Nanomaterials, 2013, Vol. 2013, pp. 1-22.
40. D. H. Reneker, A. Yarin, E. Zussman, S. Koombhongse, W. Kataphinan. Nanofiber manufacturing: Toward better process control (Chapter 2). *Polymeric nanofibers.* American Chemical Society, 2006, pp. 7-20.
41. Z. Dong, S. J. Kennedy, Y. Wu. Electrospinning materials for energy-related applications and devices. Journal of Power Sources, 2011, Vol. 196, pp. 4886-4904.
42. Z. Xu, X. Huang, L. Wan. Surface engineering of polymer membranes-nanofibrous membrane with functionalized surface. Advanced Topics in Science and Technolog, 2009, pp. 306-328.
43. Q. P. Pham, U. Sharma, A. G. Mikos. Electrospinning of polymeric nanofibers for tissue engineering applications: A review. Tissue Engineering, 2006, Vol. 12, pp. 1197-1211.
44. M. G. Tardajos, M. Nash, Y. Rochev, H. Reinecke, C. Elvira, A. Gallardo. Homologous copolymerization route to functional and biocompatible polyvinylpyrrolidone. Macromolecular Chemistry and Physics, 2012, Vol. 213, p. 529−538.
45. J. M. Deitzel, J. Kleinmeyer, D. Harris, N. C. Beck Tan. The effect of processing variables on the morphology of electrospun nanofibers and textiles. Polymer, 2001, Vol. 42, pp. 261–272.
46. C. Drew, X. Wang, L. A. Samuelson, J. Kumar. The effect of viscosity and filler on electrospun fiber morphology. Journal of Macromolecular Science, Part A-Pure and Applied Chemistry, 2003, Vol. A40, pp. 1415-1422.
47. H. Fomg, D. H. Reneker. Elastomeric nanofibers of styrene-boutadiene-styrene triblock copolymer. Journal of Polymer Science: Part B: Polymer Physics, 1999, Vol. 37, pp. 3488-3493.

48. S. B. Mitchell, J. E. Sanders. A unique device for controlled electrospinning. Journal of bimedical Materials Research: Part A, 2006, pp. 110-120.
49. I. D. Norris, M. M. Shaker, F. K. Ko, A. G. MacDiarmid. Electrostatic fabrication of ultrafine conducting fibers: polyanilinerpolyethylene oxide blends. Synthetic Metals, 2000, Vol. 114, pp. 109-114.
50. X. Zong, K. Kim, D. Fang, S. Ran, B. S. Hsiao, B. Chu. Structure and process relationship of electrospun bioabsorbable nanofiber membranes. Polymer, 2002, Vol. 43, pp. 4403-4412.
51. M. M. Demir, I. Yilgor, E. Yilgor, B. Erman. Electrospinning of polyurethane fibers. Polymer, 2002, Vol. 43, pp. 3303-3309.
52. H. L. Simons. Process and apparatus for producing patterned non-woven fabrics. Patented 3-280-229, 1966.
53. C. Huang, S. Chen, C. Lai, D. H. Renker, H. Qiu, Y. Ye, H. Hou. Electrospun polymer nanofibers with small diameters. Nanotechnology, 2006, Vol. 17, pp. 1558-1563.
54. P. Gupta, C. Elkins, T. E. Long, G. L. Wilkes. Electrospinning of linear homopolymers of poly(methyl methacrylate): exploring relationships between fiber formation, viscosity, molecular weight and concentration in a good solvent. Polymer, 2005, Vol. 46, pp. 4799-4810.
55. M. Pradny, L. Martinova, J. Michalek, T. Fenclova, E. Krumbholcova. Electrospinning of the hydrophilic poly (2-hydroxyethyl methacrylate) and its copolymers with 2-ethoxyethyl methacrylate. Central European Journal of Chemistry, 2007, Vol. 5, pp. 779-792.
56. G. Eda, J. Liu, S. Shivkumar. Solvent effects on jet evolution during electrospinning of semi-dilute polystyrene solutions. European Polymer Journal, 2007, Vol. 43, pp. 1154-1167.
57. A. Greiner, J. H. Wendorff. Functional self-assembled nanofibers by electrospinning. Advanced Polymer Science, 2008, Vol. 219, pp. 107-171.
58. P. K. Baumgarten. Electrostatic spinning of acrylic microfibers. Journal of Colloid Interface Science, 1971, Vol. 36, pp. 71-79.
59. I. Hayati, A. I. Bailey, T. F. Tadros. Investigations into the mechanisms of electrohydrodynamic spraying of liquids: I. Effect of electric field and the environment on pendant drops and factors affecting the formation of stable jets and atomization. Journal of Colloid Interface Science, 1987, Vol. 117, pp. 205-221.
60. H. Q. Liu, Y. L. Hsieh. Ultrafine fibrous cellulose membranes from electrospinning of cellulose acetate. Journal of Polymer Science: Part B: Polymer Physics, 2002, Vol. 40, pp. 2119–2129.
61. L. Wannatong, A. Sirivat, P. Supaphol. Effects of solvents on electrospun polymeric fibers: preliminary study on polystyrene. Polymer International, 2004, Vol. 53, pp. 1851-1859.
62. S. Megelski, J. S. Stephens, D. B. Chase, J. F. Rabolt. Micro- and nanostructured surface morphology on electrospun polymer. Macromolecules, 2002, Vol. 35, pp. 8456-8466.
63. P. Supaphol, O. Suwantong, P. Sangsanoh, S. Srinivasan, R. Jayakumar, S.V. Nair. Electrospinning of biocompatible polymers and their potentials in biomedical applications. Advanced Polymer Science, 2012, Vol. 246, pp. 213-240.
64. T. J. Sill, A. H. von Recum. Electrospinning: Application in dtyg delivery and tissue engineering. Biomaterials, 2008, Vol. 29, pp. 1989-2006.
65. R. Jaeger, M. M. Bergshoeft, C. Martin i Batlle, H. Schlinherr, G. J. Vancso. Electrospinning of ultra-thin polymer fibers. Macromolecular Symposia, 1998, Vol. 127, pp. 141-150.
66. X. Yuan, Y. Zhang, C. Dong, J. Sheng. Morphology of ultrafine polysulfone fibers prepared by electrospinning. Polymer International, 2004, Vol. 53, pp. 1704-1710.
67. P. Gupta, K. Vermani, S. Garg. Hydrogels: from controlled release to pH-responsive drug delivery. Drug Discovery Today, 2002, Vol. 7, pp. 569-579.
68. D. G. Yu, L. M. Zhu, K. White, C. Branford-White. Electrospun nanofiber-based drug delivery systems. Health, 2009, Vol. 1, pp. 67-75.
69. Y. Tian, M. Wu, R. Liu, Y. Li, D. Wang, J. Tan, R. Wu, Y. Huang. Electrospun membran of cellulose acetate for heavy metal ion adsorption in water treatment. Carbohydrate Polymers, 2011, Vol. 83, pp. 743-748.
70. X.Y. Ye, Z. M. Liu, Z. G. Wang, X. J. Huang, Z. K. Xu X. Y. Ye, Z.M. Liu, Z. G. Wang, X. J. Huang, Z. K. Xu. Preparation and characterization of magnetic nanofibrous composite membranes with catalytic activity. Matterial Letters, 2009, Vol. 63, pp. 1810-1813.
71. R. L. Dahlin, F. K. Kasper, A. G. Mikos. Polymeric nanofibers in tissue engineering. Tissue Engineering: Part B, 2011, Vol. 17, pp. 349-364.

72. J. G. Fernandes, D. M. Correia, G. Botelho, J. Padrao, F. Dourado, C. Ribeiro, S. Lanceros-Mendez, V. Sencadas. PHB-PEO electrospun fiber membranes containing chlorhexidine for drug delivery applications. Polymer Testing, 2014, Vol. 34, pp. 64-71.
73. C. Feng, K. C. Khulbe, T. Matsuura. Recent progress in the preparation, characterization, and application of nanofibers and nanofiber membranes via electrospinning/interfacial polymerization. Journal of Applied Polymer Science, 2010, Vol. 115, pp. 756-776.
74. J. A. Matthews, G. E. Wnek, D. G. Simpson, G. L. Bowlin. Electrospinning of collagen nanofibers. Biomacromolecules, 2002, Vol. 3, pp. 232-238.
75. K. S. Rho, L. Jeong, G. Lee, B. M. Seo, Y. J. Park, S. D. Hong, S. Roh, J. J. Cho, W. H. Park, B. M. Min. Electrospinning of collagen nanofibers: Effects on the behavior of normal human keratinocytes and early wound healing. Biomaterials, 2006, Vol. 27, pp. 1452-1461.
76. G. Ma, D.Fa,Y. Liu, X. Zhu, J. Nie. Electrospun sodium alginate/poly(ethylen oxide) core-shell nanofibers scaffolds potential for tissue engineering applications. Carbohydrate Polymers, 2012, Vol. 87, pp. 737-743.
77. J. J. Chang, Y. H. Lee, M. H. Wu, M. C. Yang, C. T. Chien. Preparation of electrospun alginate fibers with chitosan sheath. Carbohydrate Polymers, 2012, Vol. 87, pp. 2357-2361.
78. R. Vasita, D. S. Katti. Nanofibers and their applications in tissue engineering. International Journal Nanomedicine, 2006, Vol. 1, pp. 15-30.
79. J. Venugopal, S. Low, A. T. Choon, S. Ramakrishna. Interaction of cells and nanofiber scaffolds in tissue engineering. Journal of Biomedical Materials Research Part B: Applied Biomaterials, 2007, Vol. 84, pp. 34-48.
80. L. Kong, G. R. Ziegler. Fabrication of pure starch fibers by electrospinning. Food Hydrocolloids, 2014, Vol. 36, pp. 20-25.
81. X. M. Mo, C. Y. Xu, M. Kotaki, S. Ramakrishna. Electrospun P(LLA-CL) nanofiber: A biomimetic extracellular matrix for smooth muscle cell and endothelial cell proliferation. Biomaterials, 2004, Vol. 25, pp. 1883-1890.
82. H. Yoshimoto, Y. M. Shin, H. Terai, J. P. Vacanti. A bidegradable nanofiber scaffold by electrospinning and its potential for bone tissue engineering. Biomaterials, 2003, Vol. 24, pp. 2077-2082.
83. C. Y. Xu, R. Inai, M. Kotaki, S. Ramakrishna. Aligned biodegradable nanofibers structure: A potential scaffold for blood vessel engineering. Biomaterials, 2004, Vol. 25, pp. 877-886.
84. J. R. Porter, T. T. Ruckh, K. C. Popat. Bone tissue engineering: A review in bone biomimetics and drug delivery strategies. Biotechnology Progress (AlChE), 2009, Vol. 25, pp. 1539-1560.
85. J. D. Schiffman, C. L. Schauer. A review: Electrospinning of biopolymer nanofibers and their applications. Polymer Reviews, 2008, Vol. 48, pp. 317-352.
86. R. Sridhar, S. Sundarrajan, J. R. Venugopal, R. Ravichandran, S. Ramakrishna. Electrospun inorganic and polymer composite nanofibers for biomedical applications. Journals of Biomaterials Science, Polymer edition, 2013, Vol. 24, pp. 365-385.
87. W. Cui, Y. Zhou, J. Chang. Electrospun nanofibrous materials for tissue engineering and drug delivery. Science and Technology of Advanced Materials, 2010, Vol. 11, pp. 1-11.
88. Y. Zhang, C. T. Lim, S. Ramakrishna, Z. M. Huang. Recent development of polymer nanofibers for biomedical and biotechnological applications. Journal of Materials Science: Materials in Medicine, 2005, Vol. 16, pp. 933-946.
89. E. R. Kenawy, F. I. Abdel-Hay, M. H. El-Newehy, G. E. Wnek. Processing of polymer nanofibers through electrospinning as drug delivery systems. Materials Chemistry and Physics, 2009, Vol. 113, pp. 296-302.
90. D. H. Renker, H. Fong. Polymeric nanofibers. ACS Division of Polymer Chemistry, Inc, 2005, p. Chapter 13 and 14.
91. C. E. Schmidt, J. B. Leach. Neural tissue engineering: Strategies for repair and regeneration. Annual Review of Biomedical Engineering, 2003, Vol. 5, pp. 293–347.
92. X. Zong, H. Bien, C. Y. Chung, L. Yin, D. Fang, B. S. Hsiao, B. Chu, E. Entcheva. Electrospun fine-textured scaffolds for heart tissue constructs. Biomaterials, 2005, Vol. 26, pp. 5330-5338.
93. N. Bhattarai, D. Edmondson, O. Veiseh, F. A. Matsen, M. Zhang. Electrospun chitosan-based nanofibers and their cellular compatibility. Biomaterials, 2005, Vol. 26, pp. 6176-6184.

94. Z. X. Meng, Y. S. Wang, C. Ma, W. Zheng, L. Li, Y. F. Zheng. Electrospinning of PLGA/gelatin randomly-oriented and aligned nanofibers as potential scaffold in tissue engineering. Materials Science and Engineering C, 2010, Vol. 30, pp. 1204-1210.
95. W. Hua, Z. Ren-Xi, Z. Xian-Zheng. Design and development of polymeric micelles with cleavable links for intracellular drug delivery. Progress in Polymer Science, 2013, Vol. 38, pp. 503-535.
96. K. Glen S., K. Kazunori. Block copolymer micelles as long-circulating drug vehicles. Advanced Drug Delivery Reviews, 2012, Vol. 64, pp. 237-245.
97. Y. Wei, X. Zhang, Y. Song, B. Han, X. Hu, X. Wang, Y. Lin, X. Deng. Magnetic biodegradable Fe3O4/CS/PVA nanofibrous membranes for bone regeneration. Biomedical Materials, 2011, Vol. 6, pp. 1-15.
98. E. Elizondo, J. Veciana, N. Ventosa. Nanostructuring molecular materials as particles and vesicles for drug delivery, using compressed and supercritical fluids. Nanomedicine, 2012, Vol. 7, pp. 1391-1408.
99. P. Tanner, P. Baumann, R. Enea, O. Onaca, C. Palivan, W. Meier. Polymeric vesicles: From drug carriers to nanoreactors and artificial organelles. Accounts of Chemical Research, 2011, Vol. 44, pp. 1039-1049.
100. R. P. Brinkhuis, F. P. J. T. Rutjes, J. C. M. van Hest. Polymeric vesicles in biomedical applications. Polymer Chemistry, 2011, Vol. 2, pp. 1449-1462.
101. M. L. De Temmerman, J. Demeester, S. C. De Smedt, J. Rejman. Tailoring layer-by-layer capsules for biomedical applications. Nanomedicine, 2012, Vol. 7, pp. 771-788.
102. M. Delcea, H. Möhwald, A.G. Skirtach. Stimuli-responsive LbL capsules and nanoshells for drug delivery. Advanced Drug Delivery Reviews, 2011, Vol. 63, pp. 730-747.
103. S. De Koker, R. Hoogenboom, B.G. De Geest. Polymeric multilayer capsules in drug delivery. Angewandte Chemie-International Edition, 2010, Vol. 49, pp. 6954-6973.
104. C. Alvarez-Lorenzo, B. Blanco-Fermandez, A.M. Puga. Crosslinked ionic polysaccharides for stimuli-sensitive drug delivery. Advanced Drug Delivery Reviews, 2013, Vol. 65, pp. 1148-1171.
105. Q. Yong, K. Park. Environment-sensitive hydrogels for drug delivery. Advanced Drug Delivery Reviews, 2012, Vol. 64, pp. 49-60.
106. H. Chaoliang, K. Sung Wan, L. Doo Sung. In situ gelling stimuli-sensitive block copolymer hydrogels for drug delivery. Journal of Controlled Release, 2008, Vol. 127, pp. 189-207.
107. S. G. Kumbar, S. L. Nair, S. Bhattacharyya, C. T. Laurencin. Polymeric nanofibers as novel carriers for the delivery of therapeutic molecules. Journal of Nanoscience and Nanotechnology, 2006, Vol. 6, pp. 2591-2607.
108. S. Chakraborty, I. C. Liao, A. Adler, K. W. Leong. Electrohydrodynamics: A facile technique to fabricate drug delivery systems. Advanced Drug Delivery Reviews, 2009, Vol. 61, pp. 1043-1054.
109. X. Huang, C. S. Brazel. On the importance and mechanisms of burst release in matrix-controlled drug delivery systems. Journal of Controlled Release, 2001, Vol. 73, pp. 121-136.
110. Z. M. Huang, C. L. He, A. Yang. Encapsulating drugs in biodegradable ultrafine fibers through co-axial electrospinning. Journal of Biomedical Materials Research A, 2006, Vol. 77, pp. 169-179.
111. C. L. He, Z. M. Huang, X. J. Han, L. Liu, H. S. Zhang, L. S.Chen. Coaxial electrospun poly(L-lactic acid) ultrafine fibers for substained drug delivery. Jounal of Macromolecular Science B, 2006, Vol. 45, pp. 515-524.
112. A. Chunder, S. Sarkar, Y. Yu, L. Zhai. Fabrication of ultrathin polyelectrolyte fibers and their controlled release properties. Colloids and Surfaces B, 2007, Vol. 58, pp. 172-179.
113. K. S. Soppimath, T. M. Aminabhavi, A. R. Kulkarni, W. E. Rudzinski. Bidegradable polymeric nanoparticles as drug delivery devices. Journal of Controlled Release, 2001, Vol. 70, pp. 1-20.
114. E. R. Kenawy, G. L. Bowlin, K. Mansfield, J. Layman, D. G. Simpson, E. H. Sanders, G. E. Wnek. Release of tetracycline hydrochloride from electrospun poly(ethylene-co-vinylacetate), poly(lactic acid), and a blend. Journal of Controlled Release, 2002, Vol. 81, pp. 57-64.
115. V. Leung, F. Ko. Biomedical applications of nanofibers. Polymer Advanced Technologies, 2011, Vol. 22, pp. 350-365.
116. A. G. Kanani, S. H. Bahrami. Review on Electrospun Nanofibers Scaffold and Biomedical Applications. Trends in Biomaterials and Artificial Organs, 2010, Vol. 24, pp. 93-115.
117. N. Unlu, M. Ersoz. Adsorption characteristics of heavy metal ions onto a low cost biopolymeric sorbent from aqueous solutions. Journal of Hazardous Materials, 2006, Vol. B136, pp. 272-280.

118. A. Witek-Krowiak. Biosorption of malachite green from aqueous solutions bu pine sawdust: equilibrium, kinetics and the effect of process parameters. Desalination and Water Treatment, 2013, Vol. 51, pp. 3284-3294.
119. G. Crini. Recent developments in polysaccharide-based materials used as adsorbents in wastewater treatment. Progress in Polymer Science, 2005, Vol. 30, pp. 38–70.
120. J. Chung, J. O. Kim. Application of advanced oxidation process to rmove refractory compounds from dye wastewater. Desalination and Water Treatment, 2011, Vol. 25, pp. 233-240.
121. H. Wang, G. Zhang, Y. Gao. Photocata;ytic degradation of metronidazole in aqueous solution by niobate K6Nb10.8O30. Journal of Natural Sciences, 2010, Vol. 15, pp. 345-349.
122. C. Berberidou, I. Poulios, N. P. Xekoukoulotakis, D. Mantzavinos. Sonolytic, photocatalytic and sonophotocatalytic degradation of malachite green in aqueous solutions. Applied Catalysis B: Environmental, 2007, Vol. 74, pp. 63-72.
123. H. Tang, W. Zhou, L. Zhang. Adsorption isotherms and kinetics studies of malachite green on chitin hydrogels. Journal of Hazardous Materials, 2012, Vols. 209-210, pp. 218-225.
124. P. L. Hariani, M. Faizal, R. Marsi, D. Setiabudidaya. Synthesis and properties of Fe3O4 nanoparticles by co-precipitation method to removal procion dye . International Journal of Environmental Science and Development, 2013, Vol. 4, pp. 336-340.
125. M. Zarei, A. Niaei, D. Salari, A. R. Khataee. Removal of four dyes from aqueous medium by the peroxi-coagulation method using carbon nanotube-PTFE cathode and neural network modeling. Journal of Electroanalytical, 2010, Vol. 639, pp. 167-174.
126. V. K. Gupta, Suhas. Application of low-cost adsorbents for dye removal - A review. Journal of Environmental Management, 2009, Vol. 90, pp. 2313-2342.
127. M. Anbia, A. Ghaffari. Removal of malachite green from dye wastewater using mesoposous carbon adsorbent. Journal of the Iranian Chemical Society, 2001, Vol. 8, pp. S67-S76.
128. Y. C. Sharma, B. Singh, Uma. Fast removal of malachite green by adsorption on rice husk activated carbon. The Open Environmental Pollution and Toxicology Journal, 2009, Vol. 1, pp. 74-78.
129. R. Xu, M. Jia, Y. Zhang, F. Li. Sorption of malachite green on vinyl-modified mesoporous poly(acrylic acid)/SiO2 composite nanofiber membranes . Microporous and Mesoporous Materials, 2012, Vol. 149, pp. 111-118.
130. N. Sridewi, Y. F. Lee, K. Sudesh. Simultaneous adsorption and photocatalytic degradation of malachite green using electrospun P(3HB)-TiO2 nanocomposite fibers and films. International Journal of Photoenergy, 2011, Vol. 2011, pp. 1-9.
131. M. H. Beak, C. O. Ijagbemi, D. S. Kim. Treatment of malachie green-containing wastewater using poultry features as adsorbent. Journal of Environmental Science and Health Part A, 2009, Vol. 44, pp. 536-542.
132. T. Santhi, S. Manonmani. Malachite green removal from aqueous solution by the peel of cucumis sativa fruit. Clean Soli, Air, Water, 2011, Vol. 39, pp. 162-170.
133. G. Sun, X. Xu. Suflower stalks as adsorbents for color removal from textile wastewater. Industrial & Engineering Chemistry Research, 1997, Vol. 36, pp. 808-812.
134. Y. C. Lee, J. Y. Kim, H. J. Shin. Removal of malachite green (MG) from aqueous solutions by adsorption, precipitation, and alkaline fading using talc. Separation Science and Technology, 2013, Vol. 48, pp. 1093-1101.
135. M. Nageeb Rashed. Adsorption technique for the rmoval of organic pollutants from water and wastewater. OrganicPollutants - Monitoring, Risk and Treatment, 2013, pp. 167-194.
136. X. Zhu, X. Jiang, S. Cheng, K. Wang, S. Mao, L. J. Fan. Preparation of high strength ultrafine polyvinyl chloride fibrous membrane and its adsorption of cationic dye. Journal of Polymer Research, 2010, Vol. 17, pp. 769-777.
137. X. Fang, S. Xiao, M. Shen, R. Guo, S. Wang, X. Shi. Fabrication and characterization of water-stable electrospun polyethyleneimine/polyvinyl alcohol nanofibers with super dye sorption capability. New Journal of Chemistry, 2011, Vol. 35, pp. 360-368.
138. Y. Dai, J. Niu, L. Yin, J. Xu, Y. Xi. Sorption of polycyclic aromatic hydrocarbons on electrospun nanofibrous membranes: Sorption kinetics and mechanism. Journal of Hazardous Materials, 2011, Vol. 192, pp. 1409-1417.
139. F. Fu, Q. Wang. Removal of heavy metal ions from wastewaters: A review. Journal of Environments Management, 2011, Vol. 92, pp. 407-418.

140. Y. Liu, Y. J. Liu. Biosorption isotherms, kinetics and thermodynamics. Separation and Purification Technology, 2008, Vol. 61, pp. 229-242.
141. A. Gholami, A. R. Moghadassi, S. M. Hosseini, S. Shabani, F. Gholami. Preparation and characterization of polyvinyl chloride based nanocomposite nanofiltration-membrane modifided by iron oxide nanoparticles for lead removal from water. Journal of Industrial and Engineering Chemistry, 2013, Vol. 20, pp. 1517–1522.
142. S. Haider, S. Y. Park. Preparation of the electrospun chitosan nanofibers and their applications to the adsorption of Cu(II) and lead Pb(II) ions from an aqueous solution. Journal of Membrane Science, 2009, Vol. 328, pp. 90-96.
143. C. Feng, K. C. Khulbe, T. Matsuura, S. Tabe, A. F. Ismail. Preparation and characterization of electro-spun nanofiber membranes and their possible applications in water treatment. Separation and Purification Technology, 2013, Vol. 102, pp. 118-135.
144. F. Liu, M. W. Urban. Recent advances and challenges in designing stimuly-responsive polymers. Progress in Polymer Science, 2010, Vol. 35, pp. 3-23.
145. R. Sahay, P. Suresh Kumar, R. Sridhar, J. Sundaramurthy, J. Venugopal, S. G. Mhaisalkar, S. Ramakrishna. Electrospun composite nanofibers and their multifaceted applications. Journal of Materials Chemistry, 2012, Vol. 22, pp. 12953-12971.
146. B. Jeong, A. Gutowska. Lessons from nature: stimuli-responsive polymers and their biomedical applications. Trends in Biotechnology, 2002, Vol. 20, pp. 305-311.
147. D. Liang, B. S. Hsiao, B. Chu. Functional electrospun nanofibrous scaffolds for biomedical applications. Advanced Drug Delivery Reviews, 2007, Vol. 59, pp. 1392-1412.
148. G. Nie, Z. Li, X. Li, J. Lei, C. Zhang, C. Wang. Fabrication of polyacrylonitrile/CuS composite nanofibers and their recycled application in catalysis for dye degradation. Applied Surface Science, 2013, Vol. 284, pp. 595-600.
149. S. Xiao, M. Shen, R. Guo, Q. Huang, S. Wang, X. Shi. Fabrication of multiwalled carbon nanotube-reinforced electrospun polymer nanofibers containing zero-valent iron nanoparticles for environmental applications. Journal of Materials Chemistry, 2010, Vol. 20, pp. 5700-5708.
150. T. Krasia Christoforou. Organic-inorganic polymer hybrids: synthetic strategies and applications. *Hibrid and hierarchical composite materials.* 2014.
151. I. Savva, A. D. Odysseos, L. Evaggelou, O. Marinica, E. Vasile, L. Vekas, Y. Sarigiannis, T. Krasia-Christoforou. Synthesis, characterization and evaluation in drug release properties of magnetoactive poly(ethylene oxide)-poly(L-lactide) electrospun membranes. Biomacromolecules, 2013, Vol. 14, pp. 4436-4446.
152. H. Y. Li, C. M. Chang, K. Y. Hsu. Poly(lactide)-functionalized and Fe3O4 nanoparticle-decorated multiwalled carbon nanotubes for preparation of electrically-conductive and magnetic poly(lactide) films and electrospun nanofibers. Journal of Material Chemistry, 2012, Vol. 22, pp. 4855-4860.
153. T. Gong, W. Li, H. Chen. Remotely actuated shape memory effect of electrospun composite nanofibers. ACTA Biomaterialia, 2012, Vol. 8, pp. 1248-1259.
154. J. T. Kannarkat, J. Battogtokh, J. Philip. Embedding of magneticnanoparticles in polycaprolactonenanofiber scaffolds to facilitate bone healing and regeneration. Journal of Applied Physics, 2010, Vol. 107.
155. S. T. Tan, J. H. Wendorff, C. Pietzonka, Z. Hong Jia, G. Qing Wang. Biocompatible and biodegradable polymer nanofibers displaying superparamagnetic properties. A European Journal of Chemical Physics and Physical Chemistry, 2005, Vol. 6, pp. 1461-1465.
156. J. Meng, B. Xiao, Y. Zhang, J. Liu, H. Xue, J. Lei, H. Kong, Y. Huang. Super-paramagnetic responsive nanofibrous scaffolds under static magnetic field enhance osteogenesis for bone repair in vivo. Scientific Reports, 2013, Vol. 3, pp. 1-7.
157. J. Meng, Y. Zhang, X. Qi, H. Kong, C. Wang, Z. Xu, S. Xie, N. Gu, H. Xu. Paramagnetic nanofibrous composite films enhance the osteogenic responses of pre-osteoblast cells. Nanoscale, 2010, Vol. 2, pp. 2565-2569.
158. O. Kriha, M. Becker, M. Lehmann. Connection of hippocampal neurons by magnetically controlled movement of short electrospun polymer fibers - A route to magnetic micromanipulators . Advanced Materials, 2007, Vol. 19, p. 2483.
159. X. Chen, s. Wei, C. Gunesoglu. Electrospun magnetic fibrillar polystyrene nanocomposites reinforced with nickel nanoparticles. Macromolecular Chemistry and Physics, 2010, Vol. 211, pp. 1775-1783.

160. T. Song, Y. Z. Zhang, T. J. Zhou. Fabrication of magnetic composite nanofibers of poly(epsilon-caprolactone) with FePtnanoparticles by coaxial electrospinning. Journal of Magnetism and Magnetic Materials, 2006, Vol. 303, pp. E286-E289.
161. T. Song, Y. Zhang, T. Zhou, C. T. Lim, S. Ramakrishna, B. Liu. Encapsulation of self-assembled FePt magnetic nanoparticles in PCL nanofibers by coaxial electrospinning. Chemical Physics Letters, 2005, Vol. 415, pp. 317-322.
162. V. I. Shubayev, T. R. Pisanic II, S. Jin. Magnetic nanoparticles for theranostics. Advanced Drug Delivery Reviews, 2009, Vol. 61, pp. 467-477.
163. Q. A. Pankhurst, J. Connolly, S. K. Jones, J. Dobson. Applications of magnetic nanoparticles in bimedicine. Journal of Physics D: Applied Physics, 2003, Vol. 36, pp. 167-181.
164. M. Mahmoudi, S. Sant, B. Wang, S. Laurent, T. Sen. Superparamagnetic iron oxide nanoparticles (SPIONs): Development, surface modification and applications in chemotherapy. Advanced Drug Deliver Reviews, 2011, Vol. 63, pp. 24-46.
165. D. L. J. Thorek, A. K. Chen, J. Czupryna, A. Tsourkas. Superparamagnetic iron oxide nanoparticles probes for molecular imaging. Annals of Biomedical Engineering, 2006, Vol. 34, pp. 23-38.
166. S. Neveu, A. Bee, M. Robineau, D. Talbot. Size-selective chemical synthesis of tartrate stabilized cobalt ferrite ionic magnetic fluid. Journal of Colloid and Interface Science, 2002, Vol. 255, pp. 293-298.
167. C. Xu, S. Sun. Superparamagnetic nanoparticles as targeted probes for diagnostic and therapeutic applications. NIH Public Access, 2009, Vol. 29, pp. 5583-5591.
168. A. H. Lu, E. L. Salabas, F. Schuth. Magnetic nanoparticles: Synthesis, protection, functionalization, and application. Magnetic Nanoparticles, 2007, Vol. 46, pp. 1222-1244.
169. G. A. E. Chavez, Ll. J. C. Medina, C. P. de Melo, C. A. S. Andrade, M. D. L. Oliveira. Biomedical applications of magnetic nanoparticles: An overview (Chapter 1). *Magnetic nanoparticles: Synthesis, physicochemical properties and role in biomedicine.* Nanotechnology Science and Technology, 2014, pp. 1-36.
170. D. Ramimoghadam, S. Bagheri, S. B. Abd Hamid. Progress in electrochemical synthesis of magnetic iron oxide nanoparticles. Journal of Magnetism and Magnetic Materials, 2014, Vol. 368, pp. 207-229.
171. W. Wu, Q. He, C. Jiang. Magnetic iron oxide nanoparticles: Synthesis and surface functionalization strategies. Nanoscale Research Letters, 2008, Vol. 3, pp. 397-415.
172. A. K. Gupta, M. Gupta. Syntesis and surface engineering of iron oxide nanoparticles for biomedical applications. Biomaterials, 2005, Vol. 26, pp. 3995-4021.
173. G. Guangqing, W. Liyan, D. Xiangting. Electrospun Fe3O4/PVP//Tb(BA)(3)phen/PVP magnetic-photoluminescent bifunctional bistrand aligned composite nanofibers bundles. Journal of Materials Science, 2013, Vol. 48, pp. 5140-5147.
174. I. Savva, D. Constantinou, O. Marinica, E. Vasile, L. Vekas, T. Krasia-Christoforou. Fabrication and characterization of superparamagnetic poly(vinyl pyrrolidone)/poly(L-lactide) electrospun membranes. Journal of Magnetism and Magnetic Materials, 2014, Vol. 352, pp. 35-40.
175. P. Zhang, B. Wang, G. R. Williams, C. Branford-White, J. Quan, H. Nie, L. Zhu. Self-assembled core-shell Fe3O4@SiO2 nanoparticles from electrospun fibers. Materials Research Bulletin, 2013, Vol. 48, pp. 3058-3064.
176. I. Savva, G. Krekos, A. Taculescu, O. Marinica, L. Vekas, T. Krasia-Christoforou. Fabrication and characterization of magnetoresponsive electrospun membranes based on methacrylic random copolymers and magnetite nanoparticles. Journal of Nanomaterials, 2012, Vol. 2012, pp. 1-9.
177. M. Miyauchi, T. J. Simmons, J. Miao, J. E. Gagner, Z. H. Shriver, U. Aich, J. S. Dordick, R. J. Linhardt. Electrospun polyvinylpyrrolidone fibers with high concentrations of ferromagnetic and superparamagnetic nanoparticles. Applied Materials and Interfaces ACS, 2011, Vol. 3, pp. 1958-1964.
178. I. Savva, T. Krasia-Christoforou. Electrospun magnetoactive fibrous nanocomposites: Fabrication and applications in biomedicine (Chapter 6). *Magnetic nanoparticles: Synthesis, physicochemical properties, and role in biomedicine.* Nannotechnology Science and Technology, 2014, pp. 163-200.
179. I. W. Hamley. Introduction to soft matter: Polymers, colloids, amphiphiles and liquid crystals. 1988.
180. L. Vekas, D. Bica, M. V. Andeev. Magnetic nanoparticles and concentrated magnetic nanofluids: Synthesis, properties and some applications. China Particuology, 2007, Vol. 5, pp. 43-49.
181. N. Jain, Y. Wang, S. K. Jones, B. S. Hawkett, G. G. Warr. Optimized steric stabilization of aqueous ferrofluids and magnetic nanoparticles. Langmuir, 2010, Vol. 26, pp. 4465-4472.

182. Y. Sahoo, H. Pizem, T. Fried, D. Golodnitsky, L. Burstein, C. N. Sukenik, G. Markovick. Alkyl phosphonate/phosphate coating on magnetite nanoparticles: a comparison with fatty acids. Langmuir, 2001, Vol. 17, pp. 7907-7911.
183. R. Hao, R. Xing, Z. Xu, Y. Hou, S. Gao, S. Sun. Synthesis, functionalization, and biomedical applicatios of multifuntional magnetic nanoparticles. Materials View, 2010, Vol. 22, pp. 2729-2742.
184. L. Zhang, R. He, H. C. Gu. Oleic acid coating on the monodisperse megnetite nanoparticles. Applied Surface Science, 2006, Vol. 253, pp. 2611-2617.
185. J. N. K. Shimoiizaka, T. Fujita, A. Kounosu. Sink-float separators using permanent magnets and water based magnetic fluid. IEEE Transactions on Magnetics, 1980, Vol. 16, pp. 368-371.
186. Y. M. Wang, X. Cao, G. H. Liu, R. Y. Hong, Y. M. Chen, X. F. Chen, H. Z. Li, B. Xu, D. G. Wei. Synthesis of Fe3O4 magnetic fluid used for magnetic resonance imaging and hyperthermia. Journal of Magnetism and Magnetic Materials, 2011, Vol. 323, pp. 2953-2959.
187. Y. Wang, J. F. Wong, X. W. Teng, X. Z. Lin, H. Yang. "Pulling" nanoparticles into water: phase transfer of oleic acid stabilized monodisperse nanoparticles into aqueous solutions of alpha-cyclodextrin. Nanoletters, 2003, Vol. 3, pp. 1555-1559.
188. E. B. Zhulina, O. V. Borisov, V. A. Priamitsyn. Theory of steric stabilization of colloid dispersions by grafetd polymers. Journal of Colloid and Interface Science, 1990, Vol. 137, pp. 495-511.
189. C. Boyer, M. R. Whittaker, V. Bulmus, J. Liu, T. P. Davis. The design and utility of polymer-stabilized iron-oxide nanoparticles for nanomedicine applications. NPG Asia Materials, 2010, Vol. 2, pp. 23-30.
190. P. Nicolas, M. Saleta, H. Troiani, R. Zysler, V. Lassalle, M. L. Ferreira. Preparation of iron oxide nanoparticles stabilized with biomolecules: Experimental and mechanistic issues. Acta Biomaterialia, 2013, Vol. 9, pp. 4754-4762.
191. L. L. Zhou, J. Y. Yuan, W. Z. Yuan, X. F. Sui, S. Z. Wu, Z. L. Li. Synthesis, characterization, and controllable drug release of pH-sensitive hybrid magnetic nanoparticles. Journal of Magnetism and Magnetic Materials, 2009, Vol. 321, pp. 2799-2804.
192. L. L. Zhou, J. Y. Yuan, W. Z. Yuan, M. Zhou, S. Z. Wu, Z. L. Li. Synthesis and characterization of noscapine loaded magnetic polymeric nanoparticles with biodegradability, superparamagnetism, and fluorescence. Matterials Letters, 2009, Vol. 63, pp. 1567-1570.
193. J. Gao, H. Gu, B. Xu. Multifunctional magnetic nanoparticles: Design, synthesis, and biomedical applications. Accounts of Chemical Research, 2009, Vol. 42, pp. 1097-1107.
194. M. Friak, A. Schindlmayr, M. Scheffler. Ab initio study of the half-metal to metal transition in strained magnetite. New Journal of Physics, 2007, Vol. 9, pp. 1-15.
195. A. P. C. Teixeira, J. C. Tristão, M. H. Araujo, L. C. A. Oliveira, F. C. C. Moura, J. D. Ardisson, C. C. Amorim, R. M. Lago. Iron: a Versatile Element to Produce Materials for Environmental Applications. Journal of the Brazilian Chemical Society, 2012, Vol. 9, pp. 1579-1593.
196. A. G. Kolhatkar, A. C. Jamison, D. Litvinov, R. C. Willson. Tuning the magnetic properties of nanoparticles. International Journal of Molecular Science, 2013, Vol. 14, pp. 15977-16009.
197. S. P. Gubin. Magnetic nanoparticles. Wiley-VCH, 2007, pp. 1-19.
198. C. Xu, S. Sun. Mini Review-Monodisperse magnetic nanoparticles for biomedical applications. Polymer International, 2007, Vol. 56, pp. 821-826.
199. B. W. Ahn, T. J. Kang. Preparation and characterization of magnetic nanofibers with iron oxide nanoparticles and poly(ethylene terephthalate). Journal of Applied Polymer Science, 2012, Vol. 125, pp. 1567-1575.
200. J. Frenkel, J. Dorfman. Spontaneous and induced magnetisation in ferromagnetic bodies. Nature, 1930, Vol. 126, pp. 274-275.
201. P. Tartaj, M. del Puerto Morales, S. Veintemillas-Verdaguer, T. Gonzalez-Carreno, C. J. Serna. The preparation of magnetic nanoparticles for applications in biomedicine. Journal of Physics D: Applied Physics, 2003, Vol. 36, pp. R182-R197.
202. J. Chomoucka, J. Drbohlavova, D. Huska, V. Adam, R. Kizek, J. Hubalek. Magnetic nanoparticles and targeted drug delivering. Pharmacological Research, 2010, Vol. 62, pp. 144-149.
203. Y. Xiang, J. Wang, S. M. Hussain, G. P. Krestin. Superparamagnetic iron oxide contrast agents: physicochemical characteristics and applications in MR imaging. European Journal of Radiology, 2001, Vol. 11, pp. 2319-2331.
204. R. Singh, J. W. Lillard Jr. Nanoparticle-based targeteddrug delivery. NIH Public Access, 2009, Vol. 86, pp. 215-223.

205. L. Tong, M. Zhao, S. Zhu, J. Chen. Synthesis and application of superparamagnetic iron oxide nanoparticles in targeted therapy and imaging of cancer. Frontiers of Medicine, 2011, pp. 379-387.
206. S. Laurent, D. Forge, M. Port, A. Roch, C. Robic, L. Vander Elst, R. N. Muller. Magnetic iron oxide nanoparticles: Synthesis, stabilization, vectorization, physicochemical characterization, and biological applicationa. Chemical Reviews, 2008, Vol. 108, pp. 2064-2110.
207. C. S.S.R. Kumar, F. Mohammad,. Magnetic nanomaterials for hyperthermia-based therapy and controlled drug delivery. Advanced Drug Delivery Reviews, 2011, Vol. 63, pp. 789–808.
208. C. C. Berry, A. S. G. Curtis. Functionalisation of magnetic nanoparticles for applications in biomedicine. Journal of Physics D: Applied Physiscs, 2003, Vol. 36, pp. R198-R206.
209. S. Kubinova, E. Sykova. Nanotechnologies in regenerative medicine. Minimally, Invasive Therapy, 2010, Vol. 19, pp. 144-156.
210. Z. P. Chen, Y. Zhang, K. Xu, R. Z. Xu, J. W. Liu, N. Gu. Stability of hydrophilic magnetic nanoparticles under biologically relevant conditions. Journal of Nanoscience and Nanotechnology, 2008, Vol. 8, pp. 6260-6265.
211. Y. Luo, S. Nartker, M. Wiederoder, h. Miller, D. Hochhalter, L. T. Drzal, E. C. Alocilja. Novel biosensor based on electrospun nanofiber and magnetic nanoparticles for the detection of E. coli O157:H7. IEEE Transactions on Nanotechnology, 2012, Vol. 11, pp. 676-681.
212. R. Mincheva, O. Stoilova, H. Penchev, T. Ruskov, I. Spirov, N. Manolova, I. Rashkov. Synthesis of polymer-stabilized magnetic nanoparticles and fabrication of nanocomposite fibers thereof using electrospinning. European Polymer Journal, 2008, Vol. 44, pp. 615-627.
213. C. H. Park, S. J. Kang, L. D. Tijing, H. R. Pant, C. S. Kim. Inductive heating of electrospun Fe2O3/polyurethane composite mat under high-frequency magnetic field - hyperthermia. Ceramics International, 2013, Vol. 39, pp. 9785-9790.
214. J. Zhu, S. Wei, X. Chen. Electrospun polyimide nanocomposite fibers reinforced with core-shell Fe-FeO nanoparticles. Journal of Physical Chemistry C, 2010, Vol. 114, pp. 8844-8850.
215. L. Francis, J. Venugopal, M. P. Prabhakaran, V. Thavasi, E. Marsano, S. Ramakrishna. Simultaneous electrospun-electrosprayed biocomposite nanofibrous scaffolds for bone tissue engineering. Acta Biomaterialia, 2010, Vol. 6, pp. 4100-4109.
216. D. Gupta, J. Venugopal, S. Mitra, V. R. Giri Dev, S. Ramakrishna. Nanostructured biocomposite substrates by electrospinning and electrospraying for the mineralization of osteoblats. Biomaterials, 2009, Vol. 30, pp. 2085-2094.
217. W. Ji, F. Yang, H. Seyednejad, Z. Chen, W. E. Hennink, J. M. Anderson, J. J.J.P. van den Beucken, J. A. Jansen. Biocompatibility and degradation characteristics of PLGA-based electrospun nanofibrous scaffolds with nanopatite incorporation. Biomaterials, 2012, Vol. 33, pp. 6604-6614.
218. X. B. Zeng, H. Hu, L. Q. Xie, F. Lan, W. Jiang, Y. Wu, Z. W. Gu. Magnetic responsive hydroxyapatite composite scaffolds construction for bone defect reparation. International Journal of Nanomedicine, 2012, Vol. 7, pp. 3365–3378.
219. P. Singh, R.C. Yashroy, M. Hoque. Augmented bone-matrix formation and osteogenesis under magnetic field stimulation in vivo XRD, TEM and SEM investigations. Indian Journal of Biochemistry & Biophysics , 2006, Vol. 43, pp. 167-172.
220. B. Sprauch, M.K. Patel J.A. Navarro, M. Berdichevsky, H.L. Yu, A.A. Pilla. Pulsed magnetic fields accelerate cutaneous wound healing in rats. Plastic & Reconstructive Surgery, 2007, Vol. 120, p. 425.
221. M. C. Valmikinathan, J. Wang, S. Smiriglio, N. G. Golwala, X. Yu. Magnetically-induced protein gradients on electrospun nanofibers. Combinatorial Chemistry & High Throughput Screening, 2009, Vol. 12, pp. 656-663.
222. I. O. Smith, X. H. Liu, L. A. Smith, P. X. Ma. Nano-structured polymer scaffolds for tissue engineering and regenerative medicine. Wiley Interdisciplinary Reviews Nanomedicine and Nanobiotechnology, 2009, Vol. 2, pp. 226-236.
223. K. Lai, W. Jiang, J.Z. Tang, Y. Wu, B. He, G. Wang, Z. Gu. Superparamagnetic nano-composite scaffolds for promoting bone celproliferation and defect reparation without a magnetic field. RSC Advances, 2012, Vol. 2, pp. 13007-13017.
224. T. Yoshida, T. C. Lai, G. S. Kwon, K. Sako. pH- and ion-sensitive polymers for drug delivery. Expert Opinion on Drug Delivery, 2013, Vol. 10, pp. 1497-1513.
225. G. Qing, M. Li, L. Deng, Z. Lv, P. Ding, T. Sun. Smart drug release systems based on stimuli-responsive polymers. Mini-Reviews in Medicinal Chemistry, 2013, Vol. 65, pp. 1369-1380.

226. A. Chan, R. P. Orme, R. A. Fricker, P. Roach. Remote and local control of stimuli responsive materials for therapeutic applications. Advanced Drug Delivery Reviews, 2013, Vol. 65, pp. 497-514.
227. C. Huang, S. J. Soenen, J. Rejman, J. Trekker, L. Chengxun, L. Lagae, W. Ceelen, C. Wilhelm, J. Demeester, S. C. De Smedt. Magnetic electrospun fibers for cancer therapy. Advanced Functional Materials, 2012, Vol. 22, pp. 2479-2486.
228. C. S. Brazel. Magnetothermally-responsive nanomaterials: Combining magnetic nanostructures and thermally-sensitive polymers for triggered drug release. Pharmaceutical Research, 2009, Vol. 26, pp. 644-656.
229. V. Hasirci, E. Vrana, P. Zorlutuna, A. Ndreu, P. Yilgor, F. B. Basmanav, E. Aydin. Nanomaterials: A review of the excisting science and technology, and new approaches. Journal of Biomaterials Science, Polymer Edition, 2006, Vol. 17, pp. 1241-1268.
230. T. Neuberger, B. Schopf, H. Hofmann, M. Hofmann, B. von Rechenberg. Superparamagnetic nanoparticles for biomedical applications: Possibilities and limitations of a new drug delivery system. Journal of Magnetism and Magnetic Materials, 2005, Vol. 293, pp. 483-496.
231. M. L. Hans, A. M. Lowman. Biodegradable nanoparticles for drug delivery and targeting. Current Opinion in Solid and Materials Science, 2002, Vol. 6, pp. 319-327.
232. G. Bonadonna, L. Gianni, A. Santoro, V. Bonfante, P. Bidoli, P. Casalt, R. Demichaelis, P. Valagussa. Drugs ten years leter: epirubicin. Annals of Oncology, 1993, Vol. 4, pp. 359-369.
233. A. S. Lubbe, C. Alexiou, C. Bergemann. Clinical applications of magnetic drug targeting. Journal of Surgical Research, 2001, Vol. 95, pp. 200-206.
234. A. S. Lubbe, C. Bergemann, H. Riess, F. Schriever, P. Reichardt, K. Possinger, M. Matthias, B. Dorken, F. Herrmann, R. Gurtler, P. Hohenberger, N. Haas, R. Sohr, B. Sander, A. J. Lemke, D. Ohlendorf, W. Huhnt, D. Huhn. Clinical experiences with magnetic drug targeting: a phase I study with 4'-epidoxorubicin in 14 patients with advanced solid tumors. Cancer Research, 1996, Vol. 56, pp. 4686-4693.
235. A. S. Lubbe, C. Bergemann, W. Huhnt, T. Fricke, H. Riess, J. W. Brock, D. Huhn. Preclinical experiences with magnetic drug targeting: Tolerance and efficacy. Cancer Research, 1996, Vol. 11, pp. 4694-4701.
236. A. S. Lubbe, C. Bergemann, J. Brock, D. G. McClure. Physiological aspects in magnetic drug-targeting. Journal of Magnetism and Magnetic Materials, 1999, Vol. 194, pp. 149-155.
237. L. Wang, M. Wang, P. D. Tophamc, Y. Huang. Fabrication of magnetic drug-loaded polymeric composite nanofibres and their drug release characteristics. RSC Advances, 2012, Vol. 2, pp. 2433–2438.
238. G. Baldi, G. Lorenzi, C. Ravagli. Hyperthermic effect of magnetic nanoparticles under electromagnetic field. Processing and Application of Ceramics, 2009, Vol. 3, pp. 103–109.
239. T. C. Lin, F. H. Lin, J. C. Lin. In vitro feasibility study of the use of a magnetic electrospun chitosan nanofiber composite for hyperthermia treatment of tumor cells - hyperthermia. ACTA Biomaterialia, 2012, Vol. 8, pp. 2704-2711.
240. I. Hilger, A. W. Kaiser. Iron oxide-based nanostructures for MRI and magnetic hyperthermia. Nanomedicine, 2012, Vol. 7, pp. 1443-1459.
241. I. Sharifi, H. Shokrollahi, S.Amiri. Ferrite-based magnetic nanofluids used in hyperthermia applications. Journal of Magnetism and Magnetic Materials, 2012, Vol. 324, pp. 903-915.
242. G. V. Smith, F. Notheisz. Introduction to catalysis (Chapter 1). *Heterogeneous catalysis in organic chemistry.* Elsevier, 1999, pp. 1-28.
243. I. Fechete, Y. Wang, J. C. Vedrine. The past, present and future of heterogeneous catalysis. Catalysis Today, 2012, Vol. 189, pp. 2-27.
244. R. J. P. Williams. A comparison of types of catalyst: The quality of metallo-enzymes. Journal of Inorganic Biochemistry, 2008, Vol. 102, pp. 1-25.
245. B. Cornils, W. A. Herrmann. Concepts in homogeneous catalysis: The industrial view. Journal of Catalysis, 2003, Vol. 216, pp. 23-31.
246. M. Beller. Homogeneous catalysis for fine chemical synthesis - New trends and perspectives -. Elsevier Science, 1997, pp. 1-16.
247. P. Barbaro, F. Liguori. Heterogenized homogeneous catalysts for fine chemicals production. Springer, 2010, pp. v-x.
248. M. Boronat. Theoretical tools for studying gold nanoparticles as catalysts for oxidation and hydrogenation reactions. Catalysis, 2013, Vol. 25, pp. 50-76.

249. S. Bhaduri, D. Mukesh. Homogeneous catalysis. Mechanisms and industrial applications. Wiley - Interscience, 2000, pp. 1-11.
250. A. J. Bissette, S. P. Fletcher. Mechanisms of autocatalysis. Angewandte Chemie, 2013, Vol. 52, pp. 12800-12826.
251. H. Jia, G. Zhu, B. Vugrinovich, W. Kataphinan, D. H. Renker, P. Wang. Enzyme-carrying polymeric nanofibers prepared via electrospinning for use as unique biocatalysts. Biotechnology Progress, 2002, Vol. 18, pp. 1027-1032.
252. H. Groger, Y. Asano. Introduction - Principles and historical landmarks of enzyme catalysis in organic synthesis. Enzyme Catalysis in Organic Synthesis, Third Edition, 2012, pp. 1-17.
253. M. Song. New approaches to design of nanostructured catalysts (Chapter 4). *Catalysis: Principles, types and applications.* Nova Science Publishers, 2011, pp. 245-306.
254. M. Chen, C. Wang, W. Fang, J. Wang, W. Zhang, G. Jin, G. Diao. Electrospinning of calixarene-functionalized polyacrylonitrile nanofiber membranes and application as an adsorbent and catalyst support. Langmuir, 2013, Vol. 29, pp. 11858-11867.
255. E. Formo, E, Lee, D. Campbell, Y. Xia. Functionalization of electrospun TiO2 nanofibers with Pt nanoparticles and nanowires for catalytic applications. Nanoletters, 2008, Vol. 8, pp. 668-672.
256. P. Serp, M. Corrias, P. Kalck. Carbon nanotubes and nanofibers in catalysis. Applies Catalysis A: General, 2003, Vol. 253, pp. 337-358.
257. S. Xiao, W. Xu, H. Ma, X. Fang. Size-tunable Ag nanoparticles immobilized in electrospun nanofibers: synthesis, characterization, and application for catalytic reduction of 4-nitrophenol. RSC Advances, 2012, Vol. 2, pp. 319-327.
258. Z. Zhang, C. Shao, Y. Sun, J. Mu, M. Zhang, P. Zhang, Z. Guo, P. Liang, C. Wang, Y. Liu. Tubular, nanocomposite catalysts based on size-controlled and highly dispersed silver nanoparticles assembled on electrospun silica nanotubes for catalytic reduction of 4-nitrophenol. Journal of Materials Chemistry, 2012, Vol. 22, pp. 1387-1395.
259. L. Guo, J. Bai, C. Li, Q. Meng, H. Liang, W. Sun, H. Li, H. Liu. A novel catalyst containing palladium nanoparticles supported on PVP composite nanofiber films: Synthesis, characterization and efficient catalysis. Applied Surface Science, 2013, Vol. 283, pp. 107-114.
260. L. Guo, J. Bai, H. Liang, T. Xu, C. Li, Q. Meng, H. Liu, Y. Huang. A facile approach to preparing palladium nanoparticles-embedded polyvinylpyrrolidone (PVP) heterogeneous hybrid nanofibers mats by electrospinning. Korean Journal of Chemical Engineering, 2013, Vol. 30, pp. 2142-2150.
261. X. Fang, H. Ma, S. Xiao, M. Shen, R. Guo, X. Cao, X. Shi. Facile immobilization of gold nanoparticles into electrospun polyethyleneimine/polyvinyl alcohol nanofibers for catalytic applications. Journal of Materials Chemistry, 2011, Vol. 21, pp. 4493-4501.
262. M. Graeser, E. Pippel, A. Greiner, J. H. Wendorff. Polymer core-shell fibers with metal nanoparticles as nanoreactor for catalysis. Macromolecules, 2007, Vol. 40, pp. 6032-6039.
263. L. Gardella, A. Basso, M. Prato, O. Monticelli. PLA/POSS nanofibers: A novel system for the immobilization of metal nanoparticles. ACS Applied Materials and Interfaces, 2013, Vol. 5, pp. 7688-7692.
264. K. H. Jang, Y. O. Kang, W. H. Park. Functional cellulose-based nanofibers with catalytic activity: Effect of Ag content and Ag phase. International Journal of Biological Macromolecules, 2014, Vol. 67, pp. 394-400.
265. X. Y. Ye, Z. M. Liu, Z. G. Wang, X. J. Huang, Z. K. Xu. Preparation and characterization of magnetic nanofibrous composite membranes with catalytic activity. Materials Letters, 2009, Vol. 63, pp. 1810-1813.
266. R. Jayakumar, M. Prabaharan, K. T. Shalumon, K. P. Chennazhi, S.V. Nair. Biomedical applications of polymer/silver composite nanofibers. Advanced Polymer Science, 2012, Vol. 246, pp. 263-282.
267. M. M. Demir, M. A. Gulgun, Y. S. Menceloglu, S. S. Abramchuk, E. E. Makhaeva, A. R. Khokhlov, V. G. Matveeva, M. G. Sulman. Palladium nanoparticles by electrospinning from poly(acrylonitrile-co-acrylic acid)-PdCl2 solutions, relations between preparation conditions, particle size, and catalytic activity. Macromolecules, 2004, Vol. 37, pp. 1787-1792.
268. E. Formo, M. S. Yavuz, E. P. Lee, L. Lane, Y. Xia. Functionalization of electrospun ceramic nanofibre membranes with noble-metal nanostructures for catalytic applications. Journal of Materials Chemistry, 2009, Vol. 19, pp. 3878-3882.
269. F. Durap, O. Metin, M. Aydemir, S. Ozkar. New route to synthesis of PVP-stabilized palladium(0) nanoclusters and their enhanced catalytic activity in Heck and Suzuki croos-coupling reactions. Applied Organometallic Chemistry, 2009, Vol. 23, pp. 498-503.

270. A. Biffis, M. Zecca, M. Basato. Palladium metal catalysts in Heck C-C coupling reactions. Journal of Molecular Catalysis A: Chemical, 2001, Vol. 173, pp. 249-274.
271. A. D. Pomogailo, G. I. Dzhardimalieva. Hybrid polymer-immobilized nanosized Pd catalysts for hydrogenation reaction obtained via frontal polymerization. Journal of Catalysts, 2012, Vol. 2013, pp. 1-12.
272. M. C. Willis, G. N. Brace. Palladium catalysed enamine synthesis fromvinyl triflates. Tetrahedrom Letters, 2002, Vol. 43, pp. 9085-9088.
273. B. Basudeb, J. Satadru, M. K. Niranjan, H. B. Mosharef. Palladium-catalysed amination of halopyridines on a KF-alumina surface. [trans.] 43. Tetrahedron Letters, 2002, pp. 7967-7969.
274. L. Yin, J. Liebscher. Carbon-carbon coupling reactions catalyzed by heterogeneous palladium catalysts. Chemical Reviews, 2007, Vol. 107, pp. 133-173.
275. J. J. Masters, J. T. Link, Lawrence B. Snyder,. A total synthesis of Taxol. Angewandte Chemie International Edition, 1995, Vol. 107, pp. 1886-1888.
276. B. M. Bhanage, S. Fujita, M. Arai. Heck reactions with various types of palladium complex catalysis: application of multiphase catalysis and supercritical carbon dioxide. Journal of Organometallic Chemistry, 2003, Vol. 687, pp. 211-218.
277. C. Liu, Q. Ni, F. Bao, J. Qiu. A simple and efficient protocol for a palladium-catalyzed ligand-free Suzuki reaction at room temperature in aqueous DMF. Green Chemistry, 2011, Vol. 13, pp. 1260-1266.
278. H. C. Kolb, M. G. Finn, K. B. Sharpless. Click chemistry: Diverse chemical function from a few good reactions. Angewandte Chemie International Edition, 2001, Vol. 40, pp. 2004-2021.
279. M. Malkoch, R. Vestberg, N. Gupta, L. Mespoulle, P. Dubois, A. F. Mason, J. L. Hedrick, Q. Liao, C. W. Frank, K. Kingsbury, C. J. Hawker. Synthesis of well-defined hydrogel networks using Click chemistry. Chemistry Communication, 2006, Vol. 2006, pp. 2774-2776.
280. Z. Chang, Y. Fang, Q. Zhang, D. Chen. "Click" chmeistry for facile immobilization of iron phthalocyanines onto electrospun nanofiber surface. Chemistry Letters, 2009, Vol. 38, pp. 1144-1145.
281. W. H. Binder, R. Sachsenhofer. "Click" chemistry in polymer and material science. Macromolecular Rapid Communications, 2007, Vol. 28, pp. 15–54.
282. A. Lancuski, S. Fort, F. Bossard. Electrospun Azido-PCL nanofibers for enhanced surface functionalization by click chemistry. Applied Materials and Interfaces, 2012, Vol. 4, pp. 6499-6504.
283. D. D. Diaz, S. Punna, P. Holzer, A. K. Mcpherson, K. B. Sharpless, V. V. Fokin, M. G. Finn. Click chemistry in materials synthesis. 1. Adhesive polymers from copper-catalyzed azide-alkyne cycloaddition. Journal of Polymer Science: Part A: Polymer Chemistry, 2004, Vol. 42, pp. 4392-4403.
284. C. W. Tornøe, C. Christensen, M. Meldal. Peptidotriazoles on solid phase: [1,2,3]-Triazoles by regiospecific copper(I)-catalyzed 1,3- dipolar cycloadditions of terminal alkynes to azides. The Journal of Organic Chemistry, 2002, Vol. 67, pp. 3057-3064.
285. C. Wang, C. Feng, Y. Gao, X. Ma, Q. Wu, Z. Wang. Preparation of a graphene-based magnetic nanocomposite for the removal of an organic dye from aqueous solution. Chemical Engineering Journal, 2011, Vol. 173, pp. 92-97.
286. S. Qu, F. Huang, S. Yu, G. Chen, J. Kong. Magnetic removal of dyes from aqueous solution using multi-walled carbon nanotubes with Fe2O3 particles. Journal of Hazardous Materials, 2008, Vol. 160, pp. 643-647.
287. L. Ai, H. Huang, Z. Chen, X. Wei, J. Jiang. Activated carbon/CoFe2O4 composites: Facile synthesis, magnetic performance and their potential application for the removal of malachite green from water. Chemical Engineering Journal, 2010, Vol. 156, pp. 243-249.
288. S. Abbasizadeh, A. R. Keshtkar, M. A. Mousavian. Preparation of a novel electrospun polyvinyl alcohol/titanium oxide nanofiber adsorbent modified with mercapto groups for uranium(VI) and thorium(IV) removal from aqueous solution. Chemical Engineering Journal, 2013, Vol. 220, pp. 161–171.
289. A. R. Mahdavian, M. A. S. Mirrahimi. Efficient separation of heavy metal cations by anchoring polycrylic acid on superparamagnetic magnetite nanoparticlesthrough surface modification. Chemical Engineering Journal, 2010, Vol. 159, pp. 264-271.
290. P. Xu, G. M. Zeng, D. L. Huang, C. L. Feng, S. Hu, M. H. Zhao, C. Lai, Z. Wei, C. Huang, G. X. Xie, Z. F. Liu. Use of iron oxide nanomaterials in wastewater treatment: A review. Science of Total Environment, 2012, Vol. 424, pp. 1-10.
291. S. Cavaliere, S. Subiantoa, I. Savycha, D. J. Jonesa, J. Rozièrea. Electrospinning: designed architectures for energy conversion and storage devices. Energy and Environmental Science, 2011, Vol. 4, pp. 4761-4785.

292. R. Balamurugan, S. Sundarrajan, S. Ramakrishna. Recent trends in nanofibrous membranes and their suitability for air and water filtrations. Membranes, 2011, Vol. 1, pp. 232-248.
293. X. Zhao, L. Lv, B. Pan, W. Zhang, S. Zhang, Q. Zhang. Polymer-suported nanocomposites for environmental application: A review. Chemical Engineering Journal, 2011, Vol. 170, pp. 381-394.
294. A. R. Keshtkar, M. Irani. Removal of uranium(VI) from aqueous solutions by adsorption using a novel electrospun PVA/TEOS/APTES hybrid nanofiber membrane: comparison with casting PVA/TEOS/APTES hybrid membrane. Journal of Radioanalytical and Nuclear Chemistry, 2013, Vol. 295, pp. 563-571.
295. A. A. Taha, Y. N. Wu, H. Wang, F. Li. Preparation and application of functionalized cellulose/acetate/silica composite nanofibrous membrane via electrospinning for Cr(VI) ion removal from aqueous solution. Journal of Environmental Management, 2012, Vol. 112, pp. 10-16.
296. M. Aliabadi, M. Irani, J. Ismaeili, S. Najafzadeh. Design and evaluation of chitosan/hydroxyapatite composite nanofiber membrane for the removal of heavy metal ions from aqueous solution. Journal of the Taiwan Institute of Chemical Engineers, 2014, Vol. 45, pp. 518–526.
297. L. Wang, J. Li, Q. Jiang, L. Zhao. Water-soluble Fe3O4 nanoparticles with high solubility for removal of heavy-metal ions from waste water. Dalton Transactions, 2012, Vol. 41, pp. 4544-4551.
298. S. I. Moussa, R. R. Sheha, E. A. Saad, N. A. Tadros. Synthesis and characterization of magnetic nano-material for removal of Eu3+ ions from aqueous solutions. Journal of Radioanalytical and Nuclear Chemistry, 2013, Vol. 295, pp. 929-935.
299. M. P. Stevens. Polymer chemistry an introduction. New York, Oxford (second edition), 1990.
300. S. Mori, H. G. Barth. Size exclusion chromatography. Springer edition, 1999.
301. Z. Deyl, K. Macek. Liquid column Chromatography a survey of modern techniques and applications, journal of chromatography. Elsevier scientific publishing company, 1975.
302. C. E. Carraher's, Jr. Polymer chemistry an introduction. Marcel Dekker, Inc. (4th edition), 1996.
303. K. Panagiotou. Science and technology of polymers. Thessaloniki (second edition), 2000.
304. D.Dodos, Anastasios. Synthetic macromolecules. Kostaraki Edition, 2002.
305. I. W. Hamley. The physics of block copolymers. Oxford Science Publications, 1998.
306. M. D. Bruch. *NMR Spectroscopy Techniques.* Practical Spectroscopy Series (Second edition), 1996, Vol. 21.
307. J. Cavanagh, W. J. Fairbrother, A. G. Palmer, III, N. J. Skelton. *Protoein NMR spectroscopy.* Elsevier (Second edition), 2007.
308. J. McMurry. Organic Chemistry. Third edition, 2002.
309. Callaghan, P. T. *Principles of Nuclear Magnetic Resonance Microscopy.* Oxford Science publications, 1991.
310. Webb, G. A. *Nuclear magnetic resonance.* Royal Scociety of Chemistry, 1998, Vol. 17.
311. S. L. Flegler, J. W. Heckman, Jr., K. L. Klomparens. The scanning elelctron microspcopy. *Scanning and transmission elelctron microspcopy: An introduction.* Oxford University Press, 1993, pp. 65-89.
312. L. Reimer. Introduction. *Scanning electron microscopy: Physics of image formation and microanalysis.* Springer (second edition), 1998, pp. 1-12.
313. P. S. Grill, S. R. Sauerbrunn, M. Reading. Modulated differential scanning calorimetry. Journal of Thermal Analysis, 1993, Vol. 40, pp. 931-939.
314. G. Hohne, W. Hemminger, H.-J Flammersheim. Differential scanning calorimetry. Springer (Second edition), 2003.
315. J. D. Menczel, R. B. Prime. Thermal analysis of polymers fundamentals and applications. Wiley, 2009.
316. L. D. S. Yadav. *Organic Spectroscopy.* Springer-Science+Business Media, B.V., 2005.
317. B. M. Weckhuysen. Ultraviolet-visible spectroscopy. American Scientific Publishers, 2004, pp. 255-270.
318. L. Campbell-Verduyna, P. H. Elsinga, L. Mirfeizi, R. A. Dierckx, B. L. Feringa. 1,3-Dipolar cycloadditions of azides and arynes. Organic and Biomolecular Chemistry, 2008, Vol. 6, pp. 3461-3463.
319. M. H. Khan, P. Warwick, N. Evans. Spectrophotometric determination of uranium with arsenazo-III in perchloric acid. Chemosphere, 2006, Vol. 63, pp. 1165-1169.
320. S. B. Savvin. Analytical Use of Arsenazo III, Determination of thorium, zirconium, uranium, and rare earth elements. Talanta, 1961, Vol. 8, pp. 673-685.
321. D. Bica. Preparation of magnetic fluids for various applications. Romanian Reports in Physics, 1995, Vol. 47, pp. 265-272.

322. L. Vekas, M. V. Adveev, D. Bica. Magnetic nanofluids: Syntheisis and structure (Chapter 25). Nanoscience in Biomedicine, Springer, 2009, pp. 645-709.
323. J. S. Bradley, E. W. Hill , S. Behal , C. Klein , A. Duteil , B. Chaudret. Preparation and characterization of organosols of monodispersed nanoscale palladium. Particle size effects in the binding geometry of adsorbed carbon monoxide. Chemistry of Materials, 1992, Vol. 4, pp. 1234–1239.
324. M Salavati-Niasari, F Davar. Synthesis of copper and copper(I) oxide nanoparticles by thermal decomposition of a new precursor. Materials Letters, 2009, Vol. 63, pp. 441-443.
325. Solid-supported rhodium(0) nano-/microparticles: An efficient ligand-free heterogeneous catalyst for microwave-assisted Suzuki–miyaura cross-coupling reaction. [book auth.] C. B. Reddy, N. Aggarwal, D. Sharma, A. K. Shil, B. & P. Das N. R. Guha. Advanced Synthesis & Catalysis, 2012, Vol. 354, pp. 2911-2915.
326. H. A. Stefani, S. N. S. Vasconcelos, F. Manarin, D. M. Leal, F. B. Souza, L. S. Madureira, J. Zukerman-Schpector, M. N. Eberlin, M. N. Godoi, R. S. Galaverna. Synthesis of 5-Organotellanyl-1H-1,2,3-triazoles: Functionalization of the 5-Position Scaffold by the Sonogashira Cross-Coupling Reaction. European Journal of Organic Chemistry, 2013, Vol. 2013.
327. I. Savva, M. Efstathiou, I. Paschalidis, T. Krasia-Christoforou. Methacrylate-based nanocomposite electrospun adsorbents for the removal of Eu(III) from aqueous media. (in preparation).
328. P. Papaphilippou, A. Pourgouris, O. Marinica, A. Taculescu, G. I. Athanasopoulos, L. Vekas, T. Krasia-Christoforou. Fabrication and characterization of superparamagnetic and thermoresponsive hydrogels based on oleic-acid-coated Fe3O4 nanoparticles, hexa(ethylene glycol) methyl ether methacrylate and 2-(acetoacetoxy)ethyl methacrylate. Journal of Magnetism and Magnetic Materials, 2011, Vol. 323, pp. 557-563.
329. V. Perez-Dieste, O. M. Castellini, J. N. Crain, M. A, Eriksson, A. Kirakosian, J.-L. Lin, J. L. McChesney, F. J. Himpsela. Thermal decomposition of surfactant coatings on Co and Ni nanocrystals. Applied Physics Letters, 2003, Vol. 83, pp. 5053-5055.
330. E. Goiti, M. M. Salinas, G. Arias, D. Puglia, J. M. Kenny, C. Mijangos. Effect of magnetic nanoparticles on the thermal properties of some hydrogels. Polymer Degradation and Stability, 2007, Vol. 92, pp. 2198-2205.
331. C. C. Zhang, X. Li, C. Wang. Polymethylmethacrylate/Fe3O4 composite nanofiber membranes with ultra-low dielectric permittivity. Applied Physics A: Materials Science and Processing, 2009, Vol. 97, pp. 281-285.
332. B. K. Money, J. Swenson. Dynamics of poly(ethylene oxide) around its melting temperature. Macromolecules, 2013, Vol. 46, pp. 6949-6954.
333. A. Sodergard, M. Stolt. Properties of lactic acid based polymers and their correlationwith composition. Progress in Polymer Science, 2002, Vol. 27, pp. 1123-1163.
334. T. Gong, D. Yang, J. Hu, W. Yang, C. Wang, J. Q. Lu. Preparation of monodispersed hybrid nanospheres with high magnetite content from uniform Fe3O4 clusters. Colloids and Surfaces A: Physicochemical Engineering Aspects, 2009, Vol. 339, pp. 232-239.
335. S. Wan, J. Huang, H. Yan, K. Liu. Size-controlled preparation of magnetic nanoparticles in the presence of graft copolymers. Journal of Materials Chemistry, 2006, Vol. 16, pp. 298-303.
336. W. Jingjing, L. Dengxin. Preparation and characterization of magnetic Fe3O4 nanoparticles coated by oleic acid. Energy Procedia, 2011, Vol. 11, pp. 4794-4802.
337. D. H. Han, J. P. Wang, H. L. Luo. Crystallite size effect on saturation magnetization of fine ferrimagnetic particles. Journal of Magnetism and Magnetic Materials, 1994, Vol. 136, pp. 176-182.
338. C. Yee, Y. G. Kataby, A. Ulman, T. Prozorov, H. White, A. King, M. Rafailovitch, J. Sokolov, A. Gedanken. Self-assembled monolayers of alkanesulfonic and -phosphonic acids on amorphous iron oxide nanoparticles. Langmuir, 1999, Vol. 15, pp. 7111-7115.
339. P. Papaphilippou, L. Loizou, N. C. Popa, A. Han, L. Vekas, A. Odysseos, T. Krasia-Christoforou. Superparamagnetic hybrid micelles, based on ioron oxide nanoparticles and well-defined diblock copolymers possessing β-ketoester functionalities. Biomacromolecules, 2009, Vol. 10, pp. 2662-2671.
340. T. G. Kim, D. S. Lee, T. G. Park. Controlled protein release from electrospun biodegradable fiber mesh composed of poly(epsilon-caprolactone) and poly(ethylene oxide). International Journal of Pharmaceutics, 2007, Vol. 338, pp. 276-283.
341. E. Tombacz, A. Majzik, E. Horvat. Magnetite in aqueus medium: coating its surface and coated with it. Romanian Reports in Physics, 2006, Vol. 58, pp. 281-286.

342. R. V. Kulkarni, S. Biswanath. Electrically responsive smart hydrogels in drug delivery: A review. Journal of Applied Biomaterials & Biomechanics : JABB, 2007, Vol. 5, pp. 125-139.
343. M. Kallumadil, M. Tada, T. Nakagawa, M. Abe, P. Southern, Q. A. Pankhurst. Suitability of commercial colloids for magnetic hyperthermia. Journal of Magnetism and Magnetic Materials, 2009, Vol. 321, pp. 1509-1513.
344. Q. A. Pankhurst, T. Thanh, K. Jones, J. Dobson. Progress in applications of magnetic nanoparticles in biomedicine. Journal of Physics D: Applied Physics, 2009, Vol. 42, pp. 1-15.
345. J. P. Fortin, C. Wilhelm, J. Servais, C. Menager, J. C. Bacri, F. Gazeau. Size-sorted anionic iron oxide nanomagnets as colloidal mediators for magnetic hyperthermia. Journal of American Chemical Scociety, 2007, Vol. 129, pp. 2628-2635.
346. J. L. Bender, P. S. Corbin, C. L. Fraser, D. H. Metcalf, F. S. Richardson, E. L. Thomas, A. M. Urbas. Site-isolated luminescent europium complexes with polyester macroligands: Metal-centered heteroarm stars and nanoscale assemblies with labile block junctions. Journal of the American Chemistry Society, 2002, Vol. 124, pp. 8526-8527.
347. J. R. Bartlett, R. P. Cooney, R. A. Kyyd. Hydrolysis of europium cations in zeolite X: A fourier transform infrared spectroscopic study. Journal of Catalysis, 1988, Vol. 114, pp. 53-54.
348. M. Konstantinou, K. Kolokassidou, I. Pashalidis. Studies on the interaction of olive cake and its hydrophylic extracts with polyvalent metal ions (Cu(II), Eu(III)) in aqueous solutions. Journal of Hazardous Materials, 2009, Vol. 166, pp. 1169–1173.
349. E. Matijevic, W. Peter Hsu. Preparation and properties of monodispersed colloidal particles of lanthanide compounds. Journal of Colloid and Interface Science, 1987, Vol. 118, pp. 506-523.
350. G. R. Choppin. Actinide speciation in the environment. Journal of Radioanalytical and Nuclear Chemistry, 2007, Vol. 273, pp. 695-703.
351. I. Savva, M. Efstathiou, T. Krasis-Christoforou, I. Pashalidis. Adsorptive removal of U(VI) and Th(IV)from aqueous solutions using polymer-based electrospun PEO/PLLA fibrous membranes. Journal of Radioanalytical and Nuclear Chemistry, 2013, Vol. 298, pp. 1991-1997.
352. B. P. Baranwal, T. Fatma, A. Varma, A. K. Singh. Substitution reactions of Th(IV) acetate to synthesize nanosized carboxylate complexes. Spectrochim Acta, Part A, 2010, Vol. 75, pp. 1177-1180.
353. C. Hennig, S. Takao, K. Takao, S. Weiss, W. Kraus, F. Emmerling, M. Meyer, A. C. Scheinost. Identification of hexanuclear actinide(IV) carboxylates with thorium, uranium and neptunium by EXAFS spectroscopy. Journal of Physics: Conference Series, 2013, Vol. 430, pp. 1-5.
354. M. Konstantinou, I. Pashalidis. Speciation and spectrophotometric determination of uranium in seawater. Mediterranean Marine Science, 2004, Vol. 5, pp. 55-60.
355. Y. N. Vodyanitskii. Chemical aspects of uranium bahavior in soils: a review. Eurasian Soil Science, 2011, Vol. 44, pp. 862-873.
356. S. Seyhan, S. Merdivan, N. Demirel. Use of o-phenylene dioxydiacetic acid impregnated in Amberlite XAD resin for separation and preconcentration of uranium(VI) and thorium(IV). Hazardous Materials, 2008, Vol. 152, pp. 79-84.
357. T. Kiliari, I. Pashalidis, B. D. Symeopoulos. Selective separation of radium and uranium from aqueous solutions by Chelex-100. Journal of Radioanalytical and Nuclear Chemistry, 2012, Vol. 292, pp. 1273-1276.
358. T. Tang, C. M. Wai. Extraction of uranium with crown ether carboxylic acids for neutron activation analysis. Journal of Radioanalytical and Nuclear Chemistry, 1988, Vol. 128, pp. 61-69.
359. P. Liu, J. Wang, W. Qi, Zh. Li, JJ. Bi, WS. Wu. Adsorption of Eu(III) on MWCNTs: Effects of pH, ionic strength, solid-liquid ratio and water-soluble fullerence. Journal of Nanomaterials, 2013, Vol. 2013, pp. 1-9.
360. A. Demetriou, I. Pashalidis. Spectophotometric studies on the competitive adsorption of boric acid (B(III)) and chromate (Cr(VI)) onto iron(oxy)hydroxide (Fe(O)OH). Global NEST Journal, 2012, Vol. 14, pp. 32-39.
361. N. A. Travlou, G. Z. Kyzas, N. K. Lazaridis, E. A. Deliyanni. Functionalization of graphite oxide with magnetic chitosan for the preparation of nanocomposite dye adsorbent. Langmuir, 2013, Vol. 29, pp. 1657-1668.
362. I. Savva, T. Krasia-Christoforou. Evaluation of Electrospun Polymer-Fe3O4 Nanocomposite Mats in Malachite Green Adsorption. RSC Advances (Submitted).

363. S. Arellano-Cardenas, S. Lopez-Cortez, M. Cornejo-Mazon, J. C. Mares-Gutierrez. Study of malachite green adsorption by organically modified clayusing a batch method. Applied Surface Science, 2013, Vol. 280, pp. 74-78.
364. H. A. Chanzu, J. M. Onyari, P. M. Shiundu. Biosorption of malachite green from aqueous solutions onto polylactide/spent brewry grain films: kinetic and equilibrium studies . Journal of Polymers and the Environment, 2012, Vol. 20, pp. 665-672.
365. N. Ünlü, M. Ersoz. (51) Ünlü, N.; Ersoz, M. Adsorption characteristics of heavey metal ions onto a low cost biopolymeric sorbent from aqueous solutions. Journal of Hazardous Materials, 2006, Vol. B136, pp. 272-280.
366. X. Xiaoyi, W. Qiliang, C. H. Chul, Y. H. Kim. Encapsulation of iron nanoparticles with PVP nanofibrous membranes to maintain their catalytic activity. Journal of Mebrane Science, 2010, Vol. 348, pp. 231-237.
367. H. Fong, I. Chun, D. H. Renker. Beaded nanofibers formed during electrospinning. Polymer, 1999, Vol. 40, pp. 4585-4592.
368. S. Odenbach. Ferrofluids/magnetically controlled suspensions. Colloids and Surfaces A: Physicochemical and Engineering Aspects, 2003, Vol. 217, pp. 171-178.
369. R. D. Herculano, A. A. Alencar de Queiroz, A. Kinoshita, O. N. Oliveira jr., C. F. O. Graeff. On the release of metronidazole from natural rubber latex membranes. Materials Science and Engineering C, 2011, Vol. 31, pp. 272-275.
370. W. Huiyan, Z. Gaoke, G. Yuanyan. Photocatalytic degradation of metronidazole in aqueous solution by niobate K6Nb10.8O30. Journal of Natural Sciences, 2010, Vol. 15, pp. 345-349.
371. H. Shemer, Y. K. Kunukcu, K. G. Linden. Degradation of the pharmaceutical metronidazole via UV, Fenton and photo-Fenton process. Chemosphere, 2006, Vol. 63, pp. 269-276.
372. J. L. Atkinson, S. Vyazovkin. Thermal Properties and Degradation Behavior of Linear and Branched Poly(L-lactide)s and Poly(L-lactide-co-glycolide)s. Macromolecular Chemistry and Physics, 2012, Vol. 213, pp. 924-926.
373. K. Jamshidi, S. H. Hyon, Y. Ikada. Thermal characterization of polylactides. Polymer, 1988, Vol. 29, pp. 2229-2234.
374. A. E. Jablonski, A. J. Lang, S. Vyazovkin. Isoconversional kinetics of degradation of polyvinylpyrrolidone used as a matrix for ammonium nitrate stabilization. Thermochimica Acta, 2008, Vol. 474, pp. 78-80.
375. I. Savva, A. S. Kalogirou, A. Chatzinicolaou, P. Papaphilippou, A. Pantelidou, E. Vasile, E. Vasile, P. A. Koutentis, T. Krasia-Christoforou. PVP-crosslinked electrospun membranes with embedded Pd and Cu2O nanoparticles as effective heterogeneous catalytic supports. RSC Advances (Submitted), 2014.
376. J. S. Bradley, E. W. Hill, S. Behal, C. Klein, A. Duteil, B. Chaudret. Preparation and characterization of organosols of monodispersed nanoscale palladium. Particle size effects in the binding geometry of adsorbed carbon monoxide. Chemistry of Materials, 1992, Vol. 4, pp. 1234–1239.
377. A. Sarkar, T. Mukherjee, S. Kapoor. PVP-Stabilized copper nanoparticles: A reusable catalyst for “Click” reaction between terminal alkynes and azides in nonaqueous solvents. The Journal of Physical Chemistry, 2008, Vol. 112, pp. 3334–3340.
378. I. Panagiannouli, M. Demetriou, S. Couris, T. Krasia-Christoforou. Palladium-based micellar nanohybrids: Preparation and nonlinear optical response. RSC Advances, 2014, Vol. 4, pp. 8779-8788.
379. I. Papagiannouli, M. Demetriou, G. Chatzikyriakos, K. Iliopoulos, T. Krasia-Christoforou, S. Couris. Palladium micellar nanohybrids with tunable nonlinear optical response. Optical Materials, 2014, Vol. 36, pp. 123-129.
380. S. Venkatakrishnan, G. Veerappan, E. Elamparuthi, A. Veerappan. Aerobic synthesis of biocompatible copper nanoparticles: promising antibacterial agent and catalyst for nitroaromatic reduction and C–N cross coupling reaction. RSC Advances, 2014, Vol. 4, pp. 15003-15006.
381. M. Salavati-Niasari, F. Davar. Synthesis of copper and copper(I) oxide nanoparticles by thermal decomposition of a new precursor. Materials Center, 2009, Vol. 63, pp. 441-443.
382. V. V. Rostovtsev, L. G. Green, V. V. Fokin, K. B. Sharpless. A Stepwise huisgen cycloaddition process: Copper(I)-catalyzed regioselective ligation of azides and terminal alkynes. Angewandte Chemie International Edition, 2002, Vol. 41, pp. 2596-2599.

383. K. B. Sharpless, V. V. Fokin, V. V. Rostovtsev, L. Noodleman. Copper(I)-Catalyzed Synthesis of azoles. DFT study predicts unprecedented reactivity and intermediates. Journal of the American Chemical Society, 2005, Vol. 127, pp. 210–216.
384. B. H. Lipshutz, B. R. Taft. Heterogeneous copper-in-charcoal-catalyzed click chemistry. Angewandte Chemie International Edition, 2006, Vol. 45, pp. 8235-8238.
385. Q. Zhao, Z. Gan, Q. Zhuang. Electrochemical sensors based on carbon nanotubes. Electroanalysis, 2002, Vol. 14, pp. 1609-1603.
386. W. Yang, P. Thordarson, J. J. Gooding, S. P. Ringer, F. Braet. Carbon nanotubes for biological and biomedical applications. Nanotechnology, 2007, Vol. 18, pp. 1-12.
387. S. Ravindran, S. Chaudhary, B. Colburn, M. Ozkan, C. S. Ozkan. Covalent coupling of quantum dots to multiwalled carbon nanotubes for electronic device applications. Nanoletters, 2003, Vol. 3, pp. 447-453.
388. K. S. Lee, M. A. El-Sayed. Gold and silver nanoparticles in sensing and imaging: Sensitivity of plasmon response to size, shape, and metal composition. Journal of Physical Chemistry (B), 2006, Vol. 110, pp. 19220-19225.
389. P. K. Jain, X. Huang, I. H. El-Sayed, M. A. El-Sayed. Noble metals on the nanoscale: Optical and photothermal properties and some applications in imaging, sensing, biology, and medicine. Accounts of Chemical Research, 2008, Vol. 41, pp. 1578-1586.
390. R. Ruiz-Rosas, J. Bedia, J. M. Rosas, M. Lallave, I. G. Loscertales, J. Rodriguez-Mirasol, T. Cordero. Methanol decoposition on electrospun zirconia nanofibers. Catalysis Today, 2012, Vol. 187, pp. 77-87.
391. Y. Mei, Y. Lu, F. Polzer, M. Ballauff. Catalytic activity of palladium nanoparticles encapsulated in spherical polyelectrolyte brushes and core-shell microgels. Chemistry of Materials, 2007, Vol. 19, pp. 1062-1069.
392. B. Ding, M. Wang, J. Yu, G. Sun. Gas sensors based on electrospun nanofibers. Sensors, 2009, Vol. 9, pp. 1609-1624.
393. B. Ding, M. Wang, X. Wang J. Yu, G. Sun. Electrospun nanomaterials for ultrasensitive sensors. Materials Today, 2010, Vol. 13, pp. 16-27.
394. V. K. Vendra, L. Wu , S. Krishnan. Polymer thin films for biomedical applications. Nanostructured Thin Films and Surfaces., 2010, Vol. 5, pp. 1-54.
395. F. Meng, Y. Zhan, Y. Lei. Electrospun magnetic fibrillar polyarylene ether nitriles nanocomposites reinforced with Fe-phthalocyanine/Fe3O4 hybrid microspheres. Journal of Applied Polymer Science, 2012, Vol. 123, pp. 1732-1739.
396. S. Xie, Q. Zhu, B. Wang, H. Gu, W. Liu, L. Cui, L. Cen, Y. Cao. Incorporation of tripolyphosphate nanoparticles into fibrous poly-(lactide-co-glycolide) scaffolds for tissue engineering. Biomaterials, 2010, Vol. 31, pp. 5100-5109.
397. H. Liu, E. B. Slamovich, T. J. Webster. Less harmful acidic degadation of poly(lactic-co-glycolic acid) bone tissue engineering scaffolds through titania nanoparticle addition. Intrnational Journal of Nanomecine, 2006, Vol. 1, pp. 541-545.
398. —. Increased osteoblast functions on nanophase titania dispersed in poly-lactic-co-glycolic acid composites. Nanotechnology, 2005, Vol. 16, pp. S601-608.
399. D. Qi, X. Kang, L. Chen, Y. Zhang, H. wei, Z. Gu. Electrospun polymer nanofibers as a solid-phase extraction sorbent for the determination of trace pollutants in environmental water. Analytical and Bioanalytical Chemistry, 2008, Vol. 390, pp. 929-938.
400. Skoog, Holler, Nieman. Principles of instrumental analysis. 1998.
401. H. Liu, E. B. Slamovich, T. J. Webster. Improved dispersion of nanophase titania in PLGA enhances osteoblast adhesion. Ceramic Nanomaterials and Nanotechnology III, 2005, Vol. 159, pp. 247-255.